# Theoretical description of water splitting on $TiO_2$ and combined $Mo_2C$-graphene based materials

DISSERTATION

zur Erlangung des akademischen Grades

Doctor rerum naturalium
(Dr. rer. nat.)

vorgelegt

der Fakultät Mathematik und Naturwissenschaften
der Technischen Universität Dresden

von

M.Sc., Fermín Rodríguez Hernández

geboren am 04.11.1987 in Alquízar, La Habana, Kuba

Eingereicht am 12.05.2017

Gutachter:

Prof. Dr. rer. nat. habil. Gotthard Seifert

Prof. Dr. rer. nat. habil. Sibylle Gemming

# Contents

**Appendices**

# List of Abbreviations

| | |
|---|---|
| **BOA** | **B**orn-**O**ppenheimer **A**pproximation |
| **BZ** | **B**rillouin **Z**one |
| **DFT** | **D**ensity **F**unctional **T**heory |
| **DoF** | **D**egrees **o**f **F**reedom |
| **ECC** | **E**lectro**c**hemical **C**ell |
| **FTIR** | **F**ourier **T**ransform **I**nfra**r**ed Spectroscopy |
| **GGA** | **G**eneralized **G**radient **A**pproximation |
| **GTO** | **G**aussian-**T**ype **O**rbital |
| **HER** | **H**ydrogen **E**volution **R**eaction |
| **HF** | **H**artree-**F**ock |
| **HFR** | **H**igh **F**requency **R**egion |
| **IHP** | **I**nner **H**elmholtz **P**lane |
| **IR** | **I**nfra**r**ed Spectroscopy |
| **IS** | **I**mpedance **S**pectroscopy |
| **KS** | **K**ohn-**S**ham |
| **LDA** | **L**ocal **D**ensity **A**pproximation |
| **LDSA** | **L**ocal **D**ensity **S**pin **A**pproximation |
| **LFR** | **L**ow **F**requency **R**egion |
| **MFR** | **M**iddle **F**requency **R**egion |
| **MM** | **M**olecular **M**echanics |
| **NC** | **N**ano**c**rystal |
| **NG** | **N**itrogen-Doped **G**raphene Layer |
| **NP** | **N**anoparticle |
| **OER** | **O**xygen **E**volution **R**eaction |
| **OHP** | **O**uter **H**elmholtz **P**lane |
| **PAW** | **P**rojector **A**ugmented **W**ave |
| **PBC** | **P**eriodic **B**oundary **C**onditions |
| **PEC** | **P**hoto**e**lectrochemical **C**ell |
| **PES** | **P**otential **E**nergy **S**urface |
| **PVDS** | **P**artial **V**ibrational **D**ensity of **S**tates |
| **QA** | **Q**uadratic **A**pproximation |
| **QM** | **Q**uantum **M**echanics |

| | |
|---|---|
| **RDS** | **R**ate **D**etermining **S**tep |
| **SCF** | **S**elf **C**onsistent **F**ield |
| **STM** | **S**canning **T**unneling **M**icroscopy |
| **TISE** | **T**ime **I**ndependent **S**chrödinger **E**quation |
| **TM** | **T**ransition **M**etal |
| **TST** | **T**ransition **S**tate **T**heory |
| **TZV** | **T**riple-**Z**eta **V**alence Basis Set |
| **VDS** | **V**ibrational **D**ensity of **S**tates |
| **ZPEC** | **Z**ero **P**oint **E**nergy **C**orrection |

# Chapter 1

# Introduction

One of the most imperative problems of the humankind at present is to find new energy sources, and to develop efficient ways to exploit them, before the fossil fuels are complete exhausted. Solar energy represents, at present, the most promising alternative energy source due to several factors: -the amount of energy arriving to the earth surface per unit of time (e.g., in one day) largely exceeds current and envisaged levels for human needs of energy consumption; -it is going to last at least as long as life in the planet is possible; -it is innocuous for the natural environment, etc. However, several technical difficulties need to be overcome in order to attain its large scale applicability [1]. Both, the efficiency in the conversion of solar energy into more treatable ones (e.g., electrical, chemical) and, the storage and accessibility of the collected energy are two of the drawbacks which hinder the scalability of the usage of solar energy in the society.

The use of molecular hydrogen as energy carrier has been devised as a possible solution on the road towards the solar era. The transformation from solar to chemical energy could be accomplished by $H_2$ production. The highly exothermic recombination of $H_2$ and $O_2$ to form water in fuel cells leads the production of electricity, accompanied by the consumption of hydrogen and oxygen which can be taken from the atmosphere. There are some issues for the use of hydrogen to produce electricity, for example: the energetic efficiency of $H_2$ production and the difficulties associated with $H_2$ storage [2]. Although the use of hydrogen as energy carrier represents a potentially remarkable element, for the scalability of the solar energy technologies, it is clear that its applicability extends beyond the solar industry (i.e., $H_2$ production devices may be coupled to any source of energy). For instance, there is a special interest in the combination of various renewable energy sources with $H_2$ production as an efficient way of energy storage.

There are several processes which can be used to produce molecular hydrogen [2]. The decomposition of water molecules is one of the more suitable for energetic applications due to different advantages: the abundance of water, the relatively simple way to employ renewable energy sources to split $H_2O$ by electrolysis, the only residual of the process is oxygen, etc. The water splitting may take place in an electrochemical cell (ECC), which can be powered with electricity generated using any renewable energy supply. There exist even simpler devices such as photoelectrochemical cells (PEC) or photocatalytic solutions. Both PEC and photocatalytic solutions make direct use of the solar energy to obtain hydrogen and oxygen from water. The former consists in an electrochemical cell which can absorb light within an electrode to steer the reaction, whereas in the later the light is absorbed by the photocatalytic particles in the solution, and the water is decomposed at the surfaces of the dissolved particles.

Since the pioneering work of Fujishima and Honda [3], when they discovered the photocatalytic activity of $TiO_2$ electrodes, for the water splitting in a photoelectrochemical cell, a significantly amount of work has been devoted to the research of the photocatalytic activity of many other materials [4]. There has been an enormous interest in the properties of transition metal oxides to support the so-called oxygen evolution reaction (OER), to understand their photocatalytic activity in PECs and the possibility to use them as an alternative to the more expensive noble metals as cathodes in electrochemical cells [5]. While pure titanium dioxide is not a particularly promising material for the OER (Iridium and Ruthenium metal oxides behave significantly better than $TiO_2$), it is widely used as a model system for the study of this phenomenon. $TiO_2$-based electrodes (i.e., samples of $TiO_2$ with defects, transition metal (TM) impurities and special conformations like nanocrystals (NCs)) increase the efficiency of $TiO_2$ as a catalyst for the OER, approaching the performance of $IrO_2$- and $RuO_2$-based electrodes, while the later materials are both very expensive and rare on the earth crust [6]. Due to this fact, the improvement of the efficiency of $TiO_2$-based electrodes for OER on electrochemical and photoelectrochemical cells is still a very active field of research [7–15].

Likewise, the effectiveness of the hydrogen evolution reaction (HER) on the cathode is also of remarkable importance for the electrocatalytic water decomposition in the cell. Noble metals, specially platinum, are very well known for their high electrocatalytic activities for the HER, but their use in large scale technological applications is hampered by the high cost and scarcity of those metals. Thus, seeking of new materials to enhance the HER activity with low overpotentials (additional electromotive force needed to steer the electrochemical reaction), as well as for OER is of remarkable importance for the development of water splitting as an efficient way to produce $H_2$ for energetic applications.

Both the OER and the HER belong to the field of heterogeneous catalytic processes, i.e., the catalysts (electrodes) and the reactants (water molecules in the electrolyte) are in different phases. Additionally, they involve electron transfer reactions which can be steered with an external electromotive force. In an ECC, the main energetic consumption of water electrolyzers is due to the electrical power losses, which is proportional to the voltage of the supply powering the cell. At thermodynamic equilibrium, the electrochemical cell is charged and the electric potential between the electrodes $E^\circ$ is about 1.23 V at standard conditions (i.e., $pH = 0$, $p = 1$ bar, $T = 298$ K) [16]. Typical electrolyzers work with voltages $U \sim 1.9$ V and current densities $j \sim 10$ mA×cm$^{-2}$. The difference $\eta = U - E^\circ \sim 0.67$ V is the overpotential of the reaction at the working conditions of the ECC, and a contribution of about 0.5 V is due to the OER [17,18]. From the thermodynamic point of view, an ideal catalyst is characterized by a null overpotential ($\eta = 0$ V). This means that the reaction free energies for the processes which are part of the complete water splitting mechanism (i.e., the OER and the HER) are zero at the equilibrium potential $E^\circ = 1.23$ V. However, real catalysts do present finite overpotentials depending on the free energy barriers of the various intermediate processes which constitutes the OER and HER.

The efficiency of the electrolyzer can be measured in several ways [18]. One magnitude which describe the performance of the overall process is the Faradic efficiency $\Theta_{Faradic}$. It is defined as the ratio between the equilibrium potential $E^\circ = 1.23$ V and the cell potential $U = E^\circ + \eta$, needed to attain the target density current (for example $j = 10$ mA×cm$^{-2}$):

$$\Theta_{Faradic}(\eta) = \frac{E^\circ}{E^\circ + \eta}. \tag{1.1}$$

Using the aforementioned typical value for $\eta = 0.67$ V, the Faradic efficiency of the classical electrolyzers with respect to the ideal catalyst is, according to eq. (1.1), $\Theta_{Faradic}(0.67\text{ V}) = 0.65$. Since the overpotentials of the OER and HER represent the main sources of energy losses in the electrochemical cells, a strong effort has been devoted to design and synthesize new materials with higher catalytic activities for both the OER and HER [19–37]. Additionally, low costs and abundance are important aspects to be considered for row materials in order to use them as electrodes in large scale applications.

A detailed knowledge of the kinetics of both $O_2$ and $H_2$ evolution at the surface of the electrodes is needed to decrease the overpotentials for the OER and HER. Several experimental and theoretical works have been carried out to investigate the detailed mechanisms of both reactions on different surfaces [38–40]. Specifically, $TiO_2$ surfaces are among the most intensively studied systems with regard to the OER. Titanium dioxide, in its natural form, may be encountered forming the following crystalline structures: rutile, anatase and brookite. Rutile is the most abundant of them, while the other two are metastable structures and can evolve to rutile after being heated above 600 ℃. The crystallographic plane which characterize the face of the electrode exposed to the electrolyte, is a sensitive attribute to the catalytic activity of the surface. The adsorption of water on $TiO_2$ rutile (110) have been studied experimentally by Henderson in the last two decades [41–44]. Among other issues, it was established that the defects of the (110) surface constitute preferential adsorption sites for the water molecules which decompose themselves in the OER. The water-$TiO_2$ interface has been investigated by different experimental techniques [45–50]. For instance, ultraviolet photoelectron spectroscopy has been used to determine that $H_2O$ is chemisorbed on $TiO_2$ rutile (110) at low temperatures ($T < 160K$), while at higher temperature it is decomposed forming two $OH^-$ groups attached to the surface [45, 46]. One of them is formed by the decomposition of the water molecule, while the oxygen atom of the second one is removed from the titanium dioxide surface. There has been also found some disagreement between the observations reported in the scientific literature. For example, it has been suggested that $Ti^{3+}$ sites are needed for the dissociative adsorption of water on $TiO_2$ rutile (100) [47], while the opposite conclusion is supported by the results of photoemission and scanning tunneling microscopy (STM) experiments [48–50].

The mechanism of photoreduction of water in $TiO_2$-based photoelectrochemical cells is also not fully understood. Since the discovery of photocatalytic activity in $TiO_2$ electrodes, there has been an enormous interest in the amplification of the photoactivity and the description of the microscopic details of the photochemical reaction. Early works suggested that photogenerated holes can produce hydroxyl groups from the water molecules in the interface of the anodes [51–53]. The generation of the oxygen peroxide compound has been considered after the recombination of two $OH^-$ groups [54, 55]. Short live-time states like the structure (Ti-O-O-Ti) have been proposed as intermediates for the OER on rutile $TiO_2$ surfaces based on Fourier transform infrared spectroscopy (FTIR) experiments [56]. The photogeneration of $O_2$ on Pt and Nitrogen doped $TiO_2$-based electrodes has been studied by transient absorption spectroscopy [57,58]. They suggested that the photogenerated holes are required to have a life-time larger than 0.4 ps to be able to induce the $O_2$ evolution.

For the HER in electrochemical cells, a large number of metal-based catalysts has been identified, ranging from Pt and noble metals electrodes to a family of transition metals like: Co, Ni, Fe, Mo [59]. Nevertheless, different issues hamper the implementation of most of them in practical and commercial applications: the high cost, the scarcity of noble metals, and the instability due to the effect of corrosion in acidic media of transition metals [60–62]. A new generation of materials based on carbon and metal-free components has been considered very recently as an alternative to the cathodic and anodic catalysts for $H_2$ and $O_2$ evolution [59, 63–66]. Yao Zheng and coworkers have synthesized a metal-free complex composed by the deposition of $C_3N_4$ groups upon a nitrogen-doped graphene layer (NG). This nano-structured material ($C_3N_4$@NG) shows an electrocatalytic activity for the HER of the same order than metal-based electrocatalysts [59]. This hybrid compound opened the door for seeking and design new metal-free materials with higher catalytic activity for the HER.

Computational simulations have demonstrated to have a significant importance in elucidating the detailed mechanism of both OER and HER in electrochemical and photoelectrochemical cells. They permit the access to special conditions which can not be accessed experimentally, and the evaluation of specific effects which could not be separated otherwise from many others present in determined natural conditions. Many studies of the water decomposition have been also done from the theoretical chemistry perspective. For instance, density functional theory (DFT) has been used to study the electron transfer process between water molecules and the $TiO_2$ rutile (110) surface as the anodic reaction in a photoelectrochemical cell [67]. They estimated an overpotential of 0.78 V for the overall water splitting reaction at standard thermodynamic conditions. The same surface (i.e., $TiO_2$ rutile (110)) was considered to evaluate the influence of TM doping on the activity for the OER, in agreement with experimental results, and an improvement of the activity was found when the surface is doped with TMs [68]. Additionally, several $TiO_2$ anatase surfaces (i.e., (101), (102) and (001)) have been investigated to evaluate also the activity of the OER in aqueous media [69]. No significant differences were observed in the overpotentials, but they were higher than that corresponding to the reaction on $TiO_2$ rutile (110). The HER has been studied, within the framework of DFT, in a number of Pt surfaces as well as in a collection of metal electrodes [70]. The adsorption free energy of the hydrogen could be of paramount importance in the description of the HER activity. Considering metal-free electrodes, specifically the novel hybrid compound $C_3N_4$@NG, different pathways were analyzed to study the HER from the kinetic point of view [59]. They found that the reaction mechanism depends sensitively on the external potential: one reaction path is more probable at low overpotentials ($\eta < 0.33$ V), while a second mechanism is preferred at higher overpotentials.

Despite the tremendous amount of experimental and theoretical works regarding the microscopic characterization of the water decomposition at the surface of the electrodes, there is a lack of understanding concerning the detailed mechanism of the reactions. In this work we investigate both the OER and HER in different model systems, which stand for the surface of the electrodes in an electrochemical or photoelectrochemical cell (ECC and PEC, respectively).

The present work is structured as follows. After the table of content, a list of abbreviations distributed along the entire document is presented. The general topic and the major parts of this thesis are outlined in the introduction. A comprehensive overview of the water splitting on ECC and PEC, as well as the primary theoretical methods to study electrocatalytic reactions from a microscopic point of view are presented in Chap. 2. The Chapters 3, 4 and 5 encompass the major findings of this study.

The OER at the $TiO_2$-based anodes is considered in Chap. 3. New reaction mechanisms for the OER on a number of molecular representations of $TiO_2$ electrodes are proposed there. The energetics of the OER is investigated using electronic structure calculations based on Density Functional Theory (DFT). For each reaction pathway, the free energy profile is computed, at different biases, from the DFT energies, the entropic and the zero-point energy contributions. The mechanisms explored in Chap. 3 are found to be energetically more feasible than alternative reaction pathways considered in previous theoretical works based on molecular representations of the $TiO_2$ surfaces. The representation of the surface of specific, commonly occurring, titanium dioxide crystals (e.g., rutile and anatase) within the small cluster approximation is able to reproduce qualitatively the rutile (110) outperforming of the anatase (001) surface. The main results presented in Chap. 3 have been already published [71].

We subsequently investigate the influence of doping $TiO_2$ surfaces with transition metals (TMs) on the performance of $TiO_2$-based electrodes for the water splitting electrochemical reaction Chap. 4. As a direct extension of the Chap. 3, two cluster models of the TM-doped active sites which resemble both the $TiO_2$ anatase (001) and rutile (110) surfaces, respectively, are considered for the evaluation of the water decomposition reaction when a Ti is replaced by a TM atom. A set of TMs spanning from Vanadium to Nickel is considered. The late TMs explored here: Fe, Co and Ni are found to reproduce the observed experimental trends for the overpotentials in $TiO_2$-doped electrodes. In the case of Cr and Mn, the present study predicts an enhancement of the OER activity for the anatase-like clusters while a reduction of this activity is found for the rutile-like ones. The vanadium-doped structures do not show relevant influence in the OER activity compared to pure $TiO_2$-based cluster models. The main results presented in Chap. 4 have been already published [72].

The Chap. 5 is devoted to the theoretical study of the HER on recently found materials based on the synergistic combination of molybdenum carbide and graphene layers. Two major structural models are proposed there to describe the HER mechanism within the framework of DFT: $Mo_2C$-based clusters adsorbed on carbon nanosheets and the $Mo_2C$ (001) surface covered by pure and nitrogen-doped graphene layers. The former system evaluates the influence of $Mo_2C$ nanoparticles adsorbed on carbon nanosheets towards the HER. The second one is employed to gain insight about the high HER activity observed in molybdenum carbide anchored on nitrogen-doped porous carbon nanosheets ($Mo_2C$@2D-NPC), recently synthesized [73]. The H-adsorption free energy has been used as a principal descriptor to asses the HER activity at the proposed model active sites. The H-adsorption free energy resembles the one for the best state of the art catalyst for the HER (i.e., platinum at carbon substrate Pt@C) in some of the proposed structural models. Furthermore, a $pH$-correction is added within a simplified model, to the H-adsorption free energy barrier in every proposed structure. The $pH$ dependence of the H-adsorption free energy barriers allows the assessment of the HER at acidic and alkaline conditions simultaneously. An overall agreement with experimental results is found and further predictions, promoting the development of better HER catalysts, have been done. The results presented in Chap. 5 have been partially published in a combined experimental and theoretical contribution [73].

A compact summary of the complete work is presented in the General Conclusions. Supporting information regarding the discussed results is provided in the Appendices, and a detailed list of consulted references can be found in the Bibliography. This thesis finish with some lines devoted to acknowledge a number of people and institutions without their help and support it had not been possible to arrive at this point.

# Chapter 2

# Theoretical background

## 2.1 Introduction

Describing catalytic and electrocatalytic reactions within a theoretical approach is not a simple task. It requires the combination and the synergistic contribution of several methodologies, both microscopic and macroscopic, which make possible the study of different aspects of remarkable importance in determining the physical and chemical properties that underlay these processes. Among other aspects, obtaining realistic estimates of the catalytic activity of materials demands an accurate modeling of, for instance, the configurational and electronic state of the catalyst surface, the structure of the solvent, the solid-liquid interface as well as the possible mechanisms of the target reaction [74].

The electronic structure of surfaces is considered to have a direct impact on their catalytic activity. Computational simulations based on DFT have been extensively used to study the catalytic properties of several surfaces of interest for technological applications. For example, they played an important role in the development of low-cost materials which can act as catalysts to reduce carbon-, nitrogen- and sulfur-oxides from car exhaust system emissions. Moreover, a significant contribution in the design of efficient metal-, zeolite- and oxide-based catalysts have been provided by the investigation of the corresponding reaction mechanisms via theoretical calculations [75]. The solid-liquid interface, the collective behavior of the solvent constituents as well as the microscopic details of the reaction mechanisms determine the complex multidimensional free energy surface on which the reaction evolves. The exact evaluation of activation free energies in most of real systems is far beyond the current capabilities of statistical theories such as standard Transition State Theory (TST). Nevertheless, a lot of progress have been made since this theory was formulated back in 1935 by Henry Eyring [76]. Nowadays, different extensions of TST are employed, combined with suitable approximations for multidimensional systems, to determine the free energy of transition states for specific reaction mechanism and to study the kinetics of the reaction afterwards [77].

Usually, the complete understanding of catalytic or electrocatalytic processes implies the theoretical description of reaction steps which manifest a highly quantum mechanical behavior. To achieve this goal, it is necessary to solve the Schrödinger equation, in conditions which emulate those of reactions occurring at solid surfaces. Such reactions involve a huge amount of degrees of freedom and the solution of the Schrödinger equation becomes a tremendous difficultly task. However, there is a growing interest on theoretical calculations of such phenomena, since they play an important role in the determination of magnitudes which are not directly accessible experimentally, as well as for the evaluation of specific effects which come as a result of the interplay of several factors that can not be isolated under experimental conditions. There are different approaches to treat the same problem depending on its characteristic spatial and temporal scales, for example: the atomistic and electronic scale, the mesoscopic scale and the macroscale. Nevertheless, processes in nature often operate simultaneously at all of them and, subsequently, the solution of the equations of motion gets very complicated.

The present chapter is devoted to expose an overview of the theoretical techniques, commonly used to approach the detailed description of catalytic and electrocatalytic processes in electrochemical cells. The next two sections are dedicated to the solid-liquid interface and the kinetics of typical reactions which occur at these interfaces, for instance the oxygen evolution reaction (OER). The typical equilibrium charge-configurations of the interfaces are discussed for both cases: metal-liquid and semiconductor-liquid junction. A survey of models, employed in the estimation of the electrostatic potential profile across the interface, is presented, as well as the standard scheme to compute non-equilibrium current densities, upon an external potential is connected to the cell and charge-transfer reactions in stationary regimes are established. In Sec. 2.4 a detailed description of the suitable thermodynamical methodology, developed to evaluate the catalytic activity by the estimation of the overpotential, is considered. A practical descriptor to evaluate potential catalytic surfaces toward the hydrogen evolution reaction (HER), from a microscopic point of view, is presented in Sec. 2.5. Furthermore, the basis of electronic structure calculations is shown in Sec. 2.6, while relevant aspects for the microscopic description of atomic structures, along the catalytic reactions occurring on top of the electrode surface, are presented in Sec. 2.7.

## 2.2 Reaction mechanisms at solid-liquid interfaces

There are a number of chemical reactions which requires solid catalysts to take place at reasonable rates. If the species involved in the reaction are in the gas or liquid phase, such catalytic processes are called heterogeneous. The adsorption of a reactant on the surface, and its modification occur before the reaction with a second reactant starts. This is an usual reaction step in heterogeneous catalysis. The chemisorption on the surface and the subsequent reaction need to be described quantum-mechanically, in particular considering the electronic structure of the whole system. However, the latter is not composed by a few isolated particles, but fragments in a condense phase system. This fact makes the solution of the Schrödinger equation prohibitively expensive from the computational point of view, and different approximations need to be considered.

The electronic structure of the molecular degrees of freedom (DoF), as well as the electronic states of the surface are usually described using state of the art methodologies for electronic structure calculations. The molecules of the solvent may be taken into account employing a set of methods which are divided in two important groups:

i) Explicit description of solvents. Within this approach, a number of individual molecules are considered to study the influence of the solvent on the target reaction [78, 79]. The accessibility to relevant information, related to the structure of the solvent and the solvent-solid interface along the reaction mechanism, is the main feature of this formalism [80]. However, a full quantum mechanical formulation limits the number of particles which can be used to describe the solvent. To address this issue, several methodologies, based on classical and semiclassical approximations, have been developed for the description of the solvent. In the classical limit, the quantum-mechanical treatment of the electronic structure is replaced by force fields parameterizing the interactions between atoms or groups of atoms. In the so-called QM/MM methods, semiempirical force fields are used to deal with a classical part of the system (MM), while a family of hybrid models have been developed to treat the interaction between the classical and quantum-mechanical (QM) part [81–85].

ii) Implicit description of solvents. In this formalism, the molecules that participate in the reaction are placed in a cavity inside the solvent, specially constructed, and the effects of the solvent on the solute are estimated replacing the former by a continuous polarized medium outside the cavity [86, 87]. The electrostatic interaction between the particles involved in the reaction and the polarized surrounding results in an effective interaction potential $V_{es}(\mathbf{r})$ which can be evaluated, at thermodynamic equilibrium, by the Poisson-Boltzmann equation [74]:

$$\nabla[\varepsilon(\mathbf{r})\nabla V_{es}(\mathbf{r})] = -4\pi[\rho^f(\mathbf{r}) + \sum_i c_i^\infty \, z_i \, \lambda(\mathbf{r}) \exp(-z_i \frac{V_{es}(\mathbf{r})}{k_B T})] \cdot \tag{2.1}$$

Here, $\varepsilon(\mathbf{r})$ represents an effective dielectric constant of the solvent, $V_{es}$ is the electrostatic interaction potential, $\rho^f$ is the charge density of the reactants inside the cavity, $c_i$ is the bulk concentration of the ions with charge $z_i$, and $\lambda(\mathbf{r})$ is a function of the space coordinates which determine whether or not the solvent can access the position $\mathbf{r}$. The interaction energy $V_{es}$ includes two contributions for the total free energy:

$$\Delta G^{solv} = \Delta G^{chg} + \Delta G^{cav}. \tag{2.2}$$

Where $\Delta G^{chg}$ stands for the contribution of the reactants, and $\Delta G^{cav}$ correspond to the polarization of the cavity.

### 2.2.1 Charge transfer at metal-liquid interfaces

Electrodes constitute a special kind of surfaces where electrons can flow: -in (anode) and -out (cathode) as part of the so called electron transfer reactions. These reactions are extremely important for many processes like: the power production in chemical batteries, the electron conduction in metals, semiconductors and all electronic devices. In addition, most of the natural processes which involve electron transfer reactions are inefficient from the energetic point of view. Thus, understanding the kinetic properties of such reactions is of remarkable importance for the developing of many technological applications. By instance, more efficient ways to extract energy from chemical reactions.

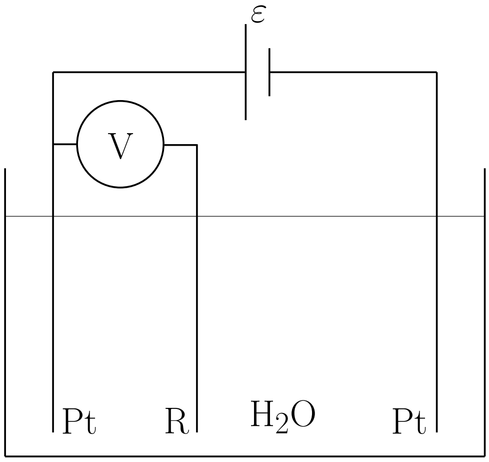

**Figure. 2.1.** *Simplified scheme of an electrochemical cell. In this case there is a direct power supply (ε), a voltmeter (V), a reference (R) and two platinum (Pt) electrodes immersed in water.*

The electron transfer reactions are typically studied in electrochemical cells. A simplified scheme of one of these devices is presented in Fig. 2.1. For illustrative purposes, we chose a configuration with two platinum electrodes (Pt) and a reference electrode (R), which might be the Standard Hydrogen Electrode (SHE): commonly used in electrochemistry [16]. The electromotive force (emf) $\varepsilon$, in Fig. 2.1, has been located in such a way that the electric current flows counterclockwise. In this situation, the left electrode acts as the anode, while the right one is the cathode. The structure of the electrolyte in contact with the electrodes plays an important role in the performance of electron transfer reactions at electrochemical cells. The creation of an equilibrium charge distribution in the cell and the establishment of a stationary current density are important aspects to be addressed in the description of electrocatalytic processes at microscopic and mesoscopic scales. A threshold potential needs to be applied in order to get an electric current circulating trough the cell. This potential depends on the set of chemical transformations occurring in the cell (i.e., the reactions at both electrodes which are known as half-reactions). In the case of water decomposition, at standard thermodynamic conditions, more than 1.23 V is necessary for the reaction to occur, eq. (2.27). If the external bias $\varepsilon$ is smaller than the threshold potential, then the electrochemical cell is charged and it behaves as two capacitors located at the interfaces. When the electrode (R) moves from left to right in Fig. 2.1, the electrostatic potential $\phi$ behaves as it is illustrated in Fig. 2.2. Two sharp potential drops of the electric potential occur at the interfaces, while it remains constant in the solution. When a current is flowing through the cell, there is also an additional potential drop $\Delta\phi$ related with the ohmic effect in the solution (i.e., $\Delta\phi = -i \times R$, $R$ being the overall resistance of the liquid).

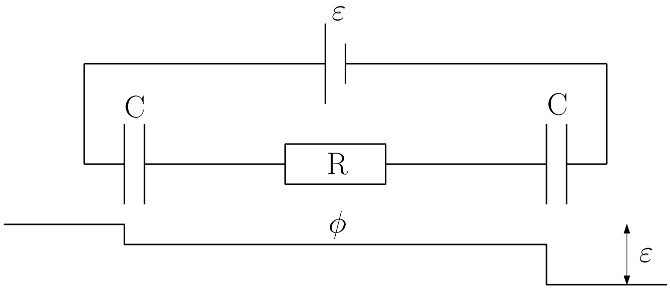

**Figure. 2.2.** *Representation of the Helmholtz model for the electrochemical cell.*

The structure of the solvent at the interfaces depends on the external potential, so the effective capacity does too. There have been several attempts to describe the structure of the liquid-solid interface, and different models have been developed. For example, in order of increasing complexity: the Helmholtz model, the Gouy-Chapman model, the Stern model and the Bockris-Devanathan-Muller model [88]. The last one, which is the most sophisticated, considers water dipoles adsorbed on the electrodes with two possible orientations: either the positive or the negative center are pointing to the surface of the electrode. This model is a natural extension of the previous ones where two planes of ions with different signs parallel to the electrode surface are included, they are known as: the Inner Helmholtz Plane (IHP) and the Outer Helmholtz Plane (OHP). These planes are separated by water dipoles attached to the ions. Between the OHP and the bulk solvent there is a diffuse layer of counter ions (i.e., whose electrical charge has opposite sign with respect to the charges on the surface), Fig. 2.3. This model is the most accepted to explain, e.g., the capacity vs voltage dependence, observed experimentally.

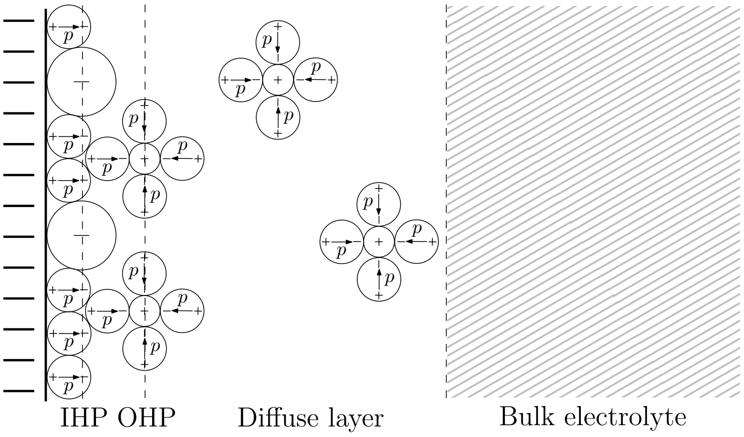

**Figure. 2.3.** *Representation of the Bockris-Devanathan-Muller model for electrochemical cells.*

If the external potential exceeds the threshold potential, then an electric current will start to flow through the cell. The behavior of this current is governed by the electron transfer reactions taking place at the electrodes. These are redox reactions, due to the reduction and oxidation processes occurring at the anode and cathode, respectively, and they can be characterized by the flux of products created at every electrode. This flux is defined as the amount of material produced at the unit area of electrode surface per unit of time.

When a first-order heterogeneous rate law is considered, the product flux $\nu$ may be written as follows, in terms of the molar concentration of the reactants $n[reactants]$:

$$\nu = k\,n[reactants]. \tag{2.3}$$

The redox processes on the electrodes have always two contributions. They are also known as half reactions: the oxidation Red $\rightarrow$ Ox + e$^-$, and the reduction Ox + e$^-$ $\rightarrow$ Red. In reactions where only one e$^-$ is transferred, the corresponding current density is obtained by the flux of the product species in the reaction multiplied by the Faraday's constant (which is defined as the absolute value of charge of a mole of electrons) $F = N_a \times e = 96485.3$ C/mol. The direction of the current is conventionally taken as opposite to the direction of motion of the electrons. Hence, the following expressions can be written down for the cathodic and anodic currents, respectively:

$$j_c = F\,k_c\,n[\mathrm{Ox}], \tag{2.4}$$

$$j_a = F\,k_a\,n[\mathrm{Red}]. \tag{2.5}$$

The rate constants $k_c$ and $k_a$ may be obtained experimentally and, up to some extent, estimated theoretically using Transition State Theory (TST). The total current density through an electrode is the sum of both contributions: eqs. (2.5) and (2.4):

$$j = F\,k_a\,n[\mathrm{Red}] - F\,k_c\,n[\mathrm{Ox}]. \tag{2.6}$$

This definition implies that, when the current density has positive values, the anodic contribution is higher than the cathodic one.

After the equilibrium is reached, and the stationary structure depicted in Fig. 2.3 is established at the electrode surface, a net charge transfer could not be a spontaneous process. Therefore, an activation energy is needed to proceed with the reaction mechanism. In the Fig. 2.3, for example, it can be appreciated that, for the recombination of a negative charge from the surface with an opposite one in the cations, it is necessary that the cation travels across the layer of water dipoles and finds its way to the charged surface. The case of anodic processes, when electrons from negatively charged ions in the electrolyte recombines with positive charges at the anode, has a similar difficulty.

The dependence of the rate constants from the temperature may be estimated as [89]:

$$k = B\exp(-\frac{\Delta G^{\ddagger}}{RT}), \tag{2.7}$$

where $B$ is a constant with the same dimensions as $k$, and $\Delta G^{\ddagger}$ is the activation Gibbs energy of the process. The expression (2.7) may be introduced into eq. (2.6):

$$j = F\,B_a\exp(-\frac{\Delta G_a^{\ddagger}}{RT})\,n[\mathrm{Red}] - F\,B_c\exp(-\frac{\Delta G_c^{\ddagger}}{RT})\,n[\mathrm{Ox}]. \tag{2.8}$$

In eq. (2.8) we have made distinction between the activation energies corresponding to every process, and the pre-exponential factors for the anodic and cathodic contributions to the total current (i.e., $B_a$ and $B_c$, respectively). This is a result that could be expected intuitively. In the Fig. 2.3, for example, it is shown that the cathodic current will have the higher contribution at negatively charged surfaces than the anodic one (i.e., the free energy barrier for electron-transfer processes to a negatively charged surface is higher than for the reverse case). In general, the negatively charged electrode will favor the cathodic current while the positive one will favor the anodic current.

Let us consider a product-like reduction process, for example: $H^+ + e^- \rightarrow \frac{1}{2}H_2$, (i.e., the transition state is closer to the $H_2$ formation along the reaction coordinate) in the vicinity of an electrode as represented in Fig. 2.4. The blue line represents the free energy profile of the reaction when the surface is not charged (i.e., when $\Delta\phi = 0$). If the electrode is charged in such a way that the electrostatic potential in the Helmholtz double layer increases linearly (represented by the black line in Fig. 2.4), the free energy profile of the considered process changes to the red line in the Fig. 2.4. The free energy of the transition state increases, due to the contribution of the electronic potential energy gained by the electrons transferred from the electrode to the electrolyte. Hence, the new activation energy for the cathodic process (i.e., the reduction reaction) is $\Delta G_c^\ddagger(\phi) = \Delta G_c^\ddagger(0) + F\Delta\phi$. In this situation, there is no change in the activation energy of the anodic process (i.e. the inverse reaction), since the transition state is very close to the products, for example $\frac{1}{2}H_2$, the the variation of the electrostatic potential is insignificant in this region. In consequence, $\Delta G_a^\ddagger(\phi) \simeq \Delta G_a^\ddagger(0)$. This analysis shows the intuitive idea that the reduction reactions are not favored at positively charged surfaces. There are several other possible combinations: for instance, reactant-like anodic and cathodic processes [90].

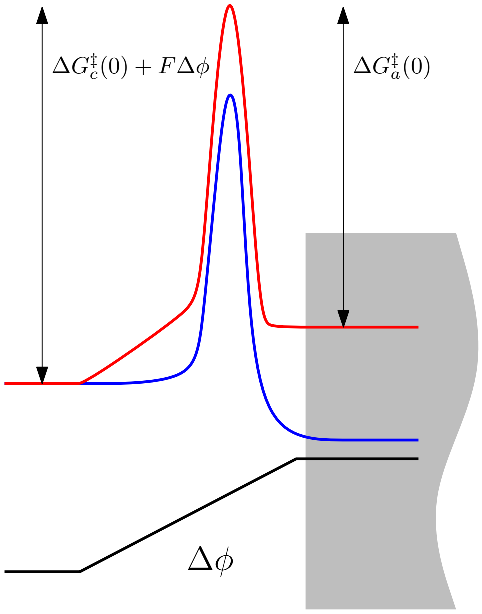

**Figure. 2.4.** *Representation of the free energy profile of a product-like reduction process at a positively charged electrode. The blue line corresponds to the case $\Delta\phi = 0$, the red one corresponds to $\Delta\phi > 0$, while the black line represents the linear variation of the potential $\phi$ in the Helmholtz double layer. The gray shaded area represents the electrode.*

In the general case in which the reaction is not either reactant nor product-like (i.e., the transition state is somewhere between the reactants and the products with respect to the reaction coordinate), the following relations are obtained, employing the same arguments as before:

$$\Delta G_c^{\ddagger}(\phi) = \Delta G_c^{\ddagger}(0) + \alpha F \Delta\phi, \tag{2.9}$$

$$\Delta G_a^{\ddagger}(\phi) = \Delta G_a^{\ddagger}(0) - (1-\alpha) F \Delta\phi, \tag{2.10}$$

where $\alpha$ (the transfer coefficient) is a dimensionless parameter which lies between 0 and 1. The situation represented in the Fig. 2.4 correspond to $\alpha \simeq 1$.

Defining the ratio $f = F/(RT)$, and inserting the expressions for the activation energies (2.9) and (2.10) in eq. (2.8), the following formula is obtained for the current density flowing through an electrode at an arbitrary potential:

$$\begin{aligned} j = F\, B_a\, n[\mathrm{Red}] \exp(-\frac{\Delta G_a^{\ddagger}(0)}{RT}) \exp[(1-\alpha) f \Delta\phi] - \\ - F\, B_c\, n[\mathrm{Ox}] \exp(-\frac{\Delta G_c^{\ddagger}(0)}{RT}) \exp(-\alpha f \Delta\phi). \end{aligned} \tag{2.11}$$

In the expression (2.11), the first term is identified as the anodic contribution to the current density (i.e., electron transfer reactions from the electrolyte to the surface), while the second one corresponds to the cathodic reaction (i.e., the inverse process). There is an equilibrium potential $\Delta\phi = E$, which can be measured by equilibrating the cell against an external source (employing a galvanic device). When $\Delta\phi = E$, both terms in eq. (2.11) become equal in absolute value and therefore the current density is zero. The value of the anodic and cathodic current densities separately, under the equilibrium conditions is known as the exchange current density $j_0$:

$$\begin{aligned} j_0 = F\, B_a\, n[\mathrm{Red}] \exp(-\frac{\Delta G_a^{\ddagger}(0)}{RT}) \exp[(1-\alpha) f E] = \\ = F\, B_c\, n[\mathrm{Ox}] \exp(-\frac{\Delta G_c^{\ddagger}(0)}{RT}) \exp(-\alpha f E). \end{aligned} \tag{2.12}$$

When an electrode is charged, for instance with a bias $\Delta\phi = E'$, supplied by an external source, the current density eq. (2.11) may be rewritten in terms of the exchange current $j_0$, the equilibrium potential $E$ and the actual potential $E'$ as follows:

$$j = j_0\{\exp[(1-\alpha) f (E' - E)] - \exp[-\alpha f (E' - E)]\}. \tag{2.13}$$

In electrochemistry the difference $E' - E$ is known as the overpotential $\eta$ of the electrode. The eq. (2.13), in terms of the overpotential, is known as the Butler-Volmer equation and it is a cornerstone in the characterization and study of heterogeneous charge transfer processes at the liquid-solid interface [90]:

$$j = j_0\{\exp[(1-\alpha)f\eta] - \exp(-\alpha f\eta)\}. \tag{2.14}$$

In the case of positive overpotentials $\eta > 0$, the electrode is directly polarized. This situation corresponds to a positive current density associated with an anodic (oxidation) reaction. The opposite case is known as inverse polarization, the current density is negative and the largest contribution is the cathodic (reduction) one.

There are two limits which may be useful to measure the exchange current density as well as the transfer coefficient. They are the limits of large and small overpotentials. When $\eta$ is very small, (e.g., $|\eta| < 0.01$ V), the Butler-Volmer equation (2.14) may be approximated up to first order in $\eta$ as follows:

$$j \simeq j_0\, f\, \eta. \tag{2.15}$$

This limit may be used to compute the exchange current density by measuring several points of the curve of overpotentials vs current densities. Nevertheless, this expression can not be used to estimate the transfer coefficient. Even for the estimation of the exchange current density, it is difficult to sample the overpotentials within such a narrow interval (-0.01 V $< \eta <$ 0.01 V). The limit of large overpotentials may correspond either to large positive values or to large negative ones. Let us take for example $\eta > 0$, in practice $\eta > 0.12$ V is high enough to assume we are in the limit of high overpotentials [90]. Within the framework of the high overpotential limit, the major contribution to the current density in the Butler-Volmer equation (2.14) is due to its first term:

$$j \simeq j_0 \exp[(1-\alpha)f\eta], \tag{2.16}$$

A more common expression is obtained after applying log to both sides of eq. (2.16):

$$\log(j) = \log(j_0) + \frac{(1-\alpha)f}{\ln 10}\eta. \tag{2.17}$$

The inverse function of eq. (2.17): $\eta$ vs $\log(j)$ is known as the Tafel plot, and the value:

$$b = \frac{\ln(10)}{(1-\alpha)f}, \tag{2.18}$$

is called the Tafel slope. The Tafel plot is widely used to characterize the catalytic activity at the surfaces of electrodes for different reactions in electrochemical cells. Small Tafel slopes are closely related with high electrocatalytic activities, and its absolute value yields information about the kinetics of the reaction. Hence, the interval of higher values of $\eta$ ($\eta > 0.12$ V) is more suitable to gather information about electrocatalytic reactions than the previous limiting case ($|\eta| \rightarrow 0$), due mainly to technical experimental reasons. Furthermore, the transfer coefficient $\alpha$ may be computed using the slope of the Tafel plot, and the exchange current density may be estimated, within the present approximation, by the intercept of the Tafel plot with the $\eta$ axis.

### 2.2.2 Charge transfer at semiconductor-liquid interfaces

The study of semiconductor-liquid interfaces is an interdisciplinary topic. Inside the semiconductor, the electrons and holes are the charge carriers which can be described within the framework of solid state physics. In the electrolyte, the mobility of charged particles (ions) in the solvent can be studied using the tools of the chemistry of solutions and electrolytes. At the interfaces, both descriptions need to be matched together, considering also the specific structure of the semiconductor surfaces from the configurational and electronic point of view.

The energy levels in semiconductor materials form broad energy bands rather than discrete molecular orbitals as are found in isolated molecules. They have a certain number of fully occupied energy bands, ideally at $T = 0\ K$, and the remaining states are unoccupied. The only difference with respect to insulators is the separation among the highest occupied band (valence band) and lowest unoccupied band (conduction band), the so called band gap energy $E_g$. While in semiconductors it ranges from 1 eV to 4 eV, in the insulators is larger than 4 eV. This value is a proper characteristic of every semiconductor and determines many of its physical properties. At $T \neq 0$ there is a probability to find electrons in the conduction band and holes (electron vacancies) in the valence band. The density of electrons and holes in the conduction and valence band, respectively, follows the Fermi's statistic which, for the case of typical semiconductors can be expressed within the Boltzmann's function [91, 92]:

$$n \simeq N_c \exp\left[-\frac{E_F - E_C}{KT}\right], \tag{2.19}$$

$$p \simeq N_v \exp\left[-\frac{E_V - E_F}{KT}\right], \tag{2.20}$$

where $n$ and $p$ are the electron concentration in the conduction band, and the hole concentration in the valence band, respectively. $E_V$ and $E_C$ are the upper valence band edge and the inferior conduction band edge, while $N_v$ and $N_c$ are the density of states at the valence and conduction band respectively. The Fermi energy $E_F$, is the electrochemical potential of electrons in the semiconductor, and it is located in the middle of the $E_V$ and $E_C$ levels, when $n = p$ (i.e., no doping). The cases of $n$ and $p$ doping can be seen, from the thermodynamical point of view as a shift of the $E_F$ toward the $E_C$ and the $E_V$, respectively.

The Nernst's equation establishes the electrochemical potential of electrons in a redox electrolyte:

$$U_{Red} = U^0_{Red} + \frac{kT}{e}\ln\left(\frac{c_{ox}}{c_{red}}\right). \tag{2.21}$$

Here, $U^0_{Red}$ is the standard potential of a redox coupled with the concentration of oxidized and reduced species represented by $c_{ox}$ and $c_{red}$, respectively, and $e$ is the absolute value of the elemental charge.

The standard potentials of redox couples in electrochemistry are usually reported with respect to a reference electrode, a typical one is the aforementioned SHE at which the standard potential is defined as $E(2H^+/H_2) = 0$ V. A general issue associated with the semiconductor-liquid interface is to express the Fermi energy of both systems using the same scale. Different methodologies have been employed to translate the relative potentials of redox couples in electrolyte solutions to an absolute scale with respect to the vacuum level, as it is used in solid state physics [93, 94]. There is some disagreement with respect to the vacuum level of the SHE. It lays in the interval [-4.7 eV, -4.3 eV] and the value of -4.5 eV is employed for practical purposes [95]. Hence, the Fermi energy of a redox coupled ($E_{F,Red}$) of an electrolyte can be expressed, with respect to the vacuum level as follows:

$$E_{F,Red} = -4.5 \text{ eV} - eU_{Red}. \tag{2.22}$$

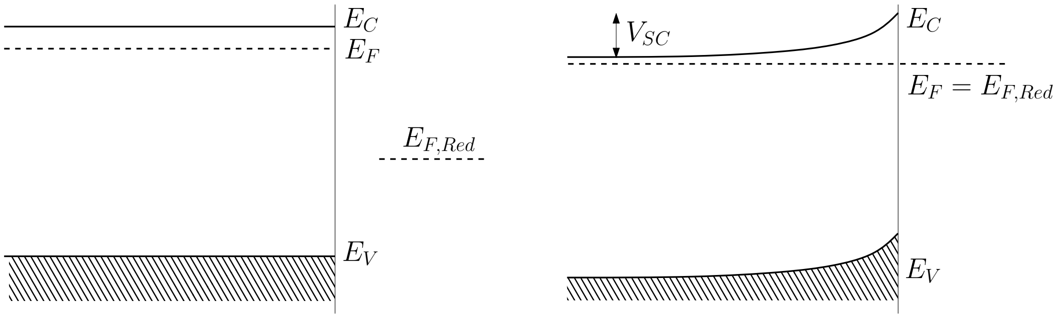

(a) (b)

**Figure. 2.5.** *Schematic representation of the Fermi energy from a redox couple $E_{F,Red}$, with respect to the Fermi energy of the semiconductor surface $E_F$.* ***a)*** *Before the equilibrium condition is reached, and* ***b)*** *after the equilibrium condition has been established.*

The energy levels of a $n$-doped semiconductor material compared with the $E_{F,Red}$ of a redox couple in an electrolyte before and after being put in contact are depicted in Fig. 2.5. If the $E_F$ in the semiconductor is higher than the $E_{F,Red}$, Fig. 2.5a, then the electrons will travel from the semiconductor to the electrolyte until both Fermi levels match themselves, Fig. 2.5b. When the equilibrium condition is reached, no current is circulating and a space charge region is created at the semiconductor surface. The space charge region leads to the band bending phenomena, in the representation of Fig. 2.5b, it corresponds to the depletion layer (lack of electrons in the semiconductor surface). This behavior is not exclusive to semiconductor-electrolyte interfaces but it is present whenever two different phases are in contact (e.g., semiconductor-metal, metal-liquid, etc.). $V_{SC}$ is the potential drop in the space charge region.

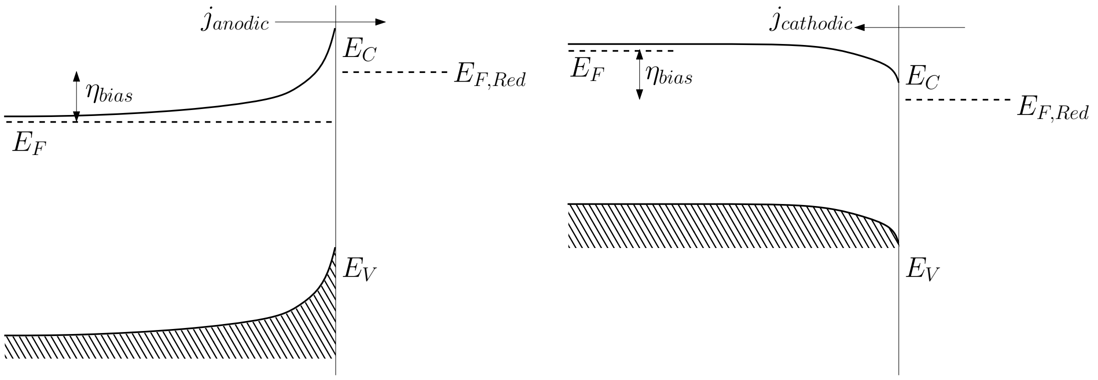

**(a)** **(b)**

**Figure. 2.6.** *Schematic representation of the Fermi energy from a redox couple $E_{F,Red}$, with respect to the Fermi energy of the semiconductor surface $E_F$ in the non-equilibrium situation corresponding to the application of external bias $\eta_{bias}$.* ***a)*** *Positive external bias, and* ***b)*** *negative external bias.*

The stationary state at the semiconductor-liquid interface is the result of two competitive processes, the anodic and the cathodic one, which cancel each other to avoid any net charge transfer along the interface, Fig. 2.5. Kinetic models for the electron transfer processes at the interfaces have shown a linear dependence of the density current with respect to the difference of electron concentrations in the semiconductor at none-equilibrium ($n_S$) and equilibrium ($n_{SO}$) conditions [96, 97]:

$$j_c = -eK_{et}\, c_{ox}\,(n_S - n_{SO}), \tag{2.23}$$

where $K_{et}$ is the electron transfer rate constant and $c_{ox}$ is the concentration of oxidized species (acceptor states in the electrolyte). At equilibrium condition $n_S \equiv n_{SO}$, there is no current flowing through the surface. The density of electrons in the surface interface at equilibrium condition $n_{SO}$, can be expressed with respect to the concentration of majority carriers in the $n$-type semiconductor by the Boltzmann equation:

$$n_{SO} = n \exp\left(-\frac{eV_{SC}}{KT}\right). \tag{2.24}$$

The application of external bias basically moves the energy of the electrons in the bulk semiconductor, Fig. 2.6. Thus the density of majority carriers at the surface (e.g., electrons in $n$-type materials) follows the expression:

$$n_S = n \exp\left(-\frac{e(V_{SC} + \eta_{bias})}{KT}\right), \tag{2.25}$$

where the $\eta_{bias}$ is measured in such a way that it is negative when it promotes the cathodic electron transfer, right panel in Fig. 2.6, and positive when the anodic one is promoted, left panel in Fig. 2.6. The eqs. (2.23), (2.24) and (2.25) lead to the following model for the density current under external bias:

$$j_c = -eK_{et}\, c_{ox}\, n_{SO} \left(\exp\left(-\frac{e\,\eta_{bias}}{KT}\right) - 1\right). \tag{2.26}$$

The general agreement which consider $j_c > 0$ for anodic bias ($\eta_{bias} > 0$) Fig. 2.6a, and $j_c < 0$ for cathodic ones ($\eta_{bias} < 0$) Fig. 2.6b, is reflected in the expression (2.26). The limit $\eta_{bias} \to -\infty$ leads to a $j_c$ divergence in the cathodic direction, while positive values of the external bias produce a saturation of the anodic density current Fig. 2.7. This is a typical behavior of an $n$-type semiconductor, the cathodic current depends on the amount of electrons which can be injected into the electrolyte, and the $n$-concentration is very sensitive to the variation of the external bias. By the contrary, the anodic current is directly related with the minority carriers in the semiconductor which varies very slow upon the external bias.

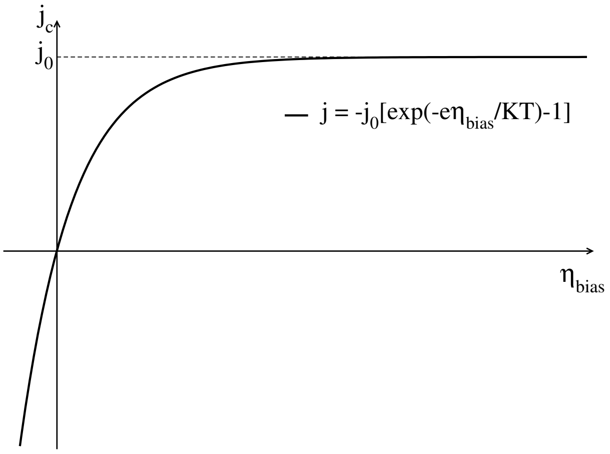

**Figure. 2.7.** *Typical current voltage response of a semiconductor-liquid interface for a n-type semiconductor, eq. (2.26). The region of positive currents and bias corresponds to anodic process (i.e., electrons flow from the electrolyte to the electrode).*

The term $j_0 = eK_{et}\, c_{ox}\, n_{SO}$ in eq. (2.26) is called exchange density current as it is in the case of metal electrodes. It corresponds to the equilibrium density current flowing in both directions (i.e., cathodic and anodic) at the interface in the absence of external bias. It is directly proportional to the $n_{SO}$, $c_{ox}$ and $K_{et}$. The typical values of $j_0$ vary in a wide range: while 1 mA×cm$^{-2}$ is the order of magnitude for the HER at Pt surfaces [98], the OER at common metal oxide materials presents values around $10^{-6}$ mA×cm$^{-2}$ [5]. Despite the low values of $j_0$ measured for the OER at metal oxide materials, their activity can be enhanced with the exposure to an external light source. Due to the generation of electron-hole pairs, the concentration of minority carriers at the semiconductor increases, and the reverse process (i.e., anodic current in an $n$-type semiconductor) is considerably favored. The kinetic limitations in both OER and HER, reflected by the reaction rate parameter $K_{et}$ represent a remarkable aspect in the performance of the overall water splitting reactions. The searching for better catalysts to enhance the activity of both reactions is still an intense working area. A brief overview of the kinetic issues which characterize those reactions is presented in the next section.

## 2.3 Kinetic models for the OER

The overall water splitting process in an electrochemical cell is described, from a thermodynamical point of view, by the following electrochemical half-reactions:

$$2H_2O \rightarrow \frac{1}{2}O_2 + 4H^+ + 4e^- \qquad E^o = -1.23\ \text{V}, \tag{2.27}$$

$$2H^+ + 2e^- \rightarrow H_2 \qquad E^o = 0.00\ \text{V}. \tag{2.28}$$

They represent the electrochemical reaction in acidic conditions, but the alkaline ones can also be studied using these equations with an additional correction, which account for the the $pH$ of the electrolyte. External bias of 1.23 V is necessary to promote the reaction ideally, but in practice a higher external potential ($V_{ext}$) needs to be used in order to observe the oxygen and hydrogen evolution:

$$V_{ext} = 1.23\ \text{V} + \eta_{an} + \eta_{cat} + \eta_{cell}, \tag{2.29}$$

where $\eta_{an}$, $\eta_{cat}$ and $\eta_{cell}$ are overpotentials due to the reaction barriers at the anode, at the cathode and the remaining energetic losses in the electrochemical cell.

The reaction overpotentials should be close to zero in the ideal case. However, in practice up to 85% of the overall energy losses in electrochemical water splitting processes are due to the sluggish kinetics at the surfaces of the electrodes [99]. The OER is specially limited from the kinetic point of view, but also the HER is highly studied at present, and many catalysts based on new materials, cheaper than the state of the art catalysts based on Pt, are matter of intensive research for OER and HER. The search for new electrocatalysts, from the theoretical point of view, is based on the determination of reaction mechanisms at the surface of electrodes in order to predict, afterwards kinetic parameters like the Tafel slope, the exchange current and the transfer coefficient among others. Experimental studies complement the theoretical ones and the measurements of kinetic properties yield information about the mechanistic behavior of the studied reaction.

The OER is a multiple step process which needs the transference of four electrons for $O_2$ molecule. After each electron transfer, different intermediate complex may be formed at the surface of the electrode. Therefore, the OER may be completed following a reaction mechanism between many possibilities. It has been the subject of many previous studies [99–104]. Among several previously proposed reaction pathways for the OER, there is an agreement in the first electron transfer process [99]:

$$\mathrm{S} + \mathrm{OH}^- \rightarrow \mathrm{S\text{-}OH} + e^-. \tag{2.30}$$

The electrochemical reaction represented in eq. (2.30) describes the first electron transfer step accompanied by the $\mathrm{OH}^-$ adsorption at the active site S of the electrocatalytic surface. Let us consider, as an illustrative example, the reaction mechanism proposed by Bockris and Otagawa for the OER on perovskites [100]:

$$1\ .\ \mathrm{S} + \mathrm{OH}^- \rightarrow \mathrm{S\text{-}OH} + e^-, \tag{2.31}$$

$$2\ .\ \mathrm{S\text{-}OH} + \mathrm{OH}^- \rightarrow \mathrm{S\text{-}O}\ +\ \mathrm{H_2O} + e^-, \tag{2.32}$$

$$3\ .\ \mathrm{2S\text{-}O} \rightarrow \mathrm{2S}\ +\ \mathrm{O_2}. \tag{2.33}$$

The adsorption of isolated oxygen atoms at the surface sites (S) is considered after the second electron transfer: step 2 eq. (2.32). The OER proceeds within the recombination of two oxygens adsorbed at neighbor active sites: step 3 eq. (2.33). If the step 2 is considered to be the rate determining step (RDS), then the current density associated to the OER will be limited by the step 2 mechanism (2.32):

$$j = k_2\, n[\mathrm{OH}^-]\, \theta_{\text{S-OH}} \exp(\beta f \eta). \tag{2.34}$$

If $j_0 = k_2\, n[\mathrm{OH}^-]\, \theta_{\mathrm{MOH}}$ and $\beta = 1 - \alpha$, then eq. (2.34) will have the same structure than eq. (2.16). $k_2$ is the rate constant for the step 2 eq. (2.32), $n[\mathrm{OH}^-]$ corresponds with $n[\mathrm{Red}]$ for the same reaction step: eq. (2.32), and $\theta_{\text{S-OH}}$ is the fractional surface coverage of the S-OH sites in the surface of the electrode.

Two main limits usually appear in practical situations: high fractional coverages ($\theta_{\text{S-OH}} \rightarrow 1$) and low fractional coverages ($\theta_{\text{S-OH}} \rightarrow 0$). The former one predicts a Tafel slope, eq. (2.18) of $b = \ln(10)(2/f) = 120\ \mathrm{mV} \times \mathrm{dec}^{-1}$ when $\beta$ is chosen to be the typical value of 0.5. The second limit requires an estimation of $\theta_{\text{S-OH}}$ to plug in eq. (2.34) as a function of non vanishing quantities. When ($\theta_{\text{S-OH}} \rightarrow 0$) the surface adsorption sites (S) are uncovered, so it is a natural assumption to consider ($\theta_{\mathrm{S}} \rightarrow 1$).

The so called quasi-equilibrium method may be invoked in order to estimate the $\theta_{\text{S-OH}}$ coverage in the second limiting case. It consists in the consideration of all the steps in the reaction mechanism to be in equilibrium but not the RDS (i.e., eqs. (2.31) and (2.33) represent equilibrium processes) [105, 106]. The current densities corresponding to the forward ($j_1$) and backward ($j_{-1}$) reactions in the first step of the example reaction mechanism: eq. (2.31) are expressed as follows, using the same notation of eq. (2.34):

$$j_1 = k_1\, n[\mathrm{OH}^-]\, \theta_{\mathrm{S}} \exp(\beta f \eta), \tag{2.35}$$

$$j_{-1} = k_{-1}\, \theta_{\text{S-OH}} \exp(-(1-\beta) f \eta), \tag{2.36}$$

here $k_1$ and $k_{-1}$ are the corresponding thermal constants, and the differences in the exponents in both expression come from the discussion already presented in Sec. 2.2.1. The equilibrium condition for the step 1 in the reaction mechanism: eq. (2.31), $j_1 = j_{-1}$ leads to the sought relation:

$$\theta_{\text{S-OH}} = K\, n[\mathrm{OH}^-]\, \theta_{\mathrm{S}} \exp(f\eta), \tag{2.37}$$

where $K = k_1/k_{-1}$. The current density for the RDS is obtained plugging $\theta_{\text{S-OH}}$ in eq. (2.36):

$$j = K k_2\, n[\mathrm{OH}^-]^2\, \theta_{\mathrm{S}} \exp((1+\beta) f\eta). \tag{2.38}$$

With the expression (2.38) a different Tafel slope is predicted by the same assumption of $\beta = 0.5$, $b = 2\ln(10)/(3f) = 40$ mV×dec$^{-1}$. As it is expected, the Tafel slopes predict more activity in the small coverage limit than in the large one. The general case of none limiting coverages ($0.2 < \theta < 0.8$) has been also the central point of several studies [100, 107]. It has been found that the kinetics of the reactions is highly influenced for the relative populations of intermediate species adsorbed on the surfaces, and different models have been proposed to study such effects [108]. In the general case where the coverage of a particular intermediate, which is directly related with the RDS, increases from zero to one with the course of the external bias, a change in the Tafel slope will be appreciated from the limiting values of 40 mV×dec$^{-1}$ and 120 mV×dec$^{-1}$.

The preceding analysis shows, throughout the sample reaction mechanism presented above, the actual difficulties in the prediction of reaction mechanisms for the OER. In addition to the availability of many reaction mechanisms, the kinetics of each of them may vary with several external factors like the applied bias or the fractional surface coverages of reaction intermediates. Hence, the application of many experimental techniques beside the usual current voltage behavior, like impedance spectroscopy (IS), cyclic voltammetry studies of surface redox properties in combination with theoretical insights are needed in the research and design of new catalytic materials to efficiently promote the OER at their surfaces.

Searching for the most probably reaction mechanism at a certain electrode surface as well as the estimation of the overpotentials from microscopic properties are among the main challenges of the theoretical approaches for the study of electrochemical reactions, and the OER in particular. A significant amount of work dedicated to elucidate these mechanisms has been published in the last decades [109–115]. A methodology based on DFT, which has been successfully applied in the estimation of overpotentials for the OER at different metal oxide surfaces is presented in the following section.

## 2.4 Thermochemistry of electrochemical reactions

To estimate the overpotential of a specific electrochemical reaction, in particular the OER at the anode in an ECC, we use a methodology based on the thermodynamical description of electrochemical reactions, which was previously developed and used in electrochemical applications [109–113]. The details of the reactions are discussed in terms of electron transfer processes as well as adsorption/desorption of fragments on/from the surface, and characterized by means of their stable intermediate states. The transition barriers between any pair of the locally stable intermediates are neglected in the present methodology. Although activation energy barriers may be present in principle between any of the stable states, there are several specific situations (i.e., for reactions at determined surfaces surrounding by a water solvent) where these barriers have been found to be rather small [114, 115].

In the framework of the present methodology, every reaction mechanism consists in a set of intermediate states which determine the free energy profile along the reaction coordinate. The algorithm was originally designed for reaction mechanisms composed only by deprotonation steps. On the contrary, we also considered here the adsorption of $H_2O$ on the surface as part of the proposed mechanisms. The calculation of the free energy at each intermediate step is carried out using the following rules:

1. The SHE is set as the reference electrode, and the target surface is located at the second one (the working electrode). The reaction $1/2H_2 \rightarrow H^+ + e^-$ is in the equilibrium at standard conditions (i.e., $T = 298K$, $p = 1$ bar, $pH = 0$). Therefore, at the standard conditions, the free energy change $\Delta G$ of the reaction S-A-H$\rightarrow$ S-A + $H^+ + e^-$ (where A is a molecular structure adsorbed on an active site of the catalytic surface represented by S-) may be calculated as the free energy change of the equivalent reaction S-A-H$\rightarrow$ S-A + $1/2H_2$ [109–113].

2. The free energy change at a particular intermediate step along the reaction path is calculated using the formula $\Delta G = \Delta E + \Delta \mathrm{ZPE} - T\Delta S$ [109–113]. Here, $\Delta E$ is the energy variation between the initial and final states of the reaction steps, computed in DFT. $\Delta$ZPE is the variation of the zero point energy correction of the ground state and $\Delta S$ is the entropic variation in the corresponding intermediate step. These values of $\Delta$ZPE and $\Delta S$ are computed using the information from normal mode analysis of the molecular species (whose optimized structures are generated by DFT) and standard tables of gas phase entropies [16].

3. The influence of an external bias is included as the energy gained by the electrons traveling across the closed circuit, with negative sign: $\Delta G_U = -eU$ [109–113]. Here $e$ is, as before, the elemental charge (with positive sign) and $U$ is the external bias, with positive sign if the considered reaction is favored and negative if, by the contrary, it is hindered by the external potential. In the case of water decomposition, the electrostatic potential at the anode should be higher than its value at the cathode in order to favor the reaction.

4. When the system is not under the standard conditions, for instance if the $pH \neq 0$ or the temperature $T \neq 298K$, then the electrode potential relative to the SHE changes by the magnitude $\Delta E = -(kT/e)\ln[\mathrm{H}^+]$. Hence, the contribution of the $pH$ to the free energy change may be estimated by the quantity $\Delta G_{pH} = kT\ln[\mathrm{H}^+] = -kT \cdot \ln(10) \times pH$ [109–113].

The electrocatalytic OER may be studied within the framework of the present methodology, by the construction of a model representation of the electrode surface, and the explicit consideration of $H_2O$, $H_2$ and $O_2$ molecules. The total energy $E$ of every structure as well as the ZPE corrections are obtained from DFT calculations. For computing the entropic contribution of every structure involved in the reaction steps, some further considerations are introduced. For example, the entropy of the surface and the compounds adsorbed on it are assumed to be zero due to the fact that the amount of degrees of freedom (DoF) comprised by the surface is infinite compared with those of the molecules enrolled in the reaction. This reasoning emphasize the fact that the entropy of the surface does not change appreciably during the reaction, this constant value is taken to be zero for simplicity. Therefore, the entropic changes at any intermediate step are due only to the contributions of the $H_2O$, $H_2$ and $O_2$ molecules. To compute these values, the gas phase approximation is employed, so they are calculated taking into account the translational, rotational and vibrational contributions of the corresponding molecule within an ideal gas approximation [16].

The total energy of the $O_2$ molecule is computed using an experimental correction. The free energy change of the reaction:

$$2H_2O \rightarrow O_2 + 2H_2, \tag{2.39}$$

is determined experimentally as 4 times the standard potential of the redox couple $E(2H_2O/O_2) = 1.23$ V because it is necessary that four electrons are transferred, in order to complete the reaction eq. (2.39), thus $\Delta G = 4.92$ eV.

## 2.5 Descriptor for the HER activity

The exchange current density $j_0$, introduced in Sec. 2.2.1, is usually considered to asses the catalytic properties of different metal surfaces for the HER [116]. It changes among several orders of magnitude: from 1 $\mathrm{mA}\times\mathrm{cm}^{-2}$ in the case of platinum electrodes to $10^{-7}$ $\mathrm{mA}\times\mathrm{cm}^{-2}$ for the worse metal electrodes like In, Cd or Pb [117]. The relation between $j_0$ and natural characteristics of the electrodes gives the possibility to make a broad analysis of their performance and to predict which would be the optimum one for a certain application. The material properties which can be directly linked with the exchange current density are called catalytic descriptors. These descriptors are useful to elucidate activity trends and to identify promising candidates in the research and design of new catalysts for the HER.

The seeking for suitable descriptors which could be used to evaluate the electrocatalytic ability of a wide set of metal electrodes goes back to the work of Bowden and Riedal [118]. After this early attempt, it was only with the work of Trasatti [117], when the experimentally accessible magnitude E(M-H): metal-hydrogen bond strength, is established as a reasonable descriptor for the catalytic properties of different metal electrodes toward the HER, Fig. 2.8. Trasatti found that the performance of available metal electrodes, assessed by the exchange current, may be visualized in a volcano plot which essentially reflects the Sabatier's principle: the optimum condition for a metal electrode towards the HER is to adsorb the hydrogen atoms at the surface with a moderate strength [119]. Too strong adsorption results in a full coverage of the surfaces and high barriers for the $H_2$ recombination, while too weak adsorption leads to very fast desorption which does not allow the hydrogen evolution.

Recently, a new descriptor based on DFT calculations have been developed by Nørscov et al. [114]. They have found that a similar volcano plot than the obtained by Trassati, Fig. 2.8, results when the free energy of H-adsorption, computed within DFT, is employed as a descriptor. The major significance of this approach is its easily implementation. Contrary to the experimental descriptor, which require independent experiments to access the E(M-H) of the studied electrodes, the computational one is easily accessible from a calculation and more important, it allows the design of new catalytic nanostructured materials and the evaluation of their

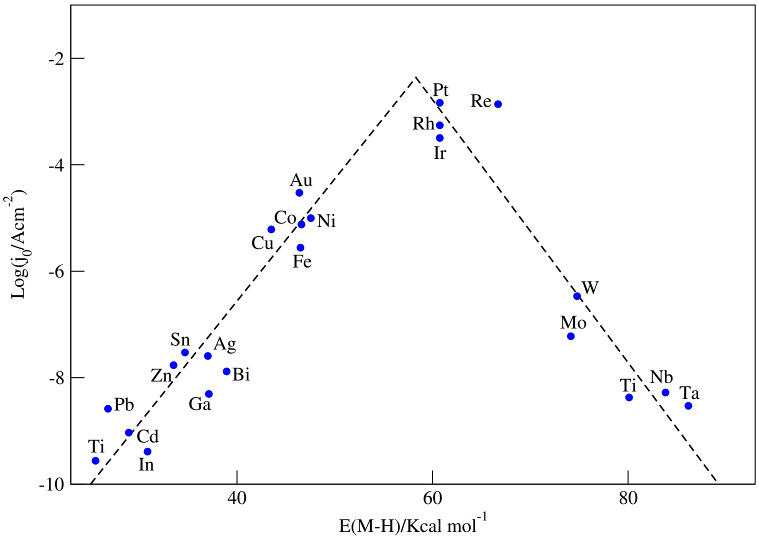

**Figure. 2.8.** *Volcano plot obtained by Trasatti (replotted here using the original data from [117]).*

activity toward the HER without even synthesize them.

The volcano plot obtained by Nørscov et al. [114], may be understood by a simple kinetic model, which is briefly presented here, a more detailed description can be found in [114]. The HER on the electrode surface occurs via a combination of the following three reactions:

$$\begin{aligned} &\text{i . } \mathrm{S} + \mathrm{H}^+ + e^- \rightarrow \text{S-H}, && (2.40)\\ &\text{ii . } \text{S-H} + \mathrm{H}^+ + e^- \rightarrow \mathrm{H}_2, && (2.41)\\ &\text{iii. } 2(\text{S-H}) \rightarrow \mathrm{H}_2, && (2.42) \end{aligned}$$

where S represent adsorption sites at the surface of the metal. They are named Volmer, Heyrovsky and Tafel steps, respectively. Assuming that the Langmuir adsorption isotherm holds at the equilibrium condition, the fractional H-adsorbed surface coverage $\theta$ can be related with the free energy change of the effective equilibrium reaction: 2S- + $H_2 \rightarrow$ 2S-H, by the following expression [120]:

$$\left[\frac{\theta}{1-\theta}\right]^2 = p_{\mathrm{H}_2} \exp\left(-\frac{\Delta G^0}{KT}\right), \tag{2.43}$$

where $p_{\mathrm{H}_2}$ is the pressure of the $H_2$ gas and $\Delta G^0$ is the free energy change of the effective reaction (i.e., 2S- + $H_2 \rightarrow$ 2S-H). $\Delta G^0$ can be considered two times the adsorption free energy of a hydrogen atom $\Delta G_H$ with respect to the $H_2$ molecule (i.e., $\Delta G^0 = 2\,\Delta G_H$), if additional barriers in the adsorption process are neglected. Making $p_{\mathrm{H}_2} = 1$ (standard conditions) and introducing $\Delta G^0 = 2\,\Delta G_H$ in eq. (2.43), the equilibrium fractional coverage may be estimated with respect to the adsorption free energy of a hydrogen atom $\Delta G_H$:

$$\left[\frac{\theta}{1-\theta}\right] = \exp\left(-\frac{\Delta G_H}{KT}\right). \tag{2.44}$$

The exchange current density $j_0$ is estimated considering the Volmer step, eq. (2.40). The equilibrium reaction rate $r_1$ of the reaction eq. (2.40) may be expressed as [114]:

$$r_1 = k_1(1-\theta)c_{\mathrm{H}^+}, \tag{2.45}$$

where $c_{\mathrm{H}^+}$ is the concentration of $\mathrm{H}^+$ in the electrolyte and can be equaled to 1 at $pH = 0$.

The exchange current $j_0$, is equal to the equilibrium rate of the reaction $r_1$ multiplied by the superficial density of adsorption sites $\sigma$, and the electron charge $e$. Combining the eqs. (2.44) and (2.45), the following expression is obtained for $j_0$ at $pH = 0$:

$$j_0 = e\,k_1\,\sigma\frac{1}{1+\exp\left(-\frac{\Delta G_H}{KT}\right)}. \tag{2.46}$$

At this point two relevant cases are considered: $\Delta G_H < 0$ and $\Delta G_H > 0$ [114]. In the former one, a high rate constant $k_1 = k_0$ is expected, and it is assuming not to depend on $\Delta G_H$. In the second case, there should be an activation barrier for the electron transfer step which is at least $\Delta G_H$, thus $k_1 = k_0 \exp(-\Delta G_H/KT)$ is proposed. These conditions may be combined in the single expression:

$$j_0 = 2\,j_0^{max}\frac{1}{1+\exp\left(\frac{|\Delta G_H|}{KT}\right)}, \tag{2.47}$$

where $j_0^{max} = \dfrac{ek_0\sigma}{2}$ is the maximum value of $j_0$ predicted within this model. If the superficial density of adsorption sites corresponding to the surface of Pt (111) is considered: $\sigma \simeq 1.5 \times 10^{15}$ cm$^{-2}$ [121], then the eq. (2.47) will represent a model with only one unknown parameter: $k_0$.

Available experimental values of $j_0$ have been plotted with respect to their correspond $\Delta G_H$ computed within DFT, for several metal electrodes [114]. The Fig. 2.9 shows this plot (blue points) together with the fitted model eq. (2.47) with $k_0$ as fitting parameter. The present model considers the computational $\Delta G_H$ value as a descriptor of the catalytic properties of metal electrodes towards the HER. It reflects the Sabatier's principle, the largest exchange current density is predicted for a material where $\Delta G_H = 0$. The shaded area in Fig. 2.9 represents an *ad-hoc* criteria selected in this work for a material to be a relatively good catalyst for the HER. When $|\Delta G_H| > 0.2$ eV the exchange current density $j_0$ is more than three order of magnitudes lower than $j_0^{max}$, obtained at $\Delta G_H = 0$. Additionally, it is known that the metals which present $\Delta G_H$ values lower than -0.2 eV may have an oxygen layer at their surfaces [70].

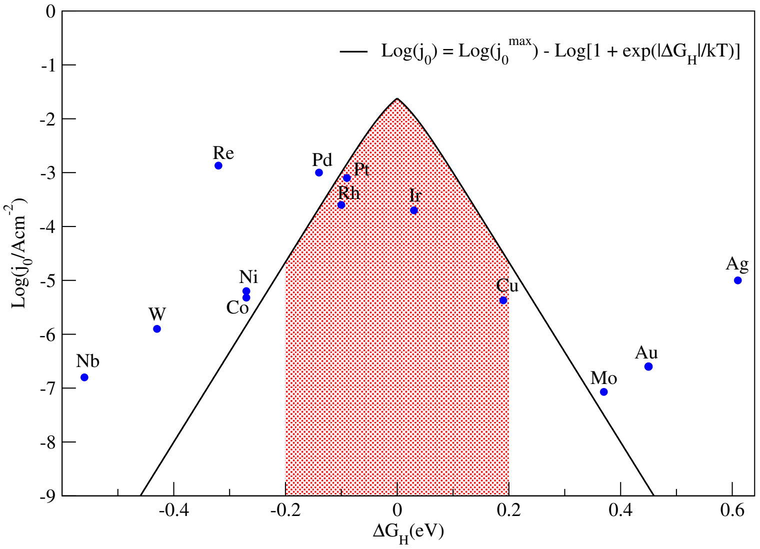

**Figure. 2.9.** *Logarithm of experimentally measured exchange currents* $j_0$ *for HER at several metal electrodes with respect to computational free energies of H-adsorption* $\Delta G_H$ *(blue points). Estimation of the same magnitude following the kinetic model introduced in [114], within the fitting parameter* $k_0$*.*

The present model is used in Chap. 5 to evaluate the catalytic properties of model structures which resembles recently synthesized materials. An additional correction can be added to take into account the influence of the electrolyte acidity ($pH$). While changes in the $pH$ do not affect qualitatively the behavior of $j_0(\Delta G_H)$, eq. (2.47), they shift the $\Delta G_H$ value due to the change in the corresponding configurational entropic barrier [122]:

$$\Delta G_H(pH) = \Delta G_H(pH = 0) + k_B T \ln(10) \times pH. \qquad (2.48)$$

The details of the calculation of $\Delta G_H$ for the studied surfaces within the framework of DFT are discussed in detail in [114], and will be also briefly presented in Chap. 5.

## 2.6 Electronic structure methods

The study of any physical situation from an atomistic point of view includes, at the most fundamental level, the description of the motion of the electrons and the nuclei which constitute the target system. From the theoretical point of view, this is a many-body problem with intrinsic quantum-mechanical behavior. The electrons and nuclei, in the ground state, distribute themselves in such a way that their interaction energy is minimized. In principle, the stationary state of the subatomic particles can be characterized by a many particle wave function $\Phi(\{\mathbf{X}_i\}, \{\mathbf{x}_i\})$, where $\{\mathbf{X}_i\}$ and $\{\mathbf{x}_i\}$ are the spatial and spin coordinates of nuclei and electrons, respectively.

Under stationary conditions, the connection between the wave function and the energy of the quantum many-body system is the Time Independent Schrödinger Equation (TISE), eq. (2.49):

$$\hat{H}\Phi = E_{tot}\Phi. \tag{2.49}$$

This equation defines an eigenvalue problem for the hermitian and linear operator $\hat{H}$ (*Hamiltonian*). Its non-trivial solutions are all the possible states $\Phi^{\alpha}$ and energies ${E_{tot}}^{\alpha}$ accessible to the system. They contain all the available information about the system of interest.

In the non-relativistic case, $\hat{H}$ does not contain any dependence on the spin of the particles. After proposing the common factorization $\Phi(\{\mathbf{X}_i\},\{\mathbf{x}_i\}) = \Psi(\{\mathbf{R}_i\},\{\mathbf{r}_i\})$ $\times\ \Theta(\{\Sigma_i\},\{\sigma_i\})$, where $(\{\mathbf{R}_i\},\{\mathbf{r}_i\})$ and $(\{\Sigma_i\},\{\sigma_i\})$ are the positions and spins of the nuclei and the electrons, respectively, while $\Psi$ and $\Theta$ are the spatial and the spin part of the wave functions, the following TISE equation is obtained for the spatial wave function:

$$\hat{H}\Psi(\{\mathbf{R}_i\},\{\mathbf{r}_i\}) = E_{tot}\Psi(\{\mathbf{R}_i\},\{\mathbf{r}_i\}). \tag{2.50}$$

The Hamiltonian operator of the system $\hat{H}$ is the quantum analog to the Hamilton's function in classical mechanics and contains the following terms:

$$\hat{H} = \hat{H}_{k,n} + \hat{H}_{k,e} + \hat{H}_{p,n-n} + \hat{H}_{p,e-e} + \hat{H}_{p,n-e}. \tag{2.51}$$

The different terms in the previous expression correspond to the kinetic energy of the nuclei $(k, n)$, kinetic energy of the electrons $(k, e)$, the potential energy due to the nuclei-nuclei interactions $(p, n\text{-}n)$, the electron-electron interactions $(p, e\text{-}e)$ and the nuclei-electron interaction $(p, n\text{-}e)$, respectively. If all the terms in eq. (2.51) are written down explicitly the Hamiltonian looks as follows:

$$\begin{aligned}\hat{H} = &-\sum_{k=1}^{M}\frac{\hbar^2}{2M_k}\nabla^2_{\mathbf{R}_k} - \sum_{i=1}^{N}\frac{\hbar^2}{2m_e}\nabla^2_{\mathbf{r}_i} + \frac{1}{2}\sum_{k_1\neq k_2=1}^{M}\frac{1}{4\pi\varepsilon_0}\frac{Z_{k_1}Z_{k_2}e^2}{|\mathbf{R}_{k_1}-\mathbf{R}_{k_2}|}+ \\ &+\frac{1}{2}\sum_{i_1\neq i_2=1}^{N}\frac{1}{4\pi\varepsilon_0}\frac{e^2}{|\mathbf{r}_{i_1}-\mathbf{r}_{i_2}|} - \sum_{k,i=1}^{M,N}\frac{1}{4\pi\varepsilon_0}\frac{Z_k e^2}{|\mathbf{R}_k-\mathbf{r}_i|},\end{aligned} \tag{2.52}$$

where $\hbar$ and $\varepsilon_0$ are the Planck's constant and the vacuum permittivity, respectively, while $m_e$ is the mass of the electrons. This is the Hamiltonian which describe a system made up of $M$ nuclei with masses $M_k$, charges $Z_k e$ and $N$ electrons.

It can be noticed, that solving eq. (2.50), when the Hamiltonian is expressed by (2.52), posses several serious technical difficulties. It is a second order partial differential equation involving a very large number of independent variables. The Schrödinger equation, when the Hamiltonian is given by the expression (2.52), can be solved exactly only for very small systems, like the hydrogen atom. Hence, a considerable amount of numerical methodologies and algorithms have been developed to solve (2.50) approximately [123].

### 2.6.1 The Born-Oppenheimer approximation

The Born-Oppenheimer approximation (BOA) is introduced here as a particular case of the more general adiabatic approximation. The adiabatic approximation is based on the fact that the motion of electrons is very fast compared with that of the nuclei. This time-scale separation supports the picture of the electrons following the nuclear motion "adiabatically" (i.e., they do not undergo electronic transitions while the nuclei change their positions). This condition may be expressed mathematically by the following ansatz [124]:

$$\Psi(\{\mathbf{R}_i\},\{\mathbf{r}_i\}) = \Psi_n(\{\mathbf{R}_i\})\Psi_e(\{\mathbf{R}_i\};\{\mathbf{r}_i\}), \tag{2.53}$$

where $\Psi_n$ is called the nuclear wave function (it depends only on the nuclear coordinates) and $\Psi_e$ is the electronic function, which depends on the electronic coordinates and parametrically also on the nuclear DoF.

If the ansatz (2.53) is inserted in eq. (2.50), it can be noticed that the electronic terms of the Hamiltonian (i.e., $\hat{H}_{k,e} + \hat{H}_{p,e-e} + \hat{H}_{p,n-e}$) do not act on $\Psi_n$, but the nuclear part of the Hamiltonian $\hat{H}$ does act on the electronic function $\Psi_e$ via the parametric dependence on the nuclear coordinates. The BOA consists in neglecting the action of the nuclear term $\hat{H}_{k,n}$ on $\Psi_e$. More explicitly it may be written as:

$$\hat{H}_{k,n}\Psi_n(\{\mathbf{R}_i\})\Psi_e(\{\mathbf{R}_i\};\{\mathbf{r}_i\}) \simeq \Psi_e(\{\mathbf{R}_i\};\{\mathbf{r}_i\})\hat{H}_{k,n}\Psi_n(\{\mathbf{R}_i\}). \tag{2.54}$$

The physical meaning of this assumption is to neglect the influence of the electronic motion on the nuclear kinetic energy. This is supported by the same reasoning as before and by the huge difference in masses between electrons and nuclei (i.e., $\frac{m_e}{M_k} \lesssim \frac{1}{1000}$). There are cases where the BOA is not valid, and there is a variety of phenomena where the so called non-adiabatic effects are present (for instance, the Jahn-Teller and Peierls' distortions or spin-density waves and superconductivity) [123].

Within the BOA, the TISE (2.50) splits in two simpler Schrödinger equations (i.e., the electronic and the nuclear ones) [123]:

$$\left[\hat{H}_{k,e} + \hat{H}_{p,e-e} + \hat{H}_{p,n-e}\right] \Psi_e(\{\mathbf{R}_i\};\{\mathbf{r}_i\}) = V(\{\mathbf{R}_i\})\Psi_e(\{\mathbf{R}_i\};\{\mathbf{r}_i\}), \tag{2.55}$$

$$\left[\hat{H}_{k,n} + \hat{H}_{p,n-n} + V(\{\mathbf{R}_i\})\right] \Psi_n(\{\mathbf{R}_i\}) = E_{tot}\Psi_n(\{\mathbf{R}_i\}). \tag{2.56}$$

This approximation is of paramount importance in the description of microscopic systems with significant quantum mechanical behavior. From the fundamental point of view, it introduces the concept of potential energy surface (PES): $V(\{\mathbf{R}_i\})$ in eq. (2.55), which is very important for the atomistic description of matter both in the framework of the BOA, but also beyond. In situations where the BOA is not valid, the time evolution of the quantum state of the system can be studied as a superposition of many components of the wave function evolving on different PESs. From the practical point of view, it serves as a basis for the development of further approximations: one may treat the nuclei as a set of point charges evolving on the corresponding PES ($V(\{\mathbf{R}_i\})$), which is previously computed by solving the electronic TISE: eq. (2.55) on a multidimensional grid of the nuclear coordinates $\{\mathbf{R}_i\}$.

The solution of the eq. (2.55) in an approximated way and for several different conditions is the main task of the so called electronic structure calculations. There are many approximations and methodologies which attempt to reach this goal. Their suitability usually depend on the specific target system and on the level of accuracy needed in each case. These methods can be divided in two groups: the wave function based methods and the density based ones. In the next sections, there will be briefly described the Hartree-Fock method and the Density Functional Theory, as paradigmatic examples of the first and second group, respectively.

### 2.6.2 The variational principle

The variational principle is a methodology commonly employed to develop new calculation schemes. It is very important for ground state calculations, although it is used less often in formulations involving excited states. Here, we begin describing the variational principle briefly, since it is a cornerstone for the development of the Hartree-Fock method (HF) and also for the DFT.

The main goal of the variational principle is to solve the electronic TISE approximately using a model ansatz for the wave function, typically based on the use of single-particle orbitals. The Hamiltonian of a physical system is a linear and Hermitian operator. Thus, it has real eigenvalues which obviously may be ordered in an increasing fashion. There is a general result from quantum mechanics, which states that if the potential energy of a Hamiltonian has a global minimum value, then the corresponding spectrum has a minimum value as well [125]. The eigenvalue problem for the Hamiltonian can be written as:

$$\hat{H}\phi_n = \epsilon_n \phi_n. \tag{2.57}$$

One of the general properties of the spectrum of Hermitian operators is that the corresponding eigenfunctions $\phi_n$ may be chosen in such a way that they form a complete set of orthonormal functions in the Hilbert space of the Hamiltonian $\hat{H}$. Thereby, they fulfill the relation:

$$\langle \phi_n | \phi_m \rangle = \delta_{n,m}. \tag{2.58}$$

Additionally, any other function $f$ of the Hilbert space may be expanded as a linear combination of the basis set $\{\phi_n\}$:

$$f = \sum_n c_n \phi_n. \tag{2.59}$$

The set of functions $\{\phi_n\}$ is in principle unknown. The variational method aims to obtain them or at least the ground state $\phi_0$ (the eigenfunction corresponding to the lowest eigenvalue $\epsilon_0$ in the spectrum $\{\epsilon_n\}$) of the Hamiltonian $\hat{H}$). Let us note that the expectation value of $\hat{H}$ in the state $f$ can be computed as:

$$\varepsilon_f = \frac{\left\langle f \middle| \hat{H} \middle| f \right\rangle}{\langle f | f \rangle}. \tag{2.60}$$

This can be considered as an approximation to the ground state by any other function $f$ of the Hilbert space. When the expansion (2.59) is substituted in (2.60), and the linearity of $\hat{H}$ is used as well as the orthonormalization condition (2.58), it is obtained:

$$\varepsilon_f = \frac{\sum_n |c_n|^2 \epsilon_n}{\sum_n |c_n|^2}. \tag{2.61}$$

If the fact that every eigenvalue $\epsilon_n \geq \epsilon_0$ is taken into account, the expression (2.61) may be rewritten as the inequality:

$$\varepsilon_f \geq \epsilon_0, \tag{2.62}$$

which constitute the basis of the variational principle. This inequality expresses that the energy of any arbitrary state will not be smaller than the energy of the ground state of the system. Hence, if a family of orthonormal functions $\{f_\alpha\}$ in the $\hat{H}$-Hilbert space is considered, and if the ground state $\phi_0$ belongs to $\{f_\alpha\}$, then the variational condition for the determination of $\phi_0$ may be obtained:

$$\frac{\delta}{\delta f_\alpha}\left\langle f_\alpha \middle| \hat{H} \middle| f_\alpha \right\rangle = 0. \tag{2.63}$$

Moreover, if there are two set of trial functions and the application of (2.63) results in two different values for $\left\langle f_0 \middle| \hat{H} \middle| f_0 \right\rangle$, where $f_0$ correspond to the function for which the relation (2.63) is fulfilled, the variational principle states that, from the energetic point of view, the function with the lowest value for the energy constitutes the better approximation to the actual ground state of the system [123].

The condition (2.63) is the practical expression of the variational principle, and it is widely used in the derivation of the fundamental equations of several electronic structure methods.

### 2.6.3 The Hartree-Fock approximation

The Hartree-Fock (HF) method to approach the ground state of a system is based on a particular approximation, which consists in the proposal of a special ansatz to construct the many-electron wave function. Thus, the goal of this methodology is to solve approximately the electronic TISE (2.55).

By inspecting carefully the three terms of the electronic Hamiltonian (i.e., $\hat{H}_e = \hat{H}_{k,e} + \hat{H}_{p,e-e} + \hat{H}_{p,n-e}$) in the general expression (2.52), $\hat{H}_e$ can be written as:

$$\hat{H}_e = \sum_{i=1}^{N} \hat{h}_1(\mathbf{r}_i) + \frac{1}{2}\sum_{i\neq j=1}^{N} \hat{h}_2(\mathbf{r}_i, \mathbf{r}_j), \tag{2.64}$$

where $\hat{h}_1$ and $\hat{h}_2$ are single-particle and two-particle operators, respectively given by:

$$\hat{h}_1(\mathbf{r}_i) = -\frac{\hbar^2}{2m_e}\nabla^2_{\mathbf{r}_i} - \sum_{k=1}^{M} \frac{1}{4\pi\varepsilon_0}\frac{Z_k e^2}{|\mathbf{R}_k - \mathbf{r}_i|} = -\frac{1}{2}\nabla^2_{\mathbf{r}_i} - \sum_{k=1}^{M}\frac{Z_k}{|\mathbf{R}_k - \mathbf{r}_i|}, \tag{2.65}$$

$$\hat{h}_2(\mathbf{r}_i, \mathbf{r}_j) = \frac{1}{4\pi\varepsilon_0}\frac{e^2}{|\mathbf{r}_i - \mathbf{r}_j|} = \frac{1}{|\mathbf{r}_i - \mathbf{r}_j|}. \tag{2.66}$$

The second equalities in both expressions correspond to the selection of the atomic units system, which is going to be used hereafter along this work [123].

The HF ansatz to approximate the many electron wave function in terms of single-particle orbitals is known as Slater determinant, namely:

$$\Phi(\mathbf{x}_1, \mathbf{x}_2, \cdots, \mathbf{x}_N) = \frac{1}{\sqrt{N!}}\begin{vmatrix} \phi_1(\mathbf{x}_1) & \phi_2(\mathbf{x}_1) & \cdots & \phi_N(\mathbf{x}_1) \\ \phi_1(\mathbf{x}_2) & \phi_2(\mathbf{x}_2) & \cdots & \phi_N(\mathbf{x}_2) \\ \vdots & \vdots & \ddots & \vdots \\ \phi_1(\mathbf{x}_N) & \phi_2(\mathbf{x}_N) & \cdots & \phi_N(\mathbf{x}_N) \end{vmatrix}. \tag{2.67}$$

The coordinates $\mathbf{x}_i$ represent, as before, the set of spatial and spin coordinates (i.e., $\mathbf{x}_i = \{\mathbf{r}_i, \sigma_i\}$). One of the main advantages of the HF approximation is that, despite the functional form in terms of the single-particle orbitals $\{\phi_i\}$ (implying an independent-particle or mean-field description), it fulfills an important condition of the quantum many-body theory (i.e., the many-body wave function of an electronic system should be antisymmetric with respect to the exchange of the coordinates of two electrons). This condition may be verified by simple inspection of eq. (2.67).

The key idea of the HF method is to get the set of orbitals $\{\phi_i\}$ which are optimal in the sense of the variational principle reviewed in the previous section, that is, the set for which the Slater determinant fits better the many-electron ground state and the energy is minimal within the restrictions imposed by the form (2.67). If an orthonormal constrain is chosen for the single-particle orbitals $\langle\phi_i|\phi_j\rangle = \delta_{i,j}$, then the Slater determinant is normalized, so $\langle\Phi|\Phi\rangle = 1$. Hence, it is required to solve the variational problem: eq. (2.63) inserting the explicit expression of the electronic Hamiltonian, the Slater determinant as the trial wave function and the additional orthonormal constrains on the orbitals. This can be achieved by constructing the auxiliary functional $F$:

$$F = \left\langle \Phi|\hat{H}_e|\Phi \right\rangle - \sum_{i,j} \lambda_{ij} \left[ \langle\phi_i|\phi_j\rangle - \delta_{i,j} \right], \tag{2.68}$$

where $\lambda_{ij}$ are Lagrange multipliers (to be determined), introduced to enforce the constrains on the orbitals. The HF method consists in the solution of the HF equations which give the solution of the variational problem $\delta F = 0$, when the set of functions $\{\phi_i\}$ are varied within a properly defined one-particle Hilbert space. The solution of the variational problem leads to the HF equations, which may be expressed as the eigenvalue problem of the Fock operator [123]:

$$\hat{F}\phi_k = \varepsilon_k \phi_k, \tag{2.69}$$

where:

$$\hat{F} = \hat{h}_1 + \sum_{i=1}^{N} \left( \hat{J}_i - \hat{K}_i \right). \tag{2.70}$$

The operators $\hat{J}_i$ and $\hat{K}_i$ are defined by their action on the orbitals:

$$\hat{J}_i \phi_k(\mathbf{x}_1) = \int \frac{|\phi_i(\mathbf{x}_2)|^2}{|\mathbf{x}_2 - \mathbf{x}_1|} \phi_k(\mathbf{x}_1) \mathrm{d}\mathbf{x}_2, \tag{2.71}$$

$$\hat{K}_i \phi_k(\mathbf{x}_1) = \int \frac{\phi_i^*(\mathbf{x}_2) \hat{P}_{12} \left[ \phi_i(\mathbf{x}_2) \phi_k(\mathbf{x}_1) \right]}{|\mathbf{x}_2 - \mathbf{x}_1|} \mathrm{d}\mathbf{x}_2. \tag{2.72}$$

They are called the Coulomb and the Exchange operators, respectively. The operators $\hat{J}_i$ represent the classical interaction energy between two charge densities $\rho_1 = |\phi_i|^2$ and $\rho_2 = |\phi_k|^2$, while the operators $\hat{K}_i$ reflect a purely quantum mechanical effect derived from the property of antisymmetry of the many-body electronic wave function.

The Fock's operator depends on the orbitals which, in turn, are obtained after the eigenvalue problem: eq. (2.69) is solved. Therefore, the solution of eq.(2.69) has to be found using the so called self-consistent algorithms. This kind of methodologies have the characteristic that the calculations are started with an approximated set of orbitals $\{\phi_i\}$, which are used in the construction of the Fock's operator. The resulting operator is use to solve eq. (2.69) approximately. As a result, new orbitals arise and the process continues until a reasonable level of convergence is reached.

A key point in the HF methodology is that, at any step of the self consistent process, more than $N$ orbitals are obtained while only $N$ of them can be used for the construction of the new Fock's operator. When the target is the ground state of the system, the Koopmans' theorem justify the selection of the $N$ orbitals which correspond to the lowest eigenvalues in eq. (2.69) [123]. However, when the HF method is intended to be used for excited state calculations, there is more discussion about how to select the relevant orbitals. There are physical situations in which it is more convenient to express the electronic wave-function in terms of more than one Slater determinant. The differences between the results of a HF approach, with only one Slater determinant, and a many Slater determinants formulation are called the correlation effects. There are many other methodologies which include correlation effects, those which are based on many-body wave-functions are called post-HF methods.

As a final comment on the HF methodology we would like to emphasize that, in practice, the space of functions which is explored via the variation of the orbitals is restricted by the selection of a basis set of functions. For a given choice of the basis set, the eigenvalue problem: eq. (2.69) is transformed in the eigenvalue problem of a numerical matrix with dimension equal to the amount of functions in the basis set.

### 2.6.4 Density Functional Theory

The Density functional theory (DFT) is a general methodology for the determination of the ground state energy of an electronic system. It is based on the electronic density rather than on the many body electronic wave function. This calculation scheme stresses the fact that knowing the density of the electronic system should be enough to compute physical observables and the knowledge of the wave function is actually an over-determination of the problem.

The DFT is based on the theorems of Hohenberg and Kohn (1964). They stated that any physical observable of a system in the ground state may be obtained with the only knowledge of the electronic density at this state.

**Theorem 1** ($1^{st}$ Hohenberg-Kohn theorem [123])**.** *Any ground state property of an electronic system is uniquely determined by the ground-state spatial electron density.*

To proof the theorem (1), it will be proved first that ones the spatial density is fixed, it determines uniquely the external potential felt by the electronic system, and so it does the wave-function and the corresponding observables.

Let us suppose there are two systems of $N$ electrons in presence of different external potentials, which may be originated by the electrostatic potential of the nuclei in a certain molecule or solid, and both of them generate the same spatial electronic density $\rho(\mathbf{r})$ in the ground state. The Hamiltonians which describe both systems are denoted by $\hat{H}_1$ and $\hat{H}_2$, respectively:

$$\hat{H}_1 = \sum_{i=1}^{N} -\frac{1}{2}\nabla^2_{\mathbf{r}_i} + \sum_{i=1}^{N} U_1(\mathbf{r_i}) + V(\mathbf{r}_1, \cdots, \mathbf{r}_N), \tag{2.73}$$

$$\hat{H}_2 = \sum_{i=1}^{N} -\frac{1}{2}\nabla^2_{\mathbf{r}_i} + \sum_{i=1}^{N} U_2(\mathbf{r_i}) + V(\mathbf{r}_1, \cdots, \mathbf{r}_N). \tag{2.74}$$

In these expressions, the one-particle functions $U_i$ represent the interaction potential of each electron with the external fields, while $V$ is the potential energy of the electronic gas due to the interactions among them (i.e., the contributions of all the terms of the type (2.66)). The ground state of these two Hamiltonians, $|\Psi_1\rangle$ and $|\Psi_2\rangle$ obey the following relations:

$$\hat{H}_1 \left|\Psi_1\right\rangle = E_1 \left|\Psi_1\right\rangle, \tag{2.75}$$

$$\hat{H}_2 \left|\Psi_2\right\rangle = E_2 \left|\Psi_2\right\rangle. \tag{2.76}$$

Nevertheless, according to the hypothesis introduced at the beginning of this proof, they both yield the same spatial electronic density:

$$\rho(\mathbf{r}) = \sum_{i=1}^{N} \langle \Psi_1 | \delta(\mathbf{r} - \mathbf{r}_i) | \Psi_1 \rangle = \sum_{i=1}^{N} \langle \Psi_2 | \delta(\mathbf{r} - \mathbf{r}_i) | \Psi_2 \rangle. \tag{2.77}$$

Since $|\Psi_1\rangle$ is the ground state of $\hat{H}_1$, according to the variational principle every other state $|\Psi\rangle \neq |\Psi_1\rangle$ satisfies the inequality (2.62):

$$\left\langle \Psi | \hat{H}_1 | \Psi \right\rangle > E_1. \tag{2.78}$$

Considering the particular case: $|\Psi\rangle = |\Psi_2\rangle$, and writing $\hat{H}_1 = \hat{H}_1 - \hat{H}_2 + \hat{H}_2$ in (2.78) we obtain:

$$\left\langle \Psi_2 | \hat{H}_1 - \hat{H}_2 + \hat{H}_2 | \Psi_2 \right\rangle = \left\langle \Psi_2 | \hat{H}_1 - \hat{H}_2 | \Psi_2 \right\rangle + \left\langle \Psi_2 | \hat{H}_2 | \Psi_2 \right\rangle > E_1, \tag{2.79}$$

which results, making use of definitions (2.73), (2.74) and (2.76), in:

$$\langle \Psi_2 | \sum_{i=1}^{N} U_1(\mathbf{r_i}) - \sum_{i=1}^{N} U_2(\mathbf{r_i}) \, | \Psi_2 \rangle + E_2 > E_1. \tag{2.80}$$

The operator inside the bra-ket in (2.80) is a single-particle operator. This fact may be combined with the expression for the density eq. (2.77) to get the following relation:

$$\int \rho(\mathbf{r}) [U_1(\mathbf{r}) - U_2(\mathbf{r})] \mathrm{d}\mathbf{r} + E_2 > E_1. \tag{2.81}$$

In a completely analog procedure to the one just presented, using the condition (2.78) with the Hamiltonian $\hat{H}_2$ and the state $|\Psi_1\rangle$ (rather than $\hat{H}_1$ and the state $|\Psi_2\rangle$, respectively) it is obtained:

$$\int \rho(\mathbf{r}) [U_2(\mathbf{r}) - U_1(\mathbf{r})] \mathrm{d}\mathbf{r} + E_1 > E_2. \tag{2.82}$$

Finally, the inequalities (2.81) and (2.82) can not be verified at the same time. Therefore, the initial assumption must be false and the statement of the theorem (1) is proved.

The first Hohenberg-Kohn theorem is a cornerstone for the further development of DFT. It guarantees that there exist a functional which express the dependence of every ground state observable on the ground state spatial electron density. If the total energy functional of a certain electronic system is denoted as $E_0[\rho]$, where $\rho$ is the electron density, the second Hohenberg-Kohn theorem states a variational principle for $E_0[\rho]$.

**Theorem 2** ($2^{nd}$ Hohenberg-Kohn theorem [123])**.** *In the hypothetic case, when the functional $E_0[\rho]$ is known, a variational principle similar to (2.62) is verified with respect to the change of arbitrary densities compared with the corresponding to the ground state. For instance, let us denote the ground state density as $\rho$ and any other density as $\rho'$, then the following inequality is fulfilled:*

$$E_0[\rho'] \geq E_0[\rho]. \tag{2.83}$$

The theorem (2) gives the basis for the development of algorithms to find the ground state spatial electron density directly (i.e., without computing the many-body wave function first). The general idea of those algorithms is to approximate the ground state functional, and to develop a methodology to find the density which minimizes it. The family of these algorithms is known as Density Functional Theory (DFT). This theory became very famous after the contribution of Kohn and Sham in 1965. They developed a powerful scheme which made the DFT calculations much more easy than the wave function based methods. Their methodology provides a reasonable accuracy, which may be even increased in the framework of the same formulation. The main aspects of the Kohn-Sham method are described in the following.

The unknown ground state functional $E_0[\rho]$ may be written as:

$$E_0[\rho] = T[\rho(\mathbf{r})] + \int V_{ext}(\mathbf{r})\rho(\mathbf{r})\mathrm{d}\mathbf{r} + \frac{1}{2}\int V_C(\mathbf{r})\rho(\mathbf{r})\mathrm{d}\mathbf{r} + E'_{xc}[\rho(\mathbf{r})], \tag{2.84}$$

where $T[\rho(\mathbf{r})]$ is the kinetic energy functional, $\int V_{ext}(\mathbf{r})\rho(\mathbf{r})\mathrm{d}\mathbf{r}$ represents the interaction energy between the electronic gas and an external field $V_{ext}(\mathbf{r})$, $\frac{1}{2}\int V_c(\mathbf{r})\rho(\mathbf{r})\mathrm{d}\mathbf{r}$ accounts for the electrostatic interaction between the electrons, $V_C(\mathbf{r}) = \int \frac{\rho(\mathbf{r}')}{|\mathbf{r}-\mathbf{r}'|}\mathrm{d}\mathbf{r}'$ is the Coulomb electrostatic potential generated by the electron density $\rho(\mathbf{r}')$ at a point $\mathbf{r}$, and the last term $E'_{xc}[\rho(\mathbf{r})]$ is an unknown functional which include the remaining electronic interactions (i.e., exchange and correlation).

The idea of the Kohn and Sham methodology is the introduction of an effective non-interacting system, with the same number of particles and subject to the constrains of having the same electron density and energy of the real system at any time. Both the real and the fictitious systems are described by the same functional $E_0[\rho]$. In the case of the non-interacting system $E_0[\rho]$ can be written as:

$$E_0[\rho] = T_0[\rho(\mathbf{r})] + \int V_{eff}(\mathbf{r})\rho(\mathbf{r})\mathrm{d}\mathbf{r}, \tag{2.85}$$

where $T_0$ is the kinetic energy functional and $V_{eff}$ is a potential energy which makes it possible that both systems have the same energy and density.

Combining the variational principle (2.83), and the functional forms proposed for $E_0[\rho]$ in eqs. (2.84) and (2.85), a formal expression for the effective potential is obtained [123]:

$$V_{eff}(\mathbf{r}) = \frac{\delta T}{\delta\rho}[\rho(\mathbf{r})] - \frac{\delta T_0}{\delta\rho}[\rho(\mathbf{r})] + V_{ext}(\mathbf{r}) + V_C\left[\rho(\mathbf{r})\right] + \frac{\delta E'_{xc}}{\delta\rho}[\rho(\mathbf{r})]. \tag{2.86}$$

In this expression, the derivatives of $T$, $T_0$ and $E'_{xc}$ are functional derivatives with respect to $\rho(\mathbf{r})$. A significant property of $V_{eff}(\mathbf{r})$ is its dependence on the electron density, which is the final goal of the DFT calculations.

The Kohn-Sham methodology continues with the solution of the TISE of the non-interacting system under the action of $V_{eff}(\mathbf{r})$. The resulting many-body

Hamiltonian reads:

$$\hat{H} = \sum_{i=1}^{N} \left[ -\frac{1}{2}\nabla^2_{\mathbf{r}_i} + V_{eff}(\mathbf{r_i}) \right] = \sum_{i=1}^{N} \hat{h}_{eff}(i), \tag{2.87}$$

where $\hat{h}_{eff}(i)$ has only single-particle interaction terms. Its ground state can be found solving the corresponding TISE equation:

$$\hat{H}\left|\Psi\right\rangle = E\left|\Psi\right\rangle. \tag{2.88}$$

At this stage, the HF approximation is recalled and the many-particle wave function $\left|\Psi\right\rangle$ in eq. (2.88) is expanded following the HF ansatz. Since this is a non-interacting system, the many-particle wave function can be expanded using a single Slater Determinant. The variational principle translates the problem of solving eq. (2.88) into an eigenvalue problem for the single-particle orbitals $\phi_i$ (Kohn-Sham orbitals):

$$\hat{h}_{eff}\phi_i = \varepsilon_i\phi_i. \tag{2.89}$$

The unknown terms in eq. (2.86) can be written in a compact form after the introduction of the exchange-correlation potential $V_{xc}$:

$$V_{xc} \equiv \frac{\delta E'_{xc}}{\delta\rho}(\rho(\mathbf{r})) = \frac{\delta T}{\delta\rho}(\rho(\mathbf{r})) - \frac{\delta T_0}{\delta\rho}(\rho(\mathbf{r})) + \frac{\delta E'_{xc}}{\delta\rho}(\rho(\mathbf{r})). \tag{2.90}$$

Employing this notation and the definition of $\hat{h}_1$ in eq. (2.65), the eigenvalue problem for the Kohn-Sham (KS) orbitals $\phi_i$ may be expressed as:

$$\left[\hat{h}_1 + V_C\left(\rho(\mathbf{r})\right) + V_{xc}\left(\rho(\mathbf{r})\right)\right]\phi_i = \varepsilon_i\phi_i. \tag{2.91}$$

The equation (2.91) is similar to (2.69), with the difference that the local exchange-correlation potential replaces the non-local exchange operator. This is an advantage of the KS method because it makes the solution of the resulting equations much more affordable from the computational point of view, and therefore it leads to the possibility to treat bigger systems compared with the HF and post-HF computational schemes.

The Slater's determinant ansatz (2.67) brings the spatial electronic density to have the following functional form in terms of the KS-orbitals:

$$\rho(\mathbf{r}) = \sum_{i=1}^{N} \left|\phi_i(\mathbf{r})\right|^2. \tag{2.92}$$

Although the eigenvalue problems for both methods: HF and KS, are very similar (as expressed by the eqs. (2.69) and (2.91)), there are important differences between the algorithms used to solve both problems. The KS equations also needs to be solved self-consistently, due to the density dependence of the potentials $V_C\left(\rho(\mathbf{r})\right)$ and $V_{xc}\left(\rho(\mathbf{r})\right)$. However, since they depend on the density rather than on the orbitals, the general algorithm is the following. First, an initial electronic density is assumed to start the iterative process. This density is employed to evaluate the single particle Hamiltonian in eq. (2.91) and, as a result, a set of KS-orbitals is obtained. This process is repeated until a self-consistent solution is found. At the end, the density of the system is given in terms of the KS-orbitals: eq. (2.92) and the total energy can be computed from the KS-orbitals and the density as follows:

$$E_0 = \sum_{i=1}^{N} \left\langle \phi_i | \hat{h}_1 | \phi_i \right\rangle + \frac{1}{2} \int V_C(\mathbf{r})\rho(\mathbf{r})\mathrm{d}\mathbf{r} + E_{xc}[\rho(\mathbf{r})]. \tag{2.93}$$

The main problem of the KS method arises from the ignorance of an explicit expression for the exchange-correlation potential $V_{xc}[\rho(\mathbf{r})]$, which is directly related with the exchange-correlation functional by the expression:

$$E_{xc}[\rho(\mathbf{r})] = \int V_{xc}[\rho(\mathbf{r})]\rho(\mathbf{r})\mathrm{d}\mathbf{r}. \tag{2.94}$$

The design of more accurate yet affordable exchange-correlation functionals is still an active research field, there are many forms which have been proposed for $E_{xc}[\rho(\mathbf{r})]$ but, at present, none of them can be said to be universal (i.e., they can not provide a satisfactory description of electron correlation effects in all situations). Typically, DFT calculations give good results, comparable with experiments. Absolute magnitudes, like total energies, present a significant dependence on the employed exchange-correlation functional but the relative quantities, like energy differences respect to a reference structure, are in general robust with respect to the functionals.

There are three major groups of exchange-correlation functionals: LDA (which stands for Local Density Approximation), GGA (Generalized Gradient Approximation) and Hybrid functionals. The main aspects of them are briefly presented here.

The LDA methods are based on a reference electronic system, namely the homogeneous electron gas. This is a physical situation in which the electrons are uniformly distributed in space $\rho(\mathbf{r}) = \rho$. There are statistical methods which allow the determination of $V_{xc}$ as a function of $\rho$ [123]. The local density approximation for real systems consists in the evaluation of $V_{xc}(\mathbf{r})$ as the value of the exchange-correlation potential at the homogeneous electron gas at the local electron density $\rho(\mathbf{r})$ of the actual system. The different methods differ in the procedure to fit $V_{xc}(\mathbf{r})$ to analytical expressions, as well as in the inclusion or not of spin polarization (the variants where the polarization is included, are known as Local Density Spin Approximation (LDSA) methods). The LDA-based methods usually approach the experimental results, and even get closer than the corresponding HF calculations. They are very convenient, specially in the calculation of equilibrium structures and vibrational frequencies of molecular complex [126]. However, there are properties, such as binding energies, which are not very well estimated. This problem is known as the overbinding problem of LDA-based exchange-correlation functionals.

The GGA methods may be considered as extensions of the LDA ones. They have included the dependence on higher order derivatives of the density, for instance $\nabla\rho$, $\frac{\delta^2\rho}{\delta x\delta y}$ [127,128]. There are various properties which are better estimated within the framework of the GGA functionals than within the LDA ones. GGA methods yield: better ground state energies for atomic species [129–131], geometric parameters and dissociation energies for molecular systems [129–131] and cohesive energies for a number of solids [132–134]. Nevertheless, they do not represent a significant improvement when it is willing to estimate ionization potentials or electron affinities [135].

In a foregoing series of papers [136–138], written by Axel D. Becke, it was probed that the introduction of the gradient corrected contributions, as well as the exact exchange operator: eq. (2.72) as an implicit functional of the electronic density, into the LDA exchange-correlation functionals $E_{xc}^{LDA}$ has a significant improving effect on the overbinding problem of the LDA-DFT formalism. However, those contributions were not able to reproduce, independently, a set of reference results like ionization potentials of previously given databases of atoms and molecules, namely: G1 and G2 [136–138]. The hybrid methods are based in the construction of an exchange-correlation potential, by the combined inclusion of the above contributions weighted in a proper way.

The exchange-correlation energy resulting for the hybrid functional, with three parameters, proposed by Becke in [138] may be written as:

$$E_{xc} = E_{xc}^{LDA} + a_0\left(E_x^{Exact} - E_x^{LDA}\right) + a_x\left(E_x^{B88} - E_x^{LDA}\right) + a_c\left(E_c^{PW91} - E_c^{LDA}\right). \tag{2.95}$$

The coefficients $a_0 = 0.20$, $a_x = 0.72$ and $a_c = 0.81$ where determined by a least-square fitting process with respect to a survey of experimental molecular heats of formation [138]. $E_x^{Exact}$ is the exact exchange energy, coming from the operator (2.72), $E_x^{LDA}$ is the only-exchange contribution of the LDA functional. $E_x^{B88}$ and $E_c^{PW91}$ are the only-, exchange and correlation, of the functionals: Becke 1988 [128] and, Perdew and Wang 1991 [139], respectively. When the GGA functional of Lee, Yang and Parr, 1988 [140] is employed instead of PW91, the expression (2.95) is called B3LYP [141]. The B3LYP is one of the most widely used functionals within the DFT-framework due to its very good comparability with experimental results in a big amount of physical systems [142].

## 2.7 Structural description of model catalysts

In the previous section a very general overview of electronic structure methods was presented, focusing on the HF and the DFT theories. At present, several useful concepts for the description of catalytic reactions are discussed. Since the main interest lays on the description of chemical transformations (i.e., catalytic reactions), contrary to the methods described in Sec. 2.6, the motion of the nuclei is at the center of the present analysis. The concept of PES, introduced within the BOA in the Sec. 2.54, is very important in the description of the structural modifications, which take place in a time scale much larger than the natural time scale of the electrons movement. Consequently, the nuclei move under the influence of the mean field created by the electrons.

### 2.7.1 Geometry optimization

The stationary states of the nuclei in a molecular system are described by the nuclear TISE, eq. (2.56), under the conditions imposed in the BOA. The potential energy surface on which the nuclei move is a combination of the electrostatic nuclear interactions $\hat{H}_{p,n-n}$ and the electronic field $V(\{\mathbf{R}_i\})$. If it is denoted by $U(\{\mathbf{R}_i\})$, then it will result as follows:

$$U(\{\mathbf{R}_i\}) = \hat{H}_{p,n-n} + V(\{\mathbf{R}_i\}) = \sum_{k\neq p=1}^{M} \frac{Z_k Z_p}{|\mathbf{R}_k - \mathbf{R}_p|} + V(\{\mathbf{R}_i\}). \tag{2.96}$$

In the second equality, we have made use of the analytic form of $\hat{H}_{p,n-n}$ in atomic units, when $M$ nuclei with atomic numbers $\{Z_k\}$ are considered.

$U(\{\mathbf{R}_i\})$ is a multidimensional surface in the configurational space $\Re^{3M}$. The determination of local minimums in $U(\{\mathbf{R}_i\})$ is of remarkable importance in the study of chemical reactions in general and of catalytic ones in particular. These are equilibrium points (i.e., the nuclei do not experience any force at these configurations) and they may be used to find the reaction mechanism of a certain molecular process. Due to their relative stability, local minima $\{\mathbf{R}_i^0\}$ on the hypersurface $U(\{\mathbf{R}_i\})$ are nuclear configurations which may represent intermediate steps in the investigated reaction.

Usually, when reaction mechanisms are investigated, one proposes a certain nuclear configuration motivated by an intuitive idea on the pathway to be followed during the process. A common question arise in this situation: is there any local minimum of $U(\{\mathbf{R}_i\})$ close enough to the initial configuration? The answer to this question and the configuration itself may be encountered by the procedure known as geometry optimization.

Most of the numerical algorithms for geometry optimization are based on the power expansion of the PES $U(\{\mathbf{R}_i\})$, up to the second order, around the sought point $\{\mathbf{R}_i^0\}$, that is:

$$U(\{\mathbf{R}_i\}) \simeq (\{\mathbf{R}_i^0\}) + \mathbf{g} \cdot (\{\mathbf{R}_i - \mathbf{R}_i^0\}) + \frac{1}{2}(\{\mathbf{R}_i - \mathbf{R}_i^0\})^\dagger \cdot \mathbb{H} \cdot (\{\mathbf{R}_i - \mathbf{R}_i^0\}), \quad (2.97)$$

where $\mathbf{g}$ is the gradient vector and $\mathbb{H}$ is the Hessian matrix:

$$\mathbf{g} = \left.\frac{\partial U}{\partial\{\mathbf{R}_i\}}\right|_{\{\mathbf{R}_i^0\}}, \quad (2.98)$$

$$\mathbb{H} = \left.\left|\left|\frac{\partial^2 U}{\partial\{\mathbf{R}_i\}\partial\{\mathbf{R}_j\}}\right|\right|\right|_{\{\mathbf{R}_i^0\}}. \quad (2.99)$$

After a ground state calculation at a fixed nuclear configuration $\{\mathbf{R}_i\}$, standard electronic structure algorithms can be used to compute the gradient of the PES: eq. (2.98). The geometry optimization procedure shifts the nuclear coordinates following some criteria which depends on the specific algorithm, but in all cases they aim to reduce the absolute value of the gradient until it vanishes. The process stops after a certain tolerance threshold is reached for the absolute value of all the components of the vector (2.98).

Therefore, it is possible to find three kinds of points: stable configurations (minima), unstable ones (maxima) and transition states (saddle points). The Hessian matrix: eq. (2.99) is used to determine to which of these three basic types each point belongs, that is:

i) If the Hessian matrix is definitely positive, the point is a minimum.

ii) If the Hessian matrix is definitely negative, the algorithm reached a maximum.

iii) If the Hessian matrix is not either definitely positive nor definitely negative, the point is a saddle point.

There are many algorithms specifically designed to look for local minimums in many-dimensional surfaces. They may use the gradient, the Hessian or even higher derivatives in the seeking process but the objective of all of them is to reach the desired point in the lowest amount of steps possible, employing the geometrical specifications of the PES. Some of the most used ones are the followings: the steepest descent method, the Newton-Raphson algorithm, and the method of the conjugate gradient [143].

### 2.7.2 Frequency calculation

The frequency calculation (or normal mode analysis) is a standard procedure that may be thought in general as the diagonalization of the Hessian matrix (2.99). Its importance goes beyond the eigenvalues themselves, since it can be used to study the internal vibrations of a molecular system in the harmonic approximation.

Let us expand the position vector of the nuclei $\{\mathbf{R}_i\}$ as $\{(R_{i,x}, R_{i,y}, R_{i,z})\}$, to get a more comfortable notation for what follows. In terms of the scalar coordinates $\{R_{i,\alpha}\}$ ($i$ runs over the number of atoms, the set of integers $\{1, M\}$, while $\alpha$ belongs to $\{1, 3\}$ which represent the cartesian axis $x, y, z$, respectively) the potential energy may be expressed as:

$$U(\{\mathbf{R}_i\}) = U(R_{1,1}, R_{1,2}, R_{1,3}, \cdots, R_{M,1}, R_{M,2}, R_{M,3}). \tag{2.100}$$

In general, we are interested in the study of molecular vibrations around stable configurations (i.e., in the vicinity of a point where $\mathbf{g} = \mathbf{0}$). Close enough to the equilibrium points $\{R^0_{i,\alpha}\}$, the PES may be expanded up to second order in powers of the deviations from the equilibrium position: eq. (2.97):

$$\begin{gathered} U(\{R_{i,\alpha}\}) \simeq U(\{R^0_{i,\alpha}\}) + \\ +\frac{1}{2}\sum_{i_1,i_2=1}^{M}\sum_{\alpha_1,\alpha_2=1}^{3}\frac{\partial^2 U(\{R^0_{i,\alpha}\})}{\partial R_{i_1,\alpha_1}\partial R_{i_2,\alpha_2}}\left(R_{i_1,\alpha_1} - R^0_{i_1,\alpha_1}\right)\left(R_{i_2,\alpha_2} - R^0_{i_2,\alpha_2}\right). \end{gathered} \tag{2.101}$$

In this expression, the term containing the gradient $\mathbf{g}$ at the equilibrium position has been removed, while the elements of $\mathbb{H}$ have been written explicitly.

The matrix $\mathbb{H}$ at equilibrium points represents a positively defined quadratic form. It is known that there are certain generalized coordinates for which the matrix of the quadratic form becomes diagonal, and all its eigenvalues are positive. The solution of the nuclear TISE in these coordinates is particularly simple. The possibility to decouple those collective nuclear DoF is shown in the following. Consequently, the solution of this problem may be expressed as a set of independent harmonic oscillators. The Hamiltonian for the nuclear TISE: eq. (2.56), within the harmonic approximation of the PES, may be written as follows:

$$\begin{gathered} \hat{H}_n = -\sum_{i=1}^{M}\frac{1}{2M_i}\nabla^2_{\mathbf{R}_i} + \\ +\frac{1}{2}\sum_{i_1,i_2=1}^{M}\sum_{\alpha_1,\alpha_2=1}^{3}\frac{\partial^2 U(\{R^0_{i,\alpha}\})}{\partial R_{i_1,\alpha_1}\partial R_{i_2,\alpha_2}}\left(R_{i_1,\alpha_1} - R^0_{i_1,\alpha_1}\right)\left(R_{i_2,\alpha_2} - R^0_{i_2,\alpha_2}\right). \end{gathered} \tag{2.102}$$

Since the quadratic form of the PES in eq. (2.102) is positively defined, its topological form about the equilibrium position is a hyper-paraboloid. If the total energy is low enough the nuclei shall be only allowed to make small oscillations about their equilibrium positions. Let us consider that this is the case, and solve the TISE within the Hamiltonian (2.102).

The new mass-scaled coordinates, defined by the eq. (2.103), shall be considered:

$$\boldsymbol{\eta}_i = \sqrt{M_i}\left(\mathbf{R}_i - \mathbf{R}_i^0\right). \tag{2.103}$$

Inserting (2.103) in (2.102) a new form for the Hamiltonian is obtained:

$$\hat{H}_n = -\sum_{i=1}^{M} \frac{1}{2}\nabla^2_{\boldsymbol{\eta}_i} + \frac{1}{2}\sum_{i_1,i_2=1}^{M}\sum_{\alpha_1,\alpha_2=1}^{3} \frac{1}{\sqrt{M_{i_1}M_{i_2}}}\frac{\partial^2 U(\{R^0_{i,\alpha}\})}{\partial R_{i_1,\alpha_1}\partial R_{i_2,\alpha_2}}\eta_{i_1,\alpha_1}\eta_{i_2,\alpha_2}. \tag{2.104}$$

The new quadratic form, which is the PES of the Hamiltonian (2.104) in terms of the new coordinates $\{\boldsymbol{\eta}_i\}$, defines a matrix which is known as the dynamical matrix, namely:

$$\mathbb{D} = \left\| \frac{1}{\sqrt{M_{i_1}M_{i_2}}}\frac{\partial^2 U(\{R^0_{i,\alpha}\})}{\partial R_{i_1,\alpha_1}\partial R_{i_2,\alpha_2}} \right\|. \tag{2.105}$$

The dynamical matrix is symmetric and real, so it can be diagonalized using a similarity transformation as follows:

$$\mathcal{D} = \mathbb{Q}\mathbb{D}\mathbb{Q}^\dagger, \tag{2.106}$$

here $\mathcal{D}$ is a diagonal matrix with positive eigenvalues $\{\Omega_i^2\}$ and $\mathbb{Q}$ is an orthogonal matrix whose existence is guaranteed. Finding the matrix $\mathbb{Q}$, for a given $\mathbb{D}$, is the well known eigenvectors-eigenvalues problem, for which efficient algorithms are available [143]. Once $\mathbb{Q}$ is known, it is used to define a new set of coordinates (i.e., the normal modes $\{\xi_i\}$):

$$\boldsymbol{\xi} = \mathbb{Q}\boldsymbol{\eta}. \tag{2.107}$$

Notice that the matrix $\mathbb{Q}$ is a square matrix with dimension $3M$, so the expression (2.107) is well defined if the $M$ vectors $\boldsymbol{\eta}_i$ are expanded in their three components to form the $3M$ column vector:

$$\boldsymbol{\eta} = \left(\eta_{1,1}, \eta_{1,2}, \eta_{1,3}, \cdots, \eta_{M,1}, \eta_{M,2}, \eta_{M,3}\right)^t. \tag{2.108}$$

An orthogonal transformation like eq. (2.107) keeps invariant the kinetic operator of the Hamiltonian with respect to the new coordinates [123]. In terms of the normal modes, the nuclear Hamiltonian results:

$$\hat{H}_n = \sum_{i=1}^{3M} \left[ -\frac{1}{2}\frac{\partial^2}{\partial \xi_i^2} + \frac{1}{2}\Omega_i^2 \xi_i^2 \right]. \tag{2.109}$$

Although this Hamiltonian describes a $3M$ dimensional system, it is obviously separable, all its DoFs are decoupled and the system may be treated as a set of independent one-dimensional harmonic oscillators. The many particle wave function $\Psi_n(\{\mathbf{R}_i\})$ which is the solution of the nuclear TISE: eq. (2.56), is expressed as a direct product of one-dimensional functions depending on the normal mode coordinates, namely:

$$\Psi_n(\{\mathbf{R}_i\}) = \psi_1(\xi_1)\psi_2(\xi_2)\cdots\psi_{3M}(\xi_{3M}). \tag{2.110}$$

The nuclear TISE: eq. (2.56), with the Hamiltonian expressed in terms of the normal modes: eq. (2.109) and the wave function ansatz: eq. (2.110), splits up in the following $3M$ one-dimensional equations for the single-particle functions $\psi_i(\xi_i)$:

$$\left[ -\frac{1}{2}\frac{\partial^2}{\partial \xi_i^2} + \frac{1}{2}\Omega_i^2 \xi_i^2 \right] \psi_i(\xi_i) = E_i \psi_i(\xi_i), \tag{2.111}$$

where the total energy of the multidimensional problem is given by: $E_{tot} = \sum_i E_i$.

The eigenvalue equations (2.111) can be solved analytically, and its solutions can be found elsewhere [125]. The eigenvalues are given by:

$$E_i = (n_i + \frac{1}{2})\Omega_i, \tag{2.112}$$

where $n_i$ can take integer values $(0, 1, 2, \cdots, n, \cdots)$, and it is called the occupation number and characterizes the excitation state of the corresponding normal modes on the given PES.

Finally, the total energy of the target system is given by:

$$E_{tot} = \sum_i (n_i + \frac{1}{2})\Omega_i. \tag{2.113}$$

Throughout the frequency calculations, different kinds of information may be obtained, for example, the oscillation frequencies $\{\Omega_i\}$, which can be compared with experimental results from infrared (IR) and Raman spectroscopy measurements. The geometrical characterization of the normal modes individually, in combination with the symmetry of the system (if there is any) gives information about the possibility to detect certain frequency by IR or Raman spectroscopy. Furthermore, at the ground state (i.e., all $n_i = 0$) the total energy is not zero:

$$E_{tot}^0 = \frac{1}{2}\sum_i \Omega_i. \tag{2.114}$$

This quantity is known as the zero point energy correction (ZPEC), and it is important in many cases for the accuracy which theoretical values can compare with and predict experimental ones.

In the described general algorithm for the frequency calculations, the more computationally intensive part is the computation of the Hessian matrix: eq. (2.99) used in the harmonic approximation of the PES: eq. (2.101). This procedure is commonly implemented in most of the electronic structure packages and it is useful, in addition, as a verification tool after a geometric optimization. If the optimization process find an actual minimum, then the Hessian matrix will be positively defined and all its eigenvalues will be positives.

### 2.7.3 Extended surfaces and molecular models

The study of catalytic reactions from a microscopic point of view is a difficult task, mainly due to the enormous amount of particles which are involved in the reaction of interest, and the quantum-mechanical nature of the particles. Typically, the reactions occur at the surface of the catalysts and they have different issues which may be difficult to include altogether in a realistic simulation (e.g., the presence of defects, dopants, etc.). One has then to chose a model representation of the surface, where a desired contribution is considered while many others (which are thought to be less important) are neglected. Most of current studies on catalytic reactions employ either an extended surface (supercell) model or a cluster model to investigate a detailed aspect of the reaction.

An extended surface is an idealized infinite surface with a perfect structure. It is not possible to deal with the infinite amount of DoFs present in such systems. However, introducing periodic boundary conditions (PBC) on the edges of a piece of structure which preserves the symmetry of the whole surface, it is possible to describe processes in a simplified way within the framework of supercell models. The Bloch's theorem [144] is the key tool which allows the combination of the PBC with any electronic structure method for the description of extended systems.

Bloch's theorem states that, any electronic orbital (e.g., the KS-orbitals) in a periodic system, may be described by the product:

$$\phi_{n,\mathbf{k}}(\mathbf{r}) = u_{n,\mathbf{k}}(\mathbf{r})\mathrm{e}^{i\mathbf{k}\cdot\mathbf{r}}. \tag{2.115}$$

Here, $n$ labels the electronic band, and $\mathbf{k}$ is a vector in the Brillouin zone (BZ). The functions $u_{n,\mathbf{k}}(\mathbf{r})$ have the periodicity of the constructed unit cell, and they may be expanded on a plane-wave basis as follows:

$$u_{n,\mathbf{k}}(\mathbf{r}) = \sum_{G} c_{n,\mathbf{k}}(G)\mathrm{e}^{i\mathbf{G}\cdot\mathbf{r}}. \tag{2.116}$$

Here the $c_{n,\mathbf{k}}(G)$ are the expansion coefficients and $\mathbf{G}$ are vectors of the reciprocal lattice, which fulfill the following condition: $\mathbf{G} \cdot \mathbf{L} = 2\pi\, l$, where $l$ is an integer. This condition reflects actually the periodicity of the unit-cell defined by the vector $\mathbf{L}$.

When the Bloch's wave functions are used in any electronic structure method, the eigenvalues which results $\varepsilon_{n,\mathbf{k}}$ depend on the discrete index $n$ and continuously about the vector $\mathbf{k}$. They represent the continuum of available electronic states in the periodic system. To compute physical observables, for instance the electronic density, it is required to perform integrals over the BZ. The integral is usually transformed in a summation process over a certain number of points inside the BZ. This procedure seeks a compromise between the amount of $\mathbf{k}$-points selected and the calculation time. More points imply a higher accuracy but demand more computational effort.

The expansion of the periodic functions $u_{n,\mathbf{k}}(\mathbf{r})$ on a plane-wave basis set has two main drawbacks:

i) The typical behavior of $u_{n,\mathbf{k}}(\mathbf{r})$ includes very fast oscillations in the vicinity of the nuclei of the target structure.

ii) An ideally infinite amount of plane-waves are needed to exactly reproduce the functions $u_{n,\mathbf{k}}(\mathbf{r})$.

The first issue i) is overcome by the implementation of the so-called pseudopotential approach. This methodology is based on the employment of an effective potential (pseudopotential), which takes into account the overall effect of the nuclei and core electrons in their interaction within the valence electrons [145]. Within this effective potential the actual behavior of the functions $u_{n,\mathbf{k}}(\mathbf{r})$ is reproduced far from the nuclei, while in their vicinities a smoother nature is guaranteed. The second problematic point ii) is solved within a compromise based on the fact that the expansion coefficients $c_{n,\mathbf{k}}(G)$ decrease with the increasing of the absolute value of the vector $\mathbf{G} + \mathbf{k}$ in the BZ. In practice, the amount of plane-waves employed in the expansion (2.116) is controlled by the energy cutoff ($E_{cut}$). The $E_{cut}$ is an upper limit of the kinetic energy of the electrons in the periodic structure, and it is related with $|\mathbf{G} + \mathbf{k}|$ [124]:

$$\frac{\hbar^2 \left|\mathbf{G} + \mathbf{k}\right|^2}{2m_e} \leqslant E_{cut} \tag{2.117}$$

The simulations of periodic systems focus on the possibility to describe the desired properties using the smallest supercell. To study bulk properties of a solid material, for example, the unit cell of the corresponding crystalline structure is usually large enough to compute bulk properties with sufficient accuracy. In the case of surface calculations, there is an evident problem with the periodicity along the direction perpendicular to the surface. The solution to this problem within the supercell method is to construct a unit cell which has a slab of the surface in the middle with the 2D-periodicity of the surface and significant vacuum space above and below it, so it will avoid the interaction with fictitious charges generated by the breaking of the translational symmetry.

The molecular methods are based on the assumption that the structure and physical properties of intermediate states in a catalytic reaction are determined by local interactions [146]. Hence, a representative portion (finite model) of the catalytic surface is employed for the description of the reaction. Usually, the infinite surface of interest is cut out considering one or many adsorption sites and their nearest neighbors. The resulting structure (molecular model), which may be a real molecule or a fictitious one, is employed to simulate an active site, or several ones, in the catalytic surface.

The detailed way in which the molecular models are constructed is an important point to be considered in order to use this methodology. There are rules which should be fulfilled to be able to approximate the electronic structure of an infinite material by a finite structural portion [146]. They can be summarized as follows: the definite number of electrons in the molecular model should be able to occupy a subset of atomic orbitals from the infinite structure in such manner their interactions with the outside electrons are minimized. In practical situations these rules are fulfilled only approximately. There are specific issues to take into account when different materials are considered (i.e., metals, metal oxides, etc.). For instance, due to the highly delocalization of the electronic states in metals, large clusters (typically more than 50 atoms) are necessary to fulfill the aforementioned rules [146]. However, there is a variety of models ranging from huge clusters [147], to small ones, which may be even only one metal atom [148–150], depending the properties of interest. There are other possibilities like, the methodology of embedded clusters, which is in between the large and small cluster models [147]. Although it takes into account a typically large cluster structure for the representation of the metallic surface, a small region of interest is picked up in the center to be considered with a higher level of theory than the surrounding part. This separation avoid the interaction between the interested subsystem and the unphysical boundaries of the complete cluster. Many examples show the usage of metallic clusters for a variety of surface processes: $Mo_6$ compound has been employed to study the adsorption of different species on molybdenum surfaces [151,152]; $Ni_{21}S_5$ was used to study the adsorption of sulfur atoms on Ni (110) surfaces at high coverages [153]; other examples may be found elsewhere in [154] and reference therein.

The procedure to build up a specific cluster model to study surface reactions on molecular or ionic crystals is easier with respect to the metallic structures. In these cases electrons are well localized in confined regions (i.e., ions or molecules), and their interaction (overlapping) with neighbors on different regions are significantly weak. However, the influence of the large range Coulomb interactions of the environment needs to be taken into account. Usually, this feature is included by an additional electrostatic potential, which may be computed with the help of a fictitious set of point charges. The key point of these models are the number of point charges to be considered. They are normally located at the ionic positions, and their absolute values are not necessary the actual ion charges. They should be determined in such a way that the resulting electric multipole moments of the polyatomic ion or molecule approach the actual ones [146].

In covalent materials, the valence electrons are shared between the atoms forming a chemical bond. Hence, a suitable molecular model of this type of systems needs to be constructed in such a way that minimize the number of broken electron couples. Unpaired electrons create artificial surface states (dangling bonds) which alter the electronic structure of the considered material, and are frequently found within the energy band gap. A general procedure, designed to solve this problem, is based in the implementation of the concept of saturator atoms. The saturator atoms may be real atoms or pseudoatoms which are bonded to the atoms in the border of the cluster, and guarantee in an approximate way, that the electronic structure of the molecular model reproduces the one from the infinite material. For example, if $TiO_4$ is used to represent the $TiO_2$ crystalline structure, the four oxygens will be negatively charged (-1$e$) due to the cutting of their respective bonds to the Ti atoms of the remaining structure. If hydrogen atoms are considered to be attached to each of the four oxygens in $TiO_4$, then the structure $Ti(OH)_4$ will represent in a more realistic way the electronic structure of the titanium dioxide. In this example, real atoms (the four hydrogens) have been used to saturate the molecular model. The concept of pseudoatoms is one step forward in the intention to reproduce the electronic structure of the crystal by molecular models. They are also saturator atoms but the effective nuclear charge, the number of valence electrons and the basis functions employed for valence orbitals are consistently modified to approach the electronic structure of the infinite material using the actual molecular model. More details about the construction of cluster models using pseudoatoms and examples of practical applications may be found elsewhere in [146].

Despite the difficulties generated by the construction of molecular models, they present several advantages in the description of catalytic processes. For example, they can be used to study such reactions using more accurate methodologies, like post-HF methods due to their lower dimensionality compared with extended surface methods. In the cluster models, a detailed inspection of the potential energy surface (PES) is affordable from the computational point of view, thereby allowing to extract more detailed information on the surface reaction from the mechanistic point of view.

# Chapter 3

# Water splitting on $TiO_2$-based electrochemical cells. Molecular models

## 3.1 Introduction

The employment of molecular hydrogen as energy carrier has become a remarkable step to support the development of the hydrogen economy. The current state of the hydrogen production process in electrochemical (ECC) or photoelectrochemical (PEC) cells, is characterized by significant energy losses. PECs and related devices are generally made of a semiconductor anode or photoanode (e.g., $TiO_2$) and a metal cathode (e.g., Pt) immersed in an electrolyte. Two half-reactions characterize the water decomposition: the $O_2$ evolution reaction (OER) at the anode and the $H_2$ evolution reaction by recombination of $H^+$ and $e^-$ at the cathode. The main source of the energy losses comes from the overpotentials of about 1 V at the anode surface [155]. This additional energy has to be employed to cover mainly kinetic limitations in the charge-transfer process at the semiconductor-liquid junction.

In the case of PECs, the photoanodes based on $TiO_2$ are relatively cheap, chemically and biologically inert and very stable under illumination. The absorption spectrum of the $TiO_2$ is centered in the UV radiation due to its band gap width (3 eV for the rutile structure and 3.2 eV for the anatase) [69,156], but the photoactivity of $TiO_2$ can be extended from UV to the visible part of the solar spectrum by chemical doping [157–163] or by using $TiO_2$ nanostructures like nanotube arrays [164]. The accepted general mechanism of the hydrogen production process contains the following main steps:

i) the creation of electron-hole pairs inside the anode by photoexcitation or the action of external bias: $S \rightarrow e^- + S^+$, where S stands for the surface of the anode and $e^-$ evolves to the cathode, and

ii) the separation of the electrons and holes due to the driving force in the semiconductor - liquid junction and the reaction of the holes with water molecules or hydroxide ions from the electrolyte: $S^+ + H_2O \rightarrow$ S-OH+$H^+$, or $S^+ + OH^- \rightarrow$ S-OH.

A commonly accepted theoretical description consists in the adsorption of two water molecules on the anode surface, followed by a reaction mechanism in which four electrons are transferred to the cathode in subsequent steps. At each step, the release of one $H^+$ is assumed to take place [40, 67]. The reaction at the anode is energetically unfavorable and an external potential is needed to make the reaction thermodynamically allowed. The anode surface can be considered as a catalyst for the water decomposition on the electrochemical cell and different studies consider a catalytic cycle in the description of this process [39, 40, 67, 156].

The theoretical study of the water splitting under the action of an external potential provides information about the reaction in two different devices: the ECC and the PEC. In the former one, the external potential is the applied potential over the electrodes whereas in the PEC it is directly related to the band gap of the photoelectrode. Despite all the experimental and theoretical attempts to explain these processes, the detailed mechanisms for both the OER at the anode and the HER at the cathode are not yet completely understood [39].

A cluster model of the surface presents several advantages in the description of the water decomposition on the electrodes, compared to the theoretical description of the overall surface. For these simplified models, electronic structure calculations more accurate than DFT-based methodologies (e.g., post Hartree-Fock methods) are affordable. A detailed inspection of the potential energy surface (PES) is tractable from the computational point of view, thereby allowing to extract information on the reaction mechanism. The atomistic description enables the identification of the rate-determining step, and also other relevant steps along the reaction path which exhibit large activation energies. High energy barriers along the OER pathway translate into the requirement of high overpotentials to make the process feasible.

This microscopic information could be important in the design of more efficient electrodes for ECC or PEC. Moreover, comparisons of the performance between calculations on extended surfaces and on small clusters within the same level of theory are useful in confirming the capability of the cluster model to reproduce the general trend of the energetics and the efficiency of the process, and it provides insight on how to build a more realistic representation of the surface in the framework of the small cluster approximation.

In this chapter, the theoretical modeling of the OER on $TiO_2$-based electrochemical cells is addressed employing small cluster models. At first, the reaction is studied on the clusters: $TiO_2$ and $Ti_2O_4$, motivated by previous works [38, 39] but within a different reaction mechanism. Then, the reaction is studied on the charged

$Ti(OH)_4^-$ cluster, and the differences to the neutral $Ti(OH)_4$ are highlighted. The charged structure may be considered as a model of the situation in which the water decomposition occurs on a site where a trapped electronic state is localized. The influence of the cluster sizes on the water splitting is addressed via the analysis of the decomposition pathways on the structures: $Ti(OH)_2$-$O_2$-$Ti(OH)_2$ and $Ti(OH)_3$-O-$Ti(OH)_3$ containing two titanium atoms. The first of these dimeric models may be regarded as a simplified representation of the active Ti-sites on the rutile (110) surface, while the second one resembles the spatial arrangement of atoms in an anatase structure which was cut exposing the (001) surface, Fig. 3.1.

The differences between the theoretical assumptions and the experimental conditions, and the neglect of the activation barriers in the proposed scheme, pose a significant challenge to the direct comparison between theoretical and experimental overpotentials [165]. Nevertheless, the methodology employed here to evaluate the overpotentials in different cluster models have been successfully used to account for experimental trends in a survey of different structures including a set of transition metal oxides [165]. In this chapter we aim to answer the following questions: Which cluster structure offers the more realistic representation of the surface of the anode for the description of the water splitting? How do the charged local sites influence the efficiency of the OER? Are the proposed models able to reproduce the trend of the overpotential with respect to the topology of the surface?

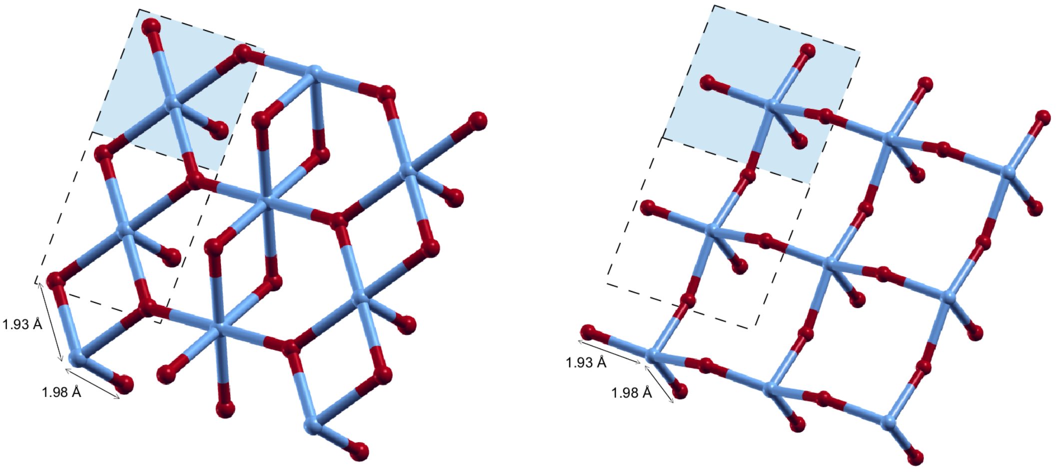

(a) (b)

**Figure. 3.1.** ***a)*** *Top view of the rutile* $TiO_2$ *(110) surface. The oxygen atoms are represented by the red points and the Ti are the blue ones. It is also represented the active site on the surface which is studied by a small cluster considering only the firsts neighbors of one 5-fold coordinated Ti (white dashed square). The extension of the cluster model including the next Ti-active site is also drown (dashed rectangle including the light blue square).* ***b)*** *Top view of the anatase* $TiO_2$ *(001) surface. The white dashed square is the smaller cluster representation for the active sites on this surface, while the rectangle including the light blue square is the representation when two Ti-centers are considered.*

The present chapter is organized as follows. In the Sec. 3.2, the general aspects of the proposed reaction mechanisms as well as the methodology to compute the *ab-initio* energy of each structure are presented. In the Sec. 3.3, the description of the OER mechanism on different titanium oxide cluster systems as well as, the comparison with experimental results is presented. Finally, a brief summary and concluding remarks are presented, Sec. 3.4.

## 3.2 Methodology

### 3.2.1 Model reaction pathways

To study the water decomposition on an electrochemical or PEC, a standard two-electrode configuration is considered in the following way. Two half equations, one for each electrode, are used to describe the process from the electrochemical point of view. The OER starts with the oxidation of a water molecule at the anode (c.f., eq. (3.1)) while the $H_2$ evolution takes place at the cathode (c.f., eq. (3.2)) after the reduction of two $H^+$ ions. Hence, the electrochemistry of the process can be summarized by the equations:

$$\mathrm{H_2O} \rightarrow \frac{1}{2}\mathrm{O_2} + 2\mathrm{H^+} + 2\mathrm{e^-} \qquad E^o = -1.23\ \mathrm{V}, \tag{3.1}$$

$$2\mathrm{H^+} + 2\mathrm{e^-} \rightarrow \mathrm{H_2} \qquad E^o = 0.00\ \mathrm{V}, \tag{3.2}$$

which characterize the global water splitting process at standard thermodynamic conditions. The water decomposition is not a spontaneous process at standard conditions, a potential higher than 1.23 V is needed to drive the overall reaction, eqs. (3.1) and (3.2).

The OER on the proposed models is described within the framework of the methodology previously developed by Nørskov and coworkers [112]. This electrochemical mechanism consists of four electron transfer steps [112]. However, it has been extended here to explicitly account for the adsorption of water molecules on the active sites of the surface. Hence, the following intermediate steps (labeled as A, B, C, D and E) are considered along all the reaction paths proposed in the present work:

$$\mathrm{A{:}\ H_2O + S \rightarrow H_2O\text{-}S}, \tag{3.3}$$

$$\mathrm{B{:}\ H_2O + S \rightarrow OH\text{-}S + H^+ + e^-}, \tag{3.4}$$

$$\mathrm{C{:}\ H_2O\text{-}S \rightarrow OH\text{-}S + H^+ + e^-}, \tag{3.5}$$

$$\mathrm{D{:}\ OH\text{-}S \rightarrow O\text{-}S + H^+ + e^-}, \tag{3.6}$$

$$\text{E: } O_2\text{-S-H} \rightarrow \text{S} + O_2 + H^+ + e^- . \tag{3.7}$$

Where S stands for the substrate or its cluster representation. The reaction A represents the adsorption of a water molecule on the cluster, it is considered to be molecularly adsorbed. Step B represents the dissociative adsorption of water: after the dissociation of a water molecule, the $OH^-$ group is attached to the cluster while a proton-electron pair is detached and the charge carriers move in opposite directions (i.e., the first goes into the electrolyte and the second move to the electrode). The reaction C may occur after reaction A, it corresponds to a deprotonation step from a water molecule attached to the cluster. A second deprotonation step is considered at D, it represents the process when one $H^+$ is extracted from an $OH^-$ attached on the cluster. The reaction E refers to the desorption of a $H^+$ simultaneously with the evolution of a preformed $O_2$ molecule, and an additional electron is transferred to the anode at the same time. The $O_2$ evolution is considered to be induced by the deprotonation process and therefore, the application of a sufficiently high external potential is able to induce it.

As a result, the reaction mechanism comprises both non electrochemical processes (e.g., the adsorption of a water molecule) and electrochemical ones (for instance: reactions B and C). The free energy barriers of the electron transfer steps may be always lowered by the external bias. The molecular adsorption of water will not be affected by the external potential, therefore it will be favorable from the thermodynamical point of view, only if it decreases the free energy even at zero bias.

The mechanism of the OER on each cluster is determined by the free energy landscape. For each of the reaction mechanisms, the optimized geometries of the intermediate structures and the corresponding zero point energies are calculated. The dependence of the free energy from the external potential U is considered within a simple heuristic model as proposed by Valdés, A. et al., [67]. This quantity is used to get information about the overpotential needed for the OER to proceed according to every one of the proposed mechanisms.

### 3.2.2 Computational details

The total energies of the stable molecular configurations are computed within the framework of the Density functional theory. The hybrid exchange-correlation functional of three semiempirical parameters due to Axel D. Becke [138] is employed in combination with the correlation contribution from the functional of Lee, Yang and Parr [140]. This merging, also known as the B3LYP exchange-correlation functional [141], has been intensively used in the study of transition metals contained systems in both cluster [38,39] and extended surfaces [109–115]. The triple-zeta valence basis set (TZV), based on constrained Gaussian type orbitals (GTOs) [166, 167], is used for every atom with the inclusion of polarization functions. The ROHF methodology, as developed by Roothaan [168], is employed to approach the ground-state energy of the open-shell electronic systems, on the presence of the effective B3LYP exchange-correlation potential. The convergence tolerance for the change of the electronic density on the DFT-SCF cycles is $10^{-4}$ electrons/bohr$^3$.

The optimization of molecular geometries, using analytic energy gradients, have been carried out within a quasi-Newton algorithm based on a quadratic approximation (QA) of the multidimensional PES [169]. The maximum of the Cartesian energy gradients at the optimum structures have been established at the value of $10^{-4}$ Ha/bohr. After every geometry optimization, a frequency calculation is performed. This guarantee the optimized geometry is a true minimum in the PES and allows the determination of the vibrational frequencies of the structure. The procedure to determine the normal modes and frequencies follows the description given above, Sec. 2.7.2, while the hessian matrix is computed in a fully analytical way. The DFT calculations of the electronic and total energies, as well as the determination of the vibrational frequencies and normal modes, are performed as it is implemented in the General Atomic and Molecular Electronic Structure System (GAMESS) package [170, 171].

## 3.3 Results and discussion

The molecular configurations in the proposed mechanisms for the water decomposition on different clusters, and the corresponding free energy profiles are shown in Fig. 3.2 - Fig. 3.7. The optimized structures and the energies of the intermediate steps show the details of the reaction mechanisms. For all the target systems, various processes are analyzed: the adsorption of two $H_2O$ molecules, the splitting of the water into a $H^+$ and an $OH^-$, the attachment of the $OH^-$ group on the Ti active sites, the formation of the $OOH^-$ group, the formation and desorption of the $O_2$ molecule, and finally the recovery of the initial cluster structure. The free energy is computed along every one of the proposed reaction paths. This quantity is employed to identify the rate-determining step in the reaction, thereby yielding the external potential required to make the free energy down-hill along the reaction coordinate.

### 3.3.1 Water splitting on $TiO_2$ and $Ti_2O_4$

The overall water splitting reaction on small $TiO_2$-based clusters has been investigated in previous works [38, 39]. There, the cluster structures were used to simulate a catalytic nanoparticle in an aqueous media. Conversely to these preceding studies [38, 39], in the present work, $TiO_2$ and $Ti_2O_4$ are employed as models for the

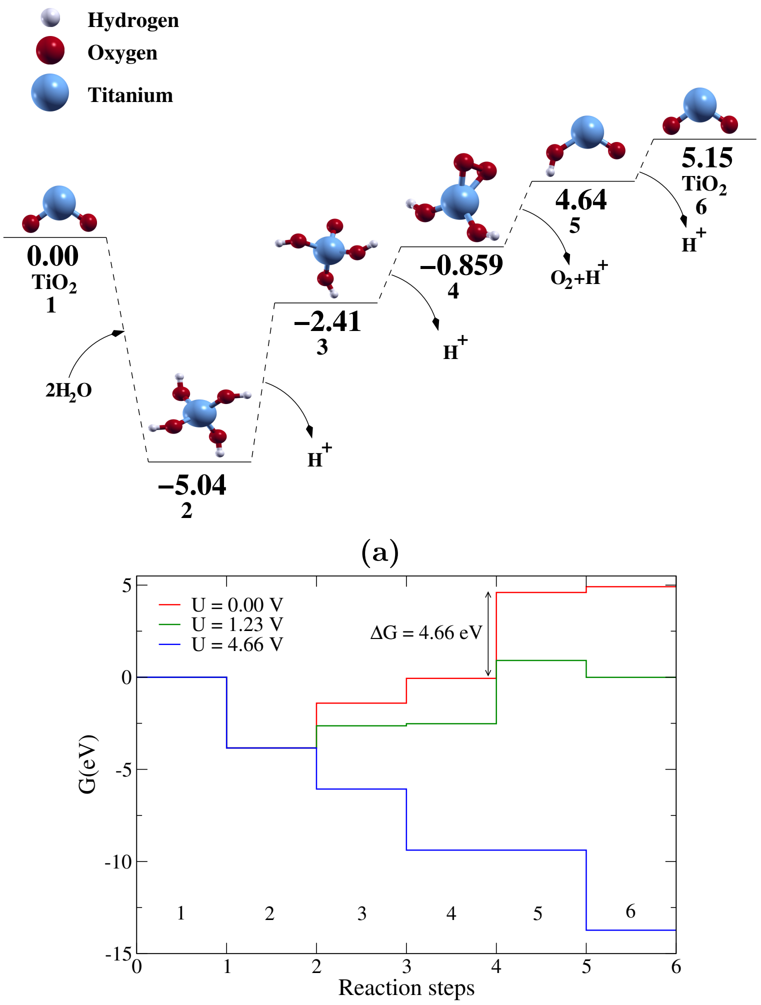

(a)

(b)

**Figure. 3.2.** ***a)*** *Water splitting on $TiO_2$: $TiO_2 + 2H_2O \rightarrow TiO_2 + 2H_2 + O_2$. The total energies are in eV.* ***b)*** *Free energy profile of the water splitting mechanism on $TiO_2$ at standard conditions under different external potentials. Zero external potential (red line), standard potential of the overall water splitting reaction: 1.23 V (green line), minimum external potential which makes the free energy of the process down-hill in the reaction steps: 4.66 V (blue line). The limiting step for this mechanism is highlighted. The corresponding overpotential is 3.43 V.*

anode of an electrochemical cell and the OER is studied using an electrochemical approach. Both structures certainly constitute oversimplified models of the surface of the anode in the cell; mainly because the electronic structure of these configurations is far from that of the $TiO_2$ surfaces. These simplified models for the anode of the electrochemical cells are compared with the model proposed in this work. Motivated by the foregoing results [38, 39], the first steps in the reaction mechanisms are taken to be the formation of $Ti(OH)_4$ and $Ti(OH)_2$-$O_2Ti(OH)_2$, respectively, which is induced by the decomposition of two water molecules on the corresponding initial structures (i.e., $TiO_2$ and $Ti_2O_4$). The mechanism advances via a cascade of electron-transfer processes in which electrons flow from the new structures (that is, from $Ti(OH)_4$ and $Ti(OH)_2$-$O_2$-$Ti(OH)_2$) to the cathode, while protons are injected into the electrolyte at the same rate.

The intermediate stable structures characterizing the process on $TiO_2$ and its energy values in eV are shown in Fig. 3.2a. The free energy profiles of this mechanism for different external potentials are depicted in Fig. 3.2b. The decomposition of two water molecules on a $TiO_2$ cluster produces the $Ti(OH)_4$ structure in an exothermic process (5.04 eV) [38, 39]. The proposed mechanism continues with the extraction of one $H^+$ from the structure while an $e^-$ is transferred to the cathode. The formation of an $O_2$ molecule is observed after the extraction of a second $H^+$. The next step is a type E reaction which consists of the desorption of the $O_2$ molecule together with a proton from the cluster. This is actually the rate-limiting step of the reaction, i.e., the one exhibiting the highest energy barrier (4.66 eV, see the curve labeled as U = 0.00 V in Fig. 3.2b). After that, the last proton is extracted from the cluster and the $TiO_2$ structure is recovered.

Taking into account the entropic and the zero-point energy contributions, the free energy of each of the structures displayed in Fig. 3.2a is evaluated. From the free energy profiles plotted in Fig. 3.2b, it can be seen that the complete process is not favorable from the thermodynamic point of view in absence of an external force to drive the reaction (or in the dark, if the case of the water splitting on a PEC is considered). The mechanism remains energetically forbidden even if a potential bias amounting to the electrochemical standard potential of the water splitting reaction (U = 1.23 V, Fig. 3.2b). As in every proposed reaction mechanism, a nonzero overpotential is necessary. For the $TiO_2$ cluster structure, an external potential of 4.66 V is required for the OER to become thermodynamically favorable, the corresponding theoretical overpotential is 3.43 V. This value of the overpotential is much larger than the results of previous calculations (1.31 V for the anatase (001) surface [69] and 0.78 V for the rutile (110) surface [67]) and the available experimental data (around 1 V [67, 69, 95, 165] for the water decomposition under standard thermodynamic conditions). These differences point to the dissimilarities in the electronic structures of the minimal $TiO_2$ cluster and the extended titanium dioxide substrate.

With the aim of studying the water decomposition on the $TiO_2$ surface, the simplest cluster model involving at least two titanium centers is $Ti_2O_4$. The stable structures tracing the oxygen evolution on $Ti_2O_4$ and their molecular energies in eV are shown in Fig. 3.3a. The free energy profiles corresponding to different external potentials are presented in Fig. 3.3b. The formation of $Ti(OH)_2$-$O_2$-$Ti(OH)_2$ takes place after the decomposition of two water molecules on $Ti_2O_4$, and the binding energy of the complex is 5.22 eV [38]. The extraction of a proton leads to the formation of an $O_2$ molecule in the cluster (Fig. 3.3a: structure-3). In the next step, the desorption of the $O_2$ molecule occurs together with the dissociation of a

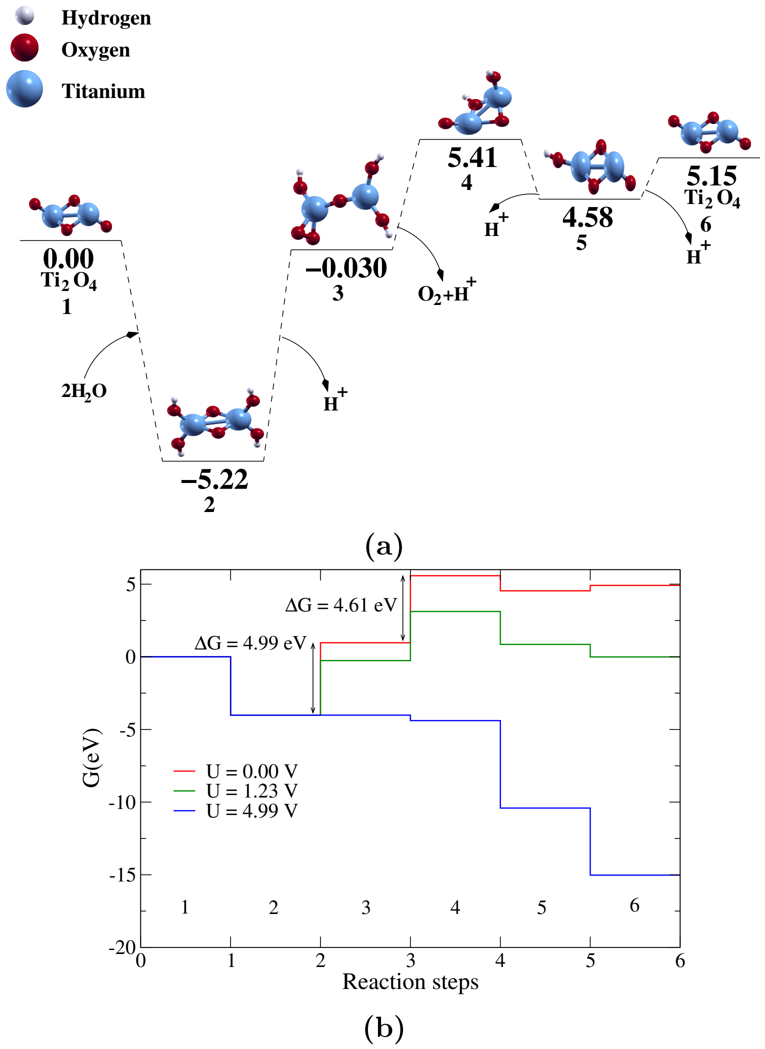

(a)

(b)

**Figure. 3.3.** ***a)*** *Water splitting on* $Ti_2O_4$*:* $Ti_2O_4 + 2H_2O \rightarrow Ti_2O_4 + 2H_2 + O_2$*. The molecular energies are in eV.* ***b)*** *Free energy profile of the water splitting mechanism on* $TiO_2$ *at standard conditions under different external potentials. Zero external potential (red line), standard potential of the overall water splitting reaction: 1.23 V (green line), minimum external potential which makes the free energy of the process down-hill in the reaction steps: 4.99 V (blue line). The limiting step for this mechanism is shown. The corresponding overpotential is 3.76 V.*

second proton giving rise to the fourth structure in Fig. 3.3a. The process goes on by means of the extraction of the two remaining protons, which completes the catalytic cycle.

The rate-limiting step is the formation of the $O_2$ molecule, which demands to overcome a free energy barrier of 4.99 eV (U = 0.00 V, Fig. 3.3b). Hence, an external potential of 4.99 V will supply the necessary energy to make the free energy landscape down-hill along the reaction path and the process thermodynamically allowed. The overpotential for the proposed mechanism is 3.76 V, which is even higher than the corresponding one for the water splitting on the $TiO_2$ cluster (3.43 V). The comparison between the two pathways (Fig. 3.2a and Fig. 3.3a) shows that the rate-limiting step is similar in both cases, and it relates to the $O_2$ desorption process. Indeed, according to the free energy profiles plotted in Fig. 3.2b and Fig. 3.3b, the activation energies for these processes are nearly the same: 4.66 eV and 4.61 eV, respectively. The difference in the performance depending on the cluster model comes from the more extensive structural modification, that takes place preceding the release of the oxygen molecule in the case of the $Ti_2O_4$ model. After the first $H^+$ is extracted (Fig. 3.3a: structure-3), striking changes of the molecular geometry occur with respect to the structure 2 (i.e., bond breaking and formation), leading to the emergence of an $O_2$ molecule. Because of this rearrangement of atomic positions, the present mechanism is thermodynamically less favorable than the previous one (i.e., it will require to overcome a somewhat higher energy barrier).

In the proposed mechanisms, based on $TiO_2$ and $Ti_2O_4$, the computed overpotentials exceed 3.4 V, while previous experimental and theoretical studies on extended surfaces report values around 1 V [67, 69, 95, 165]. In the next sections more reliable models for representing the titanium dioxide surface is presented.

### 3.3.2 Water splitting on neutral $Ti(OH)_4$

The top views of two different titanium dioxide surface morphologies commonly used as cathodes in electrochemical or PEC are shown in Fig. 3.1. The diagrams reproduce the geometric arrangement of atoms in the rutile (110), Fig. 3.1a, and the anatase (001), Fig. 3.1b, surfaces. The structures are obtained from a truncated rutile or anatase $TiO_2$ crystal. Although the Ti atoms in the bulk semiconductor are 6-fold coordinated, the 5-fold coordinated atoms located on the outer plane have been identified as the active sites for the surface chemical reactions. These 5-fold coordinated Ti atoms are highlighted in Figs. 3.1a and Fig. 3.1b. The active Ti-sites on both model surfaces have four O atoms as nearest neighbors (1.93 Å) and an additional O as second nearest neighbor (1.98 Å) [172]. This suggests that a simple cluster structure ($TiO_4$) might be used to represent the active sites on the semiconductor surfaces, by considering only a Ti atom linked to its nearest neighbors (i.e., the fourth closest O atoms). Following this idea, the present section is devoted to the study of $Ti(OH)_4$ as a cluster model for the description of the water splitting process. Actually, this structure goes one step further, since four H atoms have been considered in addition to the $TiO_4$ complex. This modification saturates the $TiO_4$ structure, and in such a way the cluster model approaches the bonding situation of the surface.

The electronic structure of $Ti(OH)_4$ has been studied before as a model representation of specific sites in $TiO_2$ surfaces [173]. Moreover, the $Ti(OH)_4$ is obtained as a product from an exothermic (5.04 eV) process after the decomposition of two water molecules on $TiO_2$ (Fig. 3.2a: structure-2) [38, 39]. These facts point to the

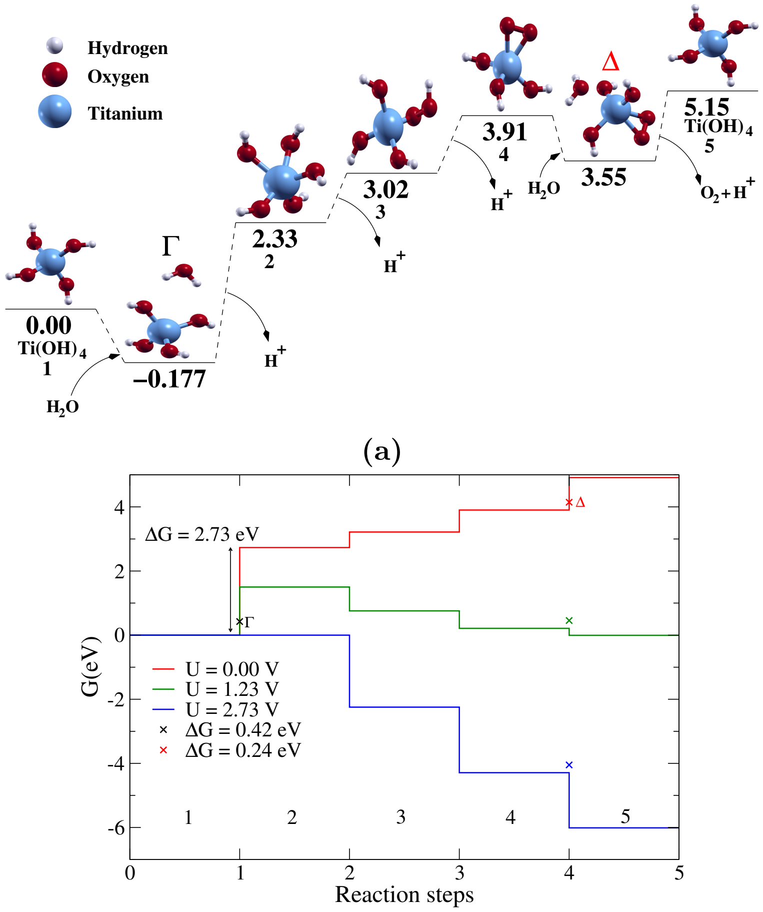

(a)

(b)

**Figure. 3.4.** ***a)*** *Water splitting on $Ti(OH)_4$: $Ti(OH)_4 + 2H_2O \rightarrow Ti(OH)_4 + 2H_2 + O_2$. The molecular energies are in eV. The $\Gamma$ and $\Delta$ structures highlight the configurations which increase the free energy independently of the external potential.* ***b)*** *Free energy profile of the water splitting mechanism on the neutral $Ti(OH)_4$ at standard conditions under different external potentials. Zero external potential (red line), standard potential of the overall water splitting reaction: 1.23 V (green line), minimum external potential which makes the free energy of the process down-hill in the reaction steps: 2.73 V (blue line). The $\Gamma$ and $\Delta$ marks represent the reaction steps with increasing free energies which can not be reduced by the external potential. The limiting step for this mechanism is shown. The corresponding overpotential is 1.5 V.*

decomposition of two additional water molecules on $Ti(OH)_4$ rather than on $TiO_2$ as a more favorable mechanism from the thermodynamic point of view. For the study of the water splitting on $Ti(OH)_4$, a reaction mechanism in which two water molecules are adsorbed on the cluster and four $H^+$ are removed in separate electron-transfer steps has been proposed. One $O_2$ molecule and four $H^+$ injected into the electrolyte are obtained as products of the reaction mechanism.

The stable structures arising from the different phases in the proposed mechanism for the water splitting on $Ti(OH)_4$, together with the corresponding energy values in eV, are presented in Fig. 3.4a. The free energy profiles along this path, for different external potentials, are plotted in Fig. 3.4b. The adsorption of one water molecule on $Ti(OH)_4$ leads to the formation of the structure labeled as $\Gamma$, and it causes the decrease of the molecular energy of the system (Fig. 3.4a: structure-$\Gamma$). According to the free energy variation, the structure-$\Gamma$ is disadvantageous, Fig. 3.4b. Since this is a reaction of type A: eq. (3.3), there is no electron-transfer happening, so the free energy change accompanying the water adsorption will be the same for all the external potentials. In order to be able to steer the reaction with the voltage applied to the electrochemical cell, an alternative mechanism needs to be considered. Here, we examine the direct transition from structure-1 to structure-2, Fig. 3.4a. The latter is a reaction of type B (i.e., a water molecule is decomposed into an $OH^-$ and a $H^+$, and the $OH^-$ is adsorbed on the cluster, cf. eq. (3.4)).

Using the same argument, the adsorption of a second water molecule (designated as structure-$\Delta$ in both Fig. 3.4a and Fig. 3.4b) is not included in the proposed mechanism, and a direct transition from structure-4 to structure-5 is favored, Fig. 3.4a. This transition corresponds to the simultaneous occurrence of two of the above mentioned typical reactions. It can be regarded as the decomposition of a water molecule in a reaction of type B: eq. (3.4), together with a reaction type E in which the $O_2$ molecule is desorbed, eq. (3.7). Since both reactions occur at the same time, only one electron is transferred to the electrode during this phase. With these assumptions, the mechanism of the water decomposition on $Ti(OH)_4$ becomes a four-step process, each of them involving an electron transfer to the electrode. Using the previously introduced classification, the process consists in one reaction type B, two reactions of type D and a combined step which merges one reaction of type B and one of type E.

Consequently, after the decomposition of a water molecule and the formation of the $Ti(OH)_5$ complex (Fig. 3.4a: structure-2), one $H^+$ is extracted from the structure. At this point, the formation of an $OOH^-$ group takes place and the $O_2$ molecule is already preformed, as it can be seen (Fig. 3.4a: structure-3). The $O_2$ molecule is released in the following consecutive steps: the extraction of the next $H^+$ in the corresponding reaction of type D: eq. (3.6), in which a $H^+$ is injected to the electrolyte while an electron is transferred to the electrode, and the combined process which leads to the direct transition from structure-4 to structure-5 in Fig. 3.4a.

The rate-determining step of the process is the decomposition of the first water molecule and the adsorption of the $OH^-$ group on the cluster, the largest energy barrier being of 2.73 eV (see the curve corresponding to $U = 0.00$ V in Fig. 3.4b). If an external potential of 2.73 V is exerted on the electrochemical cell, then it provides the charge carriers in the system (the free electrons and protons) the necessary energy to overcome the highest energy barrier), making the free energy profile down-hill along the reaction steps (curve marked as U = 2.73 V in Fig. 3.4b).

The corresponding value of the overpotential is 1.50 V. It is striking, that considering $Ti(OH)_4$ as a cluster model of the surface results in a substantial reduction of the theoretically predicted value of the overpotential, compared to those obtained for $TiO_2$ (3.43 V) and $Ti_2O_4$ (3.76 V). The comparison between the value of the overpotential corresponding to the reaction mechanism depicted in Fig. 3.4a and previously reported results (namely, experimental values in the range 0.9 - 1.1 V for $TiO_2$ rutile single crystal electrodes [95], and theoretically computed overpotentials of 0.78 V and 1.31 V for the $TiO_2$ rutile (110) surface and for the $TiO_2$ anatase (001) surface, respectively), indicates that the $Ti(OH)_4$ cluster gives a more realistic representation of the surface of the anode than the $TiO_2$ and $Ti_2O_4$ structures, at least for the simulation of the water splitting on $TiO_2$ substrates. In the following, we study the water splitting process on a charged local site on the anode, employing the $Ti(OH)_4$ cluster to approximate the interaction sites on the surface.

### 3.3.3 Water splitting on $Ti(OH)_4^-$

The influence of an extra electron on the water splitting on the $Ti(OH)_4$ structure is considered in this section. The charged structure simulates the influence, on the decomposition process, of an electron "trapped" in a local site at the surface. The $Ti(OH)_4^-$ is used as a simplistic model for such trapping sites on the surface of the anode. The structures of stable molecular configurations along the water splitting reaction path and their energy values in eV are shown in Fig. 3.5a. The free energy profiles for the proposed mechanism, in presence of different external potentials are given in Fig. 3.5b.

The mechanism initiates with the adsorption of a water molecule on $Ti(OH)_4^-$ (Fig. 3.5a: structure-2). It continues with the formation of a $Ti(OH)_5^-$ structure due to the extraction of a $H^+$ (Fig. 3.5a: structure-3). Extracting two additional protons in subsequent steps, leads to the formation of the intermediate structures $Ti(OH)_4O^-$ and $Ti(OH)_3O_2^-$ (Fig. 3.5a: structure-4 and -5). In the latter of these molecular configurations, an oxygen molecule is already preformed. Opposite to the reaction on neutral $Ti(OH)_4$, the adsorption of the first water molecule is favorable regarding the molecular energy and the free energy variations. The adsorption of a second water molecule is also accompanied by a downward shift of both the DFT energy and the free energy (Fig. 3.5a: structure-6). The last step is a reaction of type E: eq. (3.7), involving the desorption of an $O_2$ molecule together with a $H^+$ ion (Fig. 3.5a: structure-7). In fact, this step is again the one determining the overall reaction rate: its activation energy is 3.49 eV (for a vanishing external electric field). As a consequence, applying an external bias of 3.49 V to the electrochemical cell causes the free energy to decrease monotonically along the reaction path and the

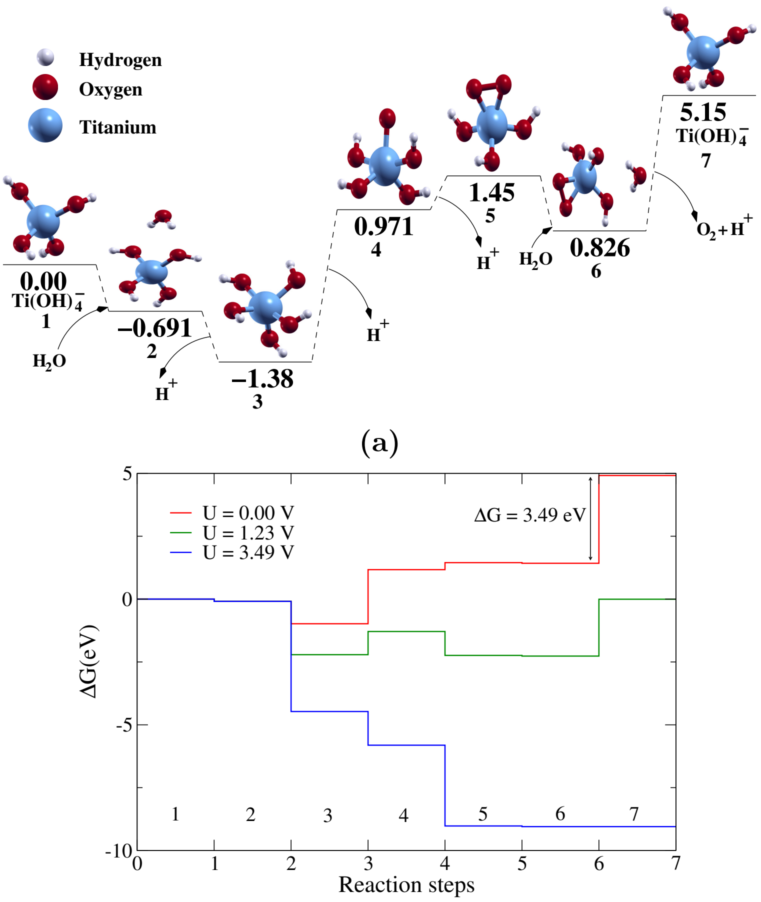

(a)

(b)

**Figure. 3.5.** ***a)*** *Water splitting on* $Ti(OH)_4^-$*:* $Ti(OH)_4^- + 2H_2O \rightarrow Ti(OH)_4^- + 2H_2 + O_2$*. The molecular energies are in eV.* ***b)*** *Free energy profile of the water splitting mechanism on the electronically activated* $Ti(OH)_4^-$ *at standard conditions under different external potentials. Zero external potential (red line), standard potential of the overall water splitting reaction: 1.23 V (green line), minimum external potential which makes the free energy of the process down-hill in the reaction steps: 3.49 V (blue line). The limiting step for this mechanism is shown. The corresponding overpotential is 2.26 V.*

decomposition can take place (U = 3.49 V, Fig. 3.5b). The overpotential is 2.26 V for the proposed reaction mechanism. This value is larger than the overpotential for the corresponding neutral cluster (1.50 V), but it is still smaller than those obtained for the $TiO_2$ and the $Ti_2O_4$ models. These results indicate that the electron trapped states do not increase the efficiency of the water decomposition process.

Alternatively, the investigation of the electrolysis on the $Ti(OH)_4^-$ cluster also gives some insight into the photocatalytic water splitting on dye-sensitized $TiO_2$ surfaces. Due to the electron-injection process from the dye into the titanium dioxide, charged sites may appear on the surface. The dye-sensitization of the surface of the anode often leads to the improvement of the efficiency of the PEC [174–176]. Therefore, the larger overpotential obtained for the $Ti(OH)_4^-$ cluster compared to the neutral $Ti(OH)_4$ model (i.e., in presence of localized charges) suggests that:

(a) there is a marked influence, on the performance of the PEC, of the delocalized character of the excess electron density in sensitized $TiO_2$ surfaces (the electron is injected in the conduction band of the semiconductor),

(b) in the case of dye-sensitized PEC, the water splitting process might occur directly on the sensitizer rather than on the surface of the anode. In this case, the $TiO_2$ surface only influences the electron transport properties of the electrochemical cell.

### 3.3.4 Water splitting on $Ti(OH)_2$-$O_2$-$Ti(OH)_2$

The $Ti(OH)_4$ cluster model was introduced above as a local representation of the active sites on the $TiO_2$ surfaces for the water splitting reaction in an electrochemical cell. Although it resembles the bonding of Ti-active sites to its nearest oxygen neighbors, considering several adjacent water adsorption sites is a natural way to progressively cover the gap between the minimal cluster representation and the extended surface. To this purpose, in the present section, we address the modeling of the water splitting process on the cluster $Ti(OH)_2$-$O_2$-$Ti(OH)_2$. This structure can be seen as a direct extension of the $Ti(OH)_4$ model, including two Ti-active sites on the rutile (110) surface (the latter are indicated by the white and the light blue areas in Fig. 3.1a, which are delimited by the dashed lines). In analogy with the treatment described in Sec. 3.3.2, the influence of the second neighboring oxygen atom (standing at 1.98 Å from the 5-fold coordinated titanium on each site) on the water splitting is neglected, while one H atom is attached to each of the four external oxygen atoms (i.e., those not connected to the two Ti centers) to emulate the electronic structure of the surface within this simplistic cluster representation. Moreover, the $Ti(OH)_2$-$O_2$-$Ti(OH)_2$ structure may be obtained as a result of a highly exothermic process (5.22 eV), namely the decomposition of two water molecules on $Ti_2O_4$ (Fig. 3.3a, structure-2) [39]. Due to this large formation energy, it is expected that the decomposition of two water molecules on $Ti(OH)_2$-$O_2$-$Ti(OH)_2$ will be a much more energetically favorable process than the desorption of an $O_2$ molecule and the extraction of four protons from $Ti(OH)_2$-$O_2$-$Ti(OH)_2$, as proposed in Fig. 3.3a.

The intermediate molecular structures representing the main steps of the $H_2O$ splitting on $Ti(OH)_2$-$O_2$-$Ti(OH)_2$ and their total energies in eV are shown in Fig. 3.6a. The corresponding free energy profiles, computed for different external potentials, are depicted in Fig. 3.6b. The proposed mechanism begins with the exothermic adsorption of a water molecule and its subsequent decomposition into an $OH^-$ group on the titanium site and the injection of a $H^+$ ion into the electrolyte. A second $H^+$ is extracted, and the recombination of two oxygen atoms

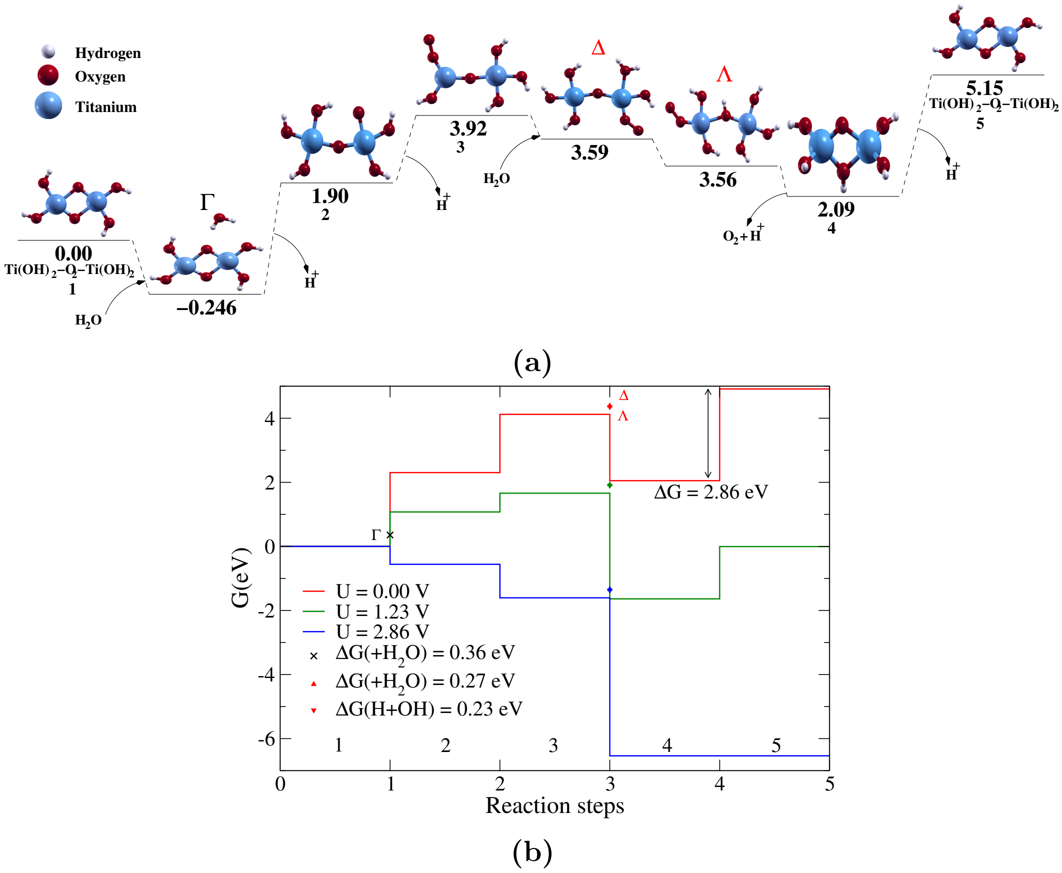

**Figure. 3.6.** ***a)*** *Water splitting on $Ti(OH)_2$-$O_2$-$Ti(OH)_2$: $Ti(OH)_2$-$O_2$-$Ti(OH)_2$ $+2H_2O \rightarrow Ti(OH)_2$-$O_2$-$Ti(OH)_2 + 2H_2 + O_2$. The total energies are in eV. The $\Gamma$, $\Delta$ and $\Lambda$ structures highlight the configurations which increase the free energy independently of the external potential.* ***b)*** *Free energy profile of the water splitting mechanism on $Ti(OH)_2$-$O_2$-$Ti(OH)_2$ at standard conditions under different external potentials. Zero external potential (red line), standard potential of the overall water splitting reaction: 1.23 V (green line), minimum external potential which makes the free energy of the process down-hill in the reaction steps: 2.86 V (blue line). The $\Gamma$, $\Delta$ and $\Lambda$ marks represent the reaction steps with increasing free energies which can not be reduced by the external potential. The limiting step for this mechanism is shown. The corresponding overpotential is 1.63 V.*

takes place. Because of the high energetic cost associated to the extraction of the preformed $O_2$ molecule, the adsorption of the second water molecule is considered as the next step. The $H_2O$ is decomposed in one $OH^-$ linked to one of the Ti-sites and one $H^+$ which is bonded to the oxygen lying between the titanium atoms. The next proposed step is an electron-transfer process, and it involves the desorption of the $O_2$ molecule together with the extraction of a proton. Finally the last proton is extracted and the catalytic cycle is completed. The structures: $\Gamma$, $\Delta$ and $\Lambda$ in Fig. 3.6a represent alternative reaction paths which do not entail electron-transfer processes (e.g., water adsorption) and they are found to be unfavorable according to the free energy variations (U = 0.00 V, Fig. 3.6b). Thus, the reaction is assumed to occur via the direct transition from structure-1 to structure-2 in Fig. 3.6a. This is a reaction of type B: eq. (3.4), whereas the transition from structure-3 to structure-4 is a combined process comprising one reaction of type B and one of type E: eqs. (3.4) and (3.7). In this case, the reaction rate is determined by the extraction of the last $H^+$ and a barrier of 2.86 eV in the free energy profile is associated with this step.

The theoretical estimate of the overpotential is 1.63 V. This value is considerably smaller than the corresponding one obtained in the Sec. 3.3.1 for the $Ti_2O_4$ dimeric structure (3.76 V) following the model suggested in [38]. As it was mentioned above, the formation of $Ti(OH)_2$-$O_2$-$Ti(OH)_2$ after the decomposition of two water molecules on $Ti_2O_4$ is an exothermic process (5.22 eV). In the $Ti_2O_4$ model of the surface, the assumption of a cyclic mechanism requires the reorganization of the $Ti(OH)_2$-$O_2$-$Ti(OH)_2$ until the initial structure is recovered. On the other hand, for the present cluster, the exothermic processes in the reaction mechanism are characterized by smaller energy variations (less than 2 eV) and rearranging the $Ti(OH)_2$-$O_2$-$Ti(OH)_2$ structure, after the decomposition of the first and second water molecules, requires overcoming lower energy barriers. Furthermore, in the present mechanism, the overpotential is quite similar to the value calculated for the monomer (1.50 V).

### 3.3.5 Water splitting on $Ti(OH)_3$-O-$Ti(OH)_3$

The structure $Ti(OH)_3$-O-$Ti(OH)_3$ is a different dimer model (i.e., it has two titanium centers) of the surface of the $TiO_2$ anode. It constitutes also a natural extension of the $Ti(OH)_4$ cluster to enclose two Ti centers: it results from the bridging of two $Ti(OH)_4$ clusters mimicking the topology of the anatase (001) surface. The analogy is based on the same assumptions as before: only the Ti centers and their first neighboring oxygen atoms are taken into account, while H atoms are attached to the external oxygens. The white and light blue areas (limited by the dashed rectangles) in Fig. 3.1b highlight the surface cut modeled in this way. Contrary to the previous system, in the present case there is only one oxygen-bridge in the structure. Moreover, the electronic structure of two spatial isomers of the present system has been studied previously [173], to represent the bonding situation of different local sites in the $TiO_2$ surface.

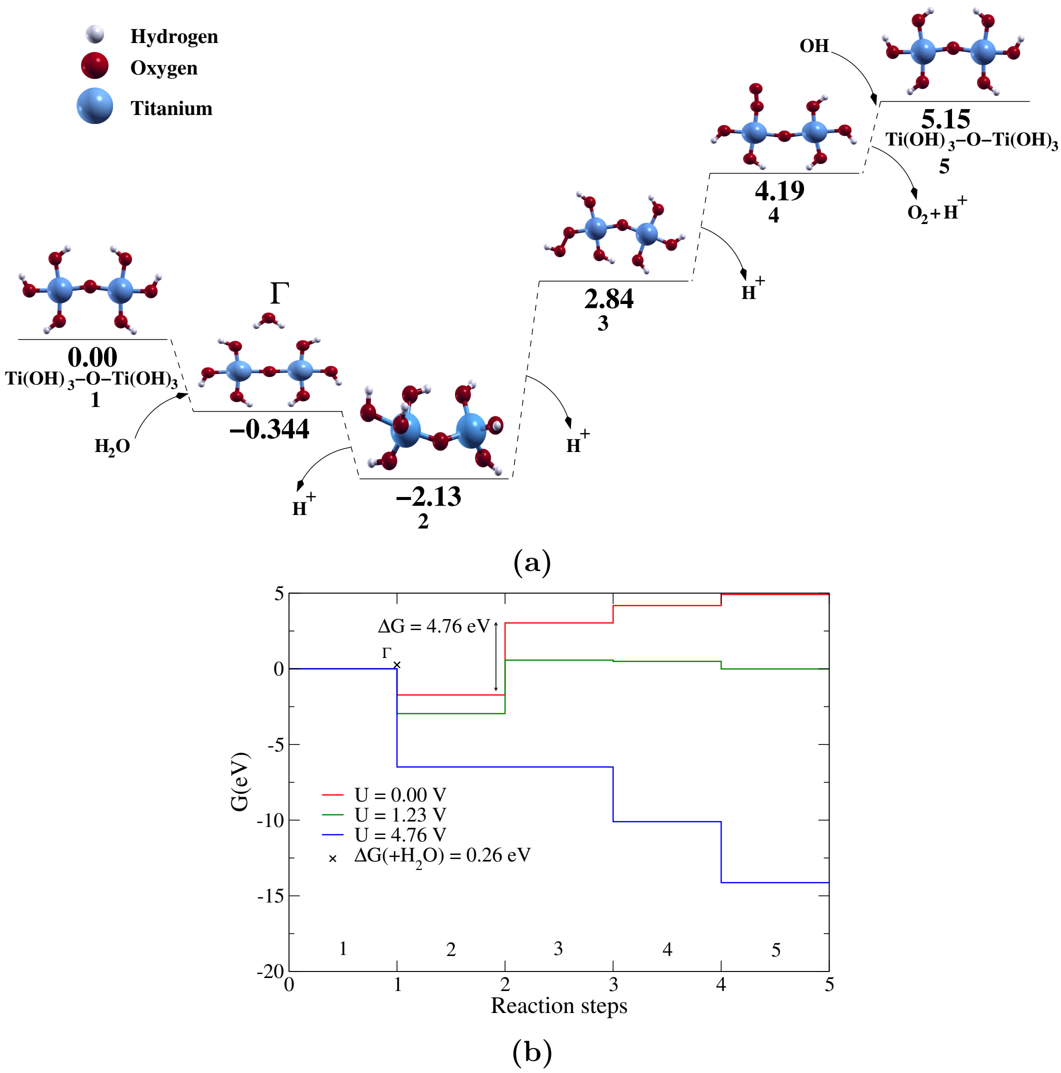

**Figure. 3.7.** ***a)*** *Water splitting on* $Ti(OH)_3$*-O-*$Ti(OH)_3$*:* $Ti(OH)_3$*-O-*$Ti(OH)_3 + 2H_2O \rightarrow Ti(OH)_3$*-O-*$Ti(OH)_3 + 2H_2 + O_2$*. The molecular energies are in eV. The structure-Γ highlight the configuration which increases the free energy independently of the external potential.* ***b)*** *Free energy profile of the water splitting mechanism on* $Ti(OH)_3$*-O-*$Ti(OH)_3$ *at standard conditions under different external potentials. Zero external potential (red line), standard potential of the overall water splitting reaction: 1.23 V (green line), minimum external potential which makes the free energy of the process down-hill in the reaction steps: 4.76 V (blue line). The structure-Γ represents the reaction step with increasing free energy which can not be reduced by the external potential. The limiting step for this mechanism is shown. The corresponding overpotential is 3.53 V.*

The stable molecular configurations, indicative of the reaction mechanism on the present cluster model are displayed in Fig. 3.7a, together with the corresponding energy values in eV. The free energy profiles resulting from adding entropic and vibrational energy contributions, for different external potentials, are depicted in Fig. 3.7b.

The adsorption of the first water molecule is an exothermic reaction (0.34 eV)

(Fig. 3.7a: structure-Γ), while a parallel increase of the free energy in the process is observed. A reaction of type B: eq. (3.4) is proposed as the following step, during which the system evolves from structure-1 to structure-2 in Fig. 3.7a. In the next two steps, an $OOH^-$ group is formed and the corresponding $H^+$ gets extracted, yielding an $O_2$ molecule adsorbed on the cluster. The proposed pathway continues with a combined process similar to the one discussed in the previous section: one reaction of type B and one of type E (eqs. (3.4) and (3.7)) take place at the same time, and the $O_2$ molecule is desorbed from the cluster together with a proton. For this path, the most energy-consuming step is the formation of the $OOH^-$ group and a barrier of 4.76 eV has to be overcome for the reaction to proceed this way (see the curve for the external voltage U = 4.76 V in Fig. 3.7b). The value of the overpotential (3.53 V) is qualitatively different than the one obtained for the neutral $Ti(OH)_4$, and it is similar to the results obtained for the $TiO_2$ and the $Ti_2O_4$ models.

The deviations in the reaction mechanisms on $Ti(OH)_3$-O-$Ti(OH)_3$ and on $Ti(OH)_2$-$O_2$-$Ti(OH)_2$ represent, within the framework of the small cluster model, the differences between the water splitting process on the $TiO_2$ anatase (001) and rutile (110) surfaces. Albeit the model calculations presented here are not able to reproduce quantitatively the overpotentials observed experimentally [95], nor the results of previous theoretical studies on extended surfaces [67, 69], the proposed reaction mechanisms are able to account for the observed trends of the overpotentials for the two representative crystallographic structures of titanium dioxide. In effect, previous calculations on extended substrates reported a smaller overpotential (0.78 V) for the water splitting on an exposed rutile (110) [67] plane, compared to the anatase (001) surface (1.31 V). The same qualitative behavior is observed here for the dimeric models of the rutile ($Ti(OH)_2$-$O_2$-$Ti(OH)_2$, 1.63 V) and the anatase ($Ti(OH)_3$-O-$Ti(OH)_3$, 3.53 V) surfaces.

### 3.3.6 Entropic contribution and normal modes analysis

As it was mentioned in the methodology, the reaction pathways to represent the mechanisms of the water splitting in small cluster models were dressed with entropic contributions in order to describe the evolution of the free energy along the reaction steps coordinate. The entropic influence to the free energy change, at standard thermodynamic conditions, is modeled by the contribution of the adsorption or desorption of the fragments ($H^+$, $H_2O$, and $O_2$) on the cluster structure. These entropic contributions have been computed in the gas phase approximation and only the translational and rotational degrees of freedom are relevant. The energetic influence of the entropic change in the desorption of a $H_2$ molecule is 0.36 eV and 0.04 eV due to the translational and rotational degrees of freedom respectively. In the case of $H_2O$ it is obtained 0.45 eV and 0.15 eV. In the $O_2$ gas the experimental value reported in the standard tables [16] for the total contribution is 0.63 eV. The translational degrees of freedom are considered to be activated at every value of T greater than 0 K. The characteristic temperatures for the activation of the different degrees of freedom in the gas-phase -obtained from *ab-initio* calculations and experimental data [177] in the case of the $O_2$ molecule- state that, at standard temperature only the translational and rotational degrees of freedom are activated: $T_{rot}(H_2) = 87.69$ K, $T_{vib}(H_2) = 6325$ K; $T_{rot}(H_2O) = 41.16$ K, $T_{vib}(H_2O) = 2408$ K and $T_{rot}(O_2) = 2.070$ K, $T_{vib}(O_2) = 2230$ K.

**Table. 3.1.** *Variation of the overpotential in every reaction mechanism when the entropic contribution of the adsorbed and desorbed fragments are included. The overpotentials without the entropic influence (i.e., 0 K overpotentials) are in all the cases the highest energy barrier in the corresponding molecular energy profiles.*

| **Cluster** | **ΔU (V)** |
|---|---|
| $TiO_2$ | -0.83 |
| $Ti_2O_4$ | -0.46 |
| $Ti(OH)_4$ | 0.22 |
| $Ti(OH)_4^-$ | -0.83 |
| $Ti(OH)_2$-$O_2$-$Ti(OH)_2$ | -0.20 |
| $Ti(OH)_3$-O-$Ti(OH)_3$ | -0.20 |

The Table 3.1 shows the change in the overpotential of every reaction mechanism when the entropy contribution to the free energy profile is considered. The overpotential without this contribution (i.e., the 0 K overpotential) is just the voltage corresponding to the highest energy barrier in the molecular energy profile of the reaction path. The overpotential decreases in general when the entropic effect is included. From this turns out that the increasing of the temperature favors the process. The overpotential of the reaction initiated on the $Ti(OH)_4$ cluster increases at standard conditions. At 0 K the adsorption of the first water molecule in the mechanism (Fig. 3.4a: structure-Γ) becomes relevant. In the new limiting step (i.e., from structure-Γ to structure-2 in Fig. 3.4a) the energy barrier is higher than the one from structure-1 to structure-2 in Fig. 3.4a, but the entropic change in the reaction mechanism at standard conditions is negative and the collective effect results in the enhancement of the overpotential. The overpotentials in the reactions initiated on $TiO_2$ and $Ti(OH)_4^-$ have the same response to the entropic effect and a similar behavior is found in the systems $Ti(OH)_2$-$O_2$-$Ti(OH)_2$ and $Ti(OH)_3$-O-$Ti(OH)_3$. The reason for such behavior is that, in each pair of systems the limiting step corresponds to the same process: $O_2$+$H^+$ and $H^+$ desorption, respectively, and the entropic contribution in each of them is exactly the same (e.g., the $H^+$ contribution is the half of the $H_2$ which is 0.20 eV if the data computed above for the $H_2$ is considered: 0.36 eV + 0.04 eV). In the case of $Ti_2O_4$ the corresponding response does not resemble any of the other values due to the change of the limiting step, in the reaction mechanism, when the entropic contribution is considered.

The vibrational density of states (VDOS, Appendix A.3) of every structure in the reaction path of the water splitting on $Ti(OH)_4$ is shown in Fig. 3.8. Each VDOS has been computed with the eigenfrequencies from the *ab-initio* calculations weighted by normal distributions of fixed variances, Sec. 3.2.2. The whole frequency domain is divided in three sub-intervals: the low frequency region (LFR) from 0 to 1000 $cm^{-1}$, the middle frequency region (MFR) from 1000 to 3500 $cm^{-1}$ and the high frequency region (HFR) from 3500 to 4500 $cm^{-1}$. The VDOS of $Ti(OH)_4$ is shown in Fig. 3.8a, it presents a peaks structure in the LFR, no relevant modes in the MFR and one additional peak in the HFR. The structure of the VDOS in the LFR are characterized by collective motion in the cluster structure. This region of the vibrational spectrum coincides approximately with the VDOS of both anatase and rutile $TiO_2$ which extend from 0 $cm^{-1}$ to almost 900 $cm^{-1}$ [178]. The structure of the spectrum in the HFR is composed by more localized oscillations. In the present case, the peak in the HFR is composed by four (almost degenerated) individuals H-stretching modes. The adsorption of the first water molecule introduces more normal modes and most of them increases the population of the LFR, Fig. 3.8b. The three normal modes of the water molecule in the gas phase also appear in the VDOS structure: the bending mode $\nu_B$ (1735 $cm^{-1}$), the symmetric stretching $\nu_{SS}$ (3713 $cm^{-1}$) and the asymmetric stretching (3789 $cm^{-1}$) which is overlapped with the O-H stretchings of the structure. The Fig. 3.8c shows the structure of the VDOS for $Ti(OH)_5$. In addition to the collective modes (LFR) and the H-stretchings (HFR) a small shoulder in the HFR-peak appear, this shoulder represents a weaker H-stretching in the structure -the corresponding OH distance is 0.974 Å while the others are between 0.961 and 0.967 Å-. The panel Fig. 3.8d corresponds to the $Ti(OH)_3OOH$ structure. In this VDOS three new peaks appear: the O-OH (894 $cm^{-1}$) which represents the O-O stretching motion, the folded OO-H (1337 $cm^{-1}$) related with the H-bending motion in the OOH group and the aligned OO-H (3667 $cm^{-1}$) corresponding with the H-stretching mode in the OOH group.

These values are in good agreement with previous results [179] for similar modes in the $H_2O_2$ molecule: 890 $cm^{-1}$ for the O-O stretching, 1295 $cm^{-1}$ for the symmetric H-bending and 3610 $cm^{-1}$ for the H-stretching. The VDOS of $Ti(OH)_3O_2$ is shown in Fig. 3.8e. The structure of the VDOS shows that the normal modes related with the H atom in the OOH group are removed (i.e., folded and aligned OO-H in Fig. 3.8d. The vibration of the preformed $O_2$ molecule shifts from O-OH in Fig. 3.8d to O-O in Fig. 3.8e (1197 $cm^{-1}$). Conversely to the former peak (O-OH in Fig. 3.8d in the second one (O-O in Fig. 3.8e) the normal mode is a combined torsional and stretching motion of the $O_2$ molecule attached on the Ti atom. The movement of the vibration has been visualized employing the Visual Molecular Dynamics (VMD) package [180].

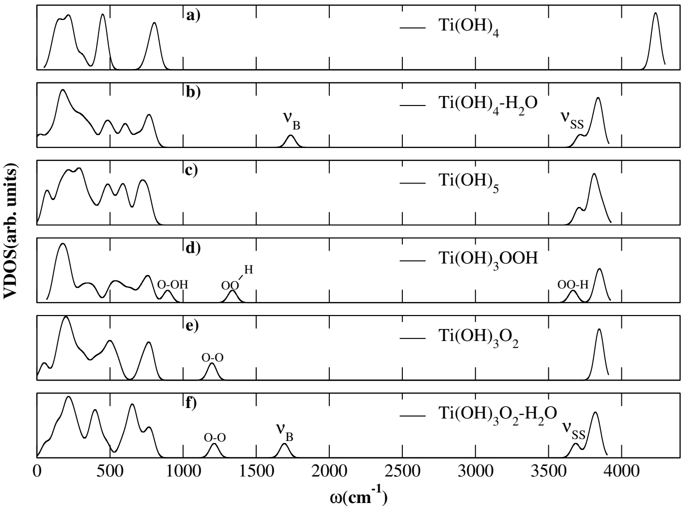

**Figure. 3.8.** *Vibrational density of states (VDOS) in arbitrary units of every structure employed in the water decomposition on Ti(OH)*$_4$*. The bending and the symmetric stretching modes of the water molecules are identified as* $\nu_B$ *(1735 cm*$^{-1}$*) and* $\nu_{SS}$ *(3713 cm*$^{-1}$*) respectively. In the panel d) three modes corresponds to the OOH group: The O-O stretching, denoted by O-OH (894 cm*$^{-1}$*); the H bending, denoted by the folded OO-H (1337 cm*$^{-1}$*) and the O-H stretching, denoted by the aligned OO-H (3667 cm*$^{-1}$*). The peaks highlighted by O-O corresponds to normal modes associated with the movement of the preformed* $O_2$ *molecule, in panel e) it represents a combined stretching and torsional mode (1197 cm*$^{-1}$*) while in panel f) it corresponds to a vibrational mode of the* $O_2$ *structure (1212 cm*$^{-1}$*).*

In the partial vibrational density of states (PVDOS) for every atom of the structure $Ti(OH)_3O_2$, Fig. 3.9, it is shown that the O-O peak in Fig. 3.8e is composed by the contribution of the oxygen atoms from the preformed $O_2$ molecule. The VDOS for the adsorption of the second water molecule is shown in Fig. 3.8 f). In this case the peaks which correspond to the water molecule ($\nu_B$ and $\nu_{SS}$) appear and an O-O mode (1212 cm$^{-1}$), similar to the O-O peak in Fig. 3.8e is also present. Despite the similarities between these two frequencies (i.e., 1197 cm$^{-1}$ and 1212 cm$^{-1}$) the second O-O mode appears in the VMD package as a stretching motion of the $O_2$ molecule while the first one is a combined motion. The change of this mode after the water adsorption makes this reaction step a better assumption for the continuation of the process than other possibilities (e.g., the $O_2$ desorption from the $Ti(OH)_3O_2$ structure).

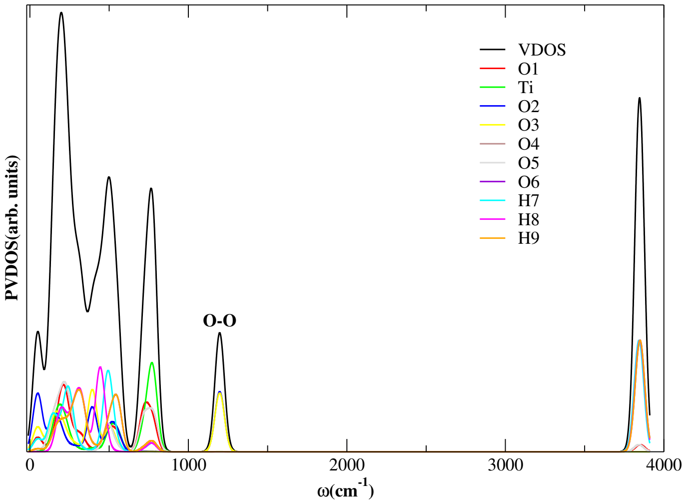

**Figure. 3.9.** *VDOS of the structure* $Ti(OH)_3O_2$ *as it is in the panel e) of the Fig. 3.8e (black line). The PVDOS for all the atoms of the structure are shown in different colors.*

## 3.4 Conclusions

In this chapter, different mechanisms of the water splitting reaction on small cluster representations of $TiO_2$ surfaces were investigated, and the relative advantages of several cluster models to simulate the main features of the process on the actual substrates were addressed. The energetics of the water decomposition pathways, was described within the framework of the Density Functional Theory. The use of this level of theory allows the comparison of the results obtained in this work with previous studies of the same process on extended surfaces. The different molecular systems we considered to mimic the surface of the anode of a $TiO_2$-based electrochemical cell enabled the study of the properties of the cluster approximations and the influence of various structural features on the water splitting reaction (e.g., charged structure or different surface topologies).

The electronic structure calculations provide a detailed picture of the water splitting process via the optimized geometries for every intermediate step, and the energy required for the system to move along the reaction path. Based on the DFT energies, the rate-determining step for every reaction mechanism is identified. In each case, applying the external potential needed to overcome the largest energy barrier tends to flatten the free energy profile in the vicinity of the most energy-consuming step. The overpotential corresponding to each reaction mechanism was estimated employing a previously developed thermochemical methodology, which explicitly takes into account the applied external potential in the free energy calculations [40]. Since the free energy landscape and the computed overpotentials depend on the chosen reaction path, other plausible pathways have been explored. Alternative mechanisms considered in previous studies (e.g., the binding of an additional $H_2O$ molecule to specific molecular structures) were found to require a larger potential bias to steer the reaction.

In most of the proposed mechanisms the inclusion of the entropic contribution to the free energy favors the reaction (i.e., it decreases the overpotential). It is found that the vibrational degrees of freedom in the gas phase of $H^+$, $H_2O$, and $O_2$ at standard conditions, do not contribute to the entropy change of different intermediate structures. Taking the reaction mechanism of the water splitting on $Ti(OH)_4$ as an example, it is shown that the VDOS of the intermediate structures reproduce the main features of the process. The information contained in the normal modes analysis also shows that the adsorption of the second water molecule before the $O_2$ desorption is a better assumption than the same steps in a reverse order.

The mechanism proposed for the water electrolysis on the $\mathrm{Ti(OH)_4}$ cluster, significantly improves the agreement between the computed overpotential and the experimental and theoretical values reported for extended surfaces, with respect to similar reaction mechanisms taking place on $TiO_2$ and $Ti_2O_4$ clusters. Therefore, the $\mathrm{Ti(OH)_4}$ structure provides a more realistic representation of the surface of the anode, compared to the molecular structures suggested in previous works [38, 39]. On the other hand, the calculations performed for the $\mathrm{Ti(OH)_4^-}$ model show that the addition of localized charges does not favor the water decomposition.

The cluster models can be considered as elementary building blocks which approximate the surface. They can be made progressively larger, eventually approaching the bulk phase. In this direction, we considered also dimeric structures to represent different topologies of the semiconducting surface: $\mathrm{Ti(OH)_2}$-$O_2$-$\mathrm{Ti(OH)_2}$, for rutile (110), and $\mathrm{Ti(OH)_3}$-O-$\mathrm{Ti(OH)_3}$, for anatase (001). For the first of these models, we obtained a similar value of the overpotential than for the $\mathrm{Ti(OH)_4}$ cluster, while it differs significantly from the overpotential for the oxygen-linked $Ti(OH)_3$ dimer. The $\mathrm{Ti(OH)_2}O_2$-$\mathrm{Ti(OH)_2}$ and the $Ti(OH)_3$-O-$Ti(OH)_3$ clusters provide reasonable representations of the spatial disposition of atoms in the neighborhood of the interaction sites on rutile and anatase surfaces. Although the corresponding overpotentials do not match the previous results reported for extended surfaces [67, 69], these cluster models correctly predict the relatively larger feasibility of decomposing water molecules on rutile (110) surfaces compared to anatase (001) substrates. These results suggest the possibility to predict, within the small cluster approximation, the relative performance of different $TiO_2$-based surfaces for the catalytic splitting of water molecules.

# Chapter 4

# Transition metals at $TiO_2$-based models for water decomposition

## 4.1 Introduction

Lately, the investigation of new materials based on abundant transition metals, to drive the OER has been strongly promoted. This is motivated by the high electrocatalytic activity of ruthenium and iridium dioxides for the OER, as part of the overall water splitting in ECC [181,182]. For instance, titanium dioxide nanowires, doped with transition metals improve their electrocatalytic activity toward the OER [183]. A recently synthesized material composed by $IrO_2$ nanoparticles deposited on Nb-$TiO_2$ substrates has been found to improve the OER activity with respect to unsupported $IrO_2$ [7]. The enhancement of the OER is attributed to the synergistic effect of the nanoparticles anchored on the substrate. $TiO_2$ nanocrystals of different morphologies, doped with transition metals (TM-$TiO_2$), have been shown to lower the OER overpotential as well [6, 181, 183, 184]. The electronic structure of the doped systems has been studied within several experimental techniques [181], and the fact that doped metal active sites may support the creation of intermediate compounds like $OH^-$ and $OOH^-$ adsorbed on the nanoparticle surfaces, has been identified as the key point in the enhancement of the OER activity. Meanwhile, the separation of d-orbitals localized in the TM impurities is associated to the appearance of electronic states inside the band gap and the lowering of the overpotential for the OER [6].

From the theoretical point of view, the OER on specific surfaces of $TiO_2$ rutile and anatase have been addressed employing a thermochemical approach in the framework of the Density Functional Theory (DFT) with periodic boundary conditions (PBC) [69, 112]. These results support the experimental trends observed for the OER activity on different topological forms of $TiO_2$ electrodes. A similar methodology has been applied to study the OER when it occurs on TM-$TiO_2$

based electrodes, and a good agreement with the experimental results have been also found [68, 165]. However, despite all the experimental and theoretical studies, the detailed mechanism of the electrochemical and photoelectrochemical OER on $TiO_2$-based devices and its high overpotentials are not completely understood.

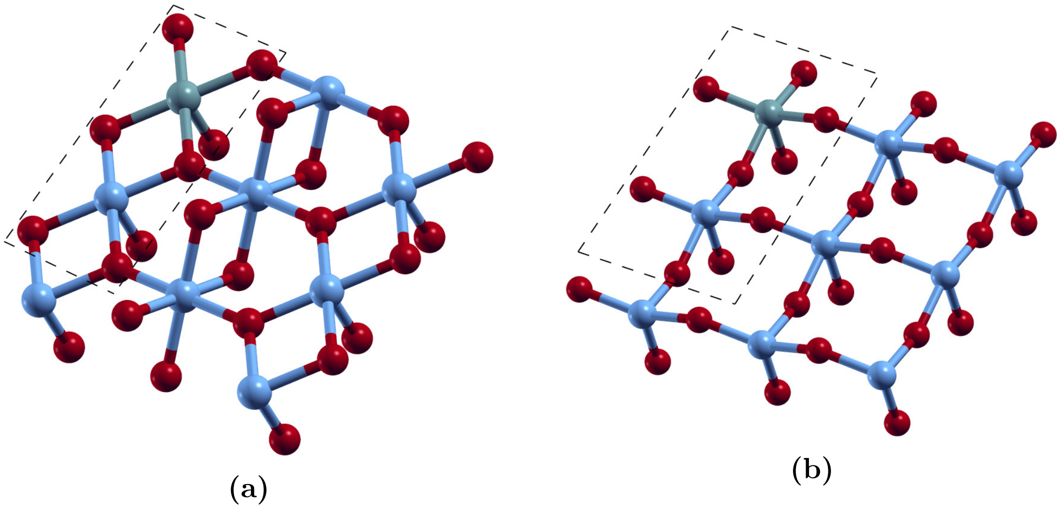

**Figure. 4.1.** ***a)*** *Top view of a TM-doping site on the rutile* $TiO_2$ *(110) surface (TM = V, Cr, Mn, Fe, Co, Ni). The oxygen atoms are represented by the red points, the Ti by blue, while the TM is the green atom. The portion of the surface corresponding to the cluster approximation is delimited by the dashed lines.* ***b)*** *Top view of a TM-doping site on the anatase* $TiO_2$ *(001) surface with the same color code as in* ***a)****, the cluster representation of the surface containing the TM-site is indicated by the dashed lines.*

The previous chapter was devoted to the theoretical modeling of the OER on $TiO_2$-based electrochemical cells employing small cluster models [71]. Among other cluster configurations, the electrochemical OER was studied on $Ti(OH)_2$-$O_2$-$Ti(OH)_2$ and $Ti(OH)_3$-O-$Ti(OH)_3$. They were considered as simplified representations of the active Ti sites on the $TiO_2$ rutile (110) and anatase (001) surfaces respectively, and they were found to perform reasonably well for the OER: the overpotentials obtained in both mechanisms for the OER correctly predict the trends observed in previous calculations on extended surfaces.

In this chapter, the OER is studied on the aforementioned cluster systems (i.e., $Ti(OH)_2$-$O_2$-$Ti(OH)_2$ and $Ti(OH)_3$-O-$Ti(OH)_3$) when one Ti atom is replaced by different transition metals (TM): Vanadium, Chromium, Manganese, Iron, Cobalt and Nickel, Fig. 4.1. They constitute a direct extension of the previously developed representations for the active sites on the corresponding titanium dioxide surfaces, to the case in which the substrate is doped with a TM. Among the abundant experimental evidence of $TiO_2$ structures doped with transition metals [6, 181], the cobalt activation sites have a significant relevance regarding the OER activity. Considering that other substitute species like: Mn, Fe and Ni are also frequently found to favor the OER, the above series of TMs is aimed to evaluate the performance of the proposed cluster structures in a complete set of TMs ranging from the pure $TiO_2$ structure to the Ni-$TiO_2$ doped one. The proposed reaction mechanisms always take place on the TM-site. The main goal of this study is to investigate the feasibility of the simplified cluster models to reproduce the relative performance of the TM-$TiO_2$ electrodes for the OER, and to get a deeper insight into the impact of the TMs on the activity of the TM-$TiO_2$ surfaces for the overall water splitting process.

The present chapter is organized as follows. In the Sec. 4.2, the methodology to compute the *ab-initio* energy of each structure, the variations of the free energy at each reaction step and the theoretical estimations of the overpotentials are described. The main results of the chapter are presented and discussed in Sec. 4.3. Finally, in Sec. 4.4, a brief summary of the most important results and concluding remarks are presented.

## 4.2 Methodology

The major concern in this chapter, similar to Chap. 3, is about the OER on cluster model representations of the electrode surfaces. There by, while the methodology employed is described in detail in Chap. 3, a briefly description is presented here for completeness. The electrochemistry of the overall water decomposition reaction can be summarized by the half-equations occurring at the anode and the cathode, respectively:

$$H_2O \rightarrow \frac{1}{2}O_2 + 2H^+ + 2e^- \qquad E^o = -1.23\text{V}, \tag{4.1}$$

$$2H^+ + 2e^- \rightarrow H_2 \qquad E^o = 0.00\text{V}, \tag{4.2}$$

Although several reaction mechanisms are proposed to drive the target reaction, they are all based on a determined sequence of the following intermediate steps (labeled as A, B, C, D and E):

$$\text{A: } H_2O + S \rightarrow H_2O\text{-}S \tag{4.3}$$

$$\text{B: } H_2O + S \rightarrow OH\text{-}S + H^+ + e^- \tag{4.4}$$

$$\text{C: } H_2O\text{-}S \rightarrow OH\text{-}S + H^+ + e^- \tag{4.5}$$

$$\text{D: } OH\text{-}S \rightarrow O\text{-}S + H^+ + e^- \tag{4.6}$$

$$\text{E: } O_2\text{-}S\text{-}H \rightarrow S + O_2 + H^+ + e^- \tag{4.7}$$

In the following, two model reaction mechanisms will be considered, in which the water splitting process proceeds from the initial structures $Ti(OH)_2$-$O_2$-(TM)$(OH)_2$ or $Ti(OH)_3$-O-(TM)$(OH)_3$ (TM = V, Cr, Mn, Fe, Co, Ni), respectively. The proposed reaction pathway starting from the $Ti(OH)_2$-$O_2$-(TM)$(OH)_2$ active sites consist of the sequence of elementary steps: A, C, D, A, E, D from the equations list (4.3) - (4.7), while for the $Ti(OH)_3$-O-(TM)$(OH)_3$ series, the reaction mechanism evolves via the sequence: A, C, D, D, A, E. Although they differ in the sequence of individual reactions, both mechanisms comprise six intermediate steps: two water adsorptions and four deprotonations. The dissociative water adsorption, reaction B: eq. (4.4) is considered when the molecular water adsorption, reaction A: eq. (4.3), is not favorable from the thermodynamical point of view.

The study of the OER according to the proposed mechanisms is carried out employing a similar methodology as in the previous chapter. For each of the reaction mechanisms, the optimized geometries and ground state energies of the intermediate structures are computed, as well as their corresponding zero point energy corrections. From these data, the free energy profiles along the reaction pathways are obtained within the framework of a previously developed model due to Nørskov and coworkers [112]. The theoretical overpotential of the OER is determined by evaluating the influence of the external bias on the free energy profile, and it is defined as the difference between the external potential needed to make the free energy profile downhill along the reaction steps and the potential of the electrochemical cell. The latter is set equal to the electrochemical potential for the whole water splitting reaction at standard thermodynamic conditions (1.23 V). The overpotential determined in this way is not amenable for a direct comparison with experimental values because several contributions have been neglected (e.g., electrical and transport resistances). However, the computed OER overpotentials provide insight on the relative performance of different catalytic surfaces [68,112,156,165].

The standard hydrogen electrode SHE [112], is employed to incorporate the contribution of the external potential to the free energy profile of the analyzed processes. Every deprotonation step causes a shift of the free energy at standard thermodynamic conditions given by the following expression: $\Delta G_U = 1/2 E_{H_2} - eU$, where $E_{H_2}$ encloses the energetic and entropic contribution of a hydrogen molecule in the gas-phase and $-eU$ is the energy delivered into the system by the external electromotive force. Due to this energy, the intermediate free energy barriers of the OER are linearly decreased by the external potential.

## 4.3 Results and discussion

In this section, the water decomposition reaction on the model clusters $TM(OH)_3$-O-$Ti(OH)_3$ and $TM(OH)_2$-$O_2$-$Ti(OH)_2$, is studied for a set of transition metals ranging from V to Ni. The case of Co, being a typical doping element used to tune the properties of $TiO_2$ surfaces [6,181,185], is described in detail. The consequences of doping the titanium-dioxide substrates with the remaining TMs are analyzed in terms of their contributions to the free energy of the intermediate states along the proposed reaction mechanisms. Finally, the theoretical overpotentials for all the studied systems are summarized and compared with previous theoretical and experimental studies. All the proposed reaction mechanisms and the corresponding free energies, as well as the Cartesian coordinates and total energies of every structure considered in this work, are included in the App. B.

### 4.3.1 Water splitting on $Co(OH)_3$-O-$Ti(OH)_3$

Here, we consider the replacement of one titanium atom by a cobalt atom in the previously studied cluster model $Ti(OH)_3$-O-$Ti(OH)_3$ resembling the $TiO_2$ anatase (001) surface [71] (i.e., the $Co(OH)_3$-O-$Ti(OH)_3$ structure is taken as the initial geometry). The previous model has been successfully employed to study, in a simplified way, the OER on a titanium-dioxide substrate. In the present case, the cluster structure represents an active site on the Co-doped surface, and the influence of such sites on the OER is considered as an extension of the study carried out for the non-doped surfaces [71].

The intermediate structures for the water decomposition reaction, starting from the $Co(OH)_3$-O-$Ti(OH)_3$ cluster, and their DFT energies relative to the initial cluster, are shown in Fig. 4.2a. The free energy profiles along this reaction path, under the action of different external potentials, are depicted in Fig. 4.2b. Initially, we consider the adsorption of the first water molecule on the cobalt site of the cluster. This is not a spontaneous process from the energetic point of view: even though the energy change in the transformation is negative (-0.546 eV), the entropic contribution of the adsorption of a water molecule in the gas-phase at standard conditions is also negative, yielding a total free energy change upon adsorption of $\Delta G = 0.06$ eV. Since the adsorption of a water molecule is energetically unfavorable, a dissociative adsorption is considered instead. This process corresponds to a reaction type B: eq. (3.4), in this case it represents the direct transition from structure-1 to structure-2. The two water adsorption processes proposed in this model (i.e., for the reaction occurring on a $Co(OH)_3$-O-$Ti(OH)_3$ cluster) result energetically unfavorable (structures labeled as $\Gamma$ and $\Delta$ in Figs. 4.2a and 4.2b). For other reaction mechanisms studied in this work (see, for example, Sec. 4.3.3), the spontaneous adsorption of a water molecule may also occur. After the dissociative adsorption of the first water molecule, a second $H^+$ ion is desorbed from the cluster leading to the formation of an OOH group on the Co site. The $H^+$ in the OOH group is removed during the next deprotonation step, and an $O_2$ molecule is preformed inside the cluster. As the second water adsorption is found to be dissociative, a more complex process is considered to steer the reaction between structures -4 and -5. It consists on the following processes: the water molecule is dissociated, the $OH^-$ is attached to the

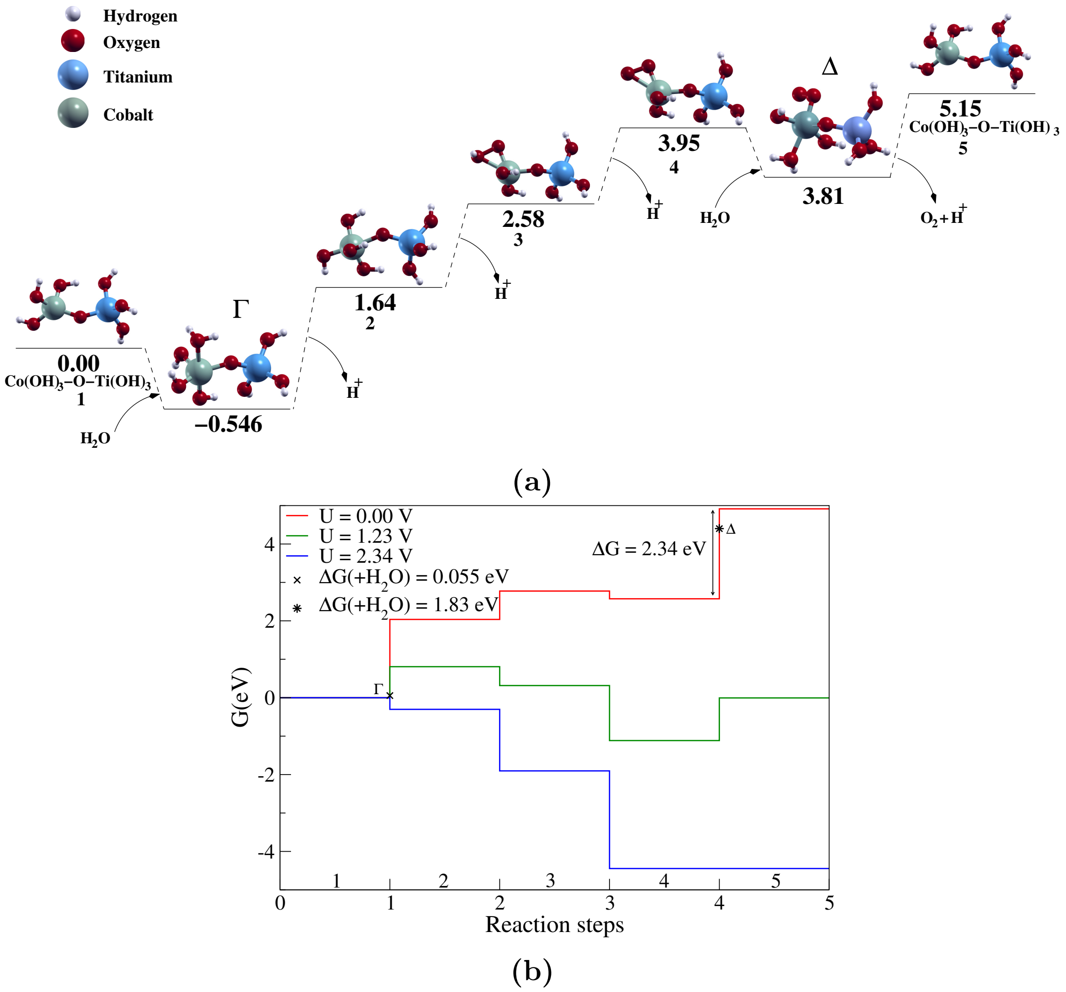

**Figure. 4.2.** ***a)*** *Water splitting on* $Ti(OH)_3$*-O-*$Co(OH)_3$*:* $Ti(OH)_3$*-O-*$Co(OH)_3$ $+ 2H_2O \rightarrow$ $Ti(OH)_3$*-O-*$Co(OH)_3$ $+ 2H_2 + O_2$*. The total energies are in eV. The* $\Gamma$ *and* $\Delta$ *structures represent the dissociative water adsorption processes.* ***b)*** *Free energy profile of the water splitting mechanism on* $Ti(OH)_3$*-O-*$Co(OH)_3$ *at standard thermodynamic conditions in presence of different external potentials. The cases of zero external potential (red line), standard potential of the overall water splitting reaction: 1.23 V (green line), and the minimum external potential which makes the free energy of the process down-hill in the reaction steps: 2.34 V (blue line) are represented in the figure. The* $\Gamma$ *and* $\Delta$ *points show the increase of the free energy when the molecular adsorption of water is considered as an intermediate structure. The higher barrier in the* $U = 0.00$ *V profile corresponds to the rate-limiting step yielding a theoretical estimate of the overpotential of 1.11 V.*

cluster, the $O_2$ and the $H^+$ separate from the surface while an electron is transferred to the anode. In this way the initial structure is recovered and the neutrality of the system is kept.

This process (the transition from structure-4 to structure-5, Fig. 4.2a) is the rate-limiting step in the reaction mechanism. An energy barrier of 2.34 eV in the free energy profile (at zero potential bias) needs to be overcome for the reaction to occur (U = 0.00 V, Fig. 4.2b). Under the influence of an external voltage equal to the ideal cell potential (1.23 V), the second deprotonation becomes energetically allowed but different barriers hamper the reaction, in particular the rate-limiting step ($U = 1.23$ V, Fig. 4.2b). Applying an external potential of 2.34 V the free energy profile of the process becomes down-hill along the reaction coordinate ($U = 2.34$ V, Fig. 4.2b) yielding a theoretical estimate of the overpotential of 1.11 V. This value is significantly smaller than the overpotential of 3.53 V obtained for the $Ti(OH)_3$-O-$Ti(OH)_3$ cluster [71]. The downwards shift of the theoretical overpotential, when a Co atom substitutes a Ti center reproduces the behavior predicted by previous theoretical calculations on extended surfaces and also experimental results for the overpotential of Co-doped titanium dioxide surfaces with respect to the pristine $TiO_2$ substrates. For example, an overpotential of 1.31 V has been obtained for the water splitting reaction on $TiO_2$ anatase (001) [69], while in the case of Co-$TiO_2$ anatase (100) a lower value of 0.32 V has been reported [185]. Likewise, in a previous experimental study of the water decomposition on $TiO_2$-based nanocrystals (NCs), an overpotential of 0.43 V was measured for the Co-doped system, while a value larger than 1.0 V was found for pure $TiO_2$ NCs [181].

### 4.3.2 Water splitting on $Co(OH)_2$-$O_2$-$Ti(OH)_2$

The influence of Co doped sites, on the OER, is also studied for the model cluster $Co(OH)_2$-$O_2$-$Ti(OH)_2$. It corresponds, as it was related before Sec. 4.1, to the case of a Co doped site on $TiO_2$ rutile (110) surface. Since the (110) surface is among the most stable ones in the $TiO_2$ rutile phase [186], the study of the water decomposition reaction on $Co(OH)_2$-$O_2$-$Ti(OH)_2$ is of particular importance for the evaluation of the adequacy of the cluster model to represent Co-active sites on the anode surface.

The energies of the intermediate structures in the proposed reaction mechanism are shown in Fig. 4.3a. The free energy profiles corresponding to different external potentials are depicted in Fig. 4.3b. Similar to the case studied above, the reaction is initiated with the adsorption of a water molecule on the initial structure. In this case the two water adsorption processes considered in the proposed mechanism are molecular adsorptions (i.e., they are favorable from the free energy point of view). After the first water adsorption on the Co site, a deprotonation step eq. (3.5), leads to the formation of an $OOH^-$ group on the cluster: structure-3. In a second deprotonation step, an $H^+$ is removed from the OOH structure and a preformed $O_2$ molecule is observed in (Fig. 4.3a, structure-4). The adsorption of a second water molecule on this structure is an exothermic process and the mechanism proceeds via a reaction type E: eq. (3.7). In this process the preformed $O_2$ molecule detaches from the cluster together with an additional proton (Fig. 4.3a, structures -5 and -6). Finally, the initial structure is recovered upon the last deprotonation step.

The free energy barrier of the rate-limiting step is highlighted in Fig. 4.3b. It

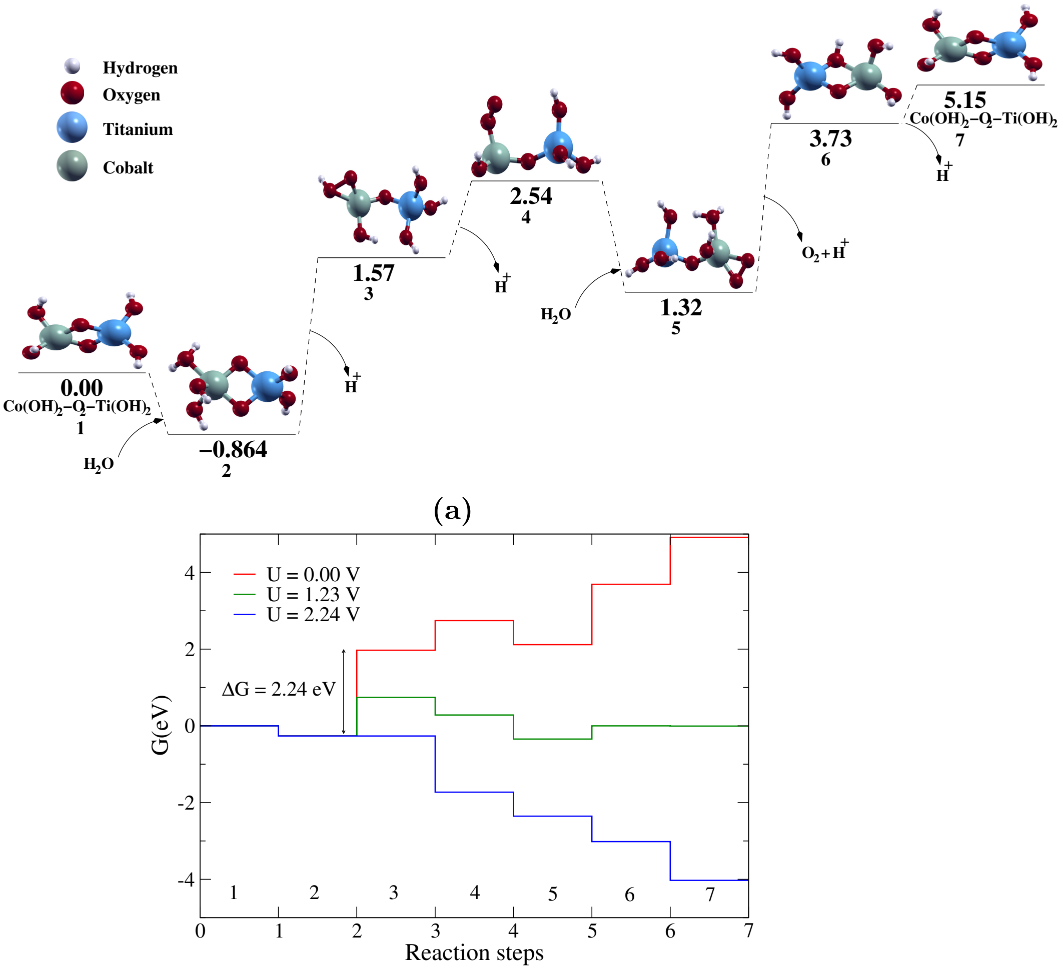

(a)

(b)

**Figure. 4.3.** ***a)*** *Water splitting on* $Ti(OH)_2$-$O_2$-$Co(OH)_2$: $Ti(OH)_2$-$O_2$-$Co(OH)_2$ $+ 2H_2O \rightarrow$ $Ti(OH)_2$-$O_2$-$Co(OH)_2$ $+ 2H_2 + O_2$. *The total energies are in eV.* ***b)*** *Free energy profile of the water splitting mechanism on* $Ti(OH)_2$-$O_2$-$Co(OH)_2$ *at standard thermodynamic conditions and under the influence of different external potentials. The cases of zero external potential (red line), standard potential of the overall water splitting reaction: 1.23 V (green line), and the minimum external potential which makes the free energy of the process down-hill in the reaction steps: 2.24 V (blue line) are represented in the figure. The higher barrier in the* $U = 0.00$ *V profile corresponds to the rate-limiting step yielding a theoretical estimate of the overpotential of 1.01 V.*

corresponds to the formation of the $OOH^-$ group on the cluster, and a barrier of 2.24 eV is associated with this step. Thus, an external potential of 2.24 V needs to be applied to overcome the highest reaction barrier. With this applied voltage, the free energy profile becomes flattened around this point and the whole reaction becomes favorable from the thermodynamic point of view (U = 2.24 V, Fig. 4.3b). The external voltage required to drive the reaction corresponds to an overpotential of 1.01 V. This value is slightly lower than the one from the previous system, thereby confirming the prediction, within the cluster model, that the Co-doped

$TiO_2$ surfaces exhibit better catalytic properties for the water splitting compared to the undoped substrates. The same trend has been observed for extended $TiO_2$ surfaces when they are doped with cobalt. This result confirms the capability of the proposed cluster models to describe the enhancement in the OER activity when Co active sites are placed on $TiO_2$ surfaces.

In the case of water decomposition on $Co(OH)_2$-$O_2$-$Ti(OH)_2$ clusters, in the framework of the employed methodology, the adsorption of $H_2O$ molecules plays an important role in reducing the overpotential: when water is molecularly adsorbed, the next deprotonation step is favored by the entropy gain of the $H^+$ desorption (i.e., $TS(H^+) = \frac{1}{2}TS(H_2) = 0.20$ eV). If the water molecule is adsorbed dissociatively, then the corresponding deprotonation step is also favored for the entropy contribution of the $H^+$, but hindered by the entropy loss due to the decomposition of the water molecule (i.e., $TS(H_2O) = 0.60$ eV). The net effect is an increase of 0.4 eV in the free energy when the water is dissociatively adsorbed.

### 4.3.3 Water splitting on $TM(OH)_3$-O-$Ti(OH)_3$ and $TM(OH)_2$-$O_2$-$Ti(OH)_2$; (TM = V, Cr, Mn, Fe, Ni)

The performance of the OER on the remaining TM-doped clusters studied in this work is discussed in the present section, considering the free energy change at every intermediate step in the proposed reaction mechanisms. The free energy changes corresponding to each of the model reaction steps (eqs. (3.3)-(3.7)) are shown in Figs. 4.4 and 4.5 for the OER on $TM(OH)_3$-O-$Ti(OH)_3$ and $TM(OH)_2$-$O_2$-$Ti(OH)_2$, respectively, when the TM changes from V to Ni. For a clearer visibility, each intermediate process (e.g., the first $H_2O$ adsorption, the third $H^+$ desorption) has been represented with a different color.

In Fig. 4.4, it can be seen that for the model reactions taking place on $TM(OH)_3$-O-$Ti(OH)_3$ (for TM dopants from Cr to Ni) the free energy changes between consecutive intermediate steps lay in an energy interval ranging from -0.27 eV (for the first $H_2O$ adsorption on the Ni-doped structure) to 2.62 eV (for the first deprotonation on the same cluster). The various crossings between several curves indicate that the rate-limiting steps vary for the clusters containing different TMs changes, although the corresponding free energy barriers remain in a narrow interval around 2 eV for dopants from Cr to Ni.

In the case of V, the rate-limiting step is the first deprotonation. It exhibits a free energy barrier of 4.72 eV, which is significantly higher than for the remaining TMs. In this case, the first water adsorption on the V-site is not a favorable process from the thermodynamic point of view, and the first deprotonation process is considered as part of the dissociative adsorption of the first water molecule. Since the second highest barrier in the $V(OH)_3$-O-$Ti(OH)_3$ structure (i.e., the 4th

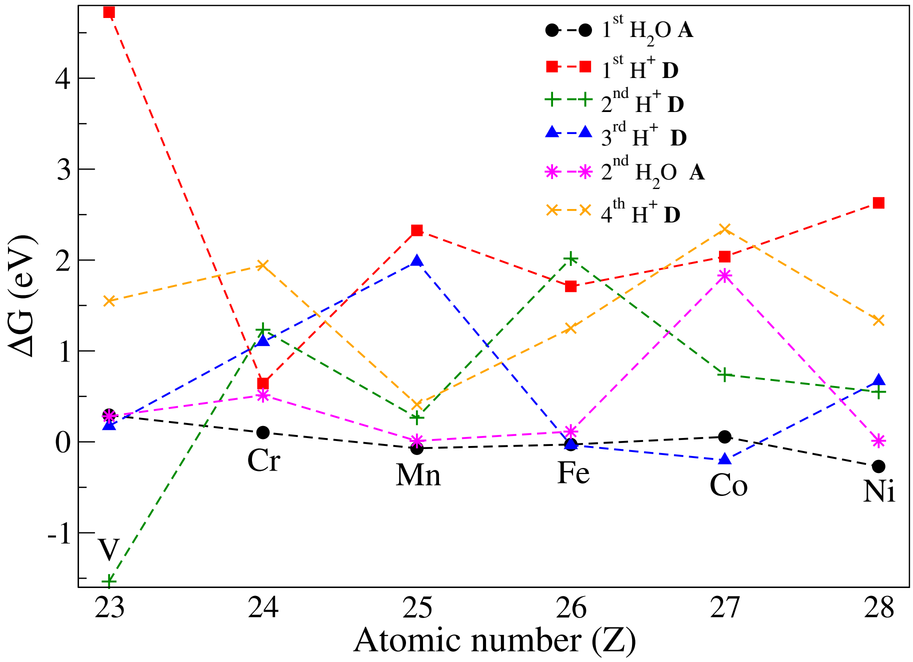

**Figure. 4.4.** *Contribution of the different intermediate steps, to the overall variation of the free energy along the proposed reaction mechanism for the water splitting on the transition-metal doped clusters* $TM(OH)_3$*-O-*$Ti(OH)_3$*. The behavior of the same elementary process on different TMs has been drawn using the same color. The abbreviations:* ***A*** *and* ***D*** *stand for water adsorption and* $H^+$ *desorption, respectively.*

deprotonation step) is laying within the interval of the free energy barriers for the remaining models, the OER activity can be enhanced significantly by decreasing the free energy barrier of the first deprotonation step.

For the OER on $TM(OH)_2$-$O_2$-$Ti(OH)_2$ clusters Fig. 4.5, the free energy differences between the intermediate steps present wider variations, with respect to the TM employed, than for the anatase-resembling clusters Fig. 4.4. The behavior observed for the Fe, Co and Ni containing $TM(OH)_2$-$O_2$-$Ti(OH)_2$ clusters is similar to that of the $TM(OH)_3$-O-$Ti(OH)_3$ structures. In these three cases, the free energy variations, ranging from -0.6 eV (for the second water molecule adsorbed on the Co-site) to 2.44 eV (for the 4th deprotonation step in the Ni-doped system) matches well the corresponding energetic interval (from -0.27 eV to 2.62 eV) for the $TM(OH)_3$-O-$Ti(OH)_3$ family. In particular, the rate-limiting step for the Fe-doped cluster is indeed the same as in the previous system (i.e., the 2nd deprotonation step) while for the Co and Ni dopants the highest energy barrier is found for the first and the fourth deprotonation steps, respectively.

On the other hand, the rate-limiting step for the $V(OH)_2$-$O_2$-$Ti(OH)_2$ clusters is the second deprotonation, and it is characterized by an energy barrier of 3.42 eV Fig. 4.5. An additional comparable energy barrier of 3.40 eV is present in this case, corresponding to the third deprotonation step. This intermediate process happens to be also the rate-determining step for the Cr- and Mn-doped structures. The

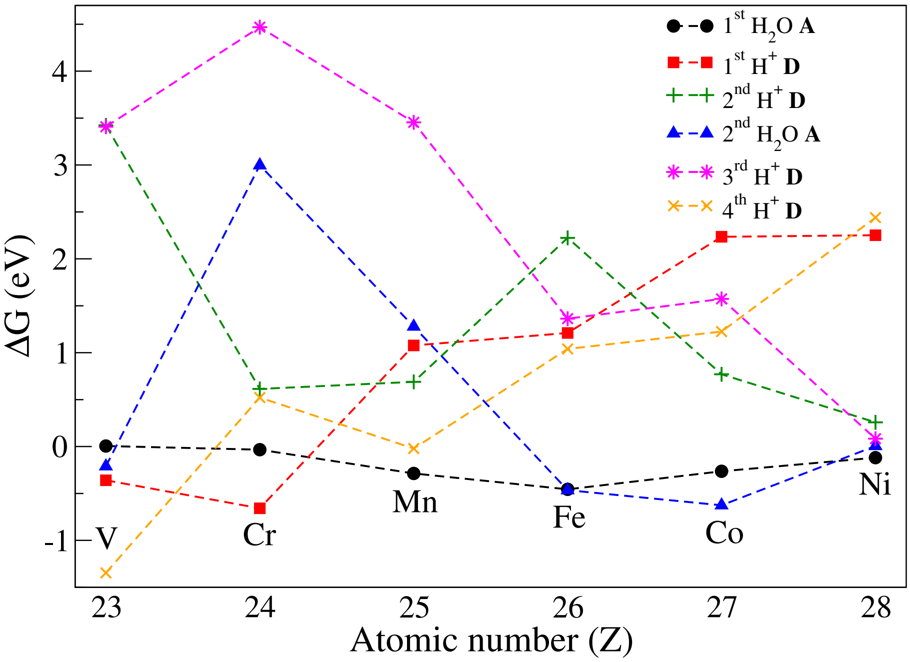

**Figure. 4.5.** *Contribution of the different intermediate processes, to the overall variation of the free energy along the proposed reaction mechanism for the water splitting on the transition-metal doped clusters TM(OH)$_2$-O$_2$-Ti(OH)$_2$. The behavior of the same elementary process on different TMs has been drawn using the same color. The abbreviations:* ***A*** *and* ***D*** *stand for water adsorption and $H^+$ desorption, respectively.*

free energy barrier of this third proton extraction shows a clearly decreasing trend as the atomic number of the TM from Cr to Ni, the only exception being the Co-doped structure (for which the barrier of the third deprotonation step is higher than that of the Fe-containing cluster by 0.21 eV). As a consequence of this depletion, the removal of the third proton is relevant for the performance of Cr- and Mn-doped structures, but it has almost no influence on the overall suitability for water decomposition of the model clusters containing late transition metals: Fe, Co and Ni.

### 4.3.4 Theoretical estimation of overpotentials for the water splitting

The theoretically computed overpotentials are obtained from the highest free energy barrier along every reaction pathway: Figs. 4.4 and 4.5, for the different reaction mechanisms studied in this work: namely the OER on $TM(OH)_3$-O-$Ti(OH)_3$ and $TM(OH)_2$-$O_2$-$Ti(OH)_2$, where TM represents the transition metals ranging from V to Ni. These theoretical estimations are summarized in Fig. 4.6. The energy barriers for the water splitting on the model structures of the type $TM(OH)_3$-O-$Ti(OH)_3$, which resemble in a simplified way the TM active sites on a doped $TiO_2$

anatase (001) surface, is represented by the black line, while $TM(OH)_2$-$O_2$-$Ti(OH)_2$ clusters (represented in red) may be related with similar sites on a $TiO_2$ rutile (110) surface. Additionally, the performance of similar cluster models mimicking pure $TiO_2$ surfaces (i.e., $Ti(OH)_3$-O-$Ti(OH)_3$ and $Ti(OH)_2$-$O_2$-$Ti(OH)_2$), presented in Chap. 3 and [71], and experimental values of onset overpotentials for doped-$TiO_2$ NCs as reported in [181] (Fig. 4.6, blue dashed line) are also plotted for the sake of comparison.

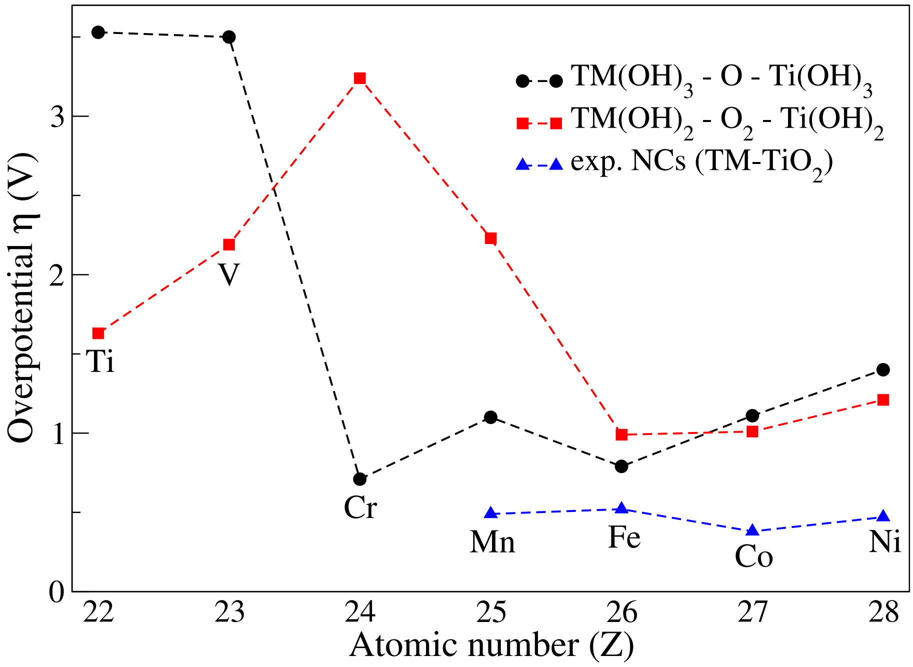

**Figure. 4.6.** *Computed overpotentials for the water splitting on different cluster models considered in the present work:* $TM(OH)_3$-O-$Ti(OH)_3$ *(black) and* $TM(OH)_2$-$O_2$-$Ti(OH)_2$ *(red). Transition metals from Ti to Ni have been considered to occupy the TM position in both models. The results for the clusters containing only Ti centers were taken from Chap. 3 and [71]. They are shown for the sake of comparison with the behavior of the doped structures, as well as the blue points which represent experimental values of the onset overpotentials in TM-doped* $TiO_2$ *nanocrystals (NCs) as reported in [181].*

Previous experimental results show an overpotential for pure $TiO_2$ (NC) above 1.0 V, while for TM-$TiO_2$ (NCs), where TM = {Mn, Fe, Co, Ni}, it decreases below 0.53 V [181]. The present cluster models yield the overpotentials of 1.63 V for $Ti(OH)_2$-$O_2$-$Ti(OH)_2$ and 3.53 V for $Ti(OH)_3$-O-$Ti(OH)_3$ [71]. When TMs are included in the cluster structures and for the OER taking place on the TM-site, the estimated overpotentials for Fe, Co and Ni decrease below 1.40 V and both models ($TM(OH)_3$-O-$Ti(OH)_3$ and $TM(OH)_2$-$O_2$-$Ti(OH)_2$) give similar overpotentials Fig. 4.6. These results confirm the capability of the proposed model to reproduce the improvement effect in the OER activity when TMs like Fe, Co and Ni are included as impurities at substitutional sites in $TiO_2$ surfaces.

In the case of Mn we observed a different behavior of the cluster resembling anatase and rutile phases of titanium dioxide. The overpotential computed for the reaction taking place on the anatase resembling model: $Mn(OH)_3$-O-$Ti(OH)_3$, is lower than for the model of the undoped surface, in agreement with the trend observed experimentally. On the other hand, an overpotential of 2.22 V is predicted for the OER on the $Mn(OH)_2$-$O_2$-$Ti(OH)_2$ structure, which is somewhat larger than that of the undoped cluster. Since the $TiO_2$ based NC samples employed in the experimental observations [181] possess a significant anatase component, the agreement between the anatase like cluster model ($Mn(OH)_3$-O-$Ti(OH)_3$) and the experimental results is considered satisfactory.

Likewise, the larger value of the overpotential (3.24 V) in the case of $Cr(OH)_2$-$O_2$-$Ti(OH)_2$ models, with respect to the cluster containing two titanium centers, predicts no enhancement of the OER activity for the $TiO_2$ rutile (110) surfaces upon doping with Cr atoms, while the water decomposition is more favorable from the energetic point of view at the Cr site in the $Cr(OH)_3$-O-$Ti(OH)_3$ cluster. To the best of our knowledge, there is not empirical data on Cr-$TiO_2$ based electrodes.

A different behavior is observed for V-$TiO_2$ systems, for which we obtained overpotentials of 3.50 V and 2.19 V for the $V(OH)_3$-O-$Ti(OH)_3$ and $V(OH)_2$-$O_2$-$Ti(OH)_2$ structures, respectively. Hence, no significant enhancement of the water decomposition process is foreseen for the vanadium-doped complexes in comparison to the pure $TiO_2$ system.

## 4.4 Conclusions

In the present chapter, the water decomposition reaction on TM active sites placed at $TiO_2$-based electrodes has been studied by means of two different cluster models: $TM(OH)_3$-O-$Ti(OH)_3$ and $TM(OH)_2$-$O_2$-$Ti(OH)_2$. They represent, in a simplified way, TM active sites on $TiO_2$ surfaces: anatase (001) and rutile (110), respectively. Transition metals ranging from V to Ni have been considered as dopants, and the reaction pathways have been investigated for each doped system and for each model structure (i.e., $TM(OH)_3$-O-$Ti(OH)_3$ and $TM(OH)_2$-$O_2$-$Ti(OH)_2$). This investigation constitutes a direct extension of our previous results Chap. 3, in which $Ti(OH)_3$-O-$Ti(OH)_3$ and $Ti(OH)_2$-$O_2$-$Ti(OH)_2$ dimeric structures were considered as models of pure $TiO_2$ surfaces [71]. Electron transfer intermediate steps as well as non electrochemical water adsorption have been considered to take place during the OER. The energetics of the reaction mechanisms were described within the framework of Density Functional Theory (DFT). The use of this level of theory allows the comparison of the results of the present simulations with those of the $TiO_2$-based cluster models [71] and previous calculations on extended surfaces [112, 156, 185].

The optimized geometry of every intermediate step and the energy required for the system to move along the reaction path provide a detailed picture of the water splitting process on the present cluster models. The rate-limiting step for every reaction mechanism has been identified on the basis of the DFT energies and the entropic contributions to the free energy changes of the adsorbed/desorbed species in the gas phase approximation.

The free energy changes computed along the proposed pathway for the OER on TM active sites in $TiO_2$ electrodes is able to reproduce, within the framework of the cluster model approximation, the general trend for the overpotentials observed in the experiments on Fe, Co and Ni doped titanium dioxide substrates. The case of Mn-doped clusters is also found to be in agreement with empirical results [181]: DFT calculations for the $Mn(OH)_3$-O-$Ti(OH)_3$ model reproduce the enhancement of the OER activity observed for Mn-$TiO_2$ anatase (001) surfaces, whereas no improvement is seen in the case of Mn-$TiO_2$ rutile (110) surfaces.

For vanadium- and chromium-doped substrates, we predict also significantly different overpotentials for the two models (i.e., $TM(OH)_3$-O-$Ti(OH)_3$ and $TM(OH)_2$-$O_2$-$Ti(OH)_2$). In the case of Vanadium, no improvement in the OER activity compared with the pure $TiO_2$-based systems is foreseen based on the theoretical estimations of the overpotentials. Likewise, when Cr dopants are considered, an enhanced activity is predicted for the anatase (001) like model: $Cr(OH)_3$-O-$Ti(OH)_3$, while a reduction is obtained for the rutile like one: $Cr(OH)_2$-$O_2$-$Ti(OH)_2$. These results illustrate the capability of the present models to reproduce the empirically observed trends for the OER activity. Moreover, they predict the influence of new TMs on the OER activity of $TiO_2$-based electrodes, which have not been still addressed experimentally.

# Chapter 5

# HER at combined $Mo_2C$ and N-doped graphene materials

## 5.1 Introduction

The growing concerns about environmental pollution and energy crises are driving considerable efforts to the development of new, clean and sustainable energy sources. Molecular hydrogen is an abundant, clean and renewable energy carrier that is considered as a promising substitute of the fossil fuels in the mean and long term future [187]. Electrocatalytic water splitting to produce $H_2$ seems to be the cleanest and most sustainable method for large-scale $H_2$ production [188]. The water splitting reaction is divided into two half-reactions: the hydrogen evolution reaction (HER) and oxygen evolution reaction (OER). The development of efficient HER electrocatalysts with low overpotentials is crucial for the successful implementation of water splitting technologies [189]. Although platinum-based electrocatalysts have been proven to be the most active and stable HER electrocatalysts, widespread applications of Pt are critically hampered by their scarcity and high cost. Thereby, the development of high-performance cost-effective HER electrocatalysts based on earth-abundant elements is highly imperative.

To date, numerous inorganic materials containing nonprecious transition metals (Fe, Co, Ni, Mo, and W), including phosphides [190], sulfides [191, 192], carbides [193] and other materials [194], have been widely explored to replace Pt as HER electrocatalysts in acid media. However, the development of highly efficient HER electrocatalysts in alkaline solutions still remains great challenge. A possible replacement for HER catalysts are molybdenum-based materials, such as molybdenum boride (MoB) [195], molybdenum disulfide ($MoS_2$) [191, 196], molybdenum carbides ($Mo_2C$) [197], and several more [198], which have already shown relative high HER activities in basic media. $Mo_2C$ has attracted large attention among these electrocatalysts, specially due to its d-band electronic structure, which is similar to that of Pt [199]. Therefore, extensive efforts have been devoted to improve the HER catalytic activity of $Mo_2C$ by the enhancement of electron conduction through phase control [200], nanostructure engineering [197, 201], intercalation [202], and doping [203]. However, most of the reported procedures often lead to aggregation or excessive growth of $Mo_2C$ nanoparticles, resulting in a low density of exposed active sites [204], and therefore poor electrocatalytic properties for the HER. It is still a considerable challenge to simultaneously provide high conductivity and abundant active sites for $Mo_2C$-based electrocatalysts for HER in alkaline media.

In the present chapter, different surface models are proposed to assess the HER at recently synthesized materials based on $Mo_2C$ and N-doped graphene layers [73, 205]. A previously developed theoretical methodology to evaluate the HER activity at the proposed model surfaces (Nørskov's theory) is employed, Sec. 2.5. Two major groups of active site models are considered:

i) $Mo_2C$ clusters adsorbed on N-doped graphene layers,

ii) N-doped graphene layers deposited on top of the $Mo_2C$ (001) surface.

The former group is aimed to get a microscopic insight on the high HER activity of new electrocatalytic materials based on $Mo_2C$-NPs adsorbed on graphene layers [205]. The latest one addresses, from a theoretical point of view, another new material based on molybdenum carbide anchored on nitrogen-doped porous carbon nanosheets ($Mo_2C$@2D-NPC) recently synthesized [73]. This new material possesses evenly distributed $Mo_2C$ nanoparticles with diameters down to 5 nm, apparent $Mo_2C$/NPC interfaces, and high specific surface areas, indicating the presence of abundant exposed active sites for electrocatalysis, Fig. 5.1. As an electrocatalyst for HER, $Mo_2C$@2D-NPC exhibited a low onset overpotential of 0 mV, an overpotential of only 45 mV at 10 $\mathrm{mA}\times\mathrm{cm}^{-2}$, a small Tafel slope of 46 $\mathrm{mV}\times\mathrm{dec}^{-1}$, and excellent stability in 1 M KOH electrolyte, which are superior to all of the previously reported $Mo_2C$-based catalysts, much better than the values of most of the reported HER electrocatalysts in alkaline media and even comparable to the noble metal catalyst Pt [73].

The theoretical approach presented in this chapter is based on the modeling of the interaction between two different type of surfaces. One is $Mo_2C$ (001) surface, it is obtained from $\beta$-$Mo_2C$ bulk, which has an orthorhombic structure with the following lattice constants: a = 4.732 Å, b = 6.040 Å and c = 5.210 Å [206]. The second one is the graphene structure which is a hexagonal surface with a distance between first neighbors of 1.42 Å. The structure along the [001] direction in $\beta$-$Mo_2C$ bulk Fig. 5.2, consists of alternating layers of Mo and C, suggesting that Mo or C terminations are possible. There are two types of Mo atoms on the ideal Mo-terminated surface, the first type has one coordination vacancy with respect to the bulk crystalline structure, while the second type has two coordination vacancies. The distinguishing factor between these two types of surface Mo atoms is whether

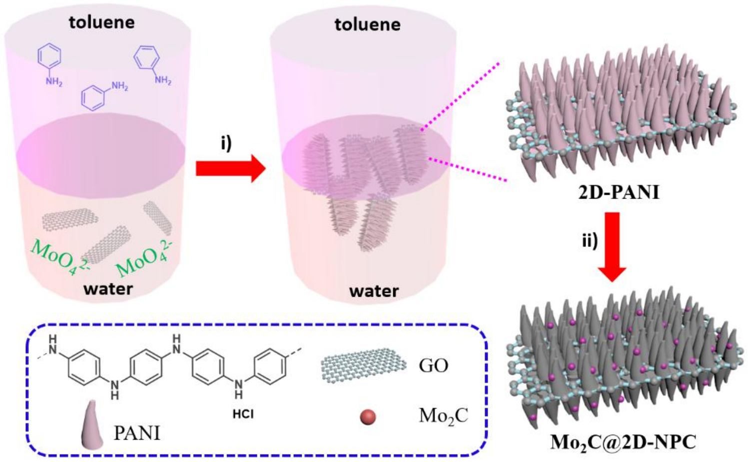

**Figure. 5.1.** *Schematic representation of the preparation procedure of* $Mo_2C$ *anchored on N-doped porous carbon nanosheets. i) In situ polymerization of aniline on graphene oxide surfaces at the toluene/water interface in presence of* $MoO_4^{2-}$*. Top: aniline in toluene; bottom: graphene oxide,* $(NH_4)_2MoO_4$*, HCl and ammonium persulfate in water. ii) Pyrolysis at 700-1100 ℃ under 5%* $H_2$*/Ar atmosphere for 2 h (taken from [73]).*

they are coordinated to one or two carbon atoms in the second layer. On the C-terminated surface, all of the Mo atoms are fully-coordinated with respect to the bulk phase.

The distance between the $Mo_2C$ and graphene is approximately 2.26 Å. Theoretical results presented in this chapter suggest that graphene structures are not good catalysts for the HER. The challenge is to find, within a theoretical methodology, new active-sites leading the enhancement of the HER activity. Different representations of the surface have been constructed to achieve this objective. Furthermore, nitrogen atoms are considered as dopant species in order to improve the HER activity. Nevertheless, the substitution of carbon atoms by nitrogen ones on the graphene surface show also low activity for the HER, within the framework of the Nørskov's theory, Sec. 2.5. The second try was the consideration of different type of defects on the N-doped graphene layer.

For one of the new proposed models, the DFT results show a value of H-adsorption free energy of -0.02 eV, which is even lower than the value obtained for the platinum electrode: $\left|\Delta G_H^{\mathrm{Pt}}\right| = 0.09$ eV [114]. In this chapter, the theoretical modeling of the HER on $Mo_2C$/Graphene -based electrodes is also addressed employing small cluster models adsorbed on N-doped graphene layers. Initially, the HER is studied on the $Mo_2C$ cluster models, motivated by previous experimental works where promising catalytic properties for the HER have been found in nanostructured systems made of $Mo_2C$ nanoparticles adsorbed on graphene layers [205,207]. Later, a second type of systems, based on the extended surface model, are considered.

Different structures have been proposed to study the $Mo_2C$ (001) surface covered with N-doped graphene layers. These models are aimed to uncover the synergy between $Mo_2C$ and N-doped graphene to improve the catalytic properties for the HER of very recently synthesized compounds [73]. In both cases a significant agreement with the experimental results is found as well as relevant predictions to enhance the HER activity of the recently synthesized material are done. The present chapter is organized as follows. In the Sec. 5.2, the general issues of the proposed reaction mechanisms as well as the methodology to compute the *ab-initio* energy of each structure are presented. In the Secs. 5.3 and 5.4, the description of the HER on different sets of model systems: $Mo_2C$ clusters adsorbed on N-doped graphene layers and the N-doped graphene layers deposited on top of the $Mo_2C$ (001) surface are presented. Comparisons with available experimental results and a number of predictions are discussed as well. Finally, a brief summary and concluding remarks are given, Sec. 5.6.

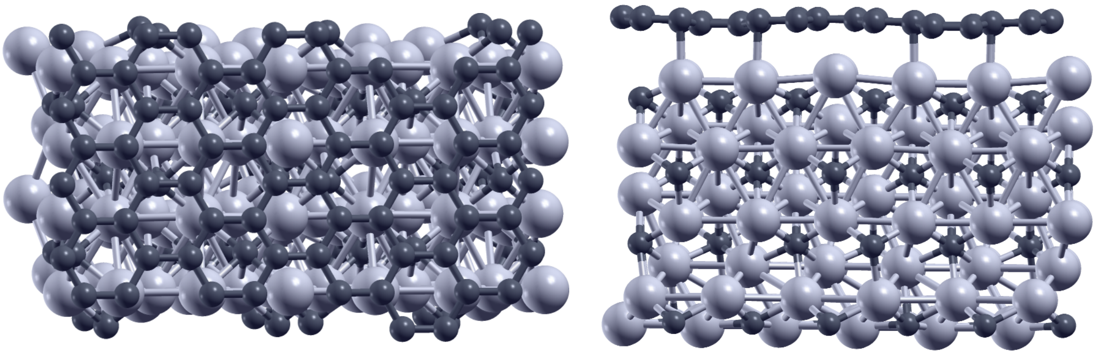
(a) (b)

**Figure. 5.2.** *Pure graphene layer adsorbed on $Mo_2C$ (001): G@$Mo_2C$.* ***a)*** *Top view: (001) crystallographic plane.* ***b)*** *Side view: (100) crystallographic plane. Dark and light gray represent carbon and molybdenum atoms, respectively.*

## 5.2 Methodology

Several model surfaces are studied in the present chapter to evaluate its catalytic properties towards the HER. The global reaction pathway can be represented as the three state effective mechanism:

$$H^+ + e^- \rightarrow \text{S-H} \rightarrow \frac{1}{2}H_2, \tag{5.1}$$

where S represents an adsorption site on the considered surface model. The free energy of hydrogen adsorption $\Delta G_H$ (i.e., the intermediate step in eq. (5.1)), computed within the framework of DFT, may be used to evaluate the electrocatalytic properties of each proposed structure, Sec. 2.5. Despite $\Delta G_H$ has been identified as a suitable descriptor to assess the HER at metal surfaces [70, 114], it has been successfully used in a wide variety of materials [59, 119].

The computation of $\Delta G_H$ is accomplished within its general definition related to the first reaction step in eq. (5.1):

$$\Delta G_H = \Delta E_H + \Delta E_{ZPE} - T\Delta S. \tag{5.2}$$

Here $\Delta E_H$ is the H-adsorption energy, $\Delta E_{ZPE}$ is the variation of the zero point energy along the firs step implicit in eq. (5.1) and $T\Delta S$ represents the entropic barrier related with the entropy losses due to the adsorption of the hydrogen atom.

The H-adsorption energy $\Delta E_H$ is defined within the expression [114]:

$$\Delta E_H = \frac{1}{n}\left(E(\mathrm{S}+n\mathrm{H}) - E(\mathrm{S}) - \frac{n}{2}E(\mathrm{H_2})\right), \tag{5.3}$$

where $n$ is the number of hydrogen atoms adsorbed on the surface S, and $E$ is the DFT energy of the structure represented inside its brackets. For example, $E(\mathrm{S}+n\mathrm{H})$ is the DFT energy of the surface model S which is hosting $n$ hydrogen atoms. In the present work $n$ is always set as one, this means that only one hydrogen atom per unit cell is considered. However, the consideration of higher values of $n$ becomes remarkable when the fractional coverage of the surface by the adsorbed atoms is an important point in the studied phenomena.

$\Delta E_{ZPE}$ has been calculated for the specific case of hydrogen adsorption on the Cu (111) metallic surface, and it has resulted a small contribution to $\Delta G_H$ (i.e., $\Delta E_{ZPE}[\mathrm{H/Cu(111)}] = 0.04$ eV) [208]. This value has been used as a reference number in the Nørskov's work for each of the studied surfaces [114]. Slightly different values of $\Delta E_{ZPE}$ have been found for the different models employed in this work. However, they are even smaller than $\Delta E_{ZPE}[\mathrm{H/Cu(111)}] = 0.04$ eV. The maximum value which have been obtained is $\Delta E_{ZPE} = 0.02$ eV, and it is considered as the contribution of the zero point energy correction for all the analyzed structures.

The last term in eq. (5.2): $T\Delta S$, is evaluated within the plausible consideration that the main contribution to the entropic barrier for the hydrogen adsorption is the loss of entropy related with the degrees of freedom of the $\mathrm{H}^+$ in the electrolyte $\Delta S_{H^+}$. Hence, $\Delta S_{H^+} = -\frac{1}{2}S^0_{\mathrm{H_2}}$ is assumed at standard conditions and $pH = 0$, where $S^0_{\mathrm{H_2}}$ $= 0.40$ eV is the standard entropy of $\mathrm{H_2}$ in the gas phase [114]. Therefore, $\Delta G_H$ may be directly related to $\Delta E_H$ at standard conditions ($T = 298.15$ K, $p = 1$ bar, $pH = 0$):

$$\Delta G_H = \Delta E_H + 0.22\text{ eV} + \Delta G(pH), \tag{5.4}$$

where $\Delta G_{pH}$ is an additional barrier which depends on the $pH$ of the electrolyte, and vanishes at $pH = 0$.

The $pH$ contribution to $\Delta G_H$ can be estimated as an additional entropic barrier, eq. (5.5), which arise from the Nernst's equation [209].

$$\Delta G(pH) = k_B T ln(10) \times pH. \tag{5.5}$$

This equation does not account for a microscopic description of the solvent but it is a thermodynamic estimation of the influence of the $H^+$ free energy change on the $pH$ of the electrolyte. This simple model for the $pH$ contribution to the $\Delta G_H$, can be easily calculated and yields a rough estimation of the $\Delta G_H$ response with respect to the acidity of the solution. The technical details related with the calculation of adsorption energies $\Delta E_H$ within the framework of DFT are presented in the following Sec. 5.2.1.

### 5.2.1 Computational details

Density functional theory calculations with periodic boundary conditions were performed using the program VASP (Vienna *Ab-Initio* Simulation Package) [210–213]. The electronic wave functions are expanded into plane waves up to an energy cutoff of 400 eV and the projector augmented wave (PAW) [214] scheme has been used to describe the interactions between the valence electrons and the nuclei (ions). The exchange-correlation interaction between electrons is treated within the generalized gradient approximation (GGA) as implemented by Perdew, Burke and Ernzerhof (PBE) [215].

The periodic systems have been modeled using a supercell for graphene, and $Mo_2C$ clusters adsorbed on graphene based surfaces of $9.872 \times 17.153 \times 14.00$ Å$^3$ Fig. 5.3. For the N-doped graphene layers deposited on the $Mo_2C$ (001) surface, a unit cell with the dimensions: $9.872 \times 17.153 \times 25.00$ Å$^3$ has been constructed. In both cases an orthorhombic structure is employed (i.e., the internal angles in the unit cell fulfill: $\alpha = \beta = \gamma = 90°$). Only one K-point, the Gamma point, is considered. Sufficient vacuum space is left inside both model supercells in the Z-direction (more than 10 Å) to reduce the effect of artificial image charges. The convergence threshold for the maximum force on each atom at geometry optimizations is set to be less than 0.01 eV/Å. The graphene model has been constructed within a rectangular supercell as it is shown in Fig. 5.3a. A four atoms unit cell with dimensions $2.468 \times 4.288 \times 14.00$ Å$^3$ is replicated $4 \times 4$ times in the XY plane to end up with the final $9.872 \times 17.153 \times 14.00$ Å$^3$ graphene supercell composed by 64 atoms. A similar method is employed to build up the $Mo_2C$ (001) surface model Fig. 5.3b. Starting by the accepted unit cell of orthorhombic $Mo_2C$ [206], with dimensions $4.732 \times 6.040 \times 5.210$ Å$^3$, a supercell made of a $2 \times 3$ replication of the initial structure in the XY plane is developed. Since there is a lattice mismatch between the $Mo_2C$ (001) and graphene, the $Mo_2C$ (001) structure has been shrunk in the a direction by approximately 4.1% and in the b direction by approximately 5.3%

to ensure exactly the same dimensions of the graphene model Fig. 5.3. Finally, the $Mo_2C$ (001) surface model is reproduced 2 times in the z direction and the graphene layer is deposited on the (001) crystalline plane. The model structure composed by the graphene layer deposited on the $Mo_2C$ (001) surface has 208 atoms. All of them have been let free for relaxation and a separation of 2.26 Å has been found between the graphene layer and the $Mo_2C$ (001) surface.

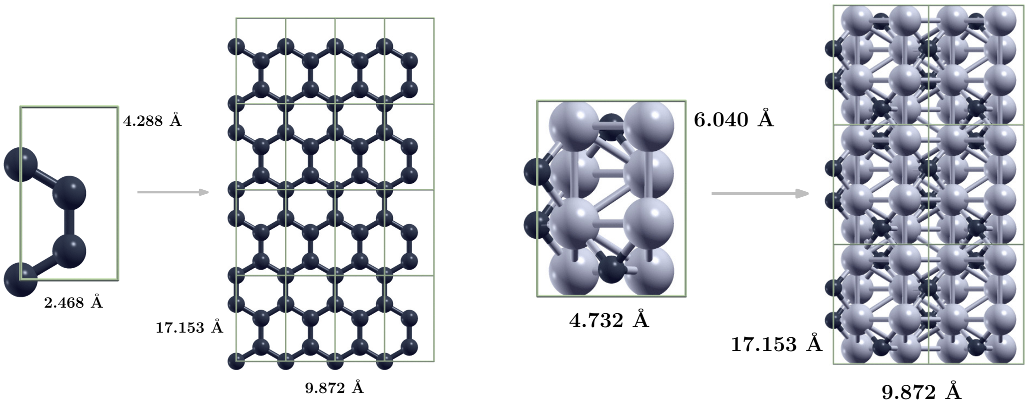

(a)

(b)

**Figure. 5.3.** *Schematic representation of the process to construct both:* ***a)*** *the graphene supercell and* ***b)*** *the $Mo_2C$ (001) surface model. The dimensions of the XY plane in both models are the same (i.e.,* $9.872 \times 17.153$ $Å^2$*), although the pictures look slightly different due to different scales. Carbon and molybdenum atoms are depicted in dark and light gray, respectively.*

## 5.3 $Mo_2C$ clusters and N-doped graphene layers

The water decomposition is considered here by focus on the HER on several model structures which combine $Mo_2C$ compounds with graphene surfaces. Molybdenum carbide compounds have been identified as potentially promising alternatives to precious metals for the enhancement of the HER activity in ECCs [205, 207, 216]. Bulk $Mo_2C$ is not very active as a cathode for the HER due to its slow electron transport properties [205]. However, nanostructured materials which combine the potential active sites on the molybdenum carbide compounds and the transport properties of graphene-like structures (i.e., carbon nanosheets, carbon nanotubes, etc.), have shown remarkable improvement for the hydrogen evolution at ECCs [205, 207, 216].

Three major model structures are considered for the evaluation of the HER activity: simplified $Mo_2C$ cluster models (i.e., $Mo_2C$ and $Mo_4C_2$) deposited on pure and nitrogen-doped graphene surfaces, and an extended surface model made of bulk $Mo_2C$ covered with a pure or a nitrogen-doped graphene layer. While the first two models are motivated by recently findings of high HER activity at the surfaces of novel materials [205,207,216], which contain $Mo_2C$ nanoparticles on top of graphene-like structures, the third one is a representation of the possible active sites at $Mo_2C$ nanoparticles covered by similar graphene-based layers, which have been synthesized in recent experiments [73].

In every case, the free energy of the adsorbed $H^+$ is used as a descriptor of the HER activity, while the contribution from the acidity of the environment is taking into account via the correction term $\Delta G(pH)$ introduced before, eq. (5.5).

### 5.3.1 HER at $Mo_2C$-bulk and N-doped graphene layers

A detailed description of the water splitting on pristine graphene and different $Mo_2C$ cluster models attached on nitrogen-doped graphene surfaces is addressed in the following. The outperform of the HER activity, when the active sites change from the graphene like structures to the $Mo_2C$ clusters adsorbed on top of them is described. A clear improvement in favor of the HER is observed when $Mo_2C$-based structures adsorb on clean graphene surfaces. Contrary to the previous chapters, the splitting of only one water molecule is investigated as precursor of hydrogen evolution following the Volmer's reaction mechanism in acidic conditions. A further correction, to assess the influence of the $H^+$ concentration in the free energy of the hydrogen adsorption, permits the discussion of the HER activity also in alkaline conditions.

The adsorption of water molecules at cathodic surfaces is not a spontaneous process at standard conditions. At present, the implicit decomposition of a water molecule is considered, while a $H^+$ is attached to the surface and the $OH^-$ group evolves to the electrolyte. The active sites on graphene surfaces or $Mo_2C$ clusters act as catalyst structures for the HER. For a wide variety of inorganic HER electrocatalysts, the H-adsorption Gibbs free energy is considered an important descriptor to assess the HER activity [114]. The optimum free energy change in the hydrogen adsorption process should be zero, which leads to a fast formation of adsorbed hydrogen and a rapid concomitant hydrogen release. In order to get profound insights into such an electrocatalytic HER performance, DFT calculations is employed to study the Gibbs free energies of the intermediates. A large negative free-energy indicates that chemical adsorption of hydrogen atoms on the surface is too strong, while a large positive free energy indicates a very weak H adsorption and easy product desorption. Both of them are unfavorable for HER (Sabatier's principle) [114].

In the present work, four typical nitrogen-doped sites at the graphene surface are considered. Thus, the following structures are employed to assess the HER activity: pure graphene (G), a single nitrogen site within a graphene layer (GN),

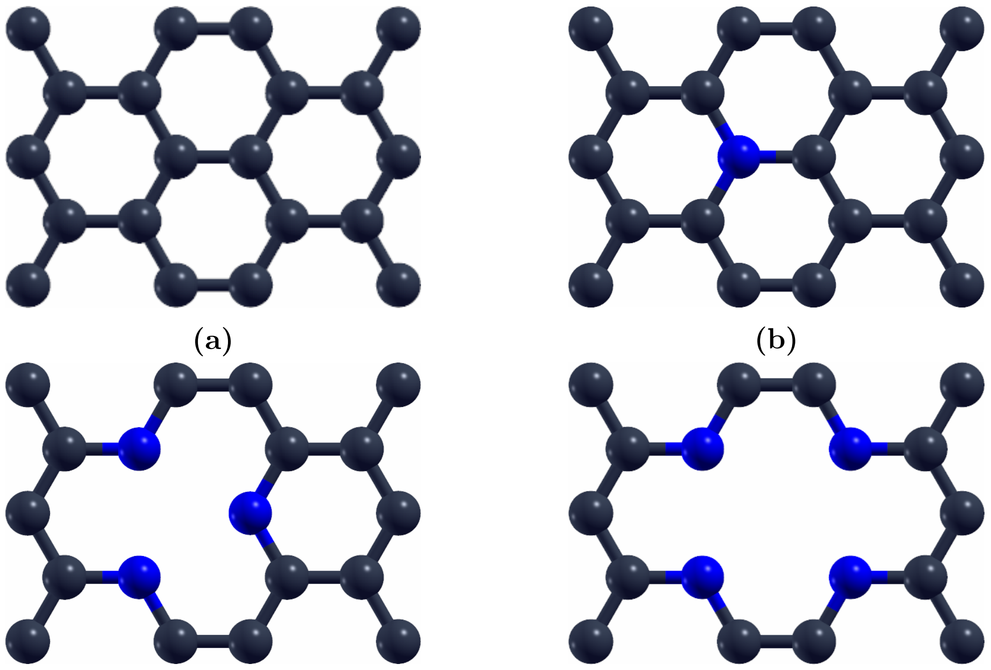

**(a)** **(b)** **(c)** **(d)**

**Figure. 5.4.** ***a)*** *Pure graphene structure (G).* ***b)*** *Nitrogen-doped graphene defect (GN).* ***c)*** *Three pyridinic atoms around a one vacancy defect (P3N).* ***d)*** *Four pyridinic atoms around a two vacancy defect (P2V4N). Carbon atoms are represented in dark gray while nitrogen ones in blue.*

three pyridinic atoms around one vacancy in the graphene structure (P3N), and four pyridinic atoms around two vacancies in the graphene structure (P2V4N), Fig. 5.4. The adsorption of a hydrogen atom on such surfaces is considered initially for comparison with subsequent calculations [216]. In pure graphene, the adsorption site may be any C atom at the surface. In the case of graphitic defects, the H-adsorption site is considered at the N-atom. In a previous theoretical work, it has been found that the hydrogen atom is very strong adsorbed on the first neighbors of the N-impurity. The literature results show an adsorption energy of H on the N-doped graphene structure as follow: - for H-N interaction a value of -0.80 eV has been found, while for the H-C interaction a value of -2.16 eV was obtained [217]. This result is sustained by the recent findings [217], in which charge doping reduces the $\pi$-bond strength in graphene and the energy required to break the $\pi$-bond, thus leading to the stability of the hydrogen atom attached on the carbon nearby the nitrogen site. Due to this fact, the carbon atom is not a suitable adsorption site for the hydrogen in order to promote the HER. The hydrogen atom will be considered to be adsorbed at the defected nitrogen sites in the remaining model surfaces.

According to our results, the H-adsorption on pristine graphene has an endothermic free-energy of 1.75 eV, Fig. 5.5. This high barrier represents an unfavorable hydrogen adsorption from the energetic point of view. The possibility to dope the graphene surface supports the enlargement of its potential utilization in technolog-

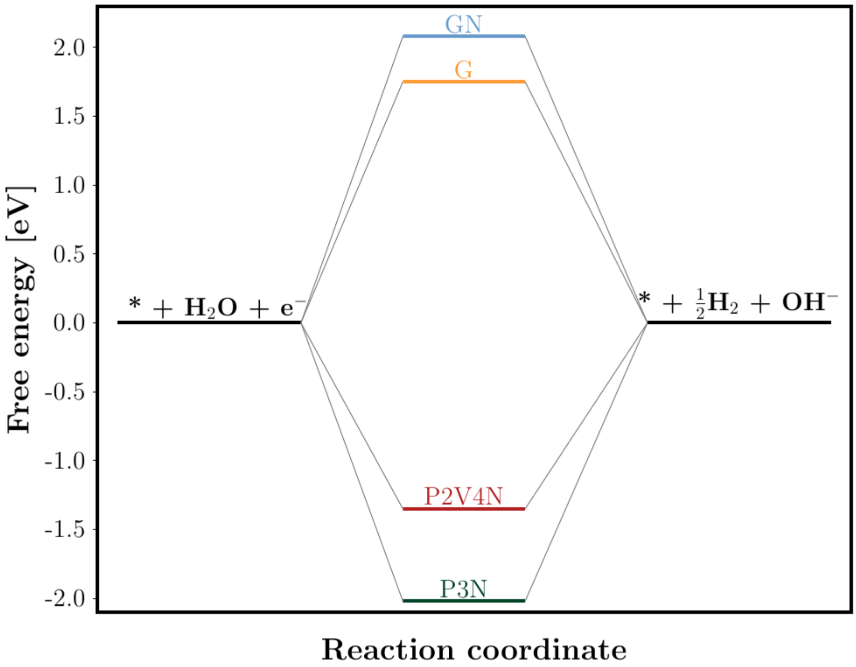

**Figure. 5.5.** *Free energy profile for the H-adsorption process at the model structures: G (orange), GN (blue), P3N (green) and P2V4N (red).*

ical applications. This reason has motivated big efforts, to prepare, characterized and understand doped graphene from both the theoretical and experimental point of view. For example, Boron and Nitrogen doped graphene have been found to exhibit semiconducting properties, p and n type, respectively. Additionally, they may be systematically tuned with the concentration of the doped material. The H-adsorption free energy have been computed in the present work, also for the graphene structure doped with N-atoms (graphitic), a value of 2.08 eV has been obtained, Fig. 5.5. The HER at the graphene and graphitic structures show that the reaction mechanism can barely proceed due to their high free energy barriers. The presence of vacancies has been considered here as well. The free energies of the H-adsorption on pyridinic nitrogen atoms around one or two vacancies, was calculated to be -2.02 eV and -1.35 eV, respectively, Fig. 5.5. This indicates low catalytic activities for the HER. The H-adsorption free energies for pyridinic with one and two vacancies, show that the hydrogen is too strong adsorbed on the structure, and a big amount of energy is required for removing the hydrogen from the structure and forming the $H_2$ molecule.

The $Mo_2C$ bulk material shows good HER activities [205], but the commercially available micron-sized $Mo_2C$ has been found to be unstable in presence of an electrolyte, being inadequate for practical applications. Several techniques may be used to achieve the stability of the catalyst, such as nanocrystallization or transition metal impregnation [205]. From a theoretical point of view, the free energy calculation of hydrogen adsorption on the $Mo_2C$ (001) surface is reported to be -0.82 eV [216]. This value shows a clear improvement of the HER activity compared with the graphene-like structures. Therefore, within the framework of the Nørskov's theory, it can be stated that $Mo_2C$ has better catalytic properties than pure graphene surfaces. This affirmation is in complete agreement with experimental observations. While bulk $Mo_2C$ shows an overpotential for the HER at 10 $mA \times cm^{-2}$ of 304 mV, a very low HER activity have been observed when pristine graphene is used as catalyst [205]. Additionally, a higher activity than for the $Mo_2C$-bulk is found for the case of molybdenum-carbide nanoparticles deposited on a graphene layer ($Mo_2C$-G), 150 mV has been observed as the overpotential for the HER at 10 $mA \times cm^{-2}$ [205]. Motivated by this observation, the next two sections are devoted to study the HER on $Mo_2C$ cluster models adsorbed on top of graphene surfaces.

### 5.3.2 HER at $Mo_2C$ adsorbed on N-doped graphene layers

The influence of $Mo_2C$ nanoparticles on the HER at the graphene-based substrates is investigated in the present section by means of simple cluster models. They consist on a $Mo_2C$ unit adsorbed on the structures presented in the previous section. This study is motivated by the striking high HER activity found on recently synthesized materials involving a distribution of $Mo_2C$ nanoparticles ($Mo_2C$-NPs) over graphene surfaces [205]. There, a very spread dispersion of 5.0 nm long $Mo_2C$-NPs on the sample has been reported [205].

The optimized model structures of the $Mo_2C$ adsorbed on the considered nitrogen-doped defects on graphene surfaces are shown in Fig. 5.6. The resulting structures are denoted as: $Mo_2C$@G, $Mo_2C$@GN, $Mo_2C$@P3N and $Mo_2C$@P2V4N, respectively, Fig. 5.6. In every case, the Mo atoms are adsorbed either in the middle of a benzene ring or in the location of a vacancy with a bond length d(Mo-Mo) laying between 2.18 and 2.24 Å. The distance between the Mo and the closest C in the graphene structure is around 2.32 Å, while its bond with the carbon atom of the cluster is 1.89 Å. The bonding distances between the Mo and nitrogen atoms are approximately 2.14 Å. These distances may be compared with the corresponding ones in the $Mo_2C$ bulk structure [218]. The bulk Mo-Mo distances vary from 2.91 to 3.02 Å, while the Mo-C interactions have their equilibrium distances between 2.0 and 2.17 Å. They both are larger than their peers in the cluster model, this reflects a stronger interaction between the atoms inside the $Mo_2C$ structure. Moreover, the shortest distance between Mo and C atoms on graphene is 0.15 Å higher than the bulk Mo-C distance. This fact shows a clear separation between the cluster structure and the graphene surface.

The HER activity on the proposed structures is evaluated by focus on the free

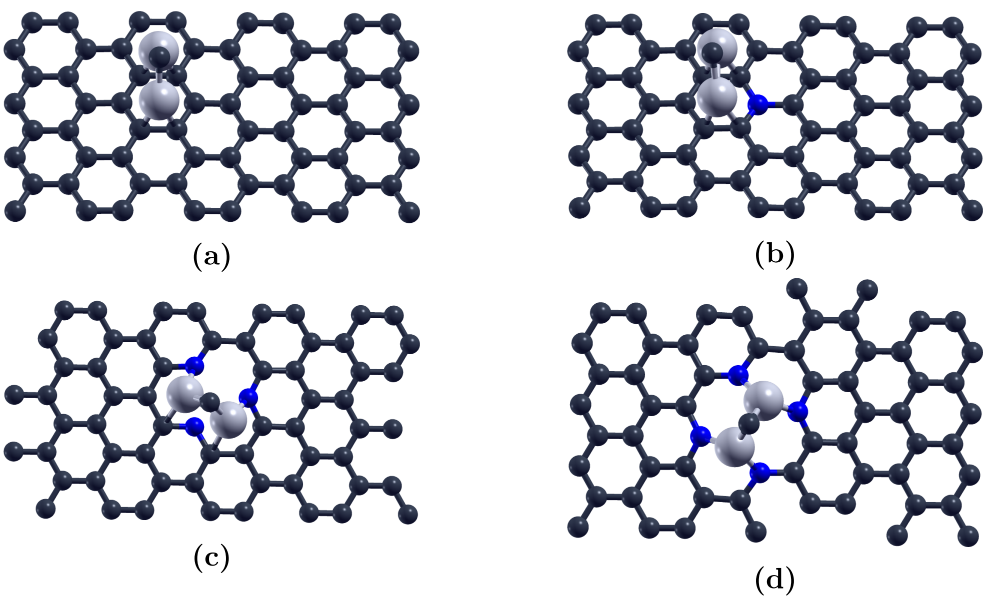

**Figure. 5.6.** *Schematic representation of* ***a)*** *$Mo_2C$ cluster adsorbed on pure graphene structure ($Mo_2C$@G).* ***b)*** *$Mo_2C$ cluster adsorbed on nitrogen-doped graphene defect ($Mo_2C$@GN).* ***c)*** *$Mo_2C$ cluster adsorbed on three pyridinic atoms around one vacancy defect on a graphene layer ($Mo_2C$@P3N).* ***d)*** *$Mo_2C$ cluster adsorbed on four pyridinic atoms around two vacancies defect on a graphene layer ($Mo_2C$@P2V4N). Carbon and molybdenum atoms are represented in dark and light gray, respectively, while nitrogens are displayed in blue.*

**Table. 5.1.** *Free energy barriers for the $H^+$ adsorption on the model compounds made of graphene-based surfaces hosting a $Mo_2C$ cluster adsorbed on top. The specified structures $Mo_2C$@G, $Mo_2C$@GN, $Mo_2C$@P3N and $Mo_2C$@P2V4N represent different adsorption models, Figs. C.1 and C.2 in App. C.*

| Catalyst | $\Delta G$ (eV) |
|---|---|
| $Mo_2C$@G | -0.17 |
| $Mo_2C$@GN | -0.80 |
| $Mo_2C$@P3N-1 | 0.81 |
| $Mo_2C$@P3N-2 | -0.05 |
| $Mo_2C$@P2V4N-1 | 1.44 |
| $Mo_2C$@P2V4N-2 | -0.36 |
| $Mo_2C$@P2V4N-3 | 0.30 |
| $Mo_2C$@P2V4N-4 | 1.15 |

energy change of the hydrogen adsorption at the different active sites. Several models for the adsorption of the $Mo_2C$ on the graphene-like surfaces have been considered. $Mo_2C$@G and $Mo_2C$@GN are represented by only one model system, while two or more structures have been constructed for $Mo_2C$@P3N and $Mo_2C$@P2V4N. Hence, the hydrogen adsorption is studied in all of them, while the molybdenum and nitrogen active sites are considered. The geometric configurations of the adsorbed hydrogen atom on every considered surface can be found in the App. C, Figs. C.1 and C.2. The free energy change for the hydrogen adsorption on every of the proposed active sites are shown in the Table 5.1. The same quantity is shown in a graphic representation at Fig. 5.7. The presence of $Mo_2C$ on top of the graphene structures influences significantly in the reduction of the H-adsorption free energies.

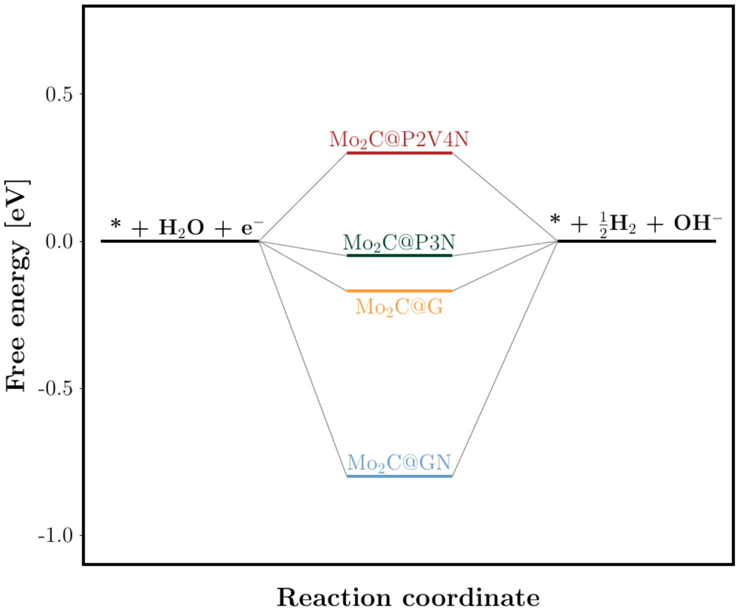

**Figure. 5.7.** *Free energy profile for the H-adsorption process at the following model structures: $Mo_2C$@G (orange), $Mo_2C$@GN (blue), $Mo_2C$@P3N (green) and $Mo_2C$@P2V4N (red).*

In the cases of $Mo_2C$@G active site (-0.17 eV) and $Mo_2C$@GN (-0.80 eV), the free energy values are substantially lower (absolute value) than the estimated free-energies for the suspended graphene (1.75 eV) and graphitic (2.06 eV) structures.

Different structure representations for $Mo_2C$@P3N have been constructed, Figs. C.1c and d. On the P3N structure there exist different adsorption sites where the $Mo_2C$ cluster can be located. The final geometry adopted by the adsorbed cluster on top of the graphene-like surface is closely related with the HER activity of the resulting compound. From many different positions where the $Mo_2C$ cluster can be placed on the P3N surface, in particular two of them are discussed below. In both cases the $Mo_2C$ cluster is adsorbed between two nitrogens and two carbons from the surface. In the former one, a molybdenum from the $Mo_2C$ is bonded with two carbon atoms while the second Mo is bonded with two nitrogen atoms. In this configuration a strong bond interaction between Mo and C has been measured. The Mo-C distance (2.15 Å) is in the same range than the ones reported in the $Mo_2C$ bulk structure [218]. In the second case, each molybdenum is connected with one carbon and one nitrogen. The first structure is almost as stable as the second one, its total energy is 0.23 eV lower than the second one. Nevertheless, different HER activities have been obtained for the two cases. In the first one ($Mo_2C$@P3N-1), a free energy change for the hydrogen adsorption of 0.81 eV has been estimated, while for the $Mo_2C$@P3N-2 model a value of -0.05 eV has been obtained. This remarkable difference can be explained by the description of the bonding situation of the hydrogen adsorption site. The hydrogen atom is adsorbed in both cases on one nitrogen from the P3N structure. In $Mo_2C$@P3N-1, Fig. C.1c, the strong bond interaction between the Mo and the carbon atoms weaken the carbon-nitrogen bond leading to a reinforcement of the H adsorption on the nitrogen atom. In $Mo_2C$@P3N-2, Fig. C.1d, the adsorption of the $Mo_2C$ does not make a strong influence on the nitrogen active site for the hydrogen adsorption. However, the charge transfer from the $Mo_2C$ towards the P3N surface, stabilizes the whole system leading to the reduction of the HER activity from -2.02 eV for P3N to a value of -0.05 for $Mo_2C$@P3N.

For the $Mo_2C$@P2V4N active sites, the model with smallest free energy in absolute value is considered the most reliable representation. The free-energy barrier for $Mo_2C$@P2V4N heterostructure was calculated to be 0.28 eV. It presents also a very favorable situation for the adsorption of hydrogen and the formation of $H_2$. The $Mo_2C$@P3N model has resulted to be the most favorable one for the HER. One of the nitrogen atoms presented in the structure has been selected as the active site for this representation, Fig. C.1d in App. C.

The absolute value of the H-adsorption free energies are clearly smaller than the ones obtained for pure graphene, $Mo_2C$-bulk or nitrogen-doped surfaces, Fig. 5.5. They confirm the reliability of the present cluster model to reproduce the outperforming of electrodes where a distribution of $Mo_2C$ nanoparticles stand over a graphene layer with respect to graphene and $Mo_2C$-bulk independently. Additionally, they predict an improving effect of the nitrogen-doped graphene surface to be used as a substrate for the $Mo_2C$ nanoparticles. In general the proposed $Mo_2C$-Graphene type of structures show a clear improvement compared with the pristine graphene type of structures. In the next section, a bigger cluster model is considered. There, two $Mo_2C$ units are employed to construct a $Mo_4C_2$ structure as a representation of the nanoparticle deposited on top of the graphene-like surfaces.

### 5.3.3 HER at $Mo_4C_2$ adsorbed on N-doped graphene layers

In this section, a second cluster model is considered to represent the $Mo_2C$ nanoparticles. The influence of considering a bigger cluster, for the HER activity, is addressed here within the natural extension of the monomer $Mo_2C$ to the dimeric representation $Mo_4C_2$. The initial geometry is chosen as the most stable structure among several proposals, which were assessed in a previous work [219]. The $Mo_4C_2$ cluster is conformed by a tetrahedral arrangement of the four Mo atoms. Here, the two carbons are located on top of different faces of the Mo-tetrahedral. The average bond length are the following: d(C-Mo) = 2.02 Å and d(Mo-Mo) = 2.59 Å [219]. The Mo-Mo distance in the cluster is smaller than the $Mo_2C$-bulk bond length, which lay between (2.91 - 3.02 Å). The C-Mo bonds are not significantly modified with respect to the $Mo_2C$-bulk ones (2.02 - 2.17 Å). The adsorption of $Mo_4C_2$ on the representative nitrogen-doped graphene surfaces, which are considered in the present work (i.e., G, GN, P3N and P2V4N) are shown in the Fig. 5.8. They will be denoted hereafter as: $Mo_4C_2$@G, $Mo_4C_2$@GN, $Mo_4C_2$@P3N and $Mo_4C_2$@P2V4N, Figs. 5.8 a, b, c and d, respectively.

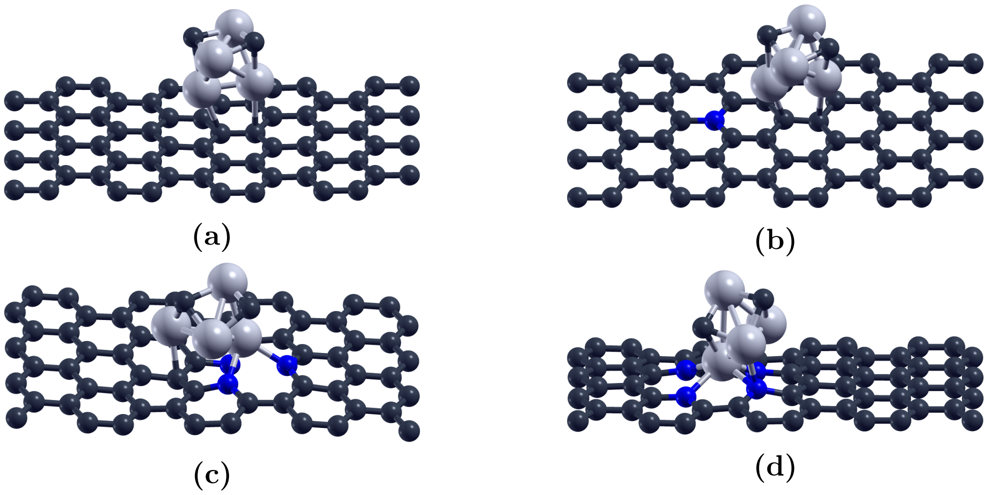

**Figure. 5.8.** *Schematic representation of $Mo_4C_2$ clusters adsorbed on nitrogen-doped graphene type structures:* ***a)*** *$Mo_4C_2$@G,* ***b)*** *$Mo_4C_2$@GN,* ***c)*** *$Mo_4C_2$@P3N and* ***d)*** *$Mo_4C_2$@P2V4N.*

In the first two models: $Mo_4C_2$@G and $Mo_4C_2$@GN, Figs. 5.8 a and b, the $Mo_4C_2$ is adsorbed on the graphene-like surface via two C-Mo bonds d(C-Mo) = 2.40 Å and 2.36 Å, respectively. The difference between these distances, which is only 0.04 Å, lays within the error bar of the present calculations and are considered equals. Indeed, the remaining characteristic bond lengths for the two model systems discussed here are very similar between them. There are not significantly differences between the two substrates (i.e., G and GN) for the $Mo_4C_2$ adsorption. In both cases, when the cluster is adsorbed on the surface, there are only small shifts on the bond lengths, the bottom most Mo couple decreases its separation distance until 2.22 Å while the distances between the Mo atoms of this pair and the closest carbons on the cluster increase up to 2.24 Å. These changes are nothing but the result of the rearrangement of electronic charges in the cluster after the interaction with the carbon atoms of the graphene-like structures.

The adsorption of $Mo_4C_2$ on top of the nitrogen-based impurities, P3N and P2V4N, is presented in Fig. 5.8: panels c and d. In both cases the most stable $Mo_4C_2$ adsorption site is located above the vacancy. The interaction between the cluster model and the adsorption site is done via the Mo-N connection. The excess electron of the nitrogen atoms enhances the coulomb interaction among the Mo metal atoms and the nitrogens in the surfaces. The Mo-N bond length in $Mo_4C_2$@P3N is around

2.10 Å, which is very close to the distances measured for the compound $Mo_2(NMe_2)_6$, where Me stands for Methyl: d(Mo-N) = 1.97 - 2.00 Å [220]. The Mo atoms, in both systems (i.e., $Mo_4C_2$@P3N and $Mo_2(NMe_2)_6$), have been found to be connected with three nitrogen atoms. The characteristic bond lengths of $Mo_4C_2$@P2V4N are comparable with the ones reported for $Mo_4C_2$@P3N above. The only difference is that, at present, the molybdenum is connected with four N atoms, d(Mo-N) = 2.10 - 2.23 Å.

The HER activity of the model configurations for the $Mo_4C_2$ cluster adsorbed on the nitrogen-doped graphene surfaces Fig. 5.8, is addressed here by the proposal of different hydrogen adsorption sites on top of the $Mo_4C_2$@G-based arrangements. The different H-adsorption possibilities considered in this section are shown in the App. D: Figs. D.1, D.2 and D.3. The free energy results for the proposed systems are presented in Table 5.2 and a schematic representation of the most significant active sites are shown in Fig. 5.9.

Table 5.2 shows that the same free energy value -0.55 eV, is obtained for both systems $Mo_4C_2$@G and $Mo_4C_2$@GN-1. The reason is that in both of them the hydrogen atom is adsorbed at the same Mo site on the cluster structure. Regarding the $Mo_4C_2$@GN-1 structure, the cluster system is adsorbed far away from the nitrogen site and its presence as an active site in the surface has no influence on the free energy variation for the H-adsorption. In the second structure for the graphitic system: $Mo_4C_2$@GN-2, the hydrogen atom is adsorbed at the nitrogen site. The free energy barrier is almost the same as the one obtained for the pure graphitic structure (GN): 2.08 eV, Sec. 5.3.1. This is due to the fact that $Mo_4C_2$ does not affect the H-adsorption on the N-site.

Forward, when the cluster $Mo_4C_2$ is adsorbed on the P3N model system, two H-adsorption sites are explored:

i) when the hydrogen is adsorbed on the Mo-atom ($Mo_4C_2$@P3N-1), with a free energy of -1.61 eV,

ii) when the hydrogen is adsorbed on the N-site at the $Mo_4C_2$@P3N-2, with a free energy of 0.97 eV.

The nitrogen site of the P3N impurity looks to be the most favorable one from the free energy point of view. This is also the case for the previous systems ($Mo_2C$@G-based structures) Sec. 5.3.2. For both cluster models (i.e., $Mo_2C$@P3N-2 and $Mo_4C_2$@P3N-2) the free energy values are significantly lower than the Mo-site model (i.e., $Mo_2C$@P3N-1 and $Mo_4C_2$@P3N-1). However, a remarkable difference between both of them is observed (i.e., $\Delta G_H$($Mo_2C$@P3N-2) = -0.05 eV and $\Delta G_H$($Mo_4C_2$@P3N-2) = 0.97 eV). This difference is due to the fact that, the hydrogen adsorption on the $Mo_4C_2$ leads to significantly geometrical changes of the cluster system on top of the surface, Fig. D.2 in App. D, while the first one ($Mo_2C$) remains very stable from the geometrical point of view upon the hydrogen

**Table. 5.2.** *Free energy barriers for the $H^+$ adsorption on the model compounds made of graphene-based surfaces hosting a $Mo_4C_2$ cluster on top. The specified structures -1, -2, -3 and -4 represent different adsorption models, Figs. D.1, D.2 and D.3 in App. D.*

| Catalyst | $\Delta G$ (eV) |
|---|---|
| $Mo_4C_2$@G | -0.55 |
| $Mo_4C_2$@GN-1 | -0.55 |
| $Mo_4C_2$@GN-2 | 1.94 |
| $Mo_4C_2$@P3N-1 | -1.61 |
| $Mo_4C_2$@P3N-2 | 0.97 |
| $Mo_4C_2$@P2V4N-1 | -0.85 |
| $Mo_4C_2$@P2V4N-2 | 1.40 |
| $Mo_4C_2$@P2V4N-3 | 0.34 |
| $Mo_4C_2$@P2V4N-4 | -1.61 |

adsorption.

The remaining systems ($Mo_4C_2$@P2V4N, from -1 to -4) are aimed to study the capability of the two vacancy impurities with four pyridinic atoms on the graphene structure, to steer the HER. Different configurations of the cluster model adsorbed on the defected graphene surface are shown in Fig. D.3 in App. D. In the Table 5.2 the smallest free energy value for the H-adsorption corresponds to one of the proposed models when four pyridinic atoms around a two vacancies defect are considered (P2V4N). For the system $Mo_4C_2$@P2V4N-3, a small free energy value of 0.34 eV has been obtained as a promising result for hydrogen evolution reaction mechanism. This result is also in good agreement with the free energy value of 0.28 eV obtained for the $Mo_2C$@P2V4N-3 system.

Within the system $Mo_4C_2$@P2V4N-3, the hydrogen adsorption site is considered to be in a nitrogen atom. The model structures $Mo_4C_2$@P2V4N-2 and $Mo_4C_2$@P2V4N-4 employed a N-site for the H-adsorption as well. However, the bonding situations relative to the N-sites are either saturated or unsaturated, leading to a higher or a lower barrier for the H-adsorption, respectively. So far, only nitrogen sites have been considered to estimate the H-adsorption free energy at the proposed models. Further, for the structure $Mo_4C_2$@P2V4N-1, the hydrogen is adsorbed on a second active site, which is located at the Mo atom. From the values obtained within the present calculations, the Mo-site has a free energy barrier of -0.85 eV. This value is similar to what has been obtained in previous calculations for the $Mo_2C$ (001) surface, Sec. 5.3.1. It shows that the Mo-H interaction is the most relevant argument for the HER activity in Mo-based compounds, while the substrate is not influencing the final results. Additionally, this barrier is still lower than the ones obtained from clean graphene-based surfaces. The strong attraction between the hydrogen and the N-atoms at the P2V3N structure makes its barrier lower than the same quantity on $Mo_4C_2$@P2V4N-3.

In a graphical representation, the lower free energy barriers in absolute value for the different proposed structures are plotted in the Fig. 5.9. Four different systems are considered: $Mo_4C_2$ adsorbed on the aforementioned graphene-like structures: G, GN, P3N and P2V4N. Two of them have negative barrier ($Mo_4C_2$@G and $Mo_4C_2$@GN) and the others two have positive values ($Mo_4C_2$@P3N and $Mo_4C_2$@P2V4N). The negative values correspond with H-adsorption on the Mo-metal site, while the positive ones correspond to the N-active sites. The best potential catalyst for the HER, from the free energy point of view, has been found to be the system $Mo_4C_2$@P2V4N-3. This system is the most promising one resembling $Mo_2C$-NP adsorbed on a nitrogen-doped graphene layer.

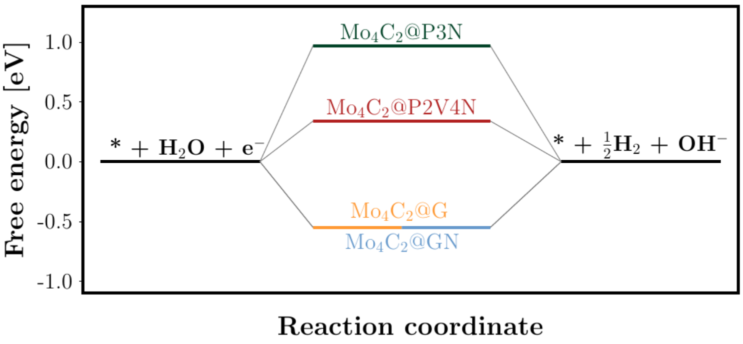

**Figure. 5.9.** *Free energy profile for the H-adsorption process at the following model structures: $Mo_4C_2$@G (orange), $Mo_4C_2$@GN (blue), $Mo_4C_2$@P3N (green) and $Mo_4C_2$@P2V4N (red).*

In general terms, the performance of the largest cluster ($Mo_4C_2$, Fig. 5.9), is similar to the former one ($Mo_2C$, Fig. 5.7). Four model structures are presented here: G, GN, P3N and P2V4N. The two cluster models are adsorbed on top of the nitrogen-doped graphene surfaces. The free energy values for the H-adsorption lay, in both cases, between 1.0 and -1.0 eV. Additionally, both model systems represent an actual improvement toward the HER activity with respect to both: the clean graphene-like surfaces and the clean $Mo_2C$ (001) surface. The minimum barrier, which has been found in these previous models based on pure and N-doped graphene layers, is 1.35 eV (absolute value). Furthermore, several trends which characterize the behavior of the proposed active sites for the HER are uncovered. For instance, due to the strong attraction among the Mo-metal and the hydrogen atom, the free energy change for the hydrogen adsorption on a Mo-site is always negative, while the same quantity for the N-site may be positive or negative depending on the bonding situation of the nitrogen atom in each system.

## 5.4 HER at N-doped graphene deposited on the $Mo_2C$ (001) surface

The previous sections have been devoted to describe the HER at nanostructured surfaces made of $Mo_2C$-based nanoparticles deposited on pure and nitrogen-doped graphene surfaces. Our theoretical results show the same trend as the experimental observations [205]. Motivated by recently experimental results [73], which show an ultra-high activity for the HER on molybdenum carbide anchored on nitrogen-doped porous carbon nanosheets ($Mo_2C$@2D-NPC), new simulations have been performed to support and understand, from a microscopic point of view, the experimental findings.

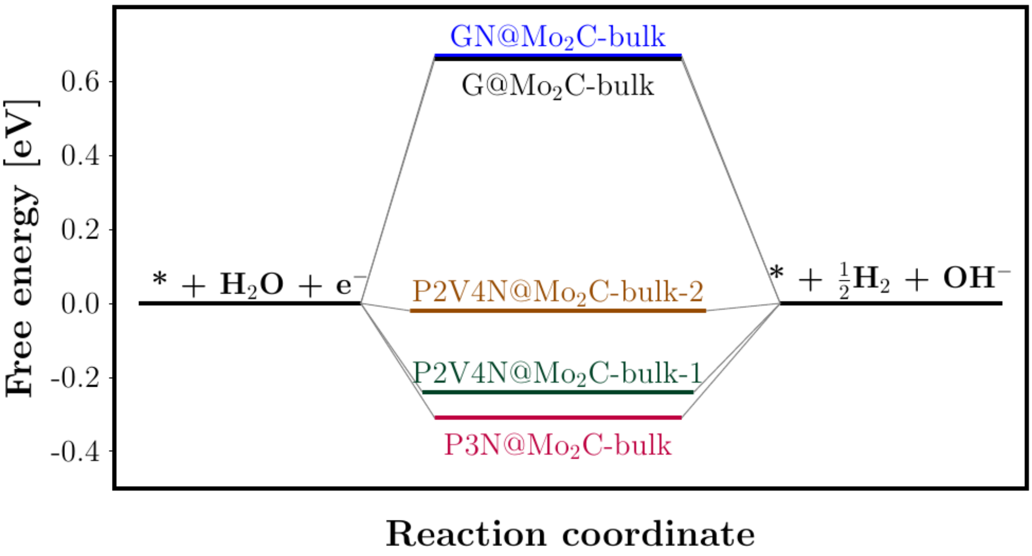

**Figure. 5.10.** *Free energy profile for the H-adsorption process at the following model structures: GN@*$Mo_2C$*-bulk (blue), G@*$Mo_2C$*-bulk (black), P3N@*$Mo_2C$*-bulk (purple), P2V4N@*$Mo_2C$*-bulk-1 (green), P2V4N@*$Mo_2C$*-bulk-2 (brown).*

Following the Nørskov's theoretical methodology, Sec. 5.2, the HER mechanisms on the interface of the proposed surface structure models, App. E, are investigated. To be in accordance with the previous results, the hydrogen atom will be adsorbed at N-sites of the new model surfaces. These sites have been already shown to be the most favorable ones to obtain lower free energy barriers. A pure graphene layer deposited on $Mo_2C$ (001) surface is considered for completeness. The evolution of the free energy along the reaction coordinate, for the four considered systems, is represented in a qualitative scheme in Fig. 5.10. The HER mechanism in alkaline media can be described by the following two steps: (1) electrochemical water dissociation (Volmer-step) and (2) subsequent recombination of two hydrogen atoms adsorbed at the surface S-H into molecular $H_2$, whereas $OH^-$ is released to the solution. An ideal catalysts for the HER should satisfy the following requirement

$\Delta G_H = 0$, which implies a fast proton-electron transfer step and a fast hydrogen release process as well, Sec. 2.5.

For the four G@$Mo_2C$-bulk like systems, $\Delta G_H$ is calculated as $\Delta E_H + 0.22$ eV. The value of 0.22 eV corresponds to the entropic contribution of the $H_2$ molecule at standard conditions (0.20 eV) plus the zero point energy contribution $\Delta E_{ZPE} = 0.02$ eV, as it is described above Sec. 5.2. The H-adsorption energy $\Delta E_H$, the free energy of adsorbed hydrogen $\Delta G$ and the geometric position of the adsorption sites are summarized in Table 5.3.

**Table. 5.3.** *Energy of adsorption, free energy barrier, and adsorption site for the HER on the model compounds made of graphene type layers deposited on the $Mo_2C$ (001) surface. The specified structures -1, -2, and -3 represent the adsorption sites A, B and C, respectively, Figs. E.1 and E.2 in App. E.*

| Catalyst | $\Delta E$ (eV) | $\Delta G$ (eV) | Ads. Site |
|---|---|---|---|
| G@$Mo_2C$-bulk | 0.44 | 0.66 | C |
| GN@$Mo_2C$-bulk-1 | 0.82 | 1.04 | N-Site A |
| GN@$Mo_2C$-bulk-2 | 0.45 | 0.67 | N-Site B |
| GN@$Mo_2C$-bulk-3 | 0.87 | 1.09 | N-Site C |
| P3N@$Mo_2C$-bulk-1 | 0.38 | 0.60 | N-Site A |
| P3N@$Mo_2C$-bulk-2 | -0.53 | -0.31 | N-Site B |
| P3N@$Mo_2C$-bulk-3 | -1.14 | -0.92 | N-Site C |
| P2V4N@$Mo_2C$-bulk-1 | -0.46 | -0.24 | N-Site A |
| P2V4N@$Mo_2C$-bulk-2 | -0.24 | -0.02 | N-Site B |
| P2V4N@$Mo_2C$-bulk-3 | -0.80 | -0.58 | N-Site C |

The deposition of graphene like structures on top of the $Mo_2C$ (001) surface favors the reduction of the free-energy barrier for the HER mechanism. Remarkably, the free-energy barriers for G@$Mo_2C$-bulk (0.66 eV) and GN@$Mo_2C$-bulk (0.67 eV) are substantially lower than the free-energy barriers for the suspended graphene (1.75 eV) and graphitic (2.08 eV), while they keep been lower than the corresponding one for clean $Mo_2C$ (001) surface (0.82 eV). Moreover, the free-energy barriers for P3N@$Mo_2C$-bulk and P2V4N@$Mo_2C$-bulk heterostructures were calculated to be -0.31 and -0.02 eV, respectively, presenting a favorable pathway for the formation of S-H on the surface and the hydrogen evolution. Among four catalysts studied, P2V4N@$Mo_2C$-bulk shows the smallest $\Delta G_H$ value of -0.02 eV, which is a clear indication of its best electrocatalytic activity from the thermochemical point of view.

Different possible H-adsorption sites are shown in Table 5.3, and in Fig. 5.11 for the GN@$Mo_2C$-bulk based systems. They are denoted as N-Site A, B and C. In the N-Site A Fig. 5.11a, the nitrogen atom is located on top of a molybdenum from the substrate, d(N-Mo) = 2.26 Å. The N-Site B Fig. 5.11b, is identified by the nitrogen impurity in the middle of two Mo atoms within longer separation distances than in the N-Site A configuration, d(N-Mo) = 3.0 Å. In the third N-defect type considered here: N-Site C Fig. 5.11c, the nitrogen atom is located also between two molybdenum atoms from the substrate but, contrary to the N-Site B, one of the Mo is significantly further away than the other one, d(N-Mo(1)) = 4.31 Å vs d(N-Mo(2)) = 2.80 Å. The same notations (i.e., N-Site A, B and C) have been used for the remaining systems as well. In the P3N@$Mo_2C$-bulk model, the N-Site A, B and C represent the same structures than in GN@$Mo_2C$-bulk within two modifications Fig. E.1 in App. E:

i) the nitrogen atom in the corresponding GN@$Mo_2C$-bulk based system is removed to create a vacancy in the surface structure,

ii) the three closest carbon atoms around the created vacancy are replaced by nitrogen ones.

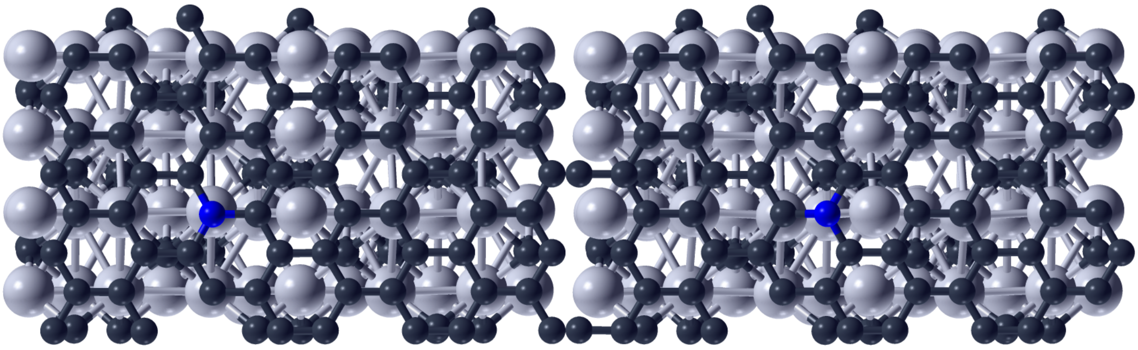

**(a)** N-Site A **(b)** N-Site B

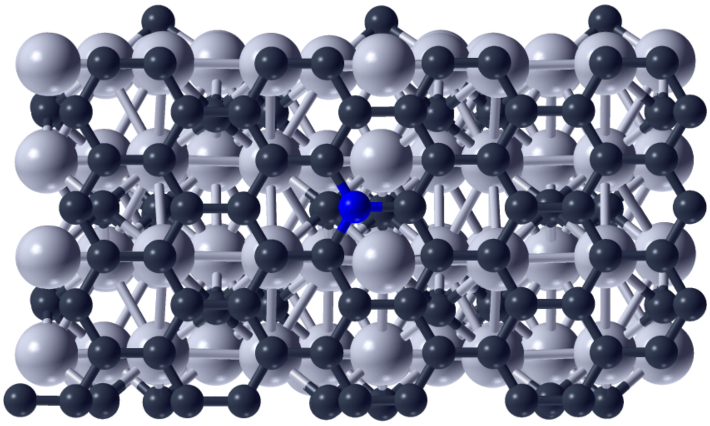

**(c)** N-Site C

**Figure. 5.11.** *Top view of the three adsorption sites considered in the surface type GN@$Mo_2C$-bulk. The nitrogen is represented in blue, while the molybdenum and carbon atoms from $Mo_2C$ and graphene are represented in light and dark gray, respectively.*

In the case of P2V4N@$Mo_2C$-bulk structures, the N-Site A, B and C are made from the GN@$Mo_2C$-bulk ones in a similar way Fig. E.2 in App. E. There, a double vacancy is located first in the graphene-like structure and the four closest carbon atoms are replaced by nitrogen ones. In all proposed models for nitrogen-doped defects the Site-B structure is identified as the most promising one for the HER activity, Table 5.3. In addition, a defect type A for the system P2V4N@$Mo_2$C-bulk shows also a very good free energy barrier for the HER, $\Delta G_H$ = -0.26 eV.

The chemical coupling between the $Mo_2C$ (001) surface and the graphene layer results into the formation of a new structure with a mediated adsorption-desorption behavior, $\Delta G_H \rightarrow 0$, facilitating the overall HER kinetics, as shown in Fig. 5.10. Such characteristic, originated from the unique structure of the new material, allows a suitable H-bonding with the nitrogen defects on the surfaces.

The experimental results indicate that the HER at the cited novel materials [73], occurs through a Volmer-Heyrovsky mechanism, and electrochemical recombination with an additional proton is the rate-limiting step. The unanticipated outstanding HER performance in alkaline media of the as-prepared 2D hybrid can be attributed to the unique 2D nanostructure, high nitrogen doping content, abundance of active sites, and strong interaction between $Mo_2C$ and the carbon matrix. Overall, theoretical results accord well with the experiments which found a low onset potential of approximately 0 mV and a current density of 10 $\mathrm{mA}\times\mathrm{cm}^{-2}$ at an overpotential of approximately 45 mV, which is much lower than the values of most reported HER electrocatalysts and comparable to the noble metal catalyst Pt [73]. Specifically, the observed overpotential (i.e., 45 mV) is significantly lower than a recently reported value when $Mo_2C$ nanoparticles adsorbed on graphene layers are used as electrocatalysts (150 mV) [205]. From the comparison between the best result for a nitrogen-doped graphene layer deposited on $Mo_2C$ (001) surface structure (i.e., $\Delta G$ = -0.02 eV in P2V4N@$Mo_2$C-bulk-2) and the previous models for the $Mo_2C$ nanoparticle adsorbed on clean graphene structure (i.e., $\Delta G$ = -0.17 eV for $Mo_2C$@G and $\Delta G$ = -0.55 for $Mo_4C_2$@G), it can be realized that the present model surfaces are able to reproduce the experimental trend for the HER activity within the framework of the Nørskov's theoretical methodology. In addition, it is predicted that, in order to enhance the HER activity of the $Mo_2C$ nanoparticles adsorbed on a clean graphene surface, the employment of nitrogen-doped graphene surfaces seems to be a significant improvement.

The electrocatalytic HER activity of the as-prepared $Mo_2C$@2D-NPC is attributed to the synergistic effects between $Mo_2C$ and pyridinic N-doping, which largely accelerate the sluggish HER kinetics in alkaline environments. All of these reveal the electrocatalytic properties of a new material which promotes the proton adsorption and the kinetic of $H_2$ recombination.

## 5.5 *pH* dependence of the HER activity

The *pH* dependence of the HER activity, within the framework of the thermochemical approach described above, is presented in this section. The proton exchange between the surface of the electrode and the electrolyte is a determining aspect in the HERs. Within the framework of the Nørskov's methodology, the free energy barrier for the H-adsorption on the electrocatalytic surface constitutes a suitable descriptor to explore new catalysts for the HER, Sec. 2.5. The entropy of the hydrogen cations in the electrolyte is directly related with the $pH$ of the solution. Assuming that all their configurational entropy is lost when they bind to an adsorption site, an entropic barrier, eq. (5.6), will affect the H-adsorption free energy.

$$\Delta G_{pH} = k_B T \ln(10) \times pH. \tag{5.6}$$

The effect of the $pH$ is addressed in the following by the correction of the H-adsorption free energies at $pH = 0$, presented in the previous model systems, with the corresponding entropic barrier due to the finite $pH$, eq. (5.6):

$$\Delta G_H = \Delta G_H^0 + k_B T \ln(10) \times pH. \tag{5.7}$$

Here $\Delta G_H^0$ is the adsorption free energy change at $pH = 0$, which has been computed above for the series of model structures considered in this work.

The eq. (5.7) is linear with respect to the $pH$ and its slope $k_B T \ln(10) = 5.92 \times 10^{-2}$ eV at 298.15 K. The $pH$ contribution to the H-adsorption free energy is 0.83 eV in the whole interval of typical $pH$ values (i.e., from 0 to 14). This value has the same order of magnitude as typical HER barriers. For example, 0.78 eV has been reported as a result of the HER on specific active-sites at 2D-$MoS_2$ nanosheets [221]. Therefore, the activity of certain surface may be tuned by varying the acidity of the electrolyte.

The free energy barriers for hydrogen adsorption at different $pH$ of the electrolyte, for the four series of models taken into account in the present work as possible catalysts towards the HER, are shown in Fig. 5.12. The typical $pH$ interval from 0 to 14 has been considered to evaluate the free energy barriers. A chosen favorable area (gray area, Fig. 5.12), ranging from -0.2 eV to 0.2 eV for all the $pH$ interval, shows the region where the structure may be considered a good catalyst within the framework of the Nørskov's theory, Sec. 2.5. The straight lines in all the schemes show the linear behavior of the $\Delta G$ with respect to the $pH$, eq. (5.7). All the lines have the same slope ($5.92 \times 10^{-2}$ eV) but they differ in their initial H-adsorption free energies ($\Delta G_H^0$).

The variation of $\Delta G_H$ with respect to the $pH$ for the pure and N-doped graphene-based electrodes, as well as for the $Mo_2C$-bulk within the eq. (5.7) is shown in Fig. 5.12a. None of the graphene type structures fulfill the criteria to be considered as a potential catalyst for the HER, their H-adsorption free energy values are far away from the desired interval (-0.2 eV, 0.2 eV) along the entire $pH$ range. This result agrees with the previous ones obtained for the case of $pH = 0$ (acidic conditions), Sec. 5.3.1. In the case of $Mo_2C$-bulk, where the reference value for

$\Delta G_H^0 = -0.82$ eV has been considered [216], an improvement in its catalytic activity may be obtained in the alkaline region (i.e., $pH > 7$). Due to the linear behavior of eq. (5.7) with a positive slope, when $\Delta G_H^0$ is higher than 0.2 eV or lower than -1.03 eV, the model active site will not show favorable conditions for the HER along the entire $pH$ interval, Fig. 5.12.

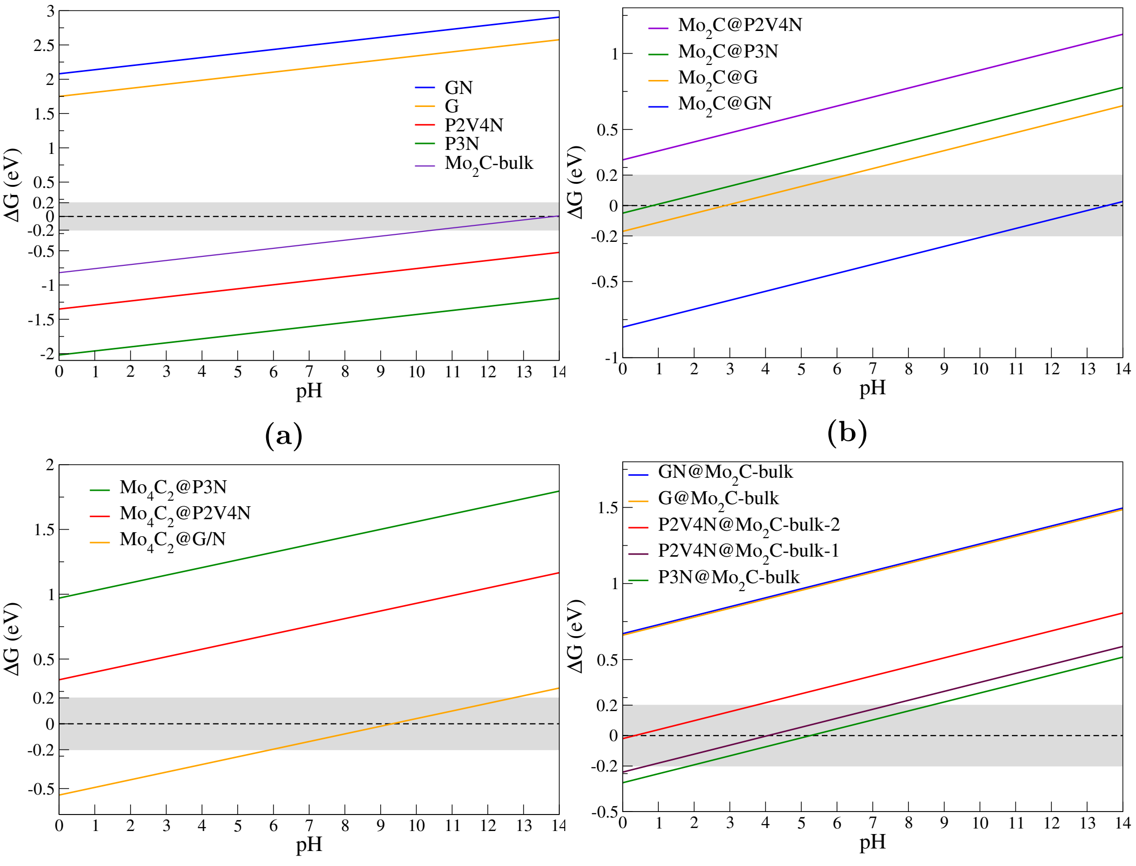

**(a)** **(b)**

**(c)** **(d)**

**Figure. 5.12.** *pH dependence of the H-adsorption free energy for the four series of structures considered in the present chapter.* ***a)*** *Pure and N-doped graphene as well as $Mo_2C$-bulk.* ***b)*** *$Mo_2C$ adsorbed on pure and N-doped graphene.* ***c)*** *$Mo_4C_2$ adsorbed on pure and N-doped graphene.* ***d)*** *Pure and N-doped graphene adsorbed on top of the $Mo_2C$ (001) face. The favorable area (gray area) shows, in all cases, the criteria for desired catalysts considered in this work (i.e., $-0.2\ eV \leqslant \Delta G \leqslant 0.2\ eV$).*

The $pH$ evolution of the H-adsorption free energy on a $Mo_2C$ unit adsorbed at the considered model surfaces: G, GN, P3N and P2V4N, is represented in Fig.5.12b. These systems show more suitable electrocatalytic properties toward the HER with respect to the pure and N-doped graphene layers, Fig. 5.12a. The $Mo_2C$ cluster, adsorbed on the P3N structure and on the graphene layer, shows good performances along almost the whole acidic region ($pH < 7$) of the $pH$ interval. The H-adsorption free energy for $Mo_2C$@P3N lays in the favorable area from $pH = 0$ to $pH = 4.2$ and for the $Mo_2C$@G the corresponding interval is even larger, from $pH = 0$ to $pH = 6.6$. The more suitable condition for the HER, $\Delta G_H = 0$, is reached for $Mo_2C$@P3N at

$pH$ = 0.8 and for $Mo_2C$@G at $pH$ = 2.9. On contrary, the $Mo_2C$@GN presents better catalytic properties in the alkaline region. It is shown that, for $pH \geq 10$ $\Delta G_H$ enters in the desired interval for improved catalytic properties (i.e., -0.2 eV $\leqslant \Delta G_H \leqslant$ 0.2 eV), at $pH$ = 13.5 the $Mo_2C$@GN structure has its more suitable condition for the HER. A very similar trend has been obtained for the $Mo_2C$-bulk presented in Fig. 5.12a. In both cases the hydrogen atom is attached at the Mo-site. Due to the similar bonding situation the values of $\Delta G^0_H$ are very close: $\Delta G^0_H = -0.80$ eV and $\Delta G^0_H$ = -0.82 eV for $Mo_2C$@GN and $Mo_2C$-bulk, respectively. The best condition for $Mo_2C$@P2V4N (i.e., the minimum $\Delta G^0_H$) is at $pH = 0$, with $\Delta G^0_H = 0.28$ eV. Higher $pH$ values lead to unfavorable free energies for the hydrogen adsorption at this model surface.

The $Mo_4C_2$-based systems do not show promising behaviors for the P3N and P2V4N substrates, Fig. 5.12c. They have $\Delta G^0_H$ values of 0.97 eV and 0.34 eV, respectively, and $\Delta G_H$ only increases along the $pH$ interval. However, the $Mo_4C_2$ adsorbed on pure graphene presents favorable conditions in the alkaline region. The H-adsorption free energy on $Mo_4C_2$@G lays into the favorable area for $pH$ values between 6 and 13. For $Mo_4C_2$@GN is obtained exactly the same behavior, it has the same $\Delta G^0_H = -0.55$ eV than $Mo_4C_2$@G. This behavior is due to the fact that the hydrogen atom is adsorbed on a Mo site and there is not distinction between G and GN from the free energy point of view. The unfavorable behavior of $Mo_4C_2$@P3N and $Mo_4C_2$@P2V4N is ascribed to the fact that the hydrogen atom is adsorbed on N-sites. However, if a molybdenum atom on top of the $Mo_4C_2$ structure is selected as the adsorption site, a similar result than for $Mo_4C_2$@G/GN is expected.

The use of $Mo_2C$-based clusters adsorbed on the considered surfaces (i.e., G, GN, P3N, P2V4N), Fig. 5.12b and c, reveals a clear enhancement of the electrocatalytic properties with respect to pure and N-doped graphene layers, Fig. 5.12a. They reproduce the experimental behavior, which shows a higher HER activity for $Mo_2C$ NPs attached to graphene layers with respect to pristine graphene, in acidic conditions [205]. The existence of active sites in the $Mo_2C$-Nps adsorbed on pure graphene is predicted for alkaline conditions within the present $pH$-correction to the H-adsorption free energy. Moreover, the N-doped graphene surfaces show the possibility to be a better substrate to host $Mo_2C$-Nps towards the HER in acidic conditions, while in alkaline ones, similar performances between $Mo_4C_2$@G and $Mo_4C_2$@GN are obtained.

The last set of model structures considered in the present chapter: G, GN, P3N and P2V4N mono-layers deposited on top of the $Mo_2C$ (001) surface, is addressed here to evaluate the influence of the $pH$ on their HER activity, Fig. 5.12d. G@$Mo_2C$-bulk and GN@$Mo_2C$-bulk are not promising catalysts along the complete $pH$ interval. Their performances, attending to the $\Delta G_H$ for the H-adsorption, is slightly better than the one from the isolated mono-layers (i.e., G and GN) Fig. 5.12a, but they are also far from the favorable area highlighted in gray, Fig. 5.12d. The remaining adsorption sites on P2V4N@$Mo_2$C-bulk and P3N@$Mo_2$C-bulk, represent a clear improvement with respect to the P2V4N and P3N clean surfaces, respectively. They lay inside the favorable area along a wide range of $pH$ values, from $pH = 0$ to $pH = 9$. The optimum electrolyte conditions are $pH = 0.6$ for P2V4N@$Mo_2$C-bulk-2, $pH = 4.0$ for P2V4N@$Mo_2$C-bulk-1 and $pH = 5.5$ for P3N@$Mo_2$C-bulk. Although these structures present their better electrocatalytic properties in acidic conditions, they show an agreement with recent experiments that have found an increasing of the HER activity on $Mo_2$C@2D-NPC with respect to pure graphene in alkaline conditions [73]. The significant influence of the P3N and P2V4N type of N-defects is uncovered, while an improvement of the HER activity of the synthesized material ($Mo_2$C@2D-NPC) is predicted in acidic conditions.

## 5.6 Conclusions

Three model representations of molybdenum carbide structures have been investigated in this chapter, as catalysts for the HER on ECCs or PECs. The first two models are based on small clusters (i.e., $Mo_2C$ and $Mo_4C_2$) adsorbed on a graphene surface. They are motivated by recent experimental results, where small $Mo_2C$ nanoparticles has been synthesized on a clean graphene surface to improve the HER activity with respect to both pristine graphene and $Mo_2$C-bulk [205]. The third model structure is constructed as a $Mo_2C$ (001) surface covered by a graphene layer. This model surface represents, in a simplified way, a novel material which shows very high HER activities in both acidic and alkaline electrolytes [73]. Furthermore, nitrogen-doped impurities at the graphene structures are considered to evaluate their influence for the HER activity. They were added to all the three models analyzed here and their effects were evaluated as a prediction for the development of new functionalized nanocatalysts for the HER.

A previously developed methodology, based on DFT calculations, due to J. K. Nørskov and coworkers [114], is employed to assess the HER activities of all the proposed representations of the active sites for H-adsorption. This model has been specifically designed for Pt and metal-based electrocatalysts, but it has been employed also to evaluate the performance of non-metal compounds to promote the HER [59].

In agreement with previous experimental results, the graphene-based surfaces do not show good catalytic performances for the HER. On the other hand, the $Mo_2C$ (001) surface shows better catalytic properties than the graphene-based structures. The proposed models are able to reproduce, within the framework of the Nørskov's methodology, the experimental trend which predicts the outperforming HER activity for $Mo_2$C-bulk with respect to pure graphene. Furthermore, the catalytic activity of the $Mo_2C$-bulk is confirmed to be lower with respect to the combined structure models (i.e., $Mo_2C$ and $Mo_4C_2$). The evaluation of the HER activity, by mean of the descriptor $\Delta G_H$ proposed in the Nørskov's methodology, reveals that the two proposed cluster models (i.e., $Mo_2C$ and $Mo_4C_2$), are able to reproduce the experimental trend observed in electrocatalysts made of $Mo_2C$-NPs adsorbed on top of the graphene layers. In addition, the $pH$-correction to the H-adsorption free energy barriers reveals the existence of active-sites, at the $Mo_2C$-NPs deposited on pristine graphene, for the HER in alkaline conditions, while in an acidic environment the $Mo_2C$-NPs adsorbed on N-doped graphene layers are predicted to be more active.

The HER mechanism has been also investigated here for nitrogen-doped graphene layers deposited on top of the $Mo_2C$ (001) surface. The hydrogen adsorption at different active sites, the influence of the acidity on the HER activity, and comparisons between experimental and theoretical results have been shown. The smallest free energy values has been obtained in the case when the proton is adsorbed on nitrogen-defected structures with either one or two vacancies. However, even in the case of a pure graphene layer deposited on top of the $Mo_2C$ (001) surface, an improvement in the HER with respect to both pure graphene and $Mo_2C$-bulk has been confirmed. In addition, the P3N@$Mo_2C$-bulk and P2V4N@$Mo_2C$-bulk systems show higher electrocatalytic activities with respect to the cluster systems adsorbed on pristine graphene layer (i.e., $Mo_2C$@G and $Mo_4C_2$@G). This result agrees with the experimental findings for the novel material based on molybdenum carbide covered by nitrogen-doped graphene surfaces [73] and the results found in [205] for $Mo_2C$ nanoparticles adsorbed on clean graphene layers. Furthermore, the inclusion of N-impurities in the graphene layer makes the activity of the cluster systems (i.e., $Mo_2C$ and $Mo_4C_2$) to be as good as the one for the novel material ($Mo_2C$@2D-NPC). Hence, the nitrogen-doped graphene layers are predicted to be a more suitable substrates to grow up $Mo_2C$ particles in order to achieve better HER activities. Higher HER activities have been obtained for P2V4N@$Mo_2C$-bulk and P3N@$Mo_2C$-bulk with respect to pristine graphene and N-doped graphene layers in alkaline conditions. This results agree with recent experimental findings [73]. In addition, an improvement of the HER activity at the cited novel material ($Mo_2C$@2D-NPC) [73], is predicted in experiments running at acidic conditions.

# Chapter 6

# General Conclusions

The electrocatalytic water decomposition has been investigated in this thesis by means of its two half standard reactions: the oxygen evolution reaction (OER) and the hydrogen evolution reaction (HER). They characterize this process from a thermodynamical point of view. These reactions occur in different locations in a typical electrochemical cell: the anode and the cathode, respectively. Motivated by the lack of understanding about the reaction mechanisms occurring at the anodes and cathodes, we have proposed first: novel representations of typical $TiO_2$ surfaces, based on small cluster systems, which can be used for a quick and more detailed assessment of the OER activities at modified $TiO_2$ surfaces, and secondly we investigated the HER in two sets of model surfaces which represent recently synthesized materials, based on $Mo_2C$ and graphene with promising activities toward the HER. We have employed Density Functional Theory (DFT) based methods within both localized and extended basis sets, as implemented in GAMESS and VASP packages, respectively, to examine the structural, electronic and vibrational properties of the proposed model structures and the molecules: $H_2O$, $H_2$ and $O_2$.

Several cluster representations of $TiO_2$ surfaces were investigated focusing on a number of possible reaction mechanisms for the OER. The relative advantages of the cluster models to reproduce the major aspects of the studied process on $TiO_2$-based substrates were addressed. The consideration of molecular systems to mimic the surface of the anode at a $TiO_2$-based electrochemical cell enables the study of the properties of catalytic surfaces and the influence of various structural features on the water splitting reaction (e.g., charged structure or different surface topologies), which would be extremely demanding from a computational point of view, within an extended surface approach. A number of reaction pathways for the OER at different models of $TiO_2$-based surfaces are addressed here. They are investigated within the electronic and vibrational structure of all desired intermediate states, and evaluating their free energy profiles. A minimum free energy barrier for the system is sought. Therefore, different reaction pathways have been investigated for the same initial structure and the more favorable one has been selected.

Based on a thermochemical methodology Sec. 2.4, the rate-determining step for every reaction mechanism is identified. In each case, the application of the external potential necessary to overcome the largest energy barrier tends to flatten the free energy profile in the vicinity of the most energy-consuming step. Since the free energy landscape and the computed overpotentials depend on the chosen reaction path, other plausible pathways have been explored.

The mechanism proposed for the water electrolysis on the $Ti(OH)_4$ cluster, significantly improves the agreement between the computed overpotential and the experimental and theoretical values reported for extended surfaces, with respect to similar reaction mechanisms taking place on previous cluster models [38, 39]. On the other hand, the calculations performed on $Ti(OH)_4^-$ show that the addition of localized charges does not favor the water decomposition. We considered further dimeric structures, to represent different topologies of the $TiO_2$ surfaces: $Ti(OH)_2$-$O_2$-$Ti(OH)_2$, for rutile (110), and $Ti(OH)_3$-O-$Ti(OH)_3$, for anatase (001). The $Ti(OH)_2$-$O_2$-$Ti(OH)_2$ and the $Ti(OH)_3$-O-$Ti(OH)_3$ clusters provide reasonable representations of the spatial disposition of atoms in the neighborhood of the interaction sites on rutile and anatase surfaces. These cluster representations correctly predict the relatively larger feasibility of decomposing water molecules on rutile (110) surfaces compared to anatase (001) substrates.

Subsequently, we studied the water decomposition reaction on transition metals (TM) active sites placed at $TiO_2$-based electrodes using of the same cluster representations: $TM(OH)_3$-O-$Ti(OH)_3$ and $TM(OH)_2$-$O_2$-$Ti(OH)_2$. They resemble, in a simplified way, TM active sites on $TiO_2$ surfaces: anatase (001) and rutile (110), respectively. Transition metals ranging from V to Ni have been considered as dopants, and the reaction pathways have been investigated for each doped system and for each model structure (i.e., $TM(OH)_3$-O-$Ti(OH)_3$ and $TM(OH)_2$-$O_2$-$Ti(OH)_2$).

The free energy profiles along the proposed pathways for the OER on these cluster representations are able to reproduce the general trend for the overpotentials observed in the experiments on Fe, Co and Ni doped titanium dioxide substrates. The case of Mn-doped clusters is also found to be in agreement with empirical results [181]: DFT calculations for the $Mn(OH)_3$-O-$Ti(OH)_3$ model reproduce the enhancement of the OER activity observed for Mn-$TiO_2$ anatase (001) surfaces, whereas no improvement is seen in the case of Mn-$TiO_2$ rutile (110) surfaces. The obtained results illustrate the capability of the present models to reproduce the empirically observed trends for the OER activity. Moreover, they predict the influence of new TMs on the OER activity of $TiO_2$-based electrodes, which have not been still addressed experimentally.

The second part of the thesis is devoted to the study of the HER at combined $Mo_2C$-graphene based electrodes. Three major model surfaces have been investigated. The first two models are based on small clusters (i.e., $Mo_2C$ and $Mo_4C_2$)

adsorbed on a graphene layers. They are motivated by recent experimental results, where small $Mo_2C$ nanoparticles has been synthesized on a clean graphene surface to improve the HER activity with respect to both pristine graphene and $Mo_2C$-bulk [205]. The third model structure is constructed as a $Mo_2C$ (001) surface covered by a graphene layer. This model surface represents, in a simplified way, a novel material which shows very high HER activities in both acidic and alkaline electrolytes [73]. Furthermore, nitrogen-doped impurities at the graphene structures are considered to evaluate their influence for the HER activity. They were added to all the three models analyzed here and their effect were evaluated as a prediction for the development of new functionalized nanocatalysts for the HER.

The proposed models are able to reproduce the experimental trend which predicts the outperforming HER activity for $Mo_2C$-bulk with respect to pure graphene layers. Furthermore, the catalytic activity of the $Mo_2C$-bulk is confirmed to be lower with respect to the combined structure models (i.e., $Mo_2C$ and $Mo_4C_2$). These models are able to reproduce the experimental trend observed in electrocatalysts made of $Mo_2C$-NPs adsorbed on top of the graphene layers. In addition, the $pH$-correction to the H-adsorption free energy barriers reveals the existence of active-sites, at the $Mo_2C$-NPs deposited on pristine graphene, for the HER in alkaline conditions, while in an acidic environment the $Mo_2C$-NPs adsorbed on N-doped graphene layers are predicted to be more active.

The HER mechanism has been also investigated here for nitrogen-doped graphene layers deposited on top of the $Mo_2C$ (001) surface. The hydrogen adsorption at different active sites, the influence of the acidity on the HER activity, and comparisons between experimental and theoretical results have been shown. The smallest free energy values have been obtained in the case when the proton is adsorbed on nitrogen-defected structures with either one or two vacancies. However, even in the case of a pure graphene layer deposited on top of the $Mo_2C$ (001) surface, an improvement in the HER with respect to both pure graphene and $Mo_2C$-bulk has been confirmed. In addition, the P3N@$Mo_2C$-bulk and P2V4N@$Mo_2C$-bulk systems show higher electrocatalytic activities with respect to the cluster systems adsorbed on pristine graphene layer (i.e., $Mo_2C$@G and $Mo_4C_2$@G). This result agrees with the experimental findings for the novel material based on molybdenum carbide covered by N-doped graphene surfaces [73] and the results found in [205] for $Mo_2C$ nanoparticles adsorbed on clean graphene layers. Furthermore, the inclusion of N-impurities in the graphene layers makes the activity of the cluster systems (i.e., $Mo_2C$ and $Mo_4C_2$) to be as good as the one for the novel material ($Mo_2C$@2D-NPC). Hence, the N-doped graphene layers are predicted to be a more suitable substrates to grow up $Mo_2C$ particles in order to achieve better HER activities. In addition, an improvement of the HER activity at the cited novel material ($Mo_2C$@2D-NPC) [73], is predicted in experiments running in acidic conditions.

# Appendix A

# Geometry optimization, frequency calculation and vibrational density of states. Supporting information

*Additional details about the calculation of the ground state energies and the optimized structures, which have been employed to describe the overall water splitting reaction on $TiO_2$-based clusters, are provided in the present appendix. These calculations have been carried out using the quantum chemical package: GAMESS-US [170, 171]. Subsequently, the input parameters employed in the geometry optimizations and the frequency calculations are described. All the electronic structure calculations performed in the present work have followed a DFT formulation within the standard B3LYP exchange correlation functional. Additionally, we provide the analytical expressions to estimate the vibrational density of states (VDOS) and partial vibrational density of states (PVDOS), using the eigenfrequencies and eigen vectors obtained as the output of the frequency calculation.*

## A.1 Energetic and entropic contributions of $H_2$, $H_2O$ and $O_2$ to the free energy

In every studied reaction mechanism the energy values and the entropic contribution to the free energy of $H_2$, $H_2O$ and $O_2$ are needed. The Cartesian coordinates in (Å) and molecular energies (in eV) of $H_2$ and $H_2O$ at 0K, employed in every considered path, are the followings:

$H_2$: $E_{0K} = -31.83295$, $ZPEC = 0.272$

| | | | |
|---|---|---|---|
| H | 0.000 | 0.000 | -0.371 |
| H | 0.000 | 0.000 | 0.371 |

$H_2O$: $E_{0K} = -2079.193$, $ZPEC = 0.575$

| | | | |
|---|---|---|---|
| O | 0.000 | 1.990 | 5.881 |
| H | 0.000 | 0.775 | -0.516 |
| H | 0.000 | -0.775 | -0.516 |

The gas phase entropic contribution to the free energies at standard thermodynamic conditions, for the $H_2$ and $H_2O$ molecules, computed by the vibrational analysis and within the same level of theory are:

$$TS(\mathrm{H_2}) = 0.402 \text{ eV} \tag{A.1}$$

$$TS(\mathrm{H_2O}) = 0.601 \text{ eV} \tag{A.2}$$

The contribution of the $O_2$ molecule is taken from experimental values [16]:

$$TS(\mathrm{O_2}) = 0.633 \text{ eV} \tag{A.3}$$

The total energy of $O_2$ is computed indirectly by fixing the experimental free energy change of the water decomposition reaction: $H_2O \rightarrow \frac{1}{2}O_2 + H_2$ ($\Delta$G $=$ 2.46 eV) and using the previous results: Eqs. (A.1), (A.2), (A.3). The total energy of the $O_2$ molecule including the zero point energy correction has been found to be:

$$E(\mathrm{O_2}) = -4088.953 \text{ eV} \tag{A.4}$$

## A.2 Geometry optimization and frequency calculation in the ground state

In the Figs. A.1 and A.2, explicit examples of *GAMESS-US* input files for the geometry optimization and the frequency calculation of model structures are shown. The general composition of any input file of this software is organized by groups enclosed between $ symbols and ended with the command "END". In the CONTROL group it is specified the type of calculation it is intended to do. In this case it corresponds to a DFT calculation within the B3LYP exchange-correlation functional;

the ROHF scheme developed by Roothaan [168] is considered for the treatment of the K-S wave function in an open-shell system. Additionally, the geometry optimization is specified and the QA algorithm to minimized the PES is selected by default Sec. 3.2.2. The second example below Fig. A.2, corresponds to the frequency calculation. They are almost the same files, but the vale of the RUNTYP keyword is different, RUNTYP=OPTIMIZE stands for the geometry optimization Fig. A.1, while RUNTYP=HESSIAN accounts for the frequency calculation Fig. A.2. The remaining keywords in the group CONTROL state the maximum amount of steps allowed to the self consistent field (SCF) calculation within the electronic system (200), the coordinate system of the given structure (Cartesian) and its multiplicity, which is 1 because we are interested in the lower energy state which is a singlet for the example below. In the case of an odd number of electrons, the ground state will be at least a doublet.

The group SYSTEM specify technical details related with the computer simulation. In the example below it is established the limit of time the program is allowed to run in minutes, which is TIMLIM = 525600 (one year). The keyword MEMORY = $10^7$ is employed to allocate memory in the computer system to be used by *GAMESS-US*. The numeric value $10^7$ is given in the unit “words” which is equivalent to 64 bits. Therefore, $10^7$ words is approximately equal to 80 MB. When the calculations are running in parallel the specified amount is allocated for each core, thereby 160 MB are used when two cores are employed.

The SCF group specifies all the requirements of the SCF electronic calculation, in this case the value CONV = $10^{-4}$ electrons/bohr$^3$ corresponds to the tolerance in the electronic density change to achieve the convergence condition. The remaining keywords in this group are convergence accelerators or additional specifications in the convergence process [170,171]. In the STATPT, several aspects of the optimization process may be modified, in this case only the maximum amount of steps (200) have been changed from the default specification. The BASIS group establishes the basis set employed in the electronic structure calculation, it has been selected a triple-zeta-valence (TZV) basis set as it was described in Sec. 3.2.2, the keywords NDFUNC and POLAR establishes the number of d-functions used as polarization functions and the parameters which define such functions, respectively.

The group GUESS is devoted to get an initial approximation of the atomic orbitals necessary to start the SCF iterative process. In the case of DFT calculations, these molecular orbitals constitute K-S orbitals which are employed to estimate the first electronic density to plug in the self consistent process. In the example below an extended Hückel theory [222] within a Huzinaga MINI basis set [223] is include. The final part of the typical input files is the DATA group. The target structure is defined there, for example by cartesian coordinates, although other coordinate systems may be used as well. In the present example, the Cartesian coordinate format is employed. It consists on five columns, namely: the notation of every element, the atomic number and the (x, y, z) Cartesian coordinates in Å. The C1 term appearing on top of the coordinates block accounts for the symmetry of the model structure. The element C1 corresponds to the identity transformation, it means that the considered structure does not have higher elements of symmetry. This aspect is of remarkable importance when more symmetric systems are studied. Highly efficient algorithms may be employed within higher symmetric structures, and lots of computational resources and time may be saved.

```
$CONTRL SCFTYP=ROHF DFTTYP=B3LYP
   RUNTYP=OPTIMIZE COORD=CART MULT=1
   MAXIT=200 $END
$SYSTEM TIMLIM=100000000 MEMORY=10000000 $END
$SCF DIRSCF=.TRUE. FDIFF=.TRUE.
   MAXDII=50 DIIS=.TRUE. ETHRSH=10.0
   EXTRAP=.TRUE. DAMP=.TRUE. SHIFT=.TRUE.
   CONV=1.0d-4 $END
$STATPT  NSTEP=200 $END
$BASIS  GBASIS=TZV NDFUNC=1 POLAR=HONDO7
$END
$GUESS  GUESS=HUCKEL $END
$DATA
C1
O       8.0      0.0577097702  -0.2200975463  -1.1295615043
TI     22.0      1.4191833242  -0.0119251073   0.0885735252
O       8.0      0.0399094367   0.1731199626   1.2924667520
TI     22.0     -1.2785311750  -0.0346101749   0.0750051534
O       8.0     -2.2974152540  -1.4665638076   0.4356950214
O       8.0     -2.3240502248   1.3711217788  -0.3100173184
O       8.0      2.4522409957  -1.4834641729   0.3330398737
O       8.0      2.4315841099   1.4775157922  -0.1299351563
H       1.0      2.3037352298   2.4080625608  -0.3396652439
H       1.0      2.3308445933  -2.4142744305   0.5458587457
H       1.0     -2.8362800596   1.9247371041   0.2941481178
H       1.0     -2.7734438424  -2.0309528687  -0.1880825733
 $END
```

**Figure. A.1.** *Model input file required to implement a geometry optimization within the electronic structure package: GAMESS-US [170, 171].*

```
$CONTRL SCFTYP=ROHF DFTTYP=B3LYP
   RUNTYP=HESSIAN COORD=CART MULT=1
   MAXIT=200 $END
$SYSTEM TIMLIM=100000000 MEMORY=10000000
$END
$SCF DIRSCF=.TRUE. FDIFF=.TRUE.
   MAXDII=50 DIIS=.TRUE. ETHRSH=10.0
   EXTRAP=.TRUE. DAMP=.TRUE. SHIFT=.TRUE.
   CONV=1.0d-4 $END
$STATPT  NSTEP=200 $END
$BASIS  GBASIS=TZV NDFUNC=1 POLAR=HONDO7
$END
$GUESS  GUESS=HUCKEL $END
$DATA
C1
O    8.0      -0.0117165661    0.1299529913   -1.2349157562
TI  22.0       1.3514520126   -0.0280177094   -0.0094126635
O    8.0      -0.0103750469   -0.1010953990    1.2245709964
TI  22.0      -1.3692672534    0.0943782514    0.0028366692
O    8.0      -2.4700034660   -1.3334810818   -0.1149116198
O    8.0      -2.2222544545    1.6915992098    0.1640726284
O    8.0       2.3407318986   -1.5441526938   -0.1430085429
O    8.0       2.3945683336    1.4516287742    0.1154444788
H    1.0       2.2555041950    2.3988236055    0.2175569035
H    1.0       2.2363725620   -2.4935574077   -0.2537282875
H    1.0      -3.1259491039    2.0123215260    0.2436131724
H    1.0      -2.5493153507   -2.2850250907   -0.2187577313
 $END
```

**Figure. A.2.** *Model input file required to implement a frequency calculation within the electronic structure package: GAMESS-US [170, 171].*

## A.3 Vibrational density of states (VDOS) and partial vibrational density of states (PVDOS)

The VDOS in each panel of the Fig. 3.8 in Sec. 3.3.6 is computed by:

$$\rho(\omega) = \sum_{i=1}^{3N-6} \frac{1}{\sqrt{2\pi}\sigma} \exp(-\frac{(\omega-\omega_i)^2}{2\sigma^2}) \tag{A.5}$$

where $N$ is the number of atoms contained in each structure and the $\{\omega_i\}$ are the vibrational frequencies of the normal modes after the exclusion of pure translational and rotational frequencies. The standard deviation in the proposed Gaussian functions has been chosen as $\sigma = 30$ cm$^{-1}$. This value fits quite good the present requirements. Smaller values of $\sigma$ would make the peak structure of the VDOS more narrow around the proper frequencies $\omega_i$, while bigger ones could hide some of the relevant picks by the broadening of every Gaussian function.

The PVDOS gives the contribution of each atom in the structure of the VDOS. To compute these functions, the eigenvectors from the frequency calculation are used as well as the $\{\omega_i\}$. The eigenvectors are expressed by the relative displacements of the atoms in the structure:

$$\vec{u}^i = \{x^i_\alpha, y^i_\alpha, z^i_\alpha\}, \tag{A.6}$$

where $\vec{u}^i$ is a $3N$ dimensional vector, $\alpha$ runs from 1 to the number of atoms in the structure ($N$) while $i$ denote the corresponding normal mode. The set of $\vec{u}^i$ computed as it is implemented in GAMESS are orthonormalized according to:

$$\sum_\alpha m_\alpha \{x^i_\alpha x^j_\alpha + y^i_\alpha y^j_\alpha + z^i_\alpha z^j_\alpha\} = \delta_{i,j}, \tag{A.7}$$

where $m_\alpha$ is the mass of the atom $\alpha$. Considering the ortonormalization rule of the $\vec{u}^i$ vectors, the VDOS can be written as:

$$\rho(\omega) = \sum_{i=1}^{3N-6} \frac{\sum_\alpha m_\alpha \{{x^i_\alpha}^2 + {y^i_\alpha}^2 + {z^i_\alpha}^2\}}{\sqrt{2\pi}\sigma} \exp(-\frac{(\omega-\omega_i)^2}{2\sigma^2}). \tag{A.8}$$

From Eq. A.8 it can be set:

$$\rho(\omega) = \sum_\alpha \rho_\alpha(\omega), \tag{A.9}$$

where:

$$\rho_\alpha(\omega) = \sum_{i=1}^{3N-6} \frac{m_\alpha \{{x^i_\alpha}^2 + {y^i_\alpha}^2 + {z^i_\alpha}^2\}}{\sqrt{2\pi}\sigma} \exp(-\frac{(\omega-\omega_i)^2}{2\sigma^2}), \tag{A.10}$$

is the PVDOS (i.e., the contribution of the atom $\alpha$ to the total VDOS) corresponding to the atom $\alpha$.

The corresponding vibrational frequencies of the structures considered in the Fig. 8 are shown in the fallowing tables:

| $\omega_i$**[Ti(OH)$_4$](cm$^{-1}$)** | $\omega_i$**[Ti(OH)$_4$-H$_2$O](cm$^{-1}$)** | $\omega_i$**[Ti(OH)$_5$](cm$^{-1}$)** |
|---|---|---|
| 108.348 | 16.834 | 62.687 |
| 133.748 | 87.718 | 72.646 |
| 157.688 | 138.865 | 144.652 |
| 157.721 | 159.145 | 163.024 |
| 200.932 | 167.004 | 200.026 |
| 215.901 | 176.069 | 213.767 |
| 235.592 | 194.305 | 235.262 |
| 235.599 | 216.661 | 269.875 |
| 309.120 | 233.063 | 288.093 |
| 437.743 | 260.783 | 305.228 |
| 452.165 | 289.179 | 331.114 |
| 452.186 | 311.751 | 378.485 |
| 457.941 | 345.541 | 446.124 |
| 760.558 | 383.268 | 484.596 |
| 802.786 | 459.750 | 499.442 |
| 811.637 | 483.841 | 557.691 |
| 811.640 | 520.104 | 591.005 |
| 4230.053 | 594.157 | 608.627 |
| 4230.284 | 613.714 | 694.332 |
| 4230.295 | 687.660 | 706.946 |
| 4238.039 | 752.887 | 745.300 |
| - | 764.304 | 765.854 |
| - | 789.449 | 3707.189 |
| - | 1735.806 | 3794.498 |
| - | 3713.506 | 3810.466 |
| - | 3789.660 | 3818.852 |
| - | 3832.199 | 3869.141 |
| - | 3835.130 | - |
| - | 3849.801 | - |
| - | 3853.709 | - |

| $\omega_i$**[Ti(OH)$_3$OOH](cm$^{-1}$)** | $\omega_i$**[Ti(OH)$_3$O$_2$](cm$^{-1}$)** | $\omega_i$**[Ti(OH)$_3$O$_2$-H$_2$O](cm$^{-1}$)** |
|---|---|---|
| 126.356 | 49.414 | 60.305 |
| 131.780 | 139.796 | 131.028 |
| 152.435 | 167.590 | 134.725 |
| 172.953 | 186.925 | 180.072 |
| 180.886 | 202.556 | 202.324 |
| 195.792 | 223.400 | 211.489 |
| 212.071 | 243.867 | 219.382 |
| 228.390 | 286.413 | 254.287 |
| 299.190 | 328.840 | 256.336 |
| 345.767 | 393.820 | 300.355 |
| 392.415 | 443.332 | 366.757 |
| 500.682 | 490.011 | 387.039 |
| 540.106 | 506.881 | 411.047 |
| 583.286 | 552.085 | 412.986 |
| 642.238 | 719.135 | 475.231 |
| 712.940 | 767.374 | 583.700 |
| 759.162 | 778.083 | 628.286 |
| 773.134 | 1197.445 | 648.087 |
| 894.399 | 3842.218 | 659.916 |
| 1337.386 | 3846.541 | 666.545 |
| 3667.607 | 3851.075 | 716.568 |
| 3834.226 | - | 767.096 |
| 3846.587 | - | 781.014 |
| 3864.476 | - | 1212.637 |
| - | - | 1693.140 |
| - | - | 3685.210 |
| - | - | 3781.141 |
| - | - | 3819.086 |
| - | - | 3821.130 |
| - | - | 3842.582 |

# Appendix B

# Water splitting on transition metal active sites at $TiO_2$-based models

*The total and zero point energies of every structure considered in the proposed reaction mechanisms are shown below (all the energies are given in eV). The cartesian coordinates (expressed in Å) of every molecular model containing cobalt active sites are provided in App. B.2.*

## B.1 Total energies and zero point energy contributions

**Water splitting on $V(OH)_3$-O-$Ti(OH)_3$:** $V(OH)_3$-O-$Ti(OH)_3$ + $2H_2O \rightarrow$ $V(OH)_3$-O-$Ti(OH)_3$ +$2H_2$ + $O_2$.

$V(OH)_3$-O-$Ti(OH)_3$: $E_{0\mathrm{K}} = -63234.0181$, $ZPEC = 2.2249$
$H_2O$-$V(OH)_3$-O-$Ti(OH)_3$: $E_{0\mathrm{K}} = -65313.7425$, $ZPEC = 3.0252$
$V(OH)_4$-O-$Ti(OH)_3$: $E_{0\mathrm{K}} = -65292.9661$, $ZPEC = 2.6616$
$V(OH)_2OOH$-O-$Ti(OH)_3$: $E_{0\mathrm{K}} = -65278.2098$, $ZPEC = 2.3512$
$V(OH)_2O_2$-O-$Ti(OH)_3$: $E_{0\mathrm{K}} = -65261.7372$, $ZPEC = 2.0347$
$H_2O$-$V(OH)_2O_2$-O-$Ti(OH)_3$: $E_{0\mathrm{K}} = -67341.4636$, $ZPEC = 2.8233$

**Water splitting on $V(OH)_2$-$O_2$-$Ti(OH)_2$:** $V(OH)_2$-$O_2$-$Ti(OH)_2$ + $2H_2O$ → $V(OH)_2$-$O_2$-$Ti(OH)_2$ +$2H_2$ + $O_2$.

$V(OH)_2$-$O_2$-$Ti(OH)_3$: $E_{0K} = -61154.0254$, $ZPEC = 1.6296$
$H_2O$-$V(OH)_2$-$O_2$-$Ti(OH)_3$: $E_{0K} = -63233.8967$, $ZPEC = 2.2879$
$V(OH)_2O$-O-$Ti(OH)_3$: $E_{0K} = -63217.9663$, $ZPEC = 1.9736$
$VOHO_2$-O-$Ti(OH)_3$: $E_{0K} = -63198.2557$, $ZPEC = 1.6673$
$H_2O$-$VOHO_2$-O-$Ti(OH)_3$: $E_{0K} = -65278.3887$, $ZPEC = 2.3710$
$V(OH)_2$-OOH-$Ti(OH)_3$: $E_{0K} = -61168.8985$, $ZPEC = 1.8673$

**Water splitting on $Cr(OH)_3$-O-$Ti(OH)_3$:** $Cr(OH)_3$-O-$Ti(OH)_3$ + $2H_2O$ → $Cr(OH)_3$-O-$Ti(OH)_3$ + $2H_2$ + $O_2$.

$Cr(OH)_3$-O-$Ti(OH)_3$: $E_{0K} = -65965.3325$, $ZPEC = 2.2830$
$H_2O$-$Cr(OH)_3$-O-$Ti(OH)_3$: $E_{0K} = -68045.2200$, $ZPEC = 3.0536$
$Cr(OH)_4$-O-$Ti(OH)_3$: $E_{0K} = -68028.3504$, $ZPEC = 2.7052$
$Cr(OH)_2OOH$-O-$Ti(OH)_3$: $E_{0K} = -68010.8179$, $ZPEC = 2.3873$
$Cr(OH)_2O_2$-O-$Ti(OH)_3$: $E_{0K} = -67993.4379$, $ZPEC = 2.0878$
$H_2O$-$Cr(OH)_2O_2$-O-$Ti(OH)_3$: $E_{0K} = -70072.8072$, $ZPEC = 2.7508$

**Water splitting on $Cr(OH)_2$-$O_2$-$Ti(OH)_2$:** $Cr(OH)_2$-$O_2$-$Ti(OH)_2$ + $2H_2O$ → $Cr(OH)_2$-$O_2$-$Ti(OH)_2$ + $2H_2$ + $O_2$.

$Cr(OH)_2$-$O_2$-$Ti(OH)_3$: $E_{0K} = -63885.2653$, $ZPEC = 1.6533$
$H_2O$-$Cr(OH)_2$-$O_2$-$Ti(OH)_3$: $E_{0K} = -65965.2304$, $ZPEC = 2.3663$
$Cr(OH)_2O$-O-$Ti(OH)_3$: $E_{0K} = -65949.5017$, $ZPEC = 1.9618$
$CrOHO_2$-O-$Ti(OH)_3$: $E_{0K} = -65932.6650$, $ZPEC = 1.7207$
$H_2O$-$CrOHO_2$-O-$Ti(OH)_3$: $E_{0K} = -68009.5975$, $ZPEC = 2.4315$
$Cr(OH)_2$-OOH-$Ti(OH)_3$: $E_{0K} = -63902.0384$, $ZPEC = 1.9226$

**Water splitting on $Mn(OH)_3$-O-$Ti(OH)_3$:** $Mn(OH)_3$-O-$Ti(OH)_3$ + $2H_2O$ → $Mn(OH)_3$-O-$Ti(OH)_3$ + $2H_2$ + $O_2$.

$Mn(OH)_3$-O-$Ti(OH)_3$: $E_{0K} = -68863.1995$, $ZPEC = 2.2913$
$H_2O$-$Mn(OH)_3$-O-$Ti(OH)_3$: $E_{0K} = -70943.2459$, $ZPEC = 3.0483$
$Mn(OH)_4$-O-$Ti(OH)_3$: $E_{0K} = -70924.6340$, $ZPEC = 2.7441$
$Mn(OH)_2OOH$-O-$Ti(OH)_3$: $E_{0K} = -70908.0756$, $ZPEC = 2.4324$
$Mn(OH)_2O_2$-O-$Ti(OH)_3$: $E_{0K} = -70889.7164$, $ZPEC = 2.0368$
$H_2O$-$Mn(OH)_2O_2$-O-$Ti(OH)_3$: $E_{0K} = -72969.6590$, $ZPEC = 2.7704$

**Water splitting on $\mathbf{Mn(OH)_2}$-$\mathbf{O_2}$-$\mathbf{Ti(OH)_2}$:** $Mn(OH)_2$-$O_2$-$Ti(OH)_2 + 2H_2O \rightarrow Mn(OH)_2$-$O_2$-$Ti(OH)_2 + 2H_2 + O_2$.

$Mn(OH)_2$-$O_2$-$Ti(OH)_3$: $E_{0K} = -66783.1999$, $ZPEC = 1.6727$
$H_2O$-$Mn(OH)_2$-$O_2$-$Ti(OH)_3$: $E_{0K} = -68863.4351$, $ZPEC = 2.4023$
$Mn(OH)_2O$-O-$Ti(OH)_3$: $E_{0K} = -68845.9940$, $ZPEC = 2.0201$
$MnOHO_2$-O-$Ti(OH)_3$: $E_{0K} = -68828.9971$, $ZPEC = 1.6947$
$H_2O$-$MnOHO_2$-O-$Ti(OH)_3$: $E_{0K} = -70907.6503$, $ZPEC = 2.4080$
$Mn(OH)_2$-OOH-$Ti(OH)_3$: $E_{0K} = -66799.4460$, $ZPEC = 1.9584$

**Water splitting on $\mathbf{Fe(OH)_3}$-O-$\mathbf{Ti(OH)_3}$:** $Fe(OH)_3$-O-$Ti(OH)_3 + 2H_2O \rightarrow Fe(OH)_3$-O-$Ti(OH)_3 + 2H_2 + O_2$.

$Fe(OH)_3$-O-$Ti(OH)_3$: $E_{0K} = -71929.3323$, $ZPEC = 2.2961$
$H_2O$-$Fe(OH)_3$-O-$Ti(OH)_3$: $E_{0K} = -74009.3033$, $ZPEC = 3.0192$
$Fe(OH)_4$-O-$Ti(OH)_3$: $E_{0K} = -73991.3441$, $ZPEC = 2.7524$
$Fe(OH)_2OOH$-O-$Ti(OH)_3$: $E_{0K} = -73973.0028$, $ZPEC = 2.4095$
$Fe(OH)_2O_2$-O-$Ti(OH)_3$: $E_{0K} = -73956.7260$, $ZPEC = 2.0796$
$H_2O$-$Fe(OH)_2O_2$-O-$Ti(OH)_3$: $E_{0K} = -76036.5920$, $ZPEC = 2.8398$

**Water splitting on $\mathbf{Fe(OH)_2}$-$\mathbf{O_2}$-$\mathbf{Ti(OH)_2}$:** $Fe(OH)_2$-$O_2$-$Ti(OH)_2 + 2H_2O \rightarrow Fe(OH)_2$-$O_2$-$Ti(OH)_2 + 2H_2 + O_2$.

$Fe(OH)_2$-$O_2$-$Ti(OH)_3$: $E_{0K} = -69849.2620$, $ZPEC = 1.6762$
$H_2O$-$Fe(OH)_2$-$O_2$-$Ti(OH)_3$: $E_{0K} = -71929.6689$, $ZPEC = 2.4080$
$Fe(OH)_2O$-O-$Ti(OH)_3$: $E_{0K} = -71912.0568$, $ZPEC = 1.9875$
$FeOHO_2$-O-$Ti(OH)_3$: $E_{0K} = -71893.5662$, $ZPEC = 1.7017$
$H_2O$-$FeOHO_2$-O-$Ti(OH)_3$: $E_{0K} = -73974.0059$, $ZPEC = 2.4574$
$Fe(OH)_2$-OOH-$Ti(OH)_3$: $E_{0K} = -69866.5655$, $ZPEC = 1.9578$

**Water splitting on $\mathbf{Co(OH)_3}$-O-$\mathbf{Ti(OH)_3}$:** $Co(OH)_3$-O-$Ti(OH)_3 + 2H_2O \rightarrow Co(OH)_3$-O-$Ti(OH)_3 + 2H_2 + O_2$.

$Co(OH)_3$-O-$Ti(OH)_3$: $E_{0K} = -75168.0855$, $ZPEC = 2.2682$
$H_2O$-$Co(OH)_3$-O-$Ti(OH)_3$: $E_{0K} = -77247.9963$, $ZPEC = 3.0150$
$Co(OH)_4$-O-$Ti(OH)_3$: $E_{0K} = -77229.7320$, $ZPEC = 2.7147$
$Co(OH)_2OOH$-O-$Ti(OH)_3$: $E_{0K} = -77212.7016$, $ZPEC = 2.4043$
$Co(OH)_2O_2$-O-$Ti(OH)_3$: $E_{0K} = -77195.2409$, $ZPEC = 2.0917$
$H_2O$-$Co(OH)_2O_2$-O-$Ti(OH)_3$: $E_{0K} = -79274.7112$, $ZPEC = 2.8055$

**Water splitting on $Co(OH)_2$-$O_2$-$Ti(OH)_2$:** $Co(OH)_2$-$O_2$-$Ti(OH)_2$ + $2H_2O$ → $Co(OH)_2$-$O_2$-$Ti(OH)_2$ +$2H_2$ + $O_2$.

$Co(OH)_2$-$O_2$-$Ti(OH)_3$: $E_{0K} = -73088.1833$, $ZPEC = 1.6113$
$H_2O$-$Co(OH)_2$-$O_2$-$Ti(OH)_3$: $E_{0K} = -75168.4343$, $ZPEC = 2.3796$
$Co(OH)_2O$-O-$Ti(OH)_3$: $E_{0K} = -75149.8837$, $ZPEC = 2.0461$
$CoOHO_2$-O-$Ti(OH)_3$: $E_{0K} = -75132.7442$, $ZPEC = 1.6586$
$H_2O$-$CoOHO_2$-O-$Ti(OH)_3$: $E_{0K} = -77213.3791$, $ZPEC = 2.4485$
$Co(OH)_2$-OOH-$Ti(OH)_3$: $E_{0K} = -73105.7168$, $ZPEC = 1.9380$

**Water splitting on $Ni(OH)_3$-O-$Ti(OH)_3$:** $Ni(OH)_3$-O-$Ti(OH)_3$ + $2H_2O$ → $Ni(OH)_3$-O-$Ti(OH)_3$ + $2H_2$ + $O_2$.

$Ni(OH)_3$-O-$Ti(OH)_3$: $E_{0K} = -78583.6595$, $ZPEC = 2.3089$
$H_2O$-$Ni(OH)_3$-O-$Ti(OH)_3$: $E_{0K} = -80663.87222$, $ZPEC = 3.0320$
$Ni(OH)_4$-O-$Ti(OH)_3$: $E_{0K} = -80644.9088$, $ZPEC = 2.6788$
$Ni(OH)_2OOH$-O-$Ti(OH)_3$: $E_{0K} = -80628.1485$, $ZPEC = 2.4503$
$Ni(OH)_2O_2$-O-$Ti(OH)_3$: $E_{0K} = -80611.1117$, $ZPEC = 2.0643$
$H_2O$-$Ni(OH)_2O_2$-O-$Ti(OH)_3$: $E_{0K} = -82691.0760$, $ZPEC = 2.8215$

**Water splitting on $Ni(OH)_2$-$O_2$-$Ti(OH)_2$:** $Ni(OH)_2$-$O_2$-$Ti(OH)_2$ + $2H_2O$ → $Ni(OH)_2$-$O_2$-$Ti(OH)_2$ + $2H_2$ + $O_2$.

$Ni(OH)_2$-$O_2$-$Ti(OH)_3$: $E_{0K} = -76503.6860$, $ZPEC = 1.6116$
$H_2O$-$Ni(OH)_2$-$O_2$-$Ti(OH)_3$: $E_{0K} = -78583.7731$, $ZPEC = 2.3614$
$Ni(OH)_2O$-O-$Ti(OH)_3$: $E_{0K} = -78565.1083$, $ZPEC = 1.9305$
$NiOHO_2$-O-$Ti(OH)_3$: $E_{0K} = -78548.6241$, $ZPEC = 1.6856$
$H_2O$-$NiOHO_2$-O-$Ti(OH)_3$: $E_{0K} = -80628.5631$, $ZPEC = 2.4117$
$Ni(OH)_2$-OOH-$Ti(OH)_3$: $E_{0K} = -76522.4458$, $ZPEC = 1.9505$

## B.2 Water splitting on Co-active site molecular models on $TiO_2$-based electrodes.

**Water splitting on $Co(OH)_3$-O-$Ti(OH)_3$:** $Co(OH)_3$-O-$Ti(OH)_3$ + $2H_2O$ → $Co(OH)_3$-O-$Ti(OH)_3$ + $2H_2$ + $O_2$.

$Co(OH)_3$-O-$Ti(OH)_3$: $E_{0\mathrm{K}} = -75168.0855$, $ZPEC = 2.2682$

| | | | |
|---|---|---|---|
| O | 0.153 | -0.008 | 0.648 |
| Ti | 1.828 | -0.074 | 0.003 |
| O | 1.457 | -0.167 | -1.814 |
| Co | -1.557 | -0.000 | 0.126 |
| O | -1.310 | -0.294 | -1.581 |
| O | -2.563 | 1.443 | 0.119 |
| O | -2.794 | -1.009 | 0.837 |
| O | 2.730 | -1.531 | 0.578 |
| O | 2.773 | 1.425 | 0.397 |
| H | -0.347 | -0.278 | -1.803 |
| H | 2.579 | -2.385 | 0.993 |
| H | 3.600 | 1.630 | 0.845 |
| H | 1.992 | -0.023 | -2.602 |
| H | -3.671 | -0.591 | 0.797 |
| H | -2.429 | 1.881 | -0.739 |

$H_2O$-$Co(OH)_3$-O-$Ti(OH)_3$: $E_{0\mathrm{K}} = -77247.9963$, $ZPEC = 3.0150$

| | | | |
|---|---|---|---|
| O | 8.000 | -0.207 | 0.366 |
| Co | 27.000 | 1.428 | -0.197 |
| O | 8.000 | 0.882 | -1.660 |
| Ti | 22.000 | -1.952 | 0.123 |
| O | 8.000 | -2.799 | -0.551 |
| O | 8.000 | -2.763 | 1.691 |
| O | 8.000 | -1.948 | -1.090 |
| O | 8.000 | 1.845 | 0.719 |
| O | 8.000 | 2.897 | -1.018 |
| O | 8.000 | 2.095 | 1.517 |
| H | 1.000 | -0.076 | -1.568 |
| H | 1.000 | -2.608 | -1.148 |
| H | 1.000 | -3.585 | 2.111 |
| H | 1.000 | -2.577 | -1.335 |
| H | 1.000 | 3.538 | -0.366 |

| | | | |
|---|---|---|---|
| H | 1.000 | 1.804 | 0.078 |
| H | 1.000 | 2.261 | 2.117 |
| H | 1.000 | 1.254 | 1.790 |

Co(OH)$_4$-O-Ti(OH)$_3$: $E_{0\mathrm{K}} = -77229.7320$, $ZPEC = 2.7147$

| | | | |
|---|---|---|---|
| O | 1.680 | -1.503 | -0.517 |
| Co | 1.627 | 0.147 | -0.053 |
| O | 1.127 | 0.520 | 1.546 |
| O | 3.363 | 0.222 | 0.395 |
| O | -0.233 | 0.106 | -0.683 |
| Ti | -1.882 | -0.043 | -0.096 |
| O | -1.552 | 0.361 | 1.707 |
| O | 1.813 | 1.393 | -1.223 |
| O | -2.440 | -1.774 | -0.295 |
| O | -3.066 | 1.107 | -0.856 |
| H | 0.784 | -1.688 | -0.869 |
| H | 0.130 | 0.507 | 1.662 |
| H | 0.931 | 1.467 | -1.640 |
| H | 3.391 | 0.244 | 1.366 |
| H | -3.113 | 1.879 | -1.425 |
| H | -3.256 | -2.184 | -0.597 |
| H | -2.070 | 0.245 | 2.510 |

Co(OH)$_2$OOH-O-Ti(OH)$_3$: $E_{0\mathrm{K}} = -77212.7016$, $ZPEC = 2.4043$

| | | | |
|---|---|---|---|
| O | -0.273 | 0.471 | 0.340 |
| Ti | -1.958 | -0.033 | 0.068 |
| O | -1.795 | -0.943 | -1.548 |
| Co | 1.401 | 0.032 | -0.158 |
| O | 1.000 | -0.824 | -1.618 |
| O | 2.138 | 1.569 | 0.345 |
| O | 2.049 | -0.989 | 1.122 |
| O | 3.248 | -0.903 | 0.367 |
| O | -3.104 | 1.375 | -0.062 |
| O | -2.594 | -1.157 | 1.347 |
| H | -2.232 | -1.794 | 1.971 |
| H | -2.436 | -1.429 | -2.077 |
| H | -3.032 | 2.303 | -0.308 |
| H | 1.474 | 2.174 | 0.710 |
| H | 0.035 | -0.933 | -1.787 |
| H | 3.725 | -0.157 | 0.789 |

$Co(OH)_2O_2$-O-$Ti(OH)_3$: $E_{0\mathrm{K}} = -77195.2409$, $ZPEC = 2.0917$

| | | | |
|---|---|---|---|
| O | -0.039 | 0.517 | 0.348 |
| Co | 1.572 | -0.079 | -0.240 |
| O | 2.329 | 1.480 | -0.077 |
| Ti | -1.781 | 0.232 | 0.123 |
| O | -2.737 | 1.767 | -0.075 |
| O | -2.537 | -0.735 | 1.462 |
| O | -1.726 | -0.767 | -1.454 |
| O | 2.152 | -1.149 | 0.929 |
| O | 3.234 | -1.322 | 0.258 |
| O | 1.004 | -0.960 | -1.612 |
| H | -2.238 | -1.353 | 2.136 |
| H | -2.416 | -1.256 | -1.913 |
| H | -2.587 | 2.649 | -0.429 |
| H | 1.677 | 2.126 | 0.250 |
| H | 0.018 | -0.941 | -1.730 |

$H_2O$-$Co(OH)_2O_2$-O-$Ti(OH)_3$: $E_{0\mathrm{K}} = -79274.7112$, $ZPEC = 2.8055$

| | | | |
|---|---|---|---|
| O | 0.329 | 0.167 | -0.583 |
| Ti | 1.981 | 0.058 | 0.034 |
| O | 1.770 | 0.310 | 1.872 |
| Co | -1.389 | 0.218 | 0.009 |
| O | -1.071 | 0.488 | 1.760 |
| O | -2.143 | 0.461 | -1.627 |
| O | -1.580 | -1.486 | 0.073 |
| O | -2.770 | -1.549 | 0.462 |
| O | 3.084 | 1.326 | -0.681 |
| O | 2.742 | -1.575 | -0.261 |
| O | -1.629 | 2.265 | 0.055 |
| H | 2.408 | -2.459 | -0.441 |
| H | 2.404 | 0.232 | 2.591 |
| H | 2.935 | 2.174 | -1.111 |
| H | -1.494 | 0.349 | -2.338 |
| H | -0.121 | 0.451 | 2.008 |
| H | -2.307 | 2.503 | -0.595 |
| H | -1.864 | 2.555 | 0.949 |

**Water splitting on $\mathrm{Co(OH)_2}$-$\mathrm{O_2}$-$\mathrm{Ti(OH)_2}$:** $\mathrm{Co(OH)_2\text{-}O_2\text{-}Ti(OH)_2 + 2H_2O} \rightarrow \mathrm{Co(OH)_2\text{-}O_2\text{-}Ti(OH)_2 + 2H_2 + O_2}$.

$\mathrm{Co(OH)_2\text{-}O_2\text{-}Ti(OH)_3}$: $E_{\mathrm{0K}} = -73088.1833$, $ZPEC = 1.6113$

| | | | |
|---|---|---|---|
| O | -0.137 | 0.110 | -1.341 |
| Ti | -1.410 | -0.059 | -0.026 |
| O | -2.217 | -1.685 | 0.041 |
| Co | 1.247 | 0.200 | -0.220 |
| O | 2.244 | 1.539 | 0.281 |
| O | 0.025 | 0.111 | 1.118 |
| O | 2.194 | -1.187 | 0.216 |
| O | -2.626 | 1.280 | 0.116 |
| H | -2.665 | 2.236 | 0.213 |
| H | -1.976 | -2.611 | -0.061 |
| H | 1.876 | -1.545 | 1.063 |
| H | 2.010 | 1.852 | 1.170 |

$\mathrm{H_2O\text{-}Co(OH)_2\text{-}O_2\text{-}Ti(OH)_3}$: $E_{\mathrm{0K}} = -75168.4343$, $ZPEC = 2.3796$

| | | | |
|---|---|---|---|
| O | -0.230 | -0.767 | 1.111 |
| Co | 1.065 | -0.057 | 0.076 |
| O | 1.836 | 1.510 | 0.231 |
| Ti | -1.577 | -0.091 | 0.028 |
| O | -2.581 | -1.397 | -0.760 |
| O | -2.633 | 1.137 | 0.867 |
| O | -0.288 | 0.614 | -1.017 |
| O | 1.938 | -0.802 | -1.265 |
| H | -2.494 | -2.026 | -1.482 |
| H | -2.560 | 2.038 | 1.194 |
| H | 1.383 | 2.110 | -0.387 |
| H | 1.495 | -0.536 | -2.088 |
| O | 2.395 | -0.897 | 1.309 |
| H | 1.895 | -1.494 | 1.887 |
| H | 3.021 | -1.411 | 0.777 |

$\mathrm{Co(OH)_2O\text{-}O\text{-}Ti(OH)_3}$: $E_{\mathrm{0K}} = -75149.8837$, $ZPEC = 2.0461$

| | | | |
|---|---|---|---|
| O | 0.158 | 0.331 | -0.859 |
| Co | -1.488 | -0.126 | -0.374 |
| O | -3.430 | 0.445 | 0.255 |
| O | -2.232 | 1.265 | 0.389 |

| | | | |
|---|---|---|---|
| Ti | 1.734 | 0.142 | -0.039 |
| O | 3.094 | 0.030 | -1.245 |
| O | 2.073 | 1.535 | 1.076 |
| O | 1.517 | -1.424 | 0.944 |
| O | -1.287 | -1.663 | 0.377 |
| H | -0.383 | -1.790 | 0.738 |
| H | -3.963 | 0.915 | -0.412 |
| H | 2.152 | -1.984 | 1.402 |
| H | 3.923 | 0.501 | -1.375 |
| H | 1.605 | 2.273 | 1.478 |

CoOHO$_2$-O-Ti(OH)$_3$: $E_{\mathrm{0K}} = -75132.7442$, $ZPEC = 1.6586$

| | | | |
|---|---|---|---|
| O | 0.122 | -0.716 | -0.528 |
| Co | -1.580 | -0.561 | -0.340 |
| O | -2.005 | 1.169 | -0.558 |
| O | -1.648 | 2.007 | 0.339 |
| Ti | 1.727 | -0.044 | 0.076 |
| O | 1.833 | -0.343 | 1.861 |
| O | 1.786 | 1.735 | -0.242 |
| O | 3.060 | -0.881 | -0.818 |
| O | -2.484 | -1.055 | 1.045 |
| H | 2.387 | -0.850 | 2.463 |
| H | 1.490 | 2.546 | 0.182 |
| H | 3.802 | -0.625 | -1.375 |
| H | -2.551 | -0.446 | 1.797 |

H$_2$O-CoOHO$_2$-O-Ti(OH)$_3$: $E_{\mathrm{0K}} = -77213.3791$, $ZPEC = 2.4485$

| | | | |
|---|---|---|---|
| O | -0.300 | 0.392 | 0.941 |
| Co | 1.325 | -0.049 | 0.211 |
| O | 3.217 | 0.254 | 0.110 |
| O | 2.575 | 1.330 | 0.452 |
| Ti | -1.842 | 0.134 | 0.112 |
| O | -1.747 | 0.911 | -1.514 |
| O | -3.319 | 0.633 | 1.058 |
| O | -1.664 | -1.766 | -0.185 |
| O | 0.978 | 0.324 | -1.529 |
| O | 0.868 | -1.944 | -0.046 |
| H | -0.832 | 0.954 | -1.868 |
| H | -4.085 | 1.203 | 0.939 |
| H | -2.229 | -2.290 | -0.762 |

| | | | |
|---|---|---|---|
| H | 1.292 | -0.420 | -2.067 |
| H | 1.171 | -2.562 | 0.631 |
| H | -0.154 | -2.019 | -0.129 |

Co(OH)$_2$-OOH-Ti(OH)$_3$: $E_{0\mathrm{K}} = -73105.7168$, $ZPEC = 1.9380$

| | | | |
|---|---|---|---|
| O | -0.070 | 0.741 | -1.380 |
| Ti | -1.330 | -0.065 | -0.168 |
| O | -2.486 | -1.216 | -0.956 |
| Co | 1.393 | -0.174 | -0.317 |
| O | 1.912 | 1.441 | 0.146 |
| O | 2.664 | -1.245 | 0.250 |
| O | 0.001 | -0.939 | 0.603 |
| O | -2.152 | 1.082 | 0.967 |
| H | 0.135 | 1.686 | -1.429 |
| H | 2.540 | 1.405 | 0.884 |
| H | 2.539 | -1.638 | 1.126 |
| H | -2.545 | -2.163 | -1.120 |
| H | -2.980 | 1.234 | 1.431 |

# Appendix C

# Mo$_2$C-graphene type compounds

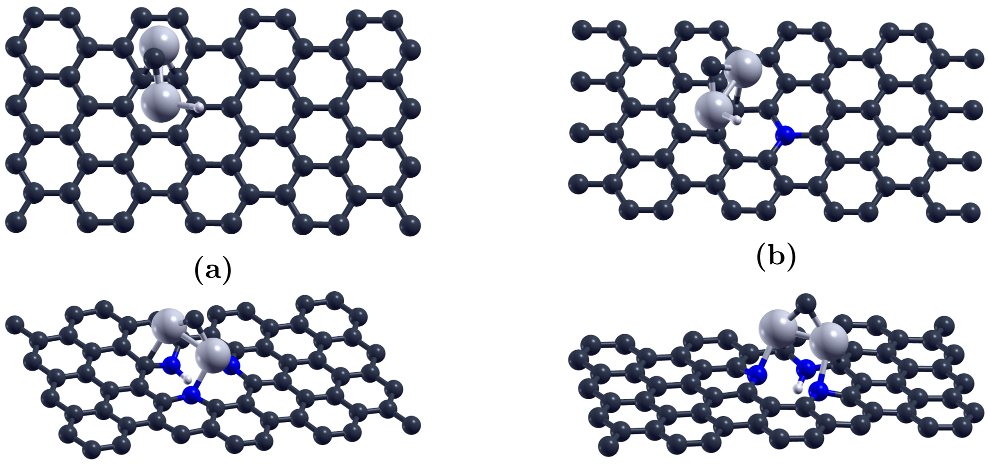
(a) (b) (c) (d)

**Figure. C.1.** ***a)*** *H adsorbed on Mo$_2$C@Graphene, model: Mo$_2$C@G.* ***b)*** *H adsorbed on Mo$_2$C@Graphitic, model: Mo$_2$C@G.* ***c)*** *H adsorbed on Mo$_2$C cluster attached at a three pyridinic atoms around one vacancy defect in a graphene layer, model: Mo$_2$C@P3N-1.* ***d)*** *H adsorbed on Mo$_2$C cluster attached at a three pyridinic atoms around one vacancy defect in a graphene layer, model: Mo$_2$C@P3N-2. Molybdenum and carbon atoms are represented in light and dark gray, respectively, while nitrogen ones are displayed in blue.*

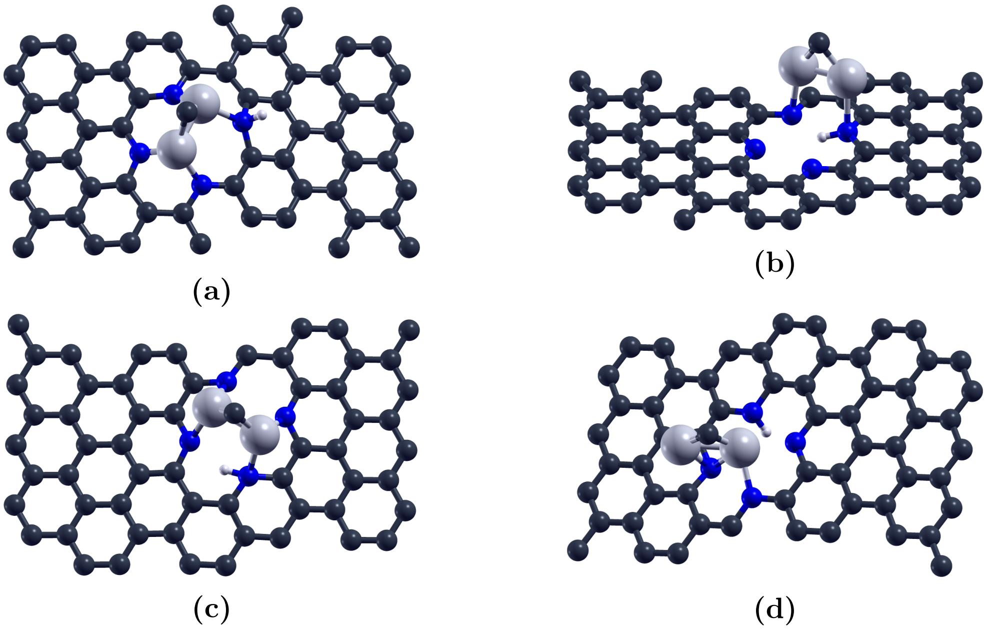

**Figure. C.2.** ***a)*** *H adsorbed on $Mo_2C$ cluster attached at a four pyridinic atoms around a two vacancy defect in a graphene layer, model: $Mo_2C$@P2V4N-1.* ***b)*** *H adsorbed on $Mo_2C$ cluster attached at a four pyridinic atoms around a two vacancy defect in a graphene layer, model: $Mo_2C$@P2V4N-2.* ***c)*** *H adsorbed on $Mo_2C$ cluster attached at a four pyridinic atoms around a two vacancy defect in a graphene layer, model: $Mo_2C$@P2V4N-3.* ***d)*** *H adsorbed on $Mo_2C$ cluster attached at a four pyridinic atoms around a two vacancy defect in a graphene layer, model: $Mo_2C$@P2V4N-4. Molybdenum and carbon atoms are represented in light and dark gray, respectively, while nitrogen ones are displayed in blue.*

# Appendix D

# $Mo_4C_2$-graphene type compounds

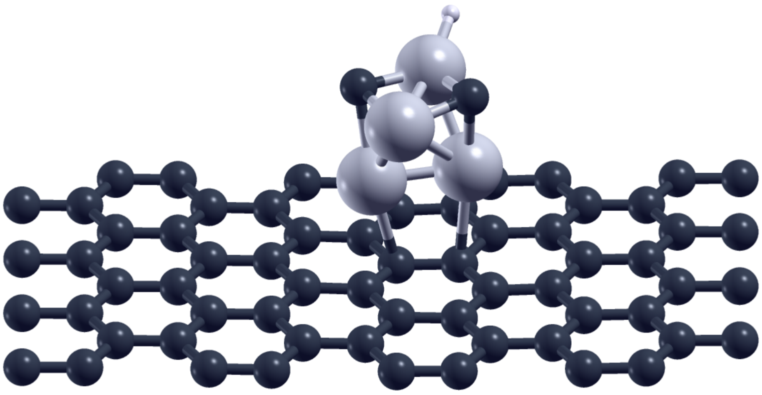

**Figure. D.1.** *H adsorbed on* $Mo_4C_2$ *cluster attached at a pure graphene surface, model:* $Mo_4C_2@G$*. Molybdenum and carbon atoms are represented in light and dark gray, respectively.*

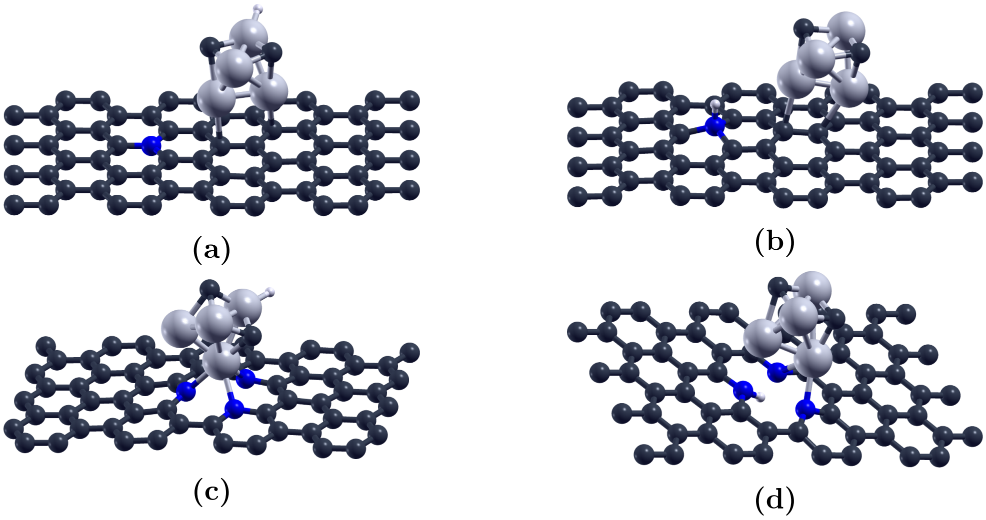

(a) (b) (c) (d)

**Figure. D.2.** ***a)*** *H adsorbed on the* $Mo_4C_2$*@Graphitic first model:* $Mo_2C$*@GN-1.* ***b)*** *H adsorbed on the* $Mo_4C_2$*@Graphitic second model:* $Mo_2C$*@GN-2.* ***c)*** *H adsorbed on a* $Mo_4C_2$ *cluster attached at a three pyridinic atoms around a one vacancy defect in a graphene layer, first model:* $Mo_2C$*@P3N-1.* ***d)*** *H adsorbed on a* $Mo_4C_2$ *cluster attached at a three pyridinic atoms around a one vacancy defect in a graphene layer, second model:* $Mo_2C$*@P3N-2. Molybdenum and carbon atoms are represented in light and dark gray, respectively, while nitrogen ones are displayed in blue.*

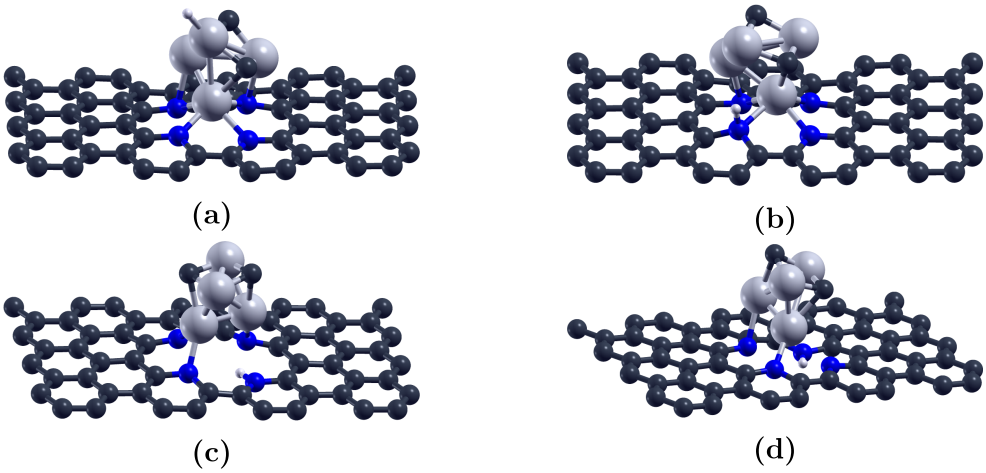

(a) (b) (c) (d)

**Figure. D.3.** *Four different models of hydrogen adsorption on a* $Mo_4C_2$ *cluster attached at a four pyridinic atoms around a two vacancy defect in a graphene layer,* ***a)*** $Mo_4C_2$*@P2V4N-1,* ***b)*** $Mo_4C_2$*@P2V4N-2,* ***c)*** $Mo_4C_2$*@P2V4N-3,* ***d)*** $Mo_4C_2$*@P2V4N-4. Molybdenum and carbon atoms are represented in light and dark gray, respectively, while nitrogen ones are displayed in blue.*

# Appendix E

# N-doped graphene deposited on the $Mo_2C$ (001) surface

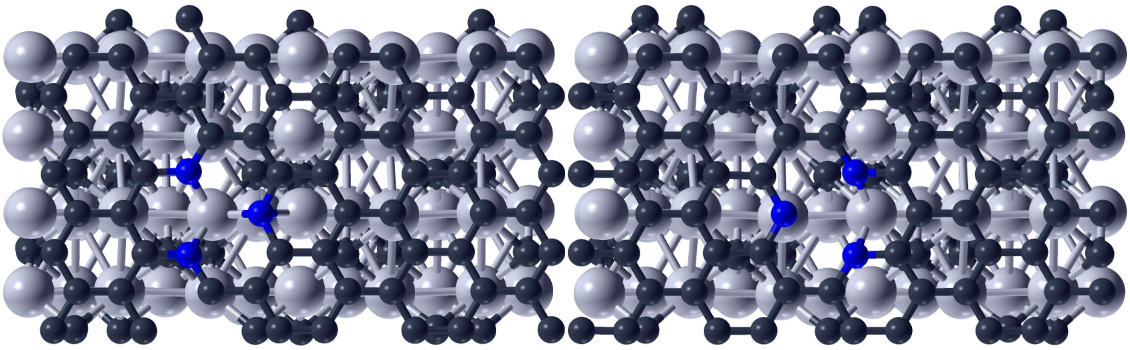

**(a)** N-Site A **(b)** N-Site B

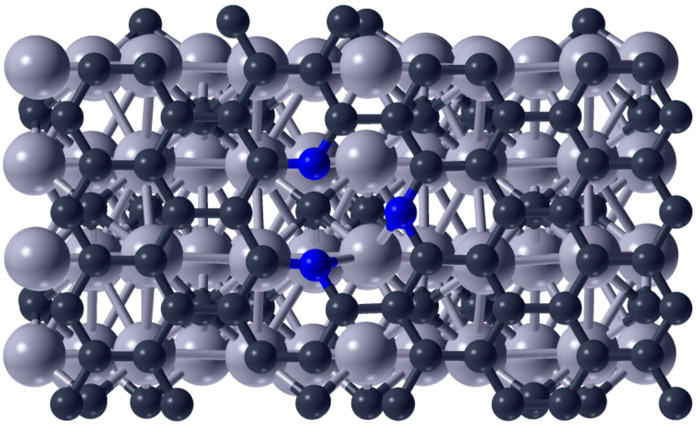

**(c)** N-Site C

**Figure. E.1.** *Top view of the three adsorption sites considered in the surface type P3N@$Mo_2C$-bulk. Molybdenum and carbon atoms are represented in light and dark gray, respectively, while nitrogen ones are displayed in blue.*

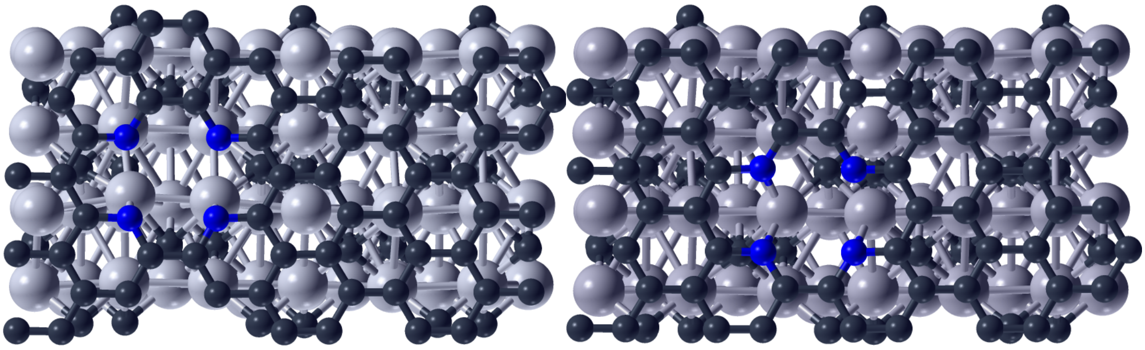

**(a)** N-Site A **(b)** N-Site B

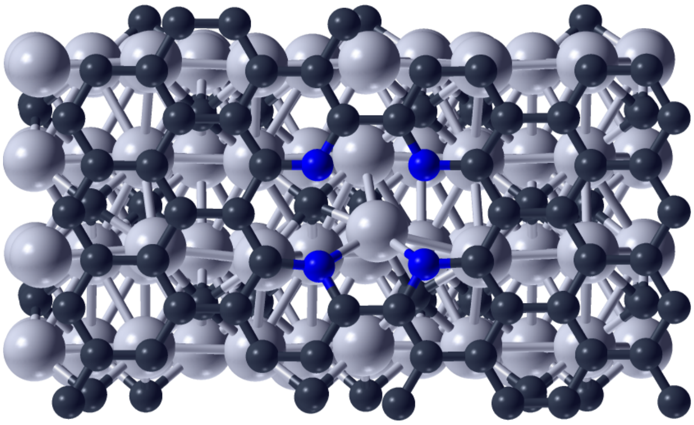

**(c)** N-Site C

**Figure. E.2.** *Top view of the three adsorption sites considered in the surface type P2V4N@*$Mo_2C$*-bulk. Molybdenum and carbon atoms are represented in light and dark gray, respectively, while nitrogen ones are displayed in blue.*

# Bibliography

[1] Razykov, T. M.; Ferekides, C. S.; Morel, D.; Stefanakos, E.; Ullal, H. S. and Upadhyaya, H. M. Solar Photovoltaic Electricity: Current Status and Future Prospects. *Solar Energy* **2011**, 85, 1580 - 1608.

[2] Stolten, D. and Emonts, B. Hydrogen Science and Engineering: Materials, Processes, Systems and Technologies. *Wiley-VCH Verlag GmbH & Co. KGaA* **2016**.

[3] Fujishima, A. and Honda, K. Electrochemical Photolysis of Water at a Semiconductor Electrode. *Nature* **1972**, 238, 37 - 38.

[4] Jafari, T.; Moharreri, E.; Amin, A. S.; Miao, R.; Song, W. and Suib, S. L. Photocatalytic Water Splitting - The Untamed Dream: A Review of Recent Advances. *Molecules* **2016**, 21, 900 - 928.

[5] Matsumoto, Y. and Sato, E. Electrocatalytic Properties of Transition Metal Oxides for Oxygen Evolution Reaction. *Mat. Chem. and Phys.* **1986**, 14, 397 - 426.

[6] Roy, N.; Sohn, Y.; Leung, K. T. and Pradhan, D. Engineered Electronic States of Transition Metal Doped $TiO_2$ Nanocrystals for Low Overpotential Oxygen Evolution Reaction. *J. Phys. Chem. C* **2014**, 118, 29499 - 29506.

[7] Hu, W.; Chen, S. and Xia, Q. $IrO_2$/Nb-$TiO_2$ Electrocatalyst for Oxygen Evolution Reaction in Acidic Medium. *Int. J. Hydrogen Energy* **2014**, 39, 6967 - 6976.

[8] Audichona, T.; Mayousse, E.; Napporn, T. W.; Moraisa, C.; Comminges, C. and Kokoha, K. B. Elaboration and Characterization of Ruthenium Nano-Oxides for the Oxygen Evolution Reaction in a Proton Exchange Membrane Water Electrolyzer Supplied by a Solar Profile. *Electrochim. Acta* **2014**, 132, 284 - 291.

[9] Lim, J. Y.; Rahman, G.; Chae, S. Y.; Lee, K. Y.; Kim, C. S and Joo, O. S. Highly Stable $RuO_2$/$SnO_2$ Nanocomposites as Anode Electrocatalysts in a PEM Water Electrolysis Cell. *Int. J. Energy Res.* **2014**, 38, 875 - 883.

[10] Stoerzinger, K. A.; Qiao, L.; Biegalski, M. D. and Shao-Horn, Y. Orientation-Dependent Oxygen Evolution Activities of Rutile $IrO_2$ and $RuO_2$. *J. Phys. Chem. Lett.* **2014**, 5, 1636 - 1641.

[11] Chen, J.; Li, Y. F.; Sit, P. and Selloni, A. Chemical Dynamics of the First Proton-Coupled Electron Transfer of Water Oxidation on $TiO_2$ Anatase. *J. Am. Chem. Soc.* **2013**, 135, 18774 - 18777.

[12] Jung, J. I.; Jeong, H. Y.; Lee, J. S.; Kim, M. G. and Cho, J. A Bifunctional Perovskite Catalyst for Oxygen Reduction and Evolution. *Angew. Chem., Int. Ed.* **2014**, 53, 4582 - 4586.

[13] Zhuang, Z.; Sheng, W. and Yan, Y. Synthesis of Monodisperse $Au@Co_3O_4$ Core-Shell Nanocrystals and Their Enhanced Catalytic Activity for Oxygen Evolution Reaction. *Adv. Mater.* **2014**, 26, 3950 - 3955.

[14] Gao, M.; Sheng, W.; Zhuang, Z.; Fang, Q.; Gu, S.; Jiang, J. and Yan, Y. Efficient Water Oxidation Using Nanostructured $\alpha$-Nickel-Hydroxide as an Electrocatalyst. *J. Am. Chem. Soc.* **2014**, 136, 7077 - 7084.

[15] Trotochaud, L.; Young, S. L.; Ranney, J. K. and Boettcher, S. W. Nickel-Iron Oxyhydroxide Oxygen-Evolution Electrocatalysts: The Role of Intentional and Incidental Iron Incorporation. *J. Am. Chem. Soc.* **2014**, 136, 6744 - 6753.

[16] Atkins, P. W. and de Paula, J. Physical Chemistry. *Oxford University Press: Oxford, UK* **1998**, 6th ed., Ch. 25 “Processes at Solid Surfaces”.

[17] Bockris, J. O’M. and Khan, S. U. M. Surface Electrochemistry, a Molecular Level Approach. *Plenum Press, New York* **1993**, Ch. 10.

[18] Zeng, K. and Zhang, D. Recent Progress in Alkaline Water Electrolysis for Hydrogen Production and Applications. *Progress in Energy and Combustion Science* **2010**, 36, 307 - 326.

[19] Miles, M. H.; Huang, Y. H. and Srinivasan, S. Oxygen-Electrode Reaction in Alkaline-Solutions on Oxide Electrodes Prepared by Thermal-Decomposition Method. *J. Electrochem. Soc.* **1978**, 125, 1931 - 1934.

[20] Damjanov, A.; Dey, A. and Bockris, J. O’M. Electrode Kinetics of Oxygen Evolution and Dissolution on Rh-Ir and Pt-Rh Alloy Electrodes. *J. Electrochem. Soc.* **1966**, 113, 739 - 746.

[21] Miles, M. H.; Kissel, G.; Lu, P. W. T. and Srinivasan, S. Effect of Temperature on Electrode Kinetic Parameters for Hydrogen and Oxygen Evolution Reactions on Nickel Electrodes in Alkaline Solutions. *J. Electrochem. Soc.* **1976**, 123, 332 - 336.

[22] Hamdani, M.; Pereira, M. I. S.; Douch, J.; Addi, A. A.; Berghoute, Y. and Mendonca, M. H. Physicochemical and Electrocatalytic Properties of Li–$Co_3O_4$ Anodes Prepared by Chemical Spray Pyrolysis for Application in Alkaline Water Electrolysis. *Electrochim. Acta* **2004**, 49, 1555 - 1563.

[23] Singh, R. N.; Mishra, D.; Anindita; Sinha, A. S. K. and Singh, A. Novel Electrocatalysts for Generating Oxygen from Alkaline Water Electrolysis. *Electrochem. Commun.* **2007**, 9, 1369 - 1373.

[24] El-Deab, M. S.; Awad, M. I.; Mohammad, A. M. and Ohsaka, T. Enhanced Water Electrolysis: Electrocatalytic Generation of Oxygen Gas at Manganese Oxide Nanorods Modified Electrodes. *Electrochem. Commun.* **2007**, 9, 2082 - 2087.

[25] Wendt, H.; Hofmann, H. and Plzak, V. Materials Research and Development of Electrocatalysts for Alkaline Water Electrolysis. *Mater. Chem. Phys.* **1989**, 22, 27 - 49.

[26] Bockris, J. O'M.; Conway, B. E.; Yeager, E. and White, R. E. Comprehensive Treatise of Electrochemistry. *New York: Plenum Press* **1981**.

[27] Krstajic, N.; Popovic, M.; Grgur, B.; Vojnovic, M. and Sepa, D. On the Kinetics of the Hydrogen Evolution Reaction on Nickel in Alkaline Solution - Part II. Effect of Temperature. *J. Electroanal. Chem.* **2001**, 512, 27 - 35.

[28] de Chialvo, M. R. G. and Chialvo, A. C. Hydrogen Evolution Reaction on a Smooth Iron Electrode in Alkaline Solution at Different Temperatures. *Phys. Chem. Chem. Phys.* **2001**, 3, 3180 - 3184.

[29] Lee, T. S. Hydrogen Overpotential on Pure Metals in Alkaline Solution. *J. Electrochem. Soc.* **1971**, 118, 1278 - 1282.

[30] Correia, A. N.; Machado, S. A. S. and Avaca, L. A. Studies of the Hydrogen Evolution Reaction on Smooth Co and Electrodeposited Ni-Co Ultramicroelectrodes. *Electrochem. Commun.* **1999**, 1, 600 - 604.

[31] Crnkovic, F. C.; Machado, S. A. S. and Avaca, L. A. Electrochemical and Morphological Studies of Electrodeposited Ni-Fe-Mo-Zn Alloys Tailored for Water Electrolysis. *Int. J. Hydrogen Energy* **2004**, 29, 249 - 254.

[32] Han, Q.; Liu, K.; Chen, J. and Wei, X. Hydrogen Evolution Reaction on Amorphous Ni-S-Co Alloy in Alkaline Medium. *Int. J. Hydrogen Energy* **2003**, 28, 1345 - 1352.

[33] Sheela, G.; Pushpavanam, M. and Pushpavanam, S. Zinc–Nickel Alloy Electrodeposits for Water Electrolysis. *Int. J. Hydrogen Energy* **2002**, 27, 627 - 363.

[34] Hu, W. Electrocatalytic Properties of New Electrocatalysts for Hydrogen Evolution in Alkaline Water Electrolysis. *Int. J. Hydrogen Energy* **2000**, 25, 111 - 118.

[35] Hu, W. and Lee, J. Y. Electrocatalytic Properties of $Ti_2Ni$/Ni-Mo Composite Electrodes for Hydrogen Evolution Reaction. *Int. J. Hydrogen Energy* **1998**, 23, 253 - 257.

[36] Los, P.; Rami, A. and Lasia, A. Hydrogen Evolution Reaction on Ni-Al Electrodes. *J. Appl. Electrochem.* **1993**, 23, 135 - 140.

[37] Raj, I. A. Nickel-Based, Binary-Composite Electrocatalysts for the Cathodes in the Energy-Efficient Industrial-Production of Hydrogen from Alkaline-Water Electrolytic Cells. *J. Mater. Sci.* **1993**, 28, 4375 - 4382.

[38] Wang, T. H.; Fang, Z.; Gist, N. W.; Li, S. and Dixon, D. A. Computational Study of the Hydrolysis Reactions of the Ground and First Excited Triplet States of Small $TiO_2$ Nanoclusters. *J. Phys. Chem. C* **2011**, 115, 9344 - 9360.

[39] Fang, Z. and Dixon, D. A. Computational Study of $H_2$ and $O_2$ Production from Water Splitting by Small $(MO_2)_n$ Clusters (M = Ti, Zr, Hf). *J. Phys. Chem. C* **2013**, 117, 3539 - 3555.

[40] Valdés, Á.; Brillet, J.; Gratzel, M.; Gudmundsdóttir, H.; Hansen, H. A.; Jónsson, H.; Klüpfel, P.; Kroes, G. J.; Le Formal, F.; Man, I. C.; Martins, R. S.; Nørskov, J. K.; Rossmeisl, J.; Sivula, K.; Vojvodicf, A. and Zächg, M. Solar Hydrogen Production with Semiconductor Metal Oxides: New Directions in Experiment and Theory. *Phys. Chem. Chem. Phys.* **2012**, 14, 49 - 70.

[41] Henderson, M. A. The Influence of Oxide Surface Structure on Adsorbate Chemistry: Desorption of Water from the Smooth, the Microfaceted and the Ion Sputtered Surfaces of $TiO_2$ (100). *Surf. Sci.* **1994**, 319, 315 - 328.

[42] Henderson, M. A. Structural Sensitivity in the Dissociation of Water on $TiO_2$ Single-Crystal Surfaces. *Langumir* **1996**, 12, 5093 - 5098.

[43] Henderson, M. A. An HREELS and TPD Study of Water on $TiO_2$ (110): The Extent of Molecular Versus Dissociative Adsorption. *Surf. Sci.* **1996**, 355, 151 - 166.

[44] Henderson, M. A. Acetone and Water on $TiO_2$ (110): Competition for Sites. *Langmuir* **2005**, 21, 3443 - 3450.

[45] Henrich, V. E.; Dresselhaus, G. and Ziger, H. J. Chemisorbed Phases of $H_2O$ on $TiO_2$ and $SrTiO_3$. *Solid State Commun.* **1977**, 24, 623 - 626.

[46] Kurtz, R. L.; Stockbauer, R.; Madey, T. E.; Roman, E. and de Segovia, J. L. Synchrotron Radiation Studies of $H_2O$ Adsorption on $TiO_2$ (110). *Surf. Sci.* **1989**, 218, 178 - 200.

[47] Lo, W. J.; Chung, Y. W. and Somorjai, G. A. Electron Spectroscopy Studies of the Chemisorption of $O_2$, $H_2$ and $H_2O$ on the $TiO_2$ (100) Surfaces With Varied Stoichiometry: Evidence for the Photogeneration of $Ti^{+3}$ and for Its Importance in Chemisorption. *Surf. Sci.* **1978**, 71, 199 - 219.

[48] Muryn, C. A.; Tirvengadum, G.; Crouch, J. J.; Warburton, D. R.; Raiker, G. N.; Thornton, G. and Law, D. S. L. $TiO_2$ (100) Structure-Reactivity Relationship. *J. Phys.: Condens. Matter* **1989**, 1, SB127 - SB132.

[49] Muryn, C. A.; Hardman, P. J.; Coruch, J. J.; Raiker, G. N.; Thornton, G. and Law, D. S. L. Step and Point Defect Effects on $TiO_2$ (100) Reactivity. *Surf. Sci.* **1991**, 251, 747 - 752.

[50] Thornton, G. Molecular Adsorption on $TiO_2$ and ZnO Surfaces. *Springer Ser. Surf. Sci.* **1993**, 33, 115 - 124.

[51] Anpo, M.; Shima, T. and Kubokawa, Y. ESR and Photo-Luminescence Evidence for the Photocatalytic Formation of $OH^\bullet$ Radicals on Small $TiO_2$ Particles. *Chem. Lett.* **1985**, 12, 1799 - 1802.

[52] Jaeger, C. D.; Bard, A. J. Spin Trapping and Electron Spin Resonance Detection of Radical Intermediates in the Photo-Decomposition of Water at Titanium Dioxide Particulate Systems. *J. Phys. Chem.* **1979**, 83, 3146 - 3152.

[53] Fujishima, A.; Rao, T. N.; Tryk, D. A. Titanium Dioxide Photocatalysis. *J. Photochem. Photobiol. C: Photochem. Rev.* **2000**, 1, 1 - 21.

[54] Salvador, P. and Gutiérrez, C. The Role of Surface State in the Electroreduction of Dissolved and/or Photogenerated Oxygen on $n$-$TiO_2$ Electrodes. *Chem. Phys. Lett.* **1982**, 86, 131 - 134.

[55] Salvador, P. and Gutierrez, C. The Nature of Surface States Involved in the Photo- and Electroluminescence Spectra of $n$-Titanium Dioxide Electrodes. *J. Phys. Chem.* **1984**, 88, 3696 - 3698.

[56] Nakamura, R. and Nakato, Y. Primary Intermediates of Oxygen Photoevolution Reaction on $TiO_2$ (Rutile) Particles, Revealed by in Situ FTIR Absorption and Photoluminescence Measurements. *J. Am. Chem. Soc.* **2004**, 126, 1290 - 1298.

[57] Tang, J.; Durrant, J. R. and Klug, D. R. Mechanism of Photocatalytic Water Splitting in $TiO_2$. Reaction of Water with Photoholes, Importance of Charge Carrier Dynamics, and Evidence for Four-Hole Chemistry. *J. Am. Chem. Soc.* **2008**, 130, 13885 - 13891.

[58] Tang, J.; Cowan, A. J.; Durrant, J. R. and Klug, D. R. Mechanism of $O_2$ Production from Water Splitting: Nature of Charge Carriers in Nitrogen Doped Nanocrystalline $TiO_2$ Films and Factors Limiting $O_2$ Production. *J. Phys. Chem. C* **2011**, 115, 3143 - 3150.

[59] Zheng, Y.; Jiao, Y.; Zhu, Y.; Li, L. H.; Han, Y.; Chen, Y.; Du, A.; Jaroniec, M. and Qiao, S. Z. Hydrogen Evolution by a Metal-Free Electrocatalyst. *Nature Commun.* **2014**, 5, 3783 - 3791.

[60] Zhuo, J.; Wang, T.; Zhang, G.; Liu, L.; Gan, L. and Li, M. Salts of $C_60(OH)_8$ Electrodeposited onto a Glassy Carbon Electrode: Surprising Catalytic Performance in the Hydrogen Evolution Reaction. *Angew. Chem. Int. Ed.* **2013**, 52, 10867 - 10870.

[61] Cook, T. R.; Dogutan, D. K.; Reece, S. Y.; Surendranath, Y.; Teets, T. S. and Nocera, D. G. Solar Energy Supply and Storage for the Legacy and Nonlegacy worlds. *Chem. Rev.* **2010**, 110, 6474 - 6502.

[62] Artero, V.; Chavarot-Kerlidou, M. and Fontecave, M. Splitting Water with Cobalt. *Angew. Chem. Int. Ed.* **2011**, 50, 7238 - 7266.

[63] Gong, K.; Du, F.; Xia, Z.; Durstock, M. and Dai, L. Nitrogen-Doped Carbon Nanotube Arrays With High Electrocatalytic Activity for Oxygen Reduction. *Science* **2009**, 323, 760 - 764.

[64] Mirzakulova, E.; Khatmullin, R.; Walpita, J.; Corrigan, T.; Vargas-Barbosa, N. M.; Vyas, S.; Oottikkal, S.; Manzer, S. F.; Hadad, C. M. and Glusac., K. D. Electrode-Assisted Catalytic Water Oxidation by a Flavin Derivative. *Nature. Chem.* **2012**, 4, 794 - 801.

[65] Zhao, Y.; Nakamura, R.; Kamiya, K.; Nakanishi, S. and Hashimoto, K. Nitrogen-Doped Carbon Nanomaterials as Non-Metal Electrocatalysts for Water Oxidation. *Nature. Commun.* **2013**, 4, 2390 - 2396.

[66] Zheng, Y.; Jiao, Y.; Chen, J.; Liu, J.; Liang, J.; Du, A.; Zhang, W.; Zhu, Z.; Smith, S. C.; Jaroniec, M.; Lu, G. Q. and Qiao, S. Z. Nanoporous Graphitic-$C_3N_4$@Carbon Metal-Free Electrocatalysts for Highly Efficient Oxygen Reduction. *J. Am. Chem. Soc.* **2011**, 133, 20116 - 20119.

[67] Valdés, Á.; Qu, Z.; Kroes, G. J.; Rossmeisl, J. and Nørskov, J. K. Oxidation and Photo-Oxidation of Water on $TiO_2$ Surface. *J. Phys. Chem. C* **2008**, 112, 9872 - 9879.

[68] García-Mota, M.; Vojvodic, A.; Metiu, H.; Man, I. C.; Su, H. Y.; Rossmeisl, J. and Nørskov, J. K. Tailoring the Activity for Oxygen Evolution Electrocatalysis on Rutile $TiO_2$ (110) by Transition-Metal Substitution. *ChemCatChem* **2011**, 3, 1607 - 1611.

[69] Li, Y.; Liu, Z.; Liu, L. and Gao, W. Mechanism and Activity of Photocatalytic Oxygen Evolution on Titania Anatase in Aqueous Surroundings. *J. Am. Chem. Soc.* **2010**, 132, 13008 - 13015.

[70] Skúlason, E.; Tripkovic, V.; Björketun, M. E.; Gudmundsdóttir, S.; Karlberg, G.; Rossmeisl, J.; Bligaard, T.; Jónsson, H. and Nørskov, J. K. Modeling the Electrochemical Hydrogen Oxidation and Evolution Reactions on the Basis of Density Functional Theory Calculations. *J. Phys. Chem. C* **2010**, 114, 18182 - 18197.

[71] Rodríguez-Hernández, F.; Tranca, D. C.; Szyja, B. M.; van Santen, R. A.; Martínez-Mesa, A.; Uranga-Piña, Ll. and Seifert, G. Water Splitting on $TiO_2$-Based Electrochemical Cells: A Small Cluster Study. *J. Phys. Chem. C* **2016**, 120, 437 - 449.

[72] Rodríguez-Hernández, F.; Tranca, D. C.; Martínez-Mesa, A.; Uranga-Piña, Ll. and Seifert, G. Water Splitting on Transition Metal Active Sites at $TiO_2$-Based Electrodes: A Small Cluster Study. *J. Phys. Chem. C* **2016**, 120, 25851 - 25860.

[73] Lu, C.; Tranca, D.; Zhang, J.; Rodríguez-Hernández, F.; Su, Y.; Zhuang, X.; Zhang, F.; Seifert, G. and Feng, X. Molybdenum Carbide-Embedded Nitrogen-Doped Porous Carbon Nanosheets as Electrocatalysts for Water Splitting in Alkaline Media. *ACSNano* **2017**, 11, 3933 - 3942.

[74] Deutschmann, O. Modeling and Simulation of Heterogeneous Catalytic Reactions: From the Molecular Process to the Technical Systems. *Wiley-VCH Verlag GmbH & Co.* **2011**, Ch.1 “Keith, J. A.; Anton, J. Kaghazchi, P. and

Jacob, T. Modeling Catalytic Reactions on Surfaces with Density Functional Theory".

[75] Sholl, D. S. and Steckel, J. A. Density Functional Theory. A Practical Introduction. *John Wiley & Sons* **2009**.

[76] Laidler, K. J. and King, M. C. The development of Transition-State Theory. *J. Phys. Chem.* **1983**, 87, 2657 - 2664.

[77] Truhlar, D. G.; Garret, B. C. and Klippenstein, S. J. Current Status of Transition-State Theory. *J. Phys. Chem.* **1996**, 100, 12771 - 12800.

[78] Gao, J. Hybrid Quantum and Molecular Mechanical Simulations: An Alternative Avenue to Solvent Effects in Organic Chemistry. *Acc. Chem. Res.* **1996**, 29, 298 - 305.

[79] Gao, J. Methods and Applications of Combined Quantum Mechanical and Molecular Mechanical Potentials. *Rev. Comput. Chem.* **1996**, 7, 119 - 185.

[80] Car, R. and Parrinello, M. Unified Approach for Molecular Dynamics and Density-Functional Theory. *Phys. Rev. Lett.* **1985**, 55, 2471 - 2474.

[81] Field, M. J.; Bash, P. A. and Karplus, M. A Combined Quantum Mechanical and Molecular Mechanical Potential for Molecular Dynamics Simulations. *J. Comput. Chem.* **1990**, 11, 700 - 733.

[82] Gao, J. and Xia, X. A Priori Evaluation of Aqueous Polarization Effects Through Monte Carlo QM-MM Simulations. *Science* **1992**, 258, 631 - 635.

[83] Dupuis, M.; Schenter, G. K.; Garrett, B. G. and Arcia, E. E. Potentials of Mean Force with Ab Initio Mixed Hamiltonian Models of Solvation. *J. Mol. Struct. Theochem.* **2003**, 632, 173 - 183.

[84] Moriarty, N.W. and Karlström, G. Electronic Polarization of a Water Molecule in Water. A Combined Quantum Chemical and Statistical Mechanical Treatment. *J. Phys. Chem.* **1996**, 100, 17791 - 17796.

[85] Moriarty, N.W. and Karlström, G. Geometry Optimization of a Water Molecule in Water. A Combined Quantum Chemical and Statistical Mechanical Treatment. *J. Chem. Phys.* **1997**, 106, 6470 - 6474.

[86] Tomasi, J. and Persico, M. Molecular Interactions in Solution: An Overview of Methods Based on Continuous Distributions of the Solvent. *Chem. Rev.* **1994**, 94, 2027 - 2094.

[87] Cramer, C. J. and Truhlar, D. G. Implicit Solvation Models: Equilibria, Structure, Spectra, and Dynamics. *Chem. Rev.* **1999**, 99, 2161 - 2200.

[88] Béguin, F. and Frackowiak, E. Supercapacitors: Materials, Systems and Applications. *Wiley-VCH Verlag GmbH & Co.* **2013**, Ch.1 "Donne, S. W. General Principles of Electrochemistry".

[89] Bard, A. J. Photoelectrochemistry and Heterogeneous Photo-Catalysis at Semiconductors. *J. Photochem.* **1979**, 10, 59 - 75.

[90] Atkins, P. W. and de Paula, J. Physical Chemistry. *Oxford University Press: Oxford, UK* **1998**, 6th ed., pp 485, 925 - 927, 942.

[91] Sato, N. Electrochemistry at Metal and Semiconductor Electrodes. *Elsevier, Amsterdam* **1998**.

[92] Newman, J. S. Electrochemical Systems. *Prentice-Hall, Englewood Cliffs, N. J.* **1991**, 2nd edition, p. 496.

[93] Gerischer, H. Electrochemical Photo and Solar Cells Principles and Some Experiments. *J. Electroanal. Chem.* **1975**, 58, 263 - 274.

[94] Lohmann, F. Z. Fermi-Niveau und Flachbandpotential von Molekülkristallen Aromatischer Kohlenwasserstoffe. *Naturforsch.* **1967**, 22A, 843 - 844.

[95] Nozik, A. J. and Memming, R. Physical Chemistry of Semiconductor-Liquid Interfaces. *J. Phys. Chem.* **1996**, 100, 13061 - 13078.

[96] Bard, A. J.; Stratmann, M. and Licht, S. Encyclopedia of Electrochemistry Vol. 6, Semiconductor Electrodes and Photoeletrochemistry. *Wiley VCH Verlag GmbH, Weinheim* **2002**.

[97] Tan, M. X.; Laibinis, P. E.; Nguyen, S. T.; Kesselman, J. M. Stanton, C. E. and Lewis, N. S. Principles and Applications of Semiconductor Photoelectrochemistry. *Prog. Inorg. Chem.* **1994**, 41, 21 - 144.

[98] Neyerlin, K. C.; Gu, W. B.; Jorne, J. and Gasteiger, H. A. Study of the Exchange Current Density for the Hydrogen Oxidation and Evolution Reactions. *J. Electrochem. Soc.* **2007**, 154, B631 - B635.

[99] Doyle, R. L. and Lyons, M. E. G. “The Oxygen Evolution Reaction: Mechanistic Concepts and Catalyst Design” in “Photoelectrochemical Solar Fuel Production. From Basic Principles to Advanced Devices”, edited by Giménez, S. and Bisquert, J. *Springer International Publishing Switzerland* **2016**.

[100] Bockris, J. O’M. and Otagawa, T. Mechanism of Oxygen Evolution on Perovskites. *J. Phys. Chem.* **1983**, 87, 2960 - 2971.

[101] Krasil’shchikov, A. I. Intermediate Stages in the Anodic Evolution of Oxygen. *Zh. Fiz. Khim.* **1963**, 37, 531 - 537.

[102] Kobussen A. G. C. and Broers G. H. J. The Oxygen Evolution on $La_{0.5}Ba_{0.5}CoO_3$: Theoretical Impedance Behavior For a Multi-Step Mechanism Involving Two Adsorbates. *J. Electroanal. Chem.* **1981**, 126, 221 - 240.

[103] Willems, H.; Kobussen, A. G. C.; De Wit, J. H. W. and Broers, G. H. J. The Oxygen Evolution Reaction on Cobalt. Part 1. Reaction Order Experiments and Impedance Measurements. *J. Electroanal. Chem.* **1984**, 170, 227 - 242.

[104] O'Grady, W.; Iwakura, C.; Huang, J. and Yeager, E. In: Breiter, M. W. (ed) Proceedings of the Symposium on Electrocatalysis. *The Electrochemical Soc. Inc., Pennington, N. J.* **1974**, p-286.

[105] Guidelli, R.; Compton, R. G.; Feliu, J. M.; Gileadi, E.; Lipkowski, J.; Schmickler, W. and Trasatti, S. Defining the Transfer Coefficient in Electrochemistry: an Assessment (IUPAC Technical Report). *Pure Appl. Chem.* **2014**, 86, 245 - 258.

[106] Guidelli, R.; Compton, R. G.; Feliu, J. M.; Gileadi, E.; Lipkowski, J.; Schmickler, W. and Trasatti, S. Definition of the Transfer Coefficient in Electrochemistry (IUPAC Recommendations). *Pure Appl. Chem.* **2014**, 86, 259 - 262.

[107] Lyons, M. E. G. and Brandon, M. P. Redox Switching and Oxygen Evolution Electrocatalysis in Polymeric Iron Oxyhydroxide Films. *Phys. Chem. Chem. Phys.* **2009**, 11, 2203 - 2217.

[108] Conway B. E. and Gileadi, E. Kinetic Theory of Pseudo-Capacitance and Electrode Reactions at Appreciable Surface Coverage. *Trans. Faraday Soc.* **1962**, 58, 2493 - 2509.

[109] Nørskov, J. K.; Rossmeisl, J.; Logadottir, A.; Lindqvist, L.; Kitchin, J. R.; Bligaard, T. and Jónsson, H. Origin of the Overpotential for Oxygen Reduction at a Fuel-Cell Cathode. *J. Chem. Phys. B* **2004**, 108, 17886 - 17892.

[110] Rossmeisl, J.; Logadottir, A. and Nørskov, J. K. Electrolysis of Water on (Oxidized) Metal Surfaces. *Chem. Phys.* **2005**, 319, 178 - 184.

[111] Rossmeisl, J.; Qu, Z. W.; Zhu, H.; Kroes, G. J. and Nørskov, J. K. Electrolysis of Water on Oxide Surfaces. *J. Electroanal. Chem.* **2007**, 607, 83 - 89.

[112] Valdeś, Á.; Qu, Z. W.; Kroes, G. J.; Rossmeisl, J. and Nørskov, J. K. Oxidation and Photo-Oxidation of Water on $TiO_2$. *J. Phys. Chem. C* **2008**, 112, 9872 - 9879.

[113] Valdeś, Á. and Kroes, G. J. First Principles Study of the Photo-Oxidation of Water on Tungsten trioxide ($WO_3$). *J. Chem. Phys.* **2009**, 130, 114701 - 114709.

[114] Nørskov, J. K.; Bligaarda, T.; Logadottira, A.; Kitchinb, J. R.; Chenb, J. G.; Pandelovc, S. and Stimming, U. Trends in the Exchange Current for Hydrogen Evolution. *J. Electrochem. Soc.* **2005**, 152, J23 - J26.

[115] Desai, S. K. and Neurock, M. First-Principles Study of the Role of Solvent in the Dissociation of Water Over a Pt-Ru Alloy. *Phys. Rev. B* **2003**, 68, 075420 - 075425.

[116] Shinagawa, T.; Garcia-Esparza, A. T. and Takanabe, K. Insight on Tafel Slopes from a Microkinetic Analysis of Aqueous Electrocatalysis for Energy Conversion. *Scientific Report* **2015**, 5, 13801 - 13821.

[117] Trasatti, S. Work Function, Electronegativity, and Electrochemical Behavior of Metals: III. Electrolytic Hydrogen Evolution in Acid Solutions. *J. Electroanal. Chem.* **1972**, 39, 163 - 184.

[118] Bowden, F. P. and Rideal, E. K. The Electrolytic Behavior of Thin Films. Part I. Hydrogen. *Proc. R. Soc. Math. Phys. Eng. Sci.* **1928**, 120, 59 - 79.

[119] Seh, Z. W.; Kibsgaard, J.; Dickens, C. F.; Chorkendorff, I.; Nørskov, J. K. and Jaramillo, T. F. Combining Theory and Experiment in Electrocatalysis: Insights into Materials Design. *Science* **2017**, 355, 146 - 159.

[120] Parsons, R. The Rate of Electrolytic Hydrogen Evolution and the Heat of Adsorption of Hydrogen. *Trans. Faraday Soc.* **1958**, 54, 1053 - 1063.

[121] Skúlason, E.; Karlberg, G. S.; Rossmeisl, J.; Bligaard, T.; Greeley, J.; Jonsson, H. and Nørskov, J. K. Density Functional Theory Calculations for the Hydrogen Evolution Reaction in an Electrochemical Double Layer on the Pt(111) Electrode. *Phys. Chem. Chem. Phys.* **2007**, 9, 3241 - 3250.

[122] Bajdich, M.; García-Mota, M.; Vojvodic, A.; Nørskov, J. K. and Bell, A. T. Theoretical Investigation of the Activity of Cobalt Oxides for the Electrochemical Oxidation of Water. *J. Am. Chem. Soc.* **2013**, 135, 13521 - 13530.

[123] Springborg, M. Methods of Electronic-Structure Calculations: from Molecules to Solids. *John Wiley & Sons Ltd, England* **2000**.

[124] Kohanoff, J. Electronic Structure Calculations for Solids and Molecules: Theory and Computational Methods. *Cambridge University Press* **2006**.

[125] Cohen-Tannoudji, C.; Diu, B. and Laloë, F. Quantum Mechanics. *Wiley-VCH* **2005**, Vol. 1.

[126] Koch, W. and Holthausen, M. C. A Chemist's Guide to Density Functional Theory. *2nd edn, Wiley-VCH Verlag GmbH* **2001**, pp. 72 - 74.

[127] Perdew, J. P. and Wang, Y. Accurate and Simple Density Functional for the Electronic Exchange Energy: Generalized Gradient Approximation. *Phys. Rev. B* **1986**, 33, 8800 - 8802.

[128] Becke, A. D. Density-Functional Exchange-Energy Approximation with Correct Asymptotic Behavior. *Phys. Rev. A* **1988**, 38, 3098 - 3100.

[129] Kutzler, F. W. and Painter, G. S. Energies of Atoms with Nonspherical Charge Densities Calculated with Nonlocal Density-Functional Theory. *Phys. Rev. Lett.* **1987**, 59, 1285 - 1288.

[130] Mlynarski, P. and Salahub, D. R. Self-Consistent Implementation of Nonlocal Exchange and Correlation in a Gaussian Density-Functional Method. *Phys. Rev. B* **1991**, 43, 1399 - 1410.

[131] Perdew, J. P.; Chevary, J. A.; Vosko, S. H.; Jackson, K. A.; Pederson, M. R.; Singh, D. J. and Fiolhais, C. Atoms, Molecules, Solids, and Surfaces: Applications of the Generalized Gradient Approximation for Exchange and Correlation. *Phys. Rev. B* **1992**, 46, 6671 - 6687.

[132] Kong, X. J.; Chan, C. T.; Ho, K. M. and Ye, Y. Y. Cohesive Properties of Crystalline Solids by the Generalized Gradient Approximation. *Phys. Rev B* **1990**, 42, 9357 - 9364.

[133] Ortiz, G. Gradient-Corrected Pseudopotential Calculations in Semiconductors. *Phys. Rev. B* **1992**, 45, 11328 - 11331.

[134] García, A.; Elsässer, Ch.; Zhu, J.; Louie, S. G. and Cohen, M. L. Use of Gradient-Corrected Functionals in Total-Energy Calculations for Solids. *Phys. Rev. B* **1992**, 46, 9829 - 9832.

[135] Kutzler, F. W. and Painter, G. S. Interconfigurational Energies in Transition-Metal Atoms Using Gradient-Corrected Density-Functional Theory. *Phys. Rev. B* **1991**, 43, 6865 - 6872.

[136] Becke, A. D. Density-Functional Thermochemistry. I. The Effect of the Exchange-Only Gradient Correction. *J. Chem. Phys.* **1992**, 96, 2155 - 2160.

[137] Becke, A. D. Density-Functional Thermochemistry. II. The Effect of the Perdew-Wang Generalized-Gradient Correlation Correction *J. Chem. Phys.* **1992**, 97, 9173 - 9177.

[138] Becke, A. D. Density-Functional Thermochemistry. III. The Role of Exact Exchange. *J. Chem. Phys.* **1993**, 98, 5648 - 5652.

[139] Levy, M. and Perdew, J. P. Tight Bound and Convexity Constraint on the Exchange-Correlation-Energy Functional in the Low-Density Limit, and Other Formal Tests of Generalized-Gradient Approximations. *Phys. Rev. B* **1993**, 48, 11638 - 11645.

[140] Lee, C.; Yang, W. and Parr, R. G. Development of the Colle-Salvetti Correlation-Energy Formula into a Functional of the Electron Density. *Phys. Rev. B* **1988**, 37, 785 - 789.

[141] Stephens, P. J.; Devlin, F. J.; Chabalowski, C. F. and Frisch, M. J. Ab Initio Calculation of Vibrational Absorption and Circular Dichroism Spectra Using Density Functional Force Fields. *J. Phys. Chem.* **1994**, 98, 11623 - 11627.

[142] Cohen, A. J.; Mori-Sánchez, P. and Yang, W. Challenges for Density Functional Theory. *Chem. Rev.* **2012**, 112, 289 - 320.

[143] Press, W.H.; Teukolsky, S.A.; Vetterling, W.T. and Flannery, B.P. Numerical Recipes in Fortran 77: The Art of Scientific Computing. *University Press, Cambridge* **1996**, 2nd edn.

[144] Payne, M.C.; Teter, M.P.; Allan, D.C.; Arias, T.A. and Joannopoulos, J.D. Iterative Minimization Techniques for Ab Initio Total-Energy Calculations: Molecular Dynamics and Conjugate Gradients. *Rev. Mod. Phys.* **1992**, 64, 1045 - 1097.

[145] Heine, V. The Pseudopotential Concept, in Ehrenreich, H.; Seitz, F. and Turnbull, D. Solid State Physics. *Academic Press, New York* **1970**, vol. 24, 1 - 36.

[146] Sauer, J. Molecular Models in Ab Initio Studies of Solids and Surfaces: from Ionic Crystals and Semiconductors to Catalysts. *Chem. Rev.* **1989**, 89, 199 - 255.

[147] Walch, S. P. Model Studies of the Interaction of H Atoms with Bcc Iron. *Surf. Sci.* **1984**, 143, 188 - 203.

[148] Blomberg, M. R. A.; Brandemark, U. B.; Siegbahn, P. E. M.; Mathisen, K. B. and Karlstrom, G. Interaction Between Nickel and the Ligand Groups Carbonyl, Water, and Phosphine. *J. Phys. Chem.* **1985**, 89, 2171 - 2180.

[149] Sauer, J.; Haberlandt, I. H. and Pacchioni, G. Bonding of Water Ligands to Copper and Nickel Atoms: Crucial Role of Intermolecular Electron Correlation. *J. Phvs. Chem.* **1986**, 90, 3051 - 3052.

[150] Čársky, P. and Dedieu, A. Ab Initio SCF Study of the Vibrational Spectra of Nickel Carbonyls $Ni(CO)_n$, $n = 1$ - 4. *Chem. Phys.* **1986**, 103, 265 - 275.

[151] Seifert, G.; Müller, H. and Großmann, G. Cluster Calculations as a Model for Adsorption on Metal Surfaces. *Proceedings of the 9th Annual International Symposium on Electronic Structure of Metals and Alloys* **1979**, 50 - 58.

[152] Seifert, G.; Großmann, G. and Müller, H. SCF-SW-X$\alpha$ Calculations on Molybdenum-Halogen Cluster Compounds. *Journal of Molecular Stnrcture* **1980**, 64, 93 - 102.

[153] Chester, M. A.; Lennon, D.; Ackermann, L.; Häberlen, O; Krüger, S. and Rösch, N. The Adsorption of Sulfur on Nickel: an Electron Energy Loss Spectroscopy Investigation of Ni(110)/c(2×2)S and a LCGTO-LDF Cluster Model Study. *Surf. Sci.* **1993**, 291, 177 - 184.

[154] Rösch, N.; Neyman, K. M.; Birkenheuer, S.; Krüger, S. and Nasluzov, V. A. Density Functional Cluster and Slab Model Studies of Catalysis-Relevant Adsorption Phenomena on Metal and Oxide Surfaces. *Kinetics and Catalysis* **1996**, 37, 651 - 660.

[155] Nozik, A. J. Photoelectrolysis of Water Using Semiconducting $TiO_2$ Crystals. *Nature* **1975**, 257, 383 - 386.

[156] Valdés, Á. and Kroes, G. J. Cluster Study of the Photo-Oxidation of Water on Rutile Titanium Dioxide ($TiO_2$). *J. Phys. Chem. C* **2010**, 114, 1701 - 1708.

[157] Neumann, B.; Bogdanoff, P.; Tributsch, H.; Sakthivel, S. and Kisch, H. Electrochemical Mass Spectroscopic and Surface Photovoltage Studies of Catalytic Water Photooxidation by Undoped and Carbon-Doped Titania. *J. Phys. Chem. B* **2005**, 109, 16579 - 16586.

[158] Volodin, A. M. Photoinduced Phenomena on the Surface of Wide-Band-Gap Oxide Catalysts. *Catal. Today* **2000**, 58, 103 - 114.

[159] Umebayashi, T.; Yamaki, T.; Itoh, H. and Asai, K. Band Gap Narrowing of Titanium Dioxide by Sulfur Doping. *Appl. Phys. Lett.* **2002**, 81, 454 - 456.

[160] Khan, S. U. M.; Al-Shahry, M. and Ingler, W. B. Jr. Efficient Photochemical Water Splitting by a Chemically Modified $n$-$TiO_2$. *Science* **2002**, 297, 2243 - 2246.

[161] Ohno, T.; Mitsui, T. and Matsumura, M. Photocatalytic Activity of S-doped $TiO_2$ Photocatalyst under Visible Light. *Chem. Lett.* **2003**, 32, 364 - 365.

[162] Sakthivel, S. and Kisch, H. Daylight Photocatalysis by Carbon-Modified Titanium Dioxide. *Ang. Chem., Int. Ed.* **2003**, 42, 4908 - 4911.

[163] Serpone, N. Is the Band Gap of Pristine $TiO_2$ Narrowed by Anion- and Cation-Doping of Titanium Dioxide in Second-Generation Photocatalysts? *J. Phys. Chem. B* **2006**, 110, 24287 - 24293.

[164] Paulose, M.; Mor, G. K.; Varghese, O. K.; Shankar, K. and Grimes, C. A. Visible Light Photoelectrochemical and Water-Photoelectrolysis Properties of Titania Nanotube Arrays. *J. Photochem. Photobiol. A* **2006**, 178, 8 - 15.

[165] Man, I. C.; Su, H.; Calle-Vallejo, F.; Hansen, H. A.; Martínez, J. I.; Inoglu, N. G.; Kitchin, J.; Jaramillo, T. F.; Nørskov, J. K. and Rossmeisl, J. Universality in Oxygen Evolution Electrocatalysis on Oxide Surfaces. *ChemCatChem* **2011**, 3, 1159 - 1165.

[166] Dunning, T. H. Gaussian Basis Functions for Use in Molecular Calculations. III. Contraction of (10s6p) Atomic Basis Sets for the FirstRow Atoms. *J. Chem. Phys.* 1971, 55, 716 - 723.

[167] Wachters, A. J. H. Gaussian Basis Set for Molecular Wave Functions Containing Third-Row Atoms. *J. Chem. Phys.* **1970**, 52, 1033 - 1036.

[168] Roothaan, C. C. J. Self-Consistent Field Theory for Open Shells of Electronic Systems. *Rev. Mod. Phys.* **1960**, 32, 179 - 185.

[169] Culot, P.; Dive, G.; Nguyen, V. H. and Ghuysen, J. M. A Quasi-Newton Algorithm for First-Order Saddle-Point Location. *Theor. Chim. Acta* **1992**, 82, 189 - 205.

[170] Schmidt, M. W.; Baldridge, K. K.; Boatz, J. A.; Elbert, S. T.; Gordon, M. S.; Jensen, J. H.; Koseki, S.; Matsunaga, N.; Nguyen, K. A.; S. J. Su; Windus, T.L.; Dupuis, M. and Montgomery, J. A. General Atomic and Molecular Electronic Structure System. *J. Comput. Chem.* **1993**, 14, 1347 - 1363.

[171] Gordon, M. S. and Schmidt, M. W. Theory and Applications of Computational Chemistry, the First Forty Years. *Elsevier, Amsterdam* **2005**, edited by Dykstra, C. E.; Frenking, G.; Kim, K. S. and Scuseria, G. E. Chap. 41, pp. 1167 - 1189.

[172] Muscat, J.; Swamy V. and Harrison N. M. First-Principles Calculations of the Phase Stability of $TiO_2$ *Phys. Rev. B* **2002**, 65, 224112 - 224126.

[173] Tsuchiya, T. and Whitten, J. L. Theoretical Study of the Molecular and Electronic Structures of $TiO_4H_4$, $Ti_2O_7H_6$, and $Ti_2O_6H_4$. *J. Phys. Chem. C* **2011**, 115, 1635 - 1642.

[174] Noufi, R. N.; Kohl, P. A. and Bard, A. J. Semiconductor Electrodes XV. Photoelectrochemical Cells with Mixed Polycrystalline $n$Type CdS CdSe Electrodes. *J. of electrochemical society* **1978**, 125, 375 - 379.

[175] Takizawa, T.; Watanabe, T. and Honda, K. Photocatalysis Through Excitation of Adsorbates. 2. A Comparative Study of Rhodamine B and Methylene Blue on Cadmium Sulfide. *J. Phys. Chem.* **1978**, 82, 1391 - 1396.

[176] Jaeger, C. D.; Fu-Ren, F.F. and Bard A. J. Semiconductor Electrodes. 26. Spectral Sensitization of Semiconductors with Phthalocyanine. *J. Am. Chem. Soc.* **1980**, 102, 2592 - 2598.

[177] Wilson, A. H. Thermodynamics and Statistical Mechanics. *Cambridge at the University Press* **1966**.

[178] Shjaee, E. and Mohammadizadeh, M. R. First-Principles Elastic and Thermal Properties of $TiO_2$: a Phonon Approach. *J. Phys.: Condens. Matter* **2010**, 22, 015401 - 015408.

[179] Dorofeeva, O. V.; Iorish, V. S; Novikov, V. P. and Neumann, D. V. NIST-JANAF Thermochemical Tables. II. Three Molecules Related to Atmospheric Chemistry: $HNO_3$, $H2SO_4$, and $H2O_2$. *J. Phys. Chem. Ref. Data* **2003**, 32, 879 - 901.

[180] Humphrey, W., Dalke, A. and Schulten, K. VMD: Visual Molecular Dynamics. *J. Molecular Graphics* **1996**, 14, 33 - 38.

[181] Myung, J. D.; Hye, K. I.; Lim, K. E.; Su, J. C.; Soon I. H.; Park, K. and Park, J. Transition-Metal Doping of Oxide Nanocrystals for Enhanced Catalytic Oxygen Evolution. *J. Phys. Chem. C* **2015**, 119, 1921 - 1927.

[182] Meng, Y.; Song, W.; Huang, H.; Ren, Z.; Chen, S. Y. and Suib, S. L. Structure-Property Relationship of Bifunctional $MnO_2$ Nanostructures: Highly Efficient, Ultra-Stable Electrochemical Water Oxidation and Oxygen Reduction Reaction Catalysts Identified in Alkaline Media. *J. Am. Chem. Soc.* **2014**, 136, 11452 - 11464.

[183] Liu, B.; Chen, H. M.; Liu, C.; Andrews, S. C.; Hahn, C. and Yang, P. Large-Scale Synthesis of Transition-Metal-Doped $TiO_2$ Nanowires with Controllable Overpotential. *J. Am. Chem. Soc.* **2013**, 135, 9995 - 9998.

[184] Resasco, J.; Dasgupta, N. P.; Roque, R. J.; Guo, J. and Yang, P. Uniform Doping of Metal Oxide Nanowires Using Solid State Diffusion. *J. Am. Chem. Soc.* **2014**, 136, 10521 - 10526.

[185] Szyja, B. M. and van Santen, R. A. Synergy Between $TiO_2$ and $Co_xO_y$ Sites in Electrocatalytic Water Decomposition. *Phys. Chem. Chem. Phys.* **2015**, 17, 12486 - 12491.

[186] Perron, H.; Domain, C.; Roques, J.; Drot, R.; Simoni, E. and Catalette, H. Optimization of Accurate Rutile $TiO_2$ (110), (100), (101) and (001) Surface Models from Periodic DFT Calculations. *Theor. Chem. Acc.* **2007**, 117, 565 - 574.

[187] Turner, J. A. Sustainable Hydrogen Production. *Science* **2004**, 305, 972 - 974.

[188] Kibsgaard, J. and Jaramillo, T. F. Molybdenum Phosphosulfide: an Active, Acid-Stable, Earth-Abundant Catalyst for the Hydrogen Evolution Reaction. *Angew. Chem. Int.* **2014**, 53, 14433 - 14437.

[189] Liang, H.-W.; Brüller, S.; Dong, R.; Zhang, J.; Feng, X. and Müllen, K. Molecular Metal-Nx Centers in Porous Carbon for Electrocatalytic Hydrogen Evolution. *Nature. Commun.* **2015**, 6, 7992 - 7999.

[190] Callejas, J. F.; Read, C. G.; Popczun, E. J.; McEnaney, J. M. and Schaak, R. E. Nanostructured $Co_2P$ Electrocatalyst for the Hydrogen Evolution Reaction and Direct Comparison with Morphologically Equivalent CoP. *Chem. Mater.* **2015**, 27, 3769 - 3774.

[191] Tang, Y. J.; Wang, Y.; Wang, X. L.; Li, S. L.; Huang, W.; Dong, L. Z.; Liu, C. H.; Li, Y. F. and Lan, Y. Q. Molybdenum Disulfide/Nitrogen-Doped Reduced Graphene Oxide Nanocomposite with Enlarged Interlayer Spacing for Electrocatalytic Hydrogen Evolution. *Adv. Energy Mater.* **2016**, 6, 1600116 - 1600122.

[192] Jaramillo, T. F.; Jørgensen, K. P.; Bonde, J.; Nielsen, J. H.; Horch, S. and Chorkendorff, I. Identification of Active Edge Sites for Electrochemical $H_2$ Evolution from $MoS_2$ Nanocatalysts. *Science* **2007**, 317, 100 - 102.

[193] Fan, X.; Peng, Z.; Ye, R.; Zhou, H. and Guo, X. $M_3C$ (M: Fe, Co, Ni) Nanocrystals Encased in Graphene Nanoribbons: An Active and Stable Bifunctional Electrocatalyst for Oxygen Reduction and Hydrogen Evolution Reactions. *ACSNano* **2015**, 9, 7407 - 7418.

[194] Wang, H.; Kong, D.; Johanes, P.; Cha, J. J.; Zheng, G.; Yan, K.; Liu, N. and Cui, Y. $MoSe_2$ and $WSe_2$ Nanofilms with Vertically Aligned Molecular Layers on Curved and Rough Surfaces. *Nano Letters* **2013**, 13, 3426 - 3433.

[195] Vrubel, H. and Hu, X. L. Molybdenum Boride and Carbide Catalyze Hydrogen Evolution in Both Acidic and Basic Solutions. *Angew. Chem. Int.* **2012**, 51, 12703 - 12706.

[196] Gao, M. R.; Liang, J. X.; Zheng, Y. R.; Xu, Y. F.; Jiang, J.; Gao, Q.; Li, J. and Yu, S. H. An Efficient Molybdenum Disulfide/Cobalt Diselenide Hybrid Catalyst for Electrochemical Hydrogen Generation. *Nature Commun.* **2015**, 6, 5982 - 5988.

[197] Ma, F. X.; Wu, H. B.; Xia, B. Y.; Xu, C. Y. and Lou, X. W. Hierarchical $\beta$-$Mo_2C$ Nanotubes Organized by Ultrathin Nanosheets as a Highly Efficient Electrocatalyst for Hydrogen Production. *Angew. Chem. Int. Ed. Engl.* **2015**, 54, 15395 - 15399.

[198] Ma, L.; Ting, L. R. L.; Molinari, V.; Giordano, C. and Yeo, B. S. Efficient Hydrogen Evolution Reaction Catalyzed by Molybdenum Carbide and Molybdenum Nitride Nanocatalysts Synthesized via the Urea Glass Route. *J. Mater. Chem. A* **2015**, 3, 8361 - 8368.

[199] Xiao, P.; Ge, X.; Wang, H.; Liu, Z.; Fisher, A. and Wang, X. Novel Molybdenum Carbide-Tungsten Carbide Composite Nanowires and their Electrochemical Activation for Efficient and Stable Hydrogen Evolution. *Adv. Funct. Mater.* **2015**, 25, 1520 - 1526.

[200] Wan, C.; Regmi, Y. N. and Leonard, B. M. Multiple Phases of Molybdenum Carbide as Electrocatalysts for the Hydrogen Evolution Reaction. *Angew. Chem.* **2014**, 126, 6525 - 6528.

[201] Wu, H. B.; Xia, B. Y.; Yu, L.; Yu, X. Y. and Lou, X. W. D. Porous Molybdenum Carbide Nano-Octahedrons Synthesized via Confined Carburization in Metal-Organic Frameworks for Efficient Hydrogen Production. *Nat. Commun.* **2015**, 6, 6512 - 6519.

[202] Ma, R.; Zhou, Y.; Chen, Y.; Li, P.; Liu, Q. and Wang, J. Ultrafine Molybdenum Carbide Nanoparticles Composited with Carbon as a Highly Active Hydrogen Evolution Electrocatalyst. *Angew. Chem. Int.* **2015**, 54, 14723 - 14727.

[203] Smith, R. D. L. and Berlinguette, C. P. Accounting for the Dynamic Oxidative Behavior of Nickel Anodes. *J. Am. Chem. Soc.* **2016**, 138, 1561 - 1567.

[204] Li, Y. H.; Liu, P. F.; Pan, L. F.; Wang, H. F.; Yang, Z. Z.; Zheng, L. R.; Hu, P.; Zhao, H. J.; Gu, L. and Yang, H. G. Local Atomic Structure Modulations Activate Metal Oxide as Electrocatalyst for Hydrogen Evolution in Acidic Water. *Nat. Commun.* **2015**, 6, 8064 - 8070.

[205] He, C. and Tao, J. Synthesis of Nanostructured Clean Surface Molibdenum Carbides on Graphene Sheets as Efficient and Stable Hydrogen Evolution Reaction Catalysts. *Chem. Commun.* **2015**, 51, 8323 - 8325.

[206] Villars, P. Pauling File in: Inorganic Solid Phases. *Springer-Verlag GmbH, Heidelberg* **2016**, Dataset ID: sd_0452157.

[207] Youn, D. H.; Han, S.; Kim, J. Y.; Kim, J. Y.; Park, H.; Choi, S. and Lee, J. S. Highly Active and Stable Hydrogen Evolution Electrocatalysts Based on Molybdenum Compounds on Carbon Nanotube-Graphene Hybrid Support. *ACS Nano* **2014**, 8, 5164 - 5173.

[208] Gokhale, A. A.; Dumesic, J. A. and Mavrikakis, M. On the Mechanism of Low-Temperature Water Gas Shift Reaction on Copper. *J. Am. Chem. Soc.* **2008**, 130, 1402 - 1414.

[209] Rossmeisl, J.; Chan, K.; Skúlason, E.; Björketun, M. E. and Tripkovic, V. On the *pH* Dependence of Electrochemical Proton Transfer Barriers. *Catalysis Today* **2016**, 262, 36 - 40.

[210] Kresse, G. and Hafner, J. Ab Initio Molecular Dynamics for Liquid Metals. *Phys. Rev. B* **1993**, 47, 558 - 561.

[211] Kresse, G. and Furthmuller, J. Efficiency of Ab-Initio Total Energy Calculations for Metals and Semiconductors Using a Plane-Wave Basis Set. *Comput. Mater. Sci.* **1996**, 6, 15 - 50.

[212] Kresse, G.; Furthmuller, J. Efficient Iterative Schemes for Ab Initio Total-Energy Calculations Using a Plane-Wave Basis Set. *Phys.Rev. B* **1996**, 54, 11169 - 11186.

[213] Kresse, G.; Joubert, D. From Ultrasoft Pseudopotentials to the Projector Augmented-Wave Method. *Phys. Rev. B* **1999**, 59, 1758 - 1775.

[214] Blöchl, P. E. Projector Augmented-Wave Method. *Phys. Rev. B* **1994**, 50, 17953 - 17979.

[215] Perdew, J. D.; Burke, K. and Ernzerhof, M. Generalized Gradient Approximation Made Simple. *Phys. Rev. Lett.* **1996**, 77, 3865 - 3868.

[216] Li, J. S.; Wang, Y.; Liu, C. H.; Li, S. L.; Wang, Y. G.; Dong, L. Z.; Dai, Z. H.; Li, Y. F. and Lan Y. Q. Coupled Molybdenum Carbide and Reduced Graphene Oxide Electrocatalysts for Efficient Hydrogen Evolution. *Nat. Commun.* **2016**, 7, 11204 - 11211.

[217] Muhammad, R.; Shuai, Y. and Tan, H. P. First-Principles Study on Hydrogen Adsorption on Nitrogen Doped Graphene. *Physica E* **2017**, 88, 115 - 124.

[218] Rudy, E.; Windisch, S.; Stosick, A. J. and Hoffman, J. R. The Constitution of Binary Molybdenum-Carbon Alloys. *Transactions of the Metallurgical Soc. of AIME* **1967**, 239, 1247 - 1267.

[219] Cruz-Olvera, D. and Calaminici, P. Investigation of Structures and Energy Properties of Molybdenum Carbide Clusters: Insight from Theory. *Comp. and Theo. Chem.* **2016**, 1078, 55 - 64.

[220] Chisholm, M. H.; Cotton, F. A.; Frenz, B. A.; Reichert, W. W.; Shive, L. W. and Stults, B. R. The Molybdenum-Molybdenum Triple Bond. 1. Hexakis (Dimethylamido) Molybdenum and Some Homologues: Preparation, Structure, and Properties. *J. Am. Chem. Soc.* **1975**, 98, 4469 - 4476.

[221] Huang, Y.; Nielsen, R. J.; Goddard, W. A. $3^{rd}$ and Soriaga, M. P. The Reaction Mechanism with Free Energy Barriers for Electrochemical Dihydrogen Evolution on $MoS_2$. *J. Am. Chem. Soc.* **2015**, 137, 6692 - 6698.

[222] Hoffmann, R. An Extended Hückel Theory. I. Hydrocarbons. *J. Chem. Phys.* **1963**, 39, 1397 - 1412.

[223] Huzinaga, S.; Andzelm, J.; Klobukowski, M.; Radzio-Andzelm, E.; Sakai Y. and Tatewaki, H. Gaussian Basis Sets for Molecular Calculations. *Elsevier, Amsterdam* **1984**.

# Acknowledgements

I have not walked alone through this journey, which is reaching the end within the present thesis. It had not been possible to arrive at this point without the help and support of many people and institutions. These lines are dedicated to express my heartfelt gratitude to all of them, even though I am convinced there would not be space in a sheet of paper to communicate all the recognition they deserve.

First of all I am profoundly grateful to my supervisor Prof. Dr. habil. Gotthard Seifert for allow me to work in his group. He dedicated time and effort to make possible all my stays in Dresden, far beyond from the scientific work. Thank you very much for all your support and concern!

I would like to thank Prof. Dr. Sibylle Gemming for accepting to be the co-referee of this thesis.

I am very much in debt with Dr. Diana C. Tranca. Her aid and support have been of invaluable importance in my research. She has taught me a lot, since the technical details of the electronic structure packages: GAMESS and VASP, many others softwares of remarkable importance in the everyday work of a theoretical chemist (e.g., Molden, XCrySDen and VMD) and additional soft skills like scientific writing. Moreover, she has been always close to look after every single problem I have had in my research. Besides the professional duties, she was always happy to help me in any other issue I could have in my private life like house hunting or many other duties separate from the university responsibilities. I do not have words to thank her for all the support from my very first stay in Dresden in 2014 to the present day.

My sincere gratitude goes to Prof. Dr. Aliezer Martínez Mesa and Prof. Dr. Llinersy Uranga Piña, my supervisors from the University of Havana. They arranged everything, in collaboration with Prof. Dr. habil. Gotthard Seifert, for my first application as a fellow student of the International Max Planck Research School (IMPRS) at the Max Plank Institute for the Physics of Complex Systems (MPIPKS). They have followed very closely my development as a Ph.D. student, have contributed to my research and have supported me in many aspects during this time, specially in my stays in Cuba. Scientifically speaking, I owe you much of what I am today!

Special thanks are devoted to our secretary Mrs. Antje Völkel for her support and assistant in many situations, ranging from advices for the registration at the TU-Dresden to several translations of German documents, and to DP Knut Vietze for his active disposal to solve any problem with the computers, and his advices concerning the scientific calculations. Thanks a lot to both of you!

I would like to say that being part of the IMPRS has represented a great experience for me. I am really thankful for its financial support, which made possible my stays in Dresden since 2014. Besides that, I have broadened my knowledge about the current state of the Theoretical Physics to treat atoms, molecules and solids, attending lectures, seminars, scientific workshops and schools organized by the IMPRS. For the organization of all these activities and keeping such a nice scientific atmosphere I would like to thank all the coordinators of the IMPRS during this time: Dr. Michael Genkin, Dr. habil. Anatole Kenfack and Dr. Paul McClarty. I thank The University of Havana for allow me to go in alternate semesters to work in my research, and the Technische Universität Dresden for hosting me as such a “part time" Ph.D. student.

What is life without friends and family? These lines are dedicated to all of them. I express my gratitude to all my friends from Cuba and from Dresden. I thank to the present and former members of the Prof. Seifert’s group at TU-Dresden, since 2014, for such a nice scientific environment. Special thanks are given to Dr. Tsegabirhan Berhane Wendumu, who helped me to give my first steps in Dresden, M.Sc. Kai Trepte and Dr. Jens Kunstmann, with whom I have shared so many afternoon coffees and have gotten several advices for the paper work and the preparation of the manuscript of my Ph.D. thesis.

Last but not at all least, I would like to appreciate here how much my family has to do with the accomplishment of this goal. I highly value the memory of my mother, to whom everything I do is dedicated, for encourage me to be a better man everyday. I thank the patience and support at any situation from my father and sister during all these years of study, as well as from my family in America, specially my aunt Cary. Deep thanks are due to my girlfriend Laura for such a great patience, understanding and love during the last two years of this important project. I love you all!

## Declaration according to Doctorate Regulations §5 paragraph 1 No. 5a)

I herewith declare that I have produced this paper without the prohibited assistance of third parties and without making use of aids other than those specified; notions taken over directly or indirectly from other sources have been identified as such. This paper has not previously been presented in identical or similar form to any other German or foreign examination board.

## Declaration according to Doctorate Regulations §5 paragraph 1 No. 5b)

The present dissertation has been produced at the Technische Universität Dresden (Faculty of Mathematics and Natural Sciences, Institute for Physical Chemistry, Chair of Theoretical Chemistry) under the supervision of Prof. Dr. rer. nat. habil. Gotthard Seifert.

Dresden,